

## The Brown Dwarf Kinematics Project (BDKP). V. Radial and Rotational Velocities of T Dwarfs from Keck/NIRSPEC High-Resolution Spectroscopy

CHIH-CHUN HSU,<sup>1</sup> ADAM J. BURGASSER,<sup>1</sup> CHRISTOPHER A. THEISSEN,<sup>1,\*</sup> CHRISTOPHER R. GELINO,<sup>2,3</sup>  
 JESSICA L. BIRKY,<sup>1,4</sup> SHARON J. M. DIAMANT,<sup>5</sup> DANIELLA C. BARDALEZ GAGLIUFFI,<sup>6</sup> CHRISTIAN AGANZE,<sup>1</sup>  
 CULLEN H. BLAKE,<sup>7</sup> AND JACQUELINE K. FAHERTY<sup>8</sup>

<sup>1</sup>*Center for Astrophysics and Space Science, University of California San Diego, La Jolla, CA 92093, USA*

<sup>2</sup>*NASA Exoplanet Science Institute, Mail Code 100-22, California Institute of Technology, 770 South Wilson Avenue, Pasadena, CA 91125, USA*

<sup>3</sup>*Infrared Processing and Analysis Center, Mail Code 100-22, California Institute of Technology, 1200 E. California Boulevard, Pasadena, CA 91125, USA*

<sup>4</sup>*Department of Astronomy, University of Washington, Seattle, WA 98195, USA*

<sup>5</sup>*Leiden Observatory, Leiden University, Leiden, the Netherlands*

<sup>6</sup>*Department of Astrophysics, American Museum of Natural History, NY, NY 10024*

<sup>7</sup>*University of Pennsylvania Department of Physics and Astronomy, 209 S 33rd St, Philadelphia, PA 19104, USA*

<sup>8</sup>*Department of Astrophysics, American Museum of Natural History, Central Park West at 79th Street, NY 10024, USA*

Submitted to ApJS

### ABSTRACT

We report multi-epoch radial velocities, rotational velocities, and atmospheric parameters for 37 T-type brown dwarfs observed with Keck/NIRSPEC. Using a Markov Chain Monte Carlo forward-modeling method, we achieve median precisions of  $0.5 \text{ km s}^{-1}$  and  $0.9 \text{ km s}^{-1}$  for radial and rotational velocities, respectively. All of the T dwarfs in our sample are thin disk brown dwarfs. We confirm previously reported moving group associations for four T dwarfs. However, the lack of spectral indicators of youth in two of these sources suggests that these are chance alignments. We confirm two previously un-resolved binary candidates, the T0+T4.5 2MASS J11061197+2754225 and the L7+T3.5 2MASS J21265916+7617440, with orbital periods of 4 yr and 12 yr, respectively. We find a kinematic age of  $3.5 \pm 0.3 \text{ Gyr}$  for local T dwarfs, consistent with nearby late-M dwarfs ( $4.1 \pm 0.3 \text{ Gyr}$ ). Removal of thick disk L dwarfs in the local ultracool dwarf sample gives a similar age for L dwarfs ( $4.2 \pm 0.3 \text{ Gyr}$ ), largely resolving the local L dwarf age anomaly. The kinematic ages of local late-M, L, and T dwarfs can be accurately reproduced with population simulations incorporating standard assumptions of the mass function, star formation rate, and brown dwarf evolutionary models. A kinematic dispersion break is found at the L4–L6 subtypes, likely reflecting the terminus of the stellar Main Sequence. We provide a compilation of precise radial velocities for 172 late-M, L, and T dwarfs within  $\sim 20 \text{ pc}$  of the Sun.

*Keywords:* brown dwarfs -- stars: kinematics and dynamics – stars: low-mass – techniques: radial velocities

### 1. INTRODUCTION

Ultracool dwarfs (UCDs) are low-mass ( $M < 0.1 M_{\odot}$ ) stellar and substellar objects with effective temperatures  $T_{\text{eff}} \leq 3,000 \text{ K}$  and spectral types M7 or later, encom-

passing late-M, L, T, and Y dwarfs (Kirkpatrick 2005; Cushing et al. 2011). UCDs are abundant in the Galaxy (20–50% of all stars; Bochanski et al. 2007; Kirkpatrick et al. 2019) and have lifetimes orders of magnitude longer than the current age of the Universe (Laughlin et al. 1997). Every UCD ever formed still exists. UCDs thus provide a means of investigating the low-mass star formation and chemical enrichment history of the Milky Way and its substructures (Bochanski et al. 2007; Burgasser 2009). Substellar UCDs, or brown dwarfs ( $M <$

Corresponding author: Chih-Chun Hsu  
 chh194@ucsd.edu

\* NASA Sagan Fellow

$0.072 M_{\odot}$ ; Kumar 1963; Hayashi & Nakano 1963), cannot sustain hydrogen fusion in their cores and cool over time. The evolutionary nature of brown dwarfs makes them useful tracers of age in various populations. Brown dwarfs have been used to age-date young clusters (Stauffer et al. 1998; Martín et al. 2018) and binaries (Song et al. 2002), and could potentially be used to age-date other Galactic populations, such as globular clusters and the Galactic halo (Burgasser 2009; Caiazzo et al. 2017).

In mixed populations such as the Galactic disk, the overlapping temperatures and luminosities of stellar and substellar UCDs results in an observational age-mass degeneracy, requiring additional diagnostics to disentangle these parameters. High-resolution spectroscopy provides several ways of doing this. Precise radial velocities (RVs) can uncover binaries with periodically variable RVs from which masses can be inferred (Basri & Martín 1999; Reid et al. 2002; Joergens & Müller 2007; Blake et al. 2008, 2010; Konopacky et al. 2010; Burgasser et al. 2012, 2015a, 2016). Kinematics can identify UCD members of young clusters and moving groups, yielding an age by association (Zuckerman & Song 2004; Gagné et al. 2015b). Kinematic association with the Galactic thin disk, thick disk, or halo can also provide coarse age constraints (Bensby et al. 2003; Pinfield et al. 2014). As the velocity dispersion of field stars increases over time due to diffuse dynamical scattering with Galactic structures, kinematics can also provide a statistical measure of age for a given population (Wielen 1977; Aumer & Binney 2009). Finally, the magnetized winds of low-mass stars reduces stellar rotation over time. Gyrochronology relations can be applied to rotational velocities ( $v \sin i$ ) or periods to infer ages (Barnes 2003; Angus et al. 2019), although it is unclear how low in mass these relations can be applied (Reiners & Basri 2009; Irwin et al. 2011; McQuillan et al. 2013; Newton et al. 2018; Popinchalk et al. 2021).

The study of UCD populations must account for the evolution of brown dwarfs. Typical analyses make use of population simulations incorporating stellar and substellar evolution to model present-day observables (Reid et al. 1999; Burgasser 2004; Kirkpatrick et al. 2019). A consistent prediction of these simulations is that L-type UCDs, a mix of stars and rapidly-cooling brown dwarfs ( $\tau \approx 0.5$ –1 Gyr; Burrows et al. 1997; Baraffe et al. 2003), should be on average younger than late M-type UCDs, which are predominantly long-lived stars (Reid et al. 1999; Burgasser 2004; Allen et al. 2005; Ryan et al. 2017). Observations of statistical ages through kinematics have mostly contradicted this prediction. In one of

the first 3D kinematic studies of UCDs, combining RVs and tangential velocities, Zapatero Osorio et al. (2007) did find that local L and T dwarfs had a lower velocity dispersion than local late-M dwarfs, although the sample for the former included only 21 sources. A 2D proper motion survey of 277 UCDs by Faherty et al. (2009) found local 20 pc L dwarfs to be marginally older than late-M and T dwarfs, while their whole sample of 841 UCDs gave consistent ages. Schmidt et al. (2010) identified both young and old L dwarf populations in a 3D kinematic survey of over 300 sources using low-resolution spectroscopy. The diagnostic power of these early studies was limited by incomplete samples and relatively low-precision measurements ( $\sigma_{\text{RV}} \gtrsim 5$ –10 km s $^{-1}$ ).

Subsequent volume-limited 3D kinematic surveys of late-M and L dwarfs using high-resolution spectra and improved astrometry have consistently found the local L dwarf population to be significantly more dispersed and hence older than the late-M dwarfs, in disagreement with simulation predictions (Reiners & Basri 2009; Seifahrt et al. 2010; Blake et al. 2010; Burgasser et al. 2015b). The most recent study by Burgasser et al. (2015b) attempted to explain this discrepancy as an evolution of the mass function over time, with a greater abundance of brown dwarfs at earlier ages. While this ansatz was able to correctly predict the relative ages of late-M and L dwarfs, the actual ages and corresponding mass function were inconsistent with observations. Whether this persistent disagreement between simulated and observed ages of L dwarfs arises from a more complex star and brown dwarf formation history, a problem with brown dwarf evolutionary models, or incompleteness or bias in the local UCD sample remains uncertain.

The kinematics of local T dwarfs can provide clarity on this issue. These low-temperature, evolved brown dwarfs having cooling ages of several Gyr, and are predicted to be kinematically older than L dwarfs (Burgasser 2004). T dwarfs are also intrinsically fainter than late-M and L dwarfs, limiting the number of sources with suitable high-precision RV measurements. While there are more than 500 T dwarfs currently known, there are fewer than 15 T dwarfs with precise RV ( $\sigma_{\text{RV}} \leq 3$  km s $^{-1}$ ) and rotational velocity ( $\sigma_{v \sin i} \leq 5$  km s $^{-1}$ ) measurements reported in the literature (Zapatero Osorio et al. 2006, 2007; Prato et al. 2015; Gagné et al. 2017, 2018a; Vos et al. 2017, 2018). This sample is insufficient to accurately measure kinematic dispersions and ages, or test population simulations. The lack of precise RV

## RADIAL AND ROTATIONAL VELOCITIES OF T DWARFS

Table 1. NIRSPEC T Dwarf Sample

Source Name	Coordinates (J2000)	SpT	2MASS $J$ (mag)	$J - K$ (mag)	$\mu_{\alpha}$ (mas yr $^{-1}$ )	$\mu_{\delta}$ (mas yr $^{-1}$ )	$d$ (pc)	Published RV (km s $^{-1}$ )	Published $v \sin i$ (km s $^{-1}$ )	References <sup>a</sup>
J0000+2354	00 00 13.54 +23 54 18.0	T4.5	15.06 ± 0.04	0.22 ± 0.13	-19 ± 2	127 ± 1	14.12 ± 0.38	...	...	(18, 14, 13)
J0034+0323	00 34 51.58 +03 23 05.1	T6.5	15.140 ± 0.04	-0.933 ± 0.03	674 ± 1	178 ± 2	8.42 ± 0.19	...	...	(8, 10, 35)
J0134+0933 <sup>b</sup>	01 36 56.56 +09 33 47.3	T2.5	13.46 ± 0.03	0.68 ± 0.04	1238 ± 1	-16 ± 0	6.12 ± 0.02	11.5 ± 0.4	50.9 ± 0.8	(1, 14, 33, 39)
J0150+3827	01 50 09.97 +38 27 35.9	T0	16.11 ± 0.08	1.63 ± 0.1	881 ± 1	-120 ± 1	22.42 ± 1.61	...	...	(17, 35)
J0213+3848	02 13 19.86 +36 48 38.0	T3	15.3 ± 0.5	0.5 ± 0.5	65 ± 65	0 ± 0	14.28 ± 0.04	...	...	(12, 32)
J0243-2453	02 43 13.72 -24 53 29.8	T6	15.38 ± 0.05	0.17 ± 0.18	-288 ± 4	-208 ± 3	10.68 ± 0.41	...	...	(5, 14, 31)
J0415-0935	04 15 19.54 -09 35 06.7	T8	15.7 ± 0.1	0.3 ± 0.2	2214 ± 1	536 ± 1	5.71 ± 0.06	49.6 ± 1.2	33.5 ± 2.0	(5, 13, 43)
J0559-1404	05 59 19.19 -14 04 39.2	T4.5	13.8 ± 0.02	0.23 ± 0.06	571 ± 1	-338 ± 1	10.5 ± 0.08	-9.0 ± 3.0	20.1 ± 4.8	(5, 20, 33, 41)
J0627-1114	06 27 20.08 -11 14 24.1	T6	15.49 ± 0.05	0.06 ± 0.19	-13 ± 1	-338 ± 1	13.37 ± 0.64	...	...	(17, 34)
J0629+2418	06 29 05.12 +24 18 08.7	T2s <sub>b</sub> e	15.89 ± 0.09	0.72 ± 0.18	-35 ± 4	-368 ± 4	26.67 ± 2.35	...	...	(23, 35)
J0755+2212	07 55 47.95 +22 12 16.9	T5	15.73 ± 0.06	0.0 ± 0.2	-21 ± 1	-256 ± 1	14.84 ± 0.7	...	...	(5, 35)
J0819-0335	08 19 58.21 -03 35 26.6	T4	14.99 ± 0.04	0.41 ± 0.11	-199 ± 3	-166 ± 2	14.01 ± 0.43	...	...	(17, 29, 35)
J0909+6325	09 09 00.86 +65 25 27.6	T1.5+T2.5 <sup>e</sup>	16.03 ± 0.09	0.86 ± 0.17	-223 ± 1	-120 ± 1	15.65 ± 0.96	...	...	(10, 9, 35)
J0937+2931	09 37 34.88 +29 31 41.0	T6	14.65 ± 0.04	-0.62 ± 0.13	973 ± 6	-1298 ± 5	6.12 ± 0.07	-5.0 ± 3.0	60 ± 10.0	(5, 14, 31, 41)
J1106+2754	11 06 11.92 +27 54 21.6	T0+T4.5f	14.82 ± 0.04	1.02 ± 0.07	-271 ± 1	-452 ± 1	20.3 ± 0.5	...	...	(21, 9, 33)
J1217-0311	12 17 11.10 -03 11 13.2	T7.5	15.86 ± 0.06	-0.03 ± 0.07	-1054 ± 2	76 ± 2	11.01 ± 0.27	5.0 ± 1.6	31.4 ± 2.1	(3, 25, 14, 31, 43)
J1225-2739	12 25 54.32 -27 39 46.7	T5.5+T8f	15.26 ± 0.05	0.19 ± 0.16	385 ± 3	-628 ± 2	13.32 ± 0.44	...	...	(3, 13, 14, 31)
J1254-0122	12 54 53.90 -01 22 47.3	T2 <sub>e</sub>	14.89 ± 0.04	1.05 ± 0.06	-492 ± 4	111 ± 3	13.48 ± 0.42	4.0 ± 3.0	27.3 ± 2.5	(19, 6, 32, 41)
J1324+6358 <sup>c</sup>	13 24 33.86 +63 58 30.7	T2p	15.6 ± 0.07	1.54 ± 0.09	-364 ± 2	-72 ± 2	10.03 ± 0.56	-23.7 ± 0.4	11.5 ± 1.0	(21, 17, 35, 40)
J1331-0116	13 31 48.95 -01 16 50.1	T0	15.46 ± 0.04	1.39 ± 0.08	-422 ± 6	-1039 ± 5	20.0 ± 2.0	...	...	(15, 26, 37)
J1346-0031	13 46 46.35 -00 31 50.1	T6.5	16.0 ± 0.1	0.23 ± 0.29	-503 ± 3	-114 ± 2	14.64 ± 0.49	-23.1 ± 1.5	< 15	(3, 9, 14, 31, 43)
J1457-2122	14 57 14.96 -21 21 47.8	T8	15.32 ± 0.05	0.08 ± 0.16	1034 ± 2	-1726 ± 1	5.91 ± 0.06	28.9 ± 2.4	28.6 ± 2.4	(4, 38, 31, 43)
J1503+2225	15 03 19.61 +25 25 19.8	T5.5	13.94 ± 0.02	-0.03 ± 0.06	87 ± 1	558 ± 1	6.42 ± 0.03	-40.5 ± 2.1	32.8 ± 2.0	(7, 33, 43)
J1506+7027	15 06 52.44 +70 27 25.1	T6	13.7 ± 0.03	-0.09 ± 0.07	-1194 ± 1	1042 ± 1	5.16 ± 0.02	...	...	(16, 17, 33)
J1520+3546	15 20 39.75 +35 46 21.0	T0	15.54 ± 0.06	1.54 ± 0.08	315 ± 2	-378 ± 2	13.59 ± 1.05	...	...	(10, 14, 35)
J1553+1532	15 53 02.28 +15 32 36.9	T6.5+T7.5f	15.83 ± 0.07	0.32 ± 0.2	-386 ± 1	166 ± 1	13.32 ± 0.16	-32.9 ± 3.0	29.4 ± 2.3	(5, 13, 43)
J1624+0029	16 24 14.37 +00 29 15.8	T6	15.49 ± 0.05	-0.02 ± 0.07	-373 ± 2	-9 ± 2	11.0 ± 0.15	-30.7 ± 3.0	38.5 ± 2.0	(27, 5, 14, 31, 43)
J1629+0335	16 29 18.41 +03 35 37.1	T2	15.29 ± 0.04	1.11 ± 0.07	234 ± 2	-144 ± 2	12.99 ± 0.67	...	...	(11, 24, 28, 29)
J1809-0448	18 09 52.56 -04 48 08.1	T1	15.14 ± 0.05	1.18 ± 0.08	-54 ± 2	-402 ± 5	20.33 ± 1.2	...	...	(2, 35)
J1928+2356	19 28 41.55 +23 56 01.6	T6	14.34 ± 0.06	0.25 ± 0.08	-248 ± 1	239 ± 1	6.46 ± 0.08	...	...	(24, 35)
J1952+7240 <sup>d</sup>	19 52 46.66 +72 40 00.8	T4	15.09 ± 0.05	0.44 ± 0.09	-294 ± 1	-355 ± 2	12.1 ± 0.3	...	...	(17, 28)
J2030+0749	20 30 42.33 +07 49 35.8	T1.5	14.22 ± 0.03	0.91 ± 0.05	664 ± 1	-712 ± 1	9.73 ± 0.08	...	...	(24, 33)
J2128+7617	21 26 59.14 +76 17 43.3	Top <sup>f</sup>	14.34 ± 0.03	1.18 ± 0.05	756 ± 1	822 ± 1	16.35 ± 0.16	...	...	(16, 17, 33)
H N Peg B	21 44 31.33 +14 46 18.9	T2.5	15.86 ± 0.03	0.46 ± 0.03	231 ± 0	-113 ± 0	18.13 ± 0.01	...	...	(22, 33)
J2236+5105	22 36 16.86 +51 05 48.7	T5	14.58 ± 0.04	0.13 ± 0.1	729 ± 2	324 ± 2	9.97 ± 0.36	...	...	(2, 35)
J2254+3123	22 54 18.92 +31 23 49.8	T5	15.26 ± 0.05	0.36 ± 0.15	60 ± 3	387 ± 2	13.89 ± 0.58	14.0 ± 3.0	15 ± 5.0	(5, 28, 36, 41)
J2356-1553	23 56 54.77 -15 53 11.1	T6	15.82 ± 0.06	0.05 ± 0.19	-423 ± 4	-616 ± 4	13.44 ± 1.05	19.0 ± 3.0	15 ± 5.0	(5, 31, 41)

Table 1 *continued*

**Table 1** (*continued*)

Source Name	Coordinates (J2000)	SpT	2MASS $J$ (mag)	$J - K$	$\mu_\alpha$ (mas yr $^{-1}$ )	$\mu_\delta$ (mas yr $^{-1}$ )	$d$ (pc)	Published RV (km s $^{-1}$ )	Published $v \sin i$ (km s $^{-1}$ )	References <i>a</i>
-------------	------------------------	-----	--------------------	---------	-----------------------------------	-----------------------------------	-------------	---------------------------------	---	---------------------

*a* References are in the order of discovery, classification, astrometry, previously published RV and  $v \sin i$  measurements.

*b* Previously identified as a member of the Carina-Near moving group.

*c* Previously identified as a member of the AB Doradus moving group.

*d* Distance is estimated using  $M_J$ /spectral type relation in Dupuy & Liu (2012).

*e* Suspected binary based on blended light spectrum; the component types are estimated to be L7+T5.5 for J0629+2418 (Mace et al. 2013) and T1.5+T2.5 for J0909+6525 (Burgasser et al. 2010).

*f* Confirmed binary as reported in Burgasser et al. (2003c, 2006b, 2010); Kirkpatrick et al. (2010); Dupuy & Liu (2012); and this paper

**References**—Source discovery/classification: (1) Artigau et al. (2006), (2) Best et al. (2013), (3) Burgasser et al. (2003a), (4) Burgasser et al. (1999), (5) Burgasser et al. (2000a), (6) Burgasser et al. (2002), (7) Burgasser et al. (2003b), (8) Burgasser et al. (2004), (9) Burgasser et al. (2010), (10) Chin et al. (2006), (11) Deacon et al. (2011), (12) Deacon et al. (2017), (13) Dupuy & Liu (2012), (14) Faherty et al. (2009), (15) Hawley et al. (2002), (16) Kirkpatrick et al. (2011), (18) Knapp et al. (2004), (19) Leggett et al. (2000), (20) Liu et al. (2006), (21)Looper et al. (2007), (22) Luhman et al. (2006), (23) Mace et al. (2013), (24) Mace (2014), (25) Metchev et al. (2008), (26) Schneider et al. (2014), (27) Strauss et al. (1999), Source astrometry: (28) Best et al. (2018), (29) Best et al. (2020a), (30) Dupuy & Liu (2017), (31) Faherty et al. (2012), (32) Gaia Collaboration et al. (2018), (33) Gaia Collaboration et al. (2020), (34) Kirkpatrick et al. (2019), (35) Kirkpatrick et al. (2021), (36) Manjavacas et al. (2013), (37) Smart et al. (2018), (38) Weinberger et al. (2016), Source previously published RV and  $v \sin i$ : (39) Gagné et al. (2017), (40) Gagné et al. (2018a), (41) Prato et al. (2015), (42) Zapatero Osorio et al. (2006), (43) Zapatero Osorio et al. (2007)

**Table 2.** NIRSPEC T Dwarf Observing Log

Source	Program PI	UT Date	UT Time <sup>a</sup> (hh:mm:ss)	Integration <sup>b</sup> (s)	Airmass <sup>a</sup>	Filter <sup>d</sup>	Slit	Angle <sup>a</sup> (deg)	Echelle	Cross-disperser	Barycentric Correction (km s <sup>-1</sup> )
J0000+2554 <sup>c</sup>	Burgasser	2019-10-17	08:39:13	2 × 1500	1.01	N3	0''.432×12	62.97	34.09	34.09	-6.329
J0034+0523 <sup>c</sup>	Burgasser	2020-09-03	08:39:31	2 × 1400	1.62	N3	0''.432×12	62.98	34.09	34.09	14.315
J0136+0933	McLean	2008-12-04	04:38:53	4 × 600	1.21	N3	0''.432×12	63.00	34.08	34.08	-21.792
...	Burgasser	2013-10-16	11:42:53	2 × 900	1.08	N7	0''.432×12	62.97	35.47	35.47	0.857
...	Burgasser	2016-02-03	05:04:31	2 × 750	1.15	N7	0''.432×12	63.03	35.46	35.46	-29.081
J0150+3827 <sup>c</sup>	Burgasser	2020-08-05	13:56:36	2 × 1500	1.10	N7	0''.432×12	62.98	35.73	35.73	26.588
J0213+3648 <sup>c</sup>	Burgasser	2020-09-03	10:08:18	1 × 750	1.54	N3	0''.432×12	62.98	34.09	34.09	24.419
J0243-2453 <sup>c</sup>	Burgasser	2021-01-01	05:27:08	2 × 1800	1.45	N3	0''.432×12	62.95	34.06	34.06	-22.462
J0415-0935	Martín	2005-10-26	12:55:37	2 × 600	1.16	N3	0''.432×12	63.00	34.08	34.08	11.18
...	Wainscoat	2006-01-18	09:01:02	2 × 600	1.39	N3	0''.432×12	63.00	34.08	34.08	-22.389
J0559-1404	Engineering	2000-10-10	13:53:03	4 × 600	1.27	N3	0''.576×12	63.00	34.08	34.08	22.527
...	McLean	2001-10-09	15:06:35	2 × 600	1.20	N3	0''.432×12	63.00	34.08	34.08	22.564
...	Rayner	2001-11-02	13:17:34	10 × 300	1.21	N3	0''.432×12	63.00	34.08	34.08	17.938
...	McLean	2001-12-29	07:49:17	2 × 600	1.41	N3	0''.432×12	63.00	34.08	34.08	-3.097
...	Martín	2002-11-25	13:06:34	3 × 600	1.25	N3	0''.576×12	63.00	34.08	34.08	10.44
...	Wainscoat	2004-12-05	13:03:11	2 × 300	1.34	N3	0''.432×12	63.00	34.08	34.08	6.31
...	Martín	2005-10-26	13:37:56	3 × 480	1.21	N3	0''.432×12	63.00	34.08	34.08	19.706
...	Martín	2005-10-27	12:35:45	3 × 480	1.29	N3	0''.432×12	63.00	34.08	34.08	19.593
...	Martín	2005-10-28	12:49:07	3 × 480	1.26	N3	0''.432×12	63.00	34.08	34.08	19.326
...	McLean	2006-01-11	07:48:54	26 × 300	1.27	N3	0''.432×12	63.00	34.08	34.08	-8.445
...	McLean	2008-03-19	05:55:54	7 × 600	1.30	N3	0''.432×12	63.00	34.08	34.08	-23.852
...	Burgasser	2015-12-29	11:17:25	2 × 1500	1.30	N7	0''.432×12	63.02	35.48	35.48	-3.265
... <sup>c</sup>	Burgasser	2021-01-01	07:58:37	2 × 1200	1.33	N3	0''.432×12	62.95	34.06	34.06	-4.434
J0627-1114 <sup>c</sup>	Burgasser	2021-01-01	09:08:11	2 × 1800	1.21	N3	0''.432×12	62.95	34.06	34.06	-1.101
J0629+2418	Burgasser	2012-11-28	12:50:54	2 × 1500	1.00	N7	0''.432×12	63.02	35.55	35.55	14.826
J0755+2212 <sup>c</sup>	Burgasser	2021-01-01	10:16:22	1 × 1800	1.05	N3	0''.432×12	62.95	34.06	34.06	8.315
J0819-0335 <sup>c</sup>	Burgasser	2021-01-01	11:36:35	2 × 1800	1.09	N3	0''.432×12	62.95	34.06	34.06	12.859
J0909+6525	Burgasser	2010-12-26	12:12:07	4 × 1200	1.45	N7	0''.432×12	63.00	35.55	35.55	7.764
J0937+2931	McLean	2002-04-23	05:15:35	4 × 300	1.03	N3	0''.432×12	63.00	34.08	34.08	-27.634
...	McLean	2003-03-24	08:12:11	6 × 600	1.02	N3	0''.432×12	63.00	34.08	34.08	-20.594
...	Prato	2003-05-12	05:30:39	13 × 300	1.03	N3	0''.432×12	63.00	34.08	34.08	-28.564
...	McLean	2006-01-10	13:10:31	24 × 300	1.02	N3	0''.432×12	63.00	34.08	34.08	13.261
...	McLean	2006-05-19	07:15:48	8 × 300	1.35	N3	0''.432×12	63.00	34.08	34.08	-28.282
J1106+2754	McLean	2008-03-19	08:19:51	12 × 600	1.06	N3	0''.432×12	63.00	34.08	34.08	-10.193
...	Burgasser	2010-12-26	15:07:25	3 × 1000	1.01	N3	0''.432×12	62.95	34.08	34.08	25.007
...	Burgasser	2012-04-02	11:07:11	3 × 1500	1.20	N7	0''.432×12	63.00	35.52	35.52	-16.475
...	Burgasser	2012-11-27	13:42:12	3 × 1200	1.43	N7	0''.432×12	63.01	35.52	35.52	28.583
...	Burgasser	2013-02-05	14:15:17	3 × 1500	1.07	N7	0''.432×12	63.03	35.46	35.46	9.608
...	Burgasser	2015-01-01	15:00:50	2 × 1500	1.01	N7	0''.432×12	63.03	35.46	35.46	23.434
...	Burgasser	2016-01-18	14:03:05	2 × 1500	1.01	N7	0''.432×12	63.02	35.48	35.48	17.818
...	Burgasser	2016-02-16	09:47:02	3 × 1400	1.13	N7	0''.432×12	63.03	35.48	35.48	5.18
...	Burgasser	2016-04-22	08:43:42	3 × 1500	1.06	N7	0''.432×12	62.98	35.48	35.48	-22.888
...	Burgasser	2016-05-22	07:56:10	3 × 1500	1.22	N7	0''.432×12	62.97	35.48	35.48	-27.661
...	Burgasser	2017-03-22	13:00:58	2 × 900	1.02	N7	0''.432×12	63.02	35.52	35.52	9.678
...	Burgasser	2017-05-06	07:14:02	2 × 1200	1.01	N7	0''.432×12	63.02	35.52	35.52	-25.802
...	Burgasser	2018-01-01	14:47:39	2 × 1500	1.01	N7	0''.432×12	63.01	35.48	35.48	23.406
...	Burgasser	2018-06-03	06:19:27	2 × 1500	1.05	N7	0''.432×12	63.01	35.38	35.38	-27.541
... <sup>c</sup>	Burgasser	2021-01-01	12:57:30	2 × 1500	1.11	N3	0''.432×12	62.95	34.06	34.06	23.544
... <sup>c</sup>	Burgasser	2021-01-01	14:20:08	2 × 1500	1.01	N7	0''.432×12	62.95	34.06	34.06	23.394

**Table 2** continued

**Table 2** (continued)

Source	Program PI	UT Date	UT Time <sup>a</sup>	Integration <sup>b</sup>	Airmass <sup>a</sup>	Filter <sup>d</sup>	Slit	Angle <sup>a</sup>	Echelle	Cross-disperser	Barycentric
			(hh:mm:ss)	(s)				(deg)	(deg)	(deg)	(km s <sup>-1</sup> )
J1217-0311	Martín	2001-06-15	06:08:18	2 × 900	1.11	N3	0''.576×12	63.00	34.08	−28.873	
...	Wainscoat	2006-01-18	14:07:41	2 × 600	1.10	N3	0''.432×12	63.00	34.08	27.977	
...	Wainscoat	2006-01-19	12:40:31	3 × 1200	1.27	N3	0''.432×12	63.00	34.08	27.929	
J1225-2739	McLean	2002-04-23	08:37:15	6 × 300	1.48	N3	0''.432×12	63.00	34.08	−6.921	
J1254-0122	McLean	2001-12-31	15:13:36	3 × 300	1.15	N3	0''.432×12	63.00	34.08	30.294	
...	Basri	2002-05-17	06:55:33	9 × 300	1.09	N3	0''.432×12	63.00	34.08	−19.715	
...	Prato	2003-05-14	05:50:51	14 × 300	1.24	N3	0''.432×12	63.00	34.08	−18.322	
...	Wainscoat	2006-01-19	13:55:21	9 × 600	1.15	N3	0''.432×12	63.00	34.08	29.206	
...	McLean	2007-05-31	06:51:50	8 × 600	1.15	N3	0''.432×12	63.00	34.08	−24.187	
...	Burgasser	2011-06-10	05:46:19	2 × 900	1.07	N7	0''.432×12	63.00	35.53	−26.549	
J1324+6358	Burgasser	2016-05-22	09:03:28	2 × 3000	1.44	N7	0''.432×12	62.97	35.48	−13.606	
J1331-0116	Burgasser	2011-03-18	12:20:39	4 × 1200	1.07	N7	0''.432×12	63.00	35.47	12.621	
...	Burgasser	2011-07-06	06:32:30	2 × 1500	1.17	N7	0''.432×12	63.00	35.53	−28.921	
...	McLean	2013-05-24	08:27:28	4 × 600	1.08	N3	0''.432×12	63.00	34.08	11.046	
J1346-0031	Martín	2001-06-15	07:10:43	3 × 900	1.08	N3	0''.576×12	63.00	34.08	−24.832	
...	Wainscoat	2006-01-18	14:55:32	3 × 600	1.14	N3	0''.432×12	63.00	34.08	29.934	
J1457-2122	Martín	2001-06-15	08:58:36	2 × 900	1.41	N3	0''.576×12	63.00	34.08	−17.283	
...	Wainscoat	2006-01-18	15:37:10	2 × 600	1.53	N3	0''.432×12	63.00	34.08	28.542	
...	McLean	2008-03-19	11:22:16	8 × 600	1.61	N3	0''.432×12	63.00	34.08	23.02	
J1503+2525	Wainscoat	2006-01-19	15:54:04	2 × 300	1.08	N3	0''.432×12	63.00	34.08	23.037	
...	McLean	2008-03-19	13:48:14	8 × 600	1.01	N3	0''.432×12	63.00	34.08	13.207	
J1506+7027 <sup>c</sup>	Burgasser	2020-09-03	05:17:38	2 × 1200	1.77	N3	0''.432×12	62.98	34.09	2.035	
J1520+3546	Burgasser	2012-04-02	14:19:49	2 × 1200	1.09	N7	0''.432×12	63.00	35.52	6.498	
J1553+1523	Martín	2001-06-15	09:38:29	2 × 900	1.03	N3	0''.576×12	63.00	34.08	−12.915	
J1624+0029	Martín	2001-06-15	10:22:21	2 × 900	1.11	N3	0''.576×12	63.00	34.08	−9.423	
...	Basri	2002-05-17	12:23:06	8 × 300	1.12	N3	0''.432×12	63.00	34.08	3.83	
...	McLean	2005-06-04	08:08:51	1 × 600	1.18	N3	0''.432×12	63.00	34.08	−4.155	
J1629+0335	Burgasser	2011-08-11	06:55:17	2 × 1500	1.11	N7	0''.432×12	63.00	35.47	−25.693	
...	Burgasser	2011-09-07	05:15:20	2 × 1200	1.12	N7	0''.432×12	63.00	35.46	−26.499	
J1809-0448 <sup>c</sup>	Burgasser	2020-08-25	06:37:23	2 × 1500	1.10	N7	0''.432×12	62.98	35.75	−24.312	
J1928+2356 <sup>c</sup>	Burgasser	2019-09-12	08:00:26	1 × 1500	1.04	N7	0''.432×12	63.00	35.76	−16.283	
...	Burgasser	2019-10-17	06:31:42	2 × 1200	1.2	N3	0''.432×12	62.97	34.09	−21.221	
J1952+7240 <sup>c</sup>	Burgasser	2019-10-17	07:31:51	2 × 1500	1.91	N3	0''.432×12	62.97	34.09	1.957	
J2030+0749 <sup>c</sup>	Burgasser	2020-07-10	09:55:16	2 × 900	1.13	N7	0''.432×12	63.00	35.73	10.869	
J2126+7617	Burgasser	2011-06-10	14:59:25	2 × 750	1.81	N7	0''.432×12	63.00	35.53	3.919	
...	Burgasser	2011-07-06	13:51:48	2 × 1200	1.83	N7	0''.432×12	63.00	35.53	7.054	
...	Burgasser	2011-08-11	11:38:20	2 × 1500	1.84	N7	0''.432×12	63.00	35.47	9.141	
...	Burgasser	2011-09-07	10:49:22	2 × 1200	1.92	N7	0''.432×12	63.00	35.46	8.549	
...	Burgasser	2013-09-17	10:46:37	2 × 1500	2.00	N7	0''.432×12	62.97	35.51	7.816	
...	Burgasser	2013-10-16	10:34:47	2 × 1500	2.38	N7	0''.432×12	62.97	35.47	4.528	
...	Burgasser	2014-09-02	09:25:11	2 × 1200	1.81	N7	0''.288×12	63.02	35.49	8.839	
... <sup>c</sup>	Burgasser	2020-08-25	08:52:17	2 × 1500	1.82	N7	0''.432×12	62.98	35.75	9.12	
... <sup>c</sup>	Burgasser	2020-09-03	06:46:14	2 × 1200	1.93	N3	0''.432×12	62.98	34.09	8.838	
HN Peg B	Skemer	2017-06-09	11:21:04	20 × 13200	1.59	N7	0''.432×12	63.01	36.60	25.737	
...	Skemer	2017-10-08	05:36:07	10 × 9000	1.07	N7	0''.432×24	62.93	36.55	−17.657	
J2236+5105 <sup>c</sup>	Burgasser	2020-09-03	07:44:53	2 × 1200	1.34	N3	0''.432×12	62.98	34.09	8.472	
J2254+3123	Prato	2003-08-10	09:20:13	10 × 300	1.32	N3	0''.432×12	63.00	34.08	16.077	
...	McLean	2005-07-19	12:17:11	4 × 600	1.06	N3	0''.432×12	63.00	34.08	21.277	
...	McLean	2004-11-21	05:38:26	1 × 300	1.03	N5	0''.288×24	62.61	36.90	−21.596	
...	McLean	2007-06-26	14:15:19	4 × 600	1.04	K	0''.432×24	63.00	35.65	23.945	
J2356-1553	McLean	2003-07-20	12:50:03	4 × 600	1.36	N3	0''.432×12	63.00	34.08	23.527	

**Table 2** continued

**Table 2** (*continued*)

Source	Program PI	UT Date	UT Time <sup>a</sup>	Integration <sup>b</sup>	Airmass <sup>a</sup>	Filter <sup>d</sup>	Slit	Angle <sup>a</sup>	Echelle	Cross-disperser	Barycentric
			(hh:mm:ss)	(s)				(deg)			
...	McLean	2005-07-19	13:52:18	3 × 600	1.25	N3	0''.432×12	63.00	34.08	23.519	
...	McLean	2005-12-10	05:21:03	6 × 600	1.23	N3	0''.432×12	63.00	34.08	-29.26	

<sup>a</sup> Values are taken from the configuration of the first file within the same night.

<sup>b</sup> The number of files times the individual integration time.

<sup>c</sup> Observed with the upgraded NIRSPEC.

<sup>d</sup> Filters: N3(NIRSPEC-3), N5(NIRSPEC-5), N7(NIRSPEC-7), and K(NIRSPEC K)

measurements for T dwarfs also hinders the identification of young moving group members and short-period binaries, both of which serve as benchmarks for disentangling the age/mass degeneracy.

To improve our sampling of brown dwarf space motions, rotation, and multiplicity, and to properly compare the kinematic distributions of T dwarfs to warmer UCDs in the vicinity of the Sun, we report RV and  $v \sin i$  measurements, and stellar atmospheric parameters, for 37 T dwarfs with Keck/NIRSPEC high-resolution spectroscopic data. In Section 2, we describe the sample and observations. In Section 3, we discuss the data reduction methods, wavelength calibration, and forward-modeling routines, and analyze the outcomes in the context of prior measurements in the literature. In Section 4, we analyze individual RV and  $v \sin i$  measurements, deriving space motions, examining cluster and Galactic population membership, characterizing Galactic orbits, and examining multi-epoch measurements for evidence of RV variability. In Section 5, we examine the kinematics of local T dwarfs as a population, evaluating their statistical age from velocity and vertical action dispersions, and we compare these to the distributions of late-M and L dwarfs and to population simulations. We find local T dwarfs have kinematic ages similar to those of late-M dwarfs and simulation predictions, and both are younger than local early- and mid-L dwarfs. Removing the thick disk L dwarfs resolves this age discrepancy. In Section 6, we evaluate sample incompleteness and bias, and conduct a more detailed analysis of L dwarf kinematics. In Section 7 we summarize our results. As Section 2 and 3 describe our analysis methods in detail, readers primarily interested in the scientific aspects of this study can start at Section 4 without loss of content.

## 2. OBSERVATIONS

Our T dwarf sample was compiled from sources observed with the Keck Near-Infrared Spectrometer (NIRSPEC; McLean et al. 1998, 2000). NIRSPEC is a high-

resolution, near-infrared, cross-dispersed spectrograph, mounted on the Keck II telescope, spanning 0.95 to 5.5  $\mu\text{m}$  with a spectral resolution of  $\sim 25,000$  (pre-upgrade) and  $\sim 35,000$  (post-upgrade) for a slit width of 0''.432. Table 1 lists the 37 T dwarfs in our sample, with photometry from the Two Micron All Sky Survey (2MASS; Skrutskie et al. 2006) and the UKIRT Infrared Deep Sky Survey (UKIDSS; Lawrence et al. 2013); astrometry from 2MASS, the *Wide-field Infrared Survey Explorer* (WISE; Cutri & et al. 2012), the Panoramic Survey Telescope and Rapid Response System (Pan-STARRS; Chambers & et al. 2017) and *Gaia* (Gaia Collaboration et al. 2018, 2020); and classifications from the literature. Our sample encompasses observations taken between 2000 and 2021, including publicly available archival data obtained from the Keck Observatory Archive (KOA)<sup>1</sup>. All public data were downloaded directly from the KOA, with the exception of data from 2001 June 15 (Zapatero Osorio et al. 2006, 2007) and 2005 July 19 (Prato et al. 2015) which were provided by the PIs of these programs. Fourteen sources were observed after the NIRSPEC upgrade (Martin et al. 2018). Table 2 lists the details for each observation, segregated by epoch. Most observations were accompanied by observation of an early type star (typically A0) for telluric absorption correction. In total, we analyzed 290 near-infrared spectra in order N3 (1.143–1.375  $\mu\text{m}$ ) and 101 near-infrared spectra in order N7 (1.839–2.630  $\mu\text{m}$ ).

## 3. METHODS

### 3.1. Spectral Data Reduction

#### 3.1.1. NSDRP Pipeline and Modifications

All of the NIRSPEC data were reduced using a modified version of the NIRSPEC Data Reduction Pipeline

<sup>1</sup> <https://koa.ipac.caltech.edu>

(NSDRP; Tran et al. 2016). Our modifications were as follows:

1. We loosened the criteria for determining the edges of each dispersion order. NSDRP determines these edges from flat field frames, but the threshold value for edge detection was too strict and cut off some science spectra in certain orders. Note that NSDRP only processes orders that are completely within the image. Orders that are cut off at the top or bottom of the detector are ignored.
2. NSDRP determines the wavelength calibration using only sky emission lines, so we added arc lamp and etalon lamp exposures as additional inputs for wavelength calibration. Arc lamp line identifications were drawn primarily from the National Institute of Standards and Technology (NIST; Kramida et al. 2019), the Atomic Line List (Van Hoof 2018), and Outred (1978). Etalon lamp lines are not tied to an absolute wavelength scale but provide a way to refine the relative wavelength calibration across an order.
3. When spatially rectifying the tilted orders, NSDRP uses the top and bottom of the edges of the flat field dispersions. This is suitable for data with low S/N, such as our science spectra. For data with high S/N, such as our telluric star spectra, we found that this rectification can be offset by 1–2 pixels across the spectral order. For these data, we used the trace of the bright object spectrum, determined by a Gaussian profile fit along each column.
4. We added a 3- $\sigma$  clipping algorithm to find the optimal spectral tilt (spatial y-direction) from the emission line traces.
5. We added new coefficients for the grating equation, determined empirically, for *N3* (*J*-band) and *N7* (*K*-band) data obtained with the upgraded NIRSPEC instrument.

These modifications have been integrated into an updated version of the NSDRP.<sup>2</sup>

In addition, we implemented an algorithm to correct for fringing features in the flat field images. Interference from reflections between the echelle gratings and internal optics in NIRSPEC produce fringing patterns, easily visible in high signal-to-noise (S/N) data and flat field

images. The interference patterns reduce both our ability to model the spectra and achieve high radial velocity precision. We therefore added a defringing algorithm for the raw flat field files using the wavelet analysis described in Rojo & Harrington (2006) and the *wavelets*<sup>3</sup> package described in Torrence & Compo (1998). Briefly, each pixel in the flat field data is substituted for the median-average value of the nearest 10 pixels in the vertical direction, making the horizontal fringe patterns more prominent. A continuum profile is determined from the binned data using a low-order cubic spline. Subtracting this continuum, we fit the difference using a wavelet analysis. The modeled fringe pattern for the flat images was then subtracted from the original flat field frame. This algorithm was only applied to flat field images, so fringing remains in the science frames. As our data were typically low S/N, we did not attempt to correct the science frames for fringing, and defer this to a future study.

### 3.1.2. Telluric Wavelength Calibration

The wavelength calibration from NSDRP is a second-order polynomial fit to the sky, arc, and etalon lamp emission lines in the science and calibration data. We found this default calibration to be insufficient for precise RV measurement. We therefore adopted the wavelength calibration method described in Burgasser et al. (2016), cross-correlating the associated telluric standard star spectrum with a telluric absorption model (Moehler et al. 2014) over discrete wavebands of width 15 Å. This fit was performed after first modeling out the continuum of the A0 V with a second-order polynomial and a Voigt absorption profile for orders containing H I absorption lines<sup>4</sup>. We used a fit to the residual shift to update the wavelength solution, both represented as fourth-order polynomial functions. This process was iterated until the wavelength solution residuals reached a minimum. The calibrated wavelength solution of each telluric standard star spectrum was applied to the corresponding science spectrum with a wavelength offset determined in the forward-modeling (Section 3.2). The typical standard deviation of velocity residuals in the calibrated telluric spectra ranges from 0.1 to 0.6 km s<sup>-1</sup>, with a median residual of 0.3 km s<sup>-1</sup>. Our baseline *N3* order 58 has a median residual of 0.2 km s<sup>-1</sup>, while our baseline *N7* order 33 has a median residual of 0.4

<sup>3</sup> <https://github.com/aaren/wavelets>

<sup>4</sup> Order 59 in *J*-band and order 35 in *K*-band are fit with a Voigt profile, multiplied by a second-order polynomial function, using *scipy*'s *special.wofz* function. The Voigt profile parameters are optimized by a least squares fit.

<sup>2</sup> <https://github.com/ctheissen/NIRSPEC-Data-Reduction-Pipeline>

$\text{km s}^{-1}$ . We also determined wavelength calibrations for orders 32, 34, 37, and 38 ( $N7$ ); and 57, 63, 64, 65, and 66 ( $N3$ ). Orders 35 and 36 ( $N7$ ), and 59, 60, 61, 62 ( $N3$ ) do not have sufficient telluric absorption features to apply this method, while orders 55 and 56 have excessively strong telluric absorption and do not provide sufficient signal for our targets.

### 3.2. Forward Modeling

#### 3.2.1. Overview

The typical approach to spectral reduction is to correct for instrumental and telluric atmospheric effects to infer the target's emitted spectrum. Here, we model these effects explicitly using a forward-modeling approach, following Blake et al. (2010) and Burgasser et al. (2016) (see also Tanner et al. 2012; Allers et al. 2016; Vos et al. 2017; Cale et al. 2019). The stellar parameters (effective temperature, surface gravity, rotational velocity, and radial velocity), and calibration factors (continuum and wavelength corrections, instrumental line-spread function, and strength of telluric absorption) are determined using a Markov Chain Monte Carlo (MCMC) algorithm (Goodman & Weare 2010) using the package *emcee* (Foreman-Mackey et al. 2013). Our forward-modeling method is optimal in those spectral orders with both strong telluric absorption features for accurate wavelength calibration, and sufficient structure in the stellar spectrum to distinguish it from the telluric absorption. We found order 33 in the  $K$ -band ( $N7$ ; 22690–23410 Å) and order 58 in the  $J$ -band ( $N3$ ; 12990–13290 Å) to be the ideal orders for the T dwarfs, similar to prior studies (Blake et al. 2010; Konopacky et al. 2010; Burgasser et al. 2012; Tanner et al. 2012). Our forward-modeling routine *Spectral Modeling Analysis and RV Tool* (SMART; Hsu et al. 2021) is open source and available online.<sup>5</sup>

To summarize, there are three main steps in our MCMC forward-modeling scheme:

1. An MCMC fit of the telluric spectrum is performed to determine the parameters for the instrumental line-spread function (LSF) and the strength of telluric absorption, which are used to initialize the MCMC of the science spectrum.
2. An initial MCMC fit of the science spectrum is conducted to estimate the stellar parameters for effective temperature ( $T_{\text{eff}}$ ), surface gravity ( $\log g$ ), rotational velocity ( $v \sin i$ ), and radial velocity

(RV), as well as calibration and nuisance parameters.

3. The residuals between the best-fit model spectrum and data are used to generate a mask array to identify discrepant pixels, and a final MCMC fit of the masked science spectrum is run to obtain the best estimates of the fit parameters.

#### 3.2.2. Telluric Star Modeling

Each telluric standard star was forward-modeled to obtain initial estimates of the LSF and strength of telluric absorption. The data ( $D$ ) are modeled as:

$$D[p] = C[p(\lambda)] \times \left[ T[p^*(\lambda)]^\alpha \otimes \kappa_G(\Delta\nu_{\text{inst}}(p)) \right] + C_{\text{flux}}. \quad (1)$$

Here,  $p$  is the pixel coordinate,  $p^*(\lambda) = p(\lambda) + C_\lambda$  is the mapping of wavelength to pixel with a small constant offset,  $C[p]$  is a second-order polynomial representing the continuum correction,  $\kappa_G(\Delta\nu_{\text{inst}})$  is the instrumental LSF, assumed to be Gaussian of velocity width  $\Delta\nu_{\text{inst}}$  ( $\otimes$  represents convolution),  $T[p]$  is a model for telluric absorption from Moehler et al. (2014),  $\alpha$  is a constant that scales with the airmass and precipitable water vapor, and  $C_{\text{flux}}$  is an additive offset for the overall flux. The default precipitable water vapor (pwv) for the Moehler et al. (2014) models used was 0.5 mm. For some data, a telluric model with pwv = 1.5 mm produced a better fit and these were used instead. We fit the parameters,  $\Delta\nu_{\text{inst}}$ ,  $C_{\text{flux}}$ ,  $C_\lambda$ , and  $\alpha$  assuming uniform priors (Table 3), while the continuum was determined after each iteration through a least-squares fit of the ratio of the data and model to a second-order polynomial (i.e., the continuum fit was done outside of the MCMC). The likelihood function was computed by assuming the noise follows a normal distribution:

$$\ln \mathcal{L} = -0.5 \times \left[ \sum \chi^2 + \sum \ln(2\pi\sigma^2) \right], \quad (2)$$

where  $\chi = \frac{\text{Data}[p] - D[p]}{\sigma[p]}$ , and *Data* and  $\sigma$  are the observed spectrum and noise. We used 50 walkers of 400 steps each and a burn-in of 300 steps, with these parameters chosen<sup>6</sup> to optimize convergence. The convergence of each fit was checked visually and quantified using both the Gelman-Rubin scale reduction factor (Gelman & Rubin 1992) and integrated autocorrelation time statistics (Goodman & Weare 2010). For each fit, we inferred the best-fit parameter values and their uncertainties by computing the 50<sup>th</sup>, 16<sup>th</sup>, and 84<sup>th</sup> percentiles of

<sup>5</sup> <https://github.com/chihchunhsu/smart>

<sup>6</sup> See Section 3.2.3 for discussions on convergence.

the marginalized posterior distributions from the residual MCMC chains.

### 3.2.3. T Dwarf Modeling

The T dwarf spectra were forward-modeled as:

$$D[p] = C[p] \times \left[ \left( M \left[ p^*(\lambda [1 + \frac{RV^*}{c}]), T_{\text{eff}}, \log g \right] \otimes \kappa_R(v \sin i) \right) \times T[p^*(\lambda)]^\alpha \right] \otimes \kappa_G(\Delta\nu_{\text{inst}}) + C_{\text{flux}}, \quad (3)$$

where the additional terms compared to equation (1) include the solar-metallicity stellar atmosphere model<sup>7</sup>  $M[p]$  drawn from the BT-Settl (Allard et al. 2012) and Sonora (Marley et al. 2018) model grids, parameterized by effective temperature ( $T_{\text{eff}}$ ) and surface gravity ( $\log g$ );  $RV^* = RV + v_{\text{bary}}$  is the radial velocity of the source plus barycentric motion of the Earth at the observed epoch;  $c$  is the speed of light;  $\kappa_R$  is the rotational broadening profile defined in Gray (1992) assuming a constant limb-darkening coefficient of  $\epsilon = 0.6$  (Claret 2000); and  $v \sin i$  is the projected rotational velocity. Atmosphere model log fluxes were linearly interpolated between grid points to approximate a continuous distribution of  $T_{\text{eff}}$  and  $\log g$  values. The likelihood function is:

$$\ln \mathcal{L} = -0.5 \times \left[ \sum \chi^2 / C_{\text{noise}}^2 + \sum \ln(2\pi(C_{\text{noise}}\sigma)^2) \right], \quad (4)$$

where  $C_{\text{noise}}$  is a constant scaling factor for the noise ( $\sigma$ ) to take into account underestimates or overestimates of observational noise in computing  $\chi^2$ ; as well as systematic errors between the model and the spectrum, such as missing line features. We performed an initial MCMC fit for the parameters  $T_{\text{eff}}$ ,  $\log g$ ,  $RV^*$ ,  $v \sin i$ ,  $\alpha$ ,  $C_\lambda$ ,  $C_{\text{flux}}$ <sup>8</sup>, and  $C_{\text{noise}}$ , modeling the continuum in the same manner as the telluric standard. The nuisance parameter  $C_\lambda$  takes into account the small shift in instrument alignment between the telluric and science integrations. RVs inferred between subsequent nods are more consistent when this nuisance parameter is included in the forward model. Stellar model parameter prior ranges were chosen to encompass the typical properties of T dwarfs, with  $T_{\text{eff}} = 600$  to  $1300$  K,  $\log g = 3.5$  to  $5.5$  dex (in units of  $\text{cm s}^{-2}$ ),  $v \sin i = 0$  to  $100$   $\text{km s}^{-1}$ , and  $RV^* = -200$  to  $+200$   $\text{km s}^{-1}$ . The MCMC bounds of  $T_{\text{eff}}$  are set for

the whole range of the available model sets (BT-Settl = 500 to 3500 K and Sonora = 200 to 2400 K) (Table 3). The initial MCMC used 50 walkers of 600 steps each and burn-in of 300 steps, and convergence was verified by inspection of parameter chains and a requirement of the Gelman-Rubin scale reduction factor (Gelman & Rubin 1992) of less than 1.32. Typically convergence occurred after the first 100–200 steps.

The Gelman-Rubin scale reduction factor and autocorrelation time suggested by Goodman & Weare (2010) were used to test convergence for a representative set of telluric and science spectra, and to set the number of walkers and steps for all fits. We tested the MCMC runs with 50 chains of 600 to 8,000 steps each. The  $\chi^2$  values were similar, and the best-fit parameters were fully consistent within the uncertainties, but longer chains reduced the scale reduction factor from 1.2 to 1.01. The longest autocorrelation time was 120 steps, estimated from the runs with 8000 steps. Among these select sets of fits, we found that longer chains did not significantly improve the fits, which only have lower Gelman-Rubin scale reduction factor and converged autocorrelation times, but not change to the parameter values or uncertainties. Due to our limited computational resources, we chose to run only 600 steps, where the convergence was checked visually and confirmed by the requirement that the Gelman-Rubin scale reduction factors were all less than 1.32 (50<sup>th</sup>, 16<sup>th</sup>, and 84<sup>th</sup> percentiles of  $R = 1.05, 1.03$ , and  $1.13$ ).

Residuals between the best-fit model and data from this first pass were used to generate a pixel mask rejecting  $2.5\sigma$  outliers<sup>9</sup>, typically cosmic rays and bad pixels in the detector. A second MCMC was then run on the masked data using the same MCMC fit parameters and initializing model parameters from the first MCMC fit plus a random offset drawn from uniform parameter ranges spanning  $\Delta T_{\text{eff}} = \pm 20$  K,  $\Delta \log g = \pm 0.1$  dex,  $\Delta v \sin i = \pm 1$   $\text{km s}^{-1}$ , and  $\Delta RV = \pm 1$   $\text{km s}^{-1}$ . The masking step considerably improved the RV and  $v \sin i$  uncertainties and the overall spectral fit. The derived RVs were corrected to the heliocentric frame using the *astropy* function `radial_velocity_correction` to compute  $v_{\text{bary}}$ .

Each individual spectrum was forward-modeled, and measurements both within an epoch and across epochs (for multi-epoch data) were averaged using uncertainty weighting, with weight  $W \propto 1/(\sigma_{\text{lower}}^2 + \sigma_{\text{upper}}^2)$ , where  $\sigma_{\text{lower}}$ ,  $\sigma_{\text{upper}}$  are the uncertainties associated with the 16<sup>th</sup> and 84<sup>th</sup> percentiles of each marginalized parameter

<sup>7</sup> See Section 3.3.2 for discussions of model selection

<sup>8</sup> The values are determined based on the percentage of median flux  $C_{\text{flux}} = C_{\text{flux}^*} \times F$ , where  $F$  is the median flux.

<sup>9</sup> Typically,  $\sim 3\%$  of the pixels are masked.

**Table 3.** Modeling Parameter Ranges

Description	Symbol (unit)	Priors <sup>a</sup>	Bounds
Telluric Standard Star			
Line Spread Func.	$\Delta\nu_{\text{inst}}$ (km s <sup>-1</sup> )	(3.0, 6.0)	(2.0, 10.0)
Flux Offset	$C_{\text{flux}}$	(−1.0, +1.0)	(−500, +500) <sup>b</sup>
Wavelength Offset	$C_{\lambda}$ (Å)	(−0.02, +0.02)	(−0.04, +0.04) <sup>b</sup>
Telluric Scaling	$\alpha$	(0.3, 3.0)	(0.3, 10.0)
T Dwarf			
Effective Temp.	$T_{\text{eff}}$ (K)	(600, 1300)	B <sup>c</sup> =(500, 3500)
...	...	...	S <sup>d</sup> =(200, 2400)
Surface Gravity	$\log g$ (cm s <sup>−2</sup> )	(3.5, 5.5)	(3.5, 5.5)
Rotational Velocity	$v \sin i$ (km s <sup>−1</sup> )	(0, 100)	(0, 100)
Radial Velocity	RV (km s <sup>−1</sup> )	(−200, +200)	(−200, +200)
Flux Offset	$C_{\text{flux}*}$	(−0.01, +0.01)	(−0.05, +0.05) <sup>e</sup>
Wavelength Offset	$C_{\lambda}$ (Å)	(−0.6, +0.6)	(−0.6, +0.6) <sup>b</sup>
Telluric Scaling	$\alpha$	(0.9, 1.1)	(0.1, 10.0)
Noise Factor	$C_{\text{noise}}$	(0.99, 1.01)	(0.1, 5.0)

<sup>a</sup> Uniform priors

<sup>b</sup> The Telluric Standard Star wavelength offset bounds range is much smaller than the T Dwarf offset bounds range as the data for the former are used to formally derive the wavelength solution while the data for the latter incur pixel shifts due to instrumental flexure between pointings. See Section 3.2.3 for more details.

<sup>c</sup> BT-Settl model

<sup>d</sup> Sonora model

<sup>e</sup> The values are determined based on the percentage of median flux  $C_{\text{flux}} = C_{\text{flux}*} \times F$ , where  $F$  is the median flux.

distribution. In a few cases where the S/N of an individual spectrum is lower than 10, all spectra in an epoch were coadded before forward-modeling. Table 4 lists the RV,  $v \sin i$ ,  $T_{\text{eff}}$  and  $\log g$  values inferred for each source and epoch, along with previously published values from the literature.

### 3.3. Evaluating the Fits

#### 3.3.1. Fit Quality and Parameter Correlations

Figures 1–4 illustrate representative fits to science data in orders 33 (T2.5 J0136+0933) and 58 (T4.5 J0559−1404).

For the order 33 fit, residuals between the data and the best-fit BT-Settl model are on par with the scaled noise

( $\chi^2_r = 1.3$ ,<sup>10</sup> for  $C_{\text{noise}} = 0.7$ ), and all of the marginalized distributions show normal distributions, modulo parameter limits (e.g.,  $\log g$ ). This fit exemplifies parameter correlations found in some (but not all) of the order 33 fits. First, we find a negative correlation between  $v \sin i$  ( $\Delta v \sin i = 3$  km s<sup>−1</sup>) and  $\log g$  ( $\Delta \log g = 0.2$  dex) that we attribute to a degeneracy between rotational and pressure broadening. A larger  $\log g$  results in greater pressure broadening, which is compensated for by a smaller  $v \sin i$ , and vice-versa. Disentangling this correlation in the line spread shape would require higher resolution and higher signal-to-noise data than is available with the current dataset. Second, we find a positive correlation between  $T_{\text{eff}}$  ( $\Delta T_{\text{eff}} = 50$  K) and  $\log g$  ( $\Delta \log g = 0.2$  dex) that we attribute to temperature and pressure effects in the primary carbon reduction reaction,  $\text{CO} + 3\text{H}_2 \rightleftharpoons \text{CH}_4 + \text{H}_2\text{O}$ . This reaction is driven toward the right (weaker CO and stronger CH<sub>4</sub>) at low temperatures and high pressures. Disentangling the  $T_{\text{eff}}\text{-}\log g$  correlation could be achieved with an accurate measure of the surface flux, and hence the luminosity and radius of each source, which is beyond the scope of this work. Finally, we find a positive correlation between RV ( $\Delta RV = 0.4$  km s<sup>−1</sup>) and  $C_{\lambda}$  ( $\Delta C_{\lambda} = 0.03$  Å) which is inherent to the simultaneous fitting of the Doppler shift of the source and instrumental shift of the wavelength calibration. As noted above, the  $C_{\lambda}$  term is necessary to enforce agreement of RVs measured within a single epoch, which far exceed the slight increase to our marginalized RV uncertainties.

For the order 58 fit, residuals between the data and the best-fit Sonora model are again consistent with uncertainty ( $\chi^2_r = 1.7$  for  $C_{\text{noise}} = 1.2$ ), and marginalized distributions for most parameters reflect normal distributions with the exception of  $\log g$  (parameter limit) and  $v \sin i$ , the latter of which shows a sharp lower cutoff at 17 km s<sup>−1</sup>. We find only a slight positive correlation between RV ( $\Delta RV = 0.2$  km s<sup>−1</sup>) and  $C_{\lambda}$  ( $\Delta C_{\lambda} = 0.01$  Å).

#### 3.3.2. Substellar Atmosphere Model Selection

Both BT-Settl and Sonora model sets were used for all forward-modeling analyses, and we determined the best choice between these sets for each source and order through a combination of visual inspection,  $\chi^2$ , F-test,

<sup>10</sup>  $\chi^2_r$  is the reduced chi-square statistic computed as  $\chi^2_r = \frac{1}{N_{\text{DOF}}} \sum \text{Mask}[p] \left( \frac{\text{Data}[p] - D[p]}{C_{\text{noise}} \sigma[p]} \right)^2$ , where  $\text{Mask}[p]$  is the pixel mask ( $\text{Mask} = 1$  for good data,  $\text{Mask} = 0$  for bad data) and  $N_{\text{DOF}}$  is the number of degrees of freedom computed as  $N_{\text{DOF}} = [\text{number of unmasked data pixels}] / 3 - [\text{number of fit parameters}]$ . The factor of 1/3 takes into account the pixel-to-pixel correlations caused by the finite slit width, typically 3 pixels (0''.432). We consider fits with  $\chi^2_r < 2.5$  to be consistent within uncertainties.

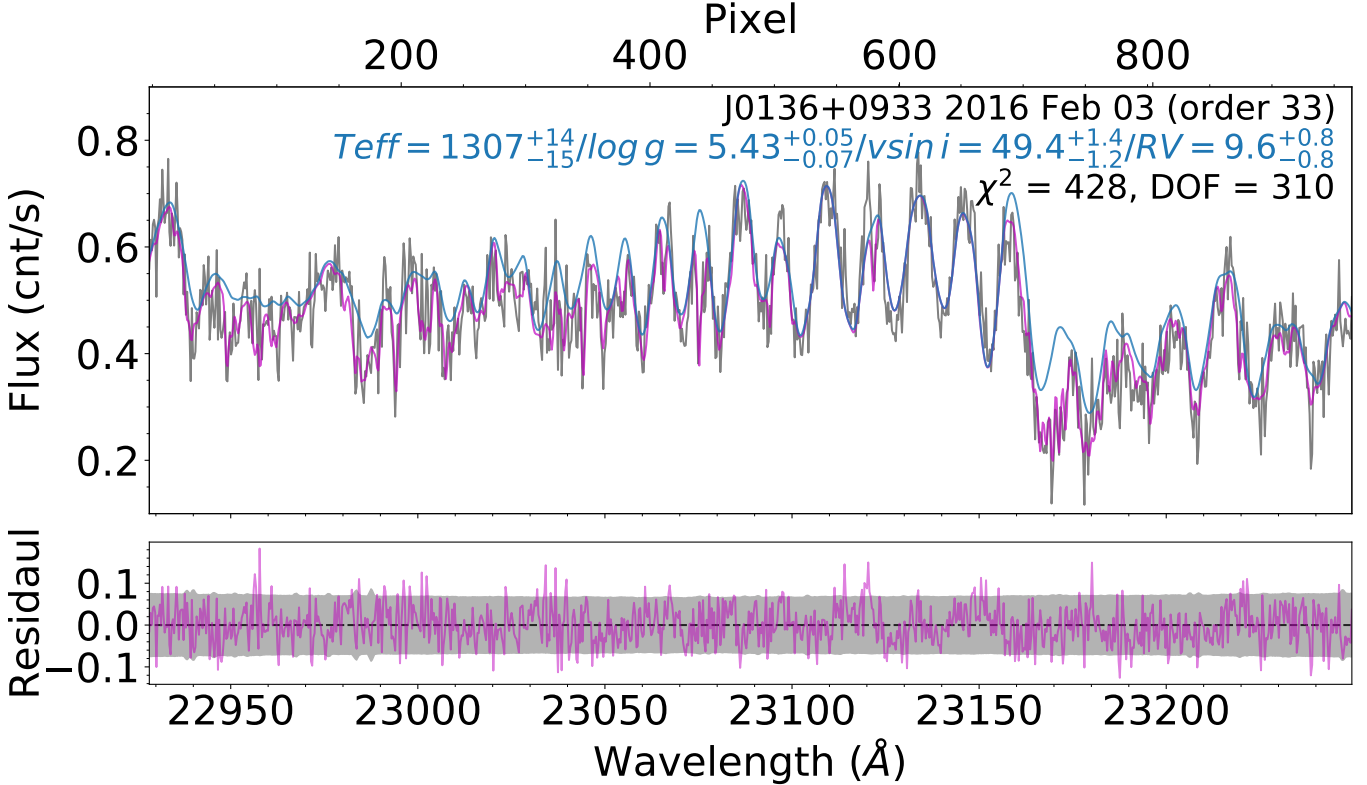


**Figure 1.** BT-Settl model fit of the order 33 spectrum of the T2.5 J0136+0933, observed on 2016 February 3 (UT). The horizontal axis displays both pixel position (top axis) and wavelength (bottom axis). Upper panel: the grey line is the observed spectra; the magenta and blue lines are the stellar model with and without telluric absorption, respectively. Lower panel: difference of the data minus model (magenta) with  $\pm 1\sigma$  data uncertainty shaded in grey. The best-fit parameters are listed at the upper right corner of the top panel, with effective temperature ( $T_{\text{eff}}$ ) in K, surface gravity ( $\log g$ ) in  $\text{cm s}^{-2}$ , rotational velocity ( $v \sin i$ ) in  $\text{km s}^{-1}$ , and radial velocity (RV) in  $\text{km s}^{-1}$ .

and Bayesian information criterion<sup>11</sup> (BIC). In general, the Sonora models provide significantly better fits to order 58 ( $J$ -band) spectra of mid- and late-T dwarfs, while the BT-Settl models provide marginally better fits for order 33 ( $K$ -band) spectra of early-T dwarfs. We attribute the significant improvement in Sonora model fits to the  $J$ -band data to the updated CH<sub>4</sub> opacities in these models, a particularly important factor for the coldest brown dwarfs. The slightly better fits for the BT-Settl models at  $K$ -band may be due to the inclusion of cloud opacity in these models, which are absent in the Sonora grid, although such opacity should have relatively modest influence in the 2  $\mu\text{m}$  region.

<sup>11</sup>  $BIC = \chi^2_{\min} + k \log_{10} N$ , where  $\chi^2$  is the chi-square statistic for the best-fitting model,  $k$  is the number of parameters, and  $N$  is the number of data points (Schwarz 1978). Statistical significance for ruling out the null hypothesis (in this case, that the model sets provide equivalent fits) is assessed following Kass & Raftery (1995), in which the  $\Delta BIC$  ranges of 0–2, 2–6, 6–10, and  $> 10$  are categorized as insignificant, positive, strong, and very strong evidence against the null hypothesis, respectively.

The choice of model does influence the physical parameters inferred for each source. Comparing the best-fit parameters between the two models across all sources, orders, and epochs, we found that measured RV and  $v \sin i$  values are relatively robust to model choice, with median model discrepancies (Sonora minus BT-Settl) of  $\Delta RV = 0.6 \pm 1.5 \text{ km s}^{-1}$  and  $\Delta v \sin i = -2 \pm 4 \text{ km s}^{-1}$ . The RV offset between the models is dominated by order 58 fits of mid- and late-T dwarfs, for which  $\Delta RV = 1.2 \text{ km s}^{-1}$ . Order 33 fits of early-T dwarfs have  $\Delta RV = 0.4 \text{ km s}^{-1}$ . The  $v \sin i$  offsets are again dominated by order 58 fits, where the velocity kernel must be broadened for the BT-Settl models to compensate for missing CH<sub>4</sub> opacities. The median  $\Delta v \sin i$  for order 58 is  $-2.9 \text{ km s}^{-1}$  while the median  $\Delta v \sin i$  for order 33 is  $0.0 \text{ km s}^{-1}$ . The most discrepant  $v \sin i$  measurements are among the order 58 fits for mid-T dwarfs, where the Sonora models are far more robust.

The atmosphere parameters  $T_{\text{eff}}$  and  $\log g$  show considerably more variance between the models (Figure 5).  $T_{\text{eff}}$  inferred from the Sonora model fits are consistently hotter than those inferred from the BT-Settl model fits

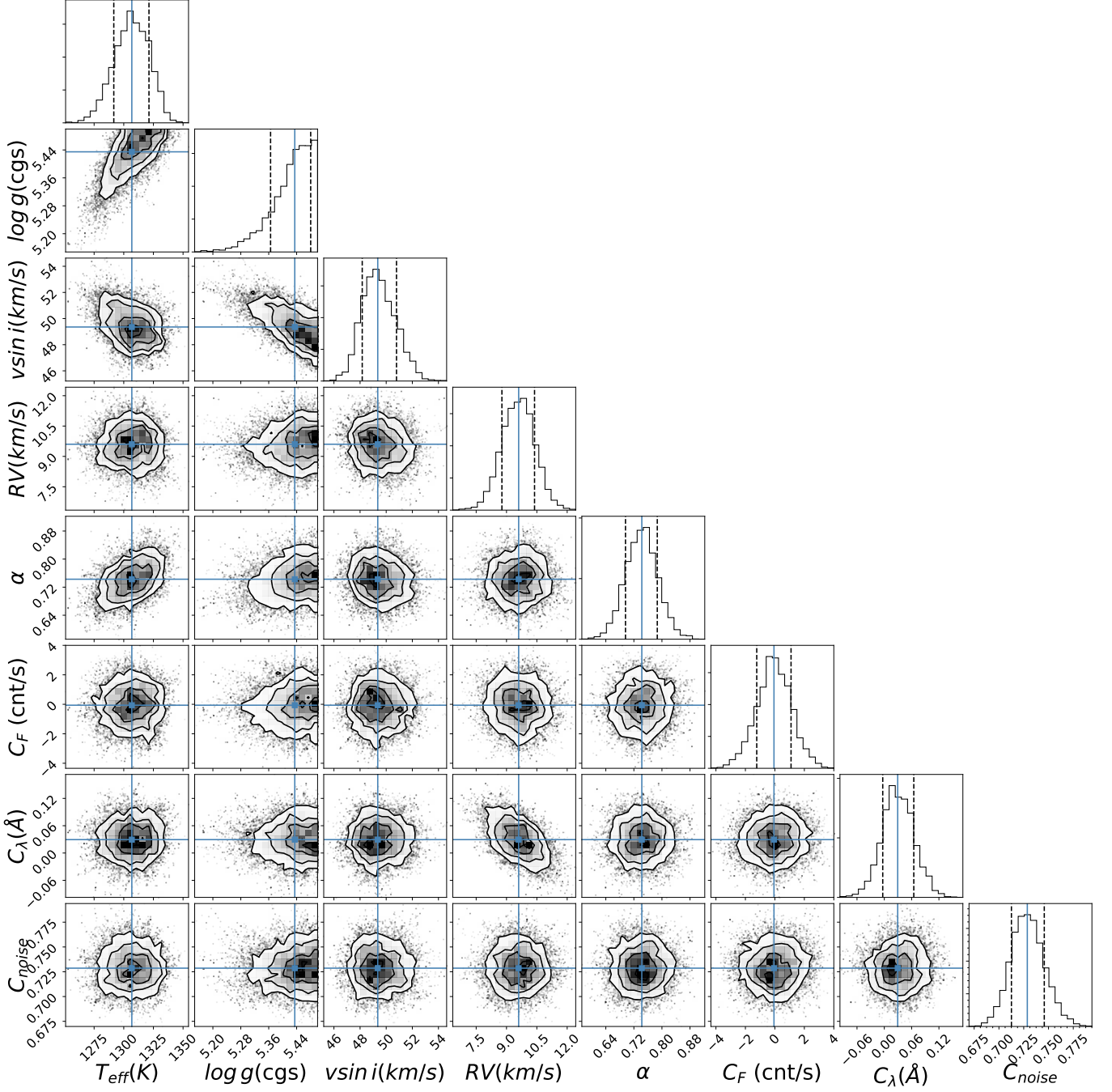


**Figure 2.** The posterior probability distribution of fits to the order 33 spectrum of the T2.5 J0136+0933 observed on 2016 February 3 (UT). The parameters shown are effective temperatures ( $T_{\text{eff}}$ ) in K, surface gravity ( $\log g$ ) in  $\text{cm s}^{-2}$ , projected rotational velocity ( $v \sin i$ ) in  $\text{km s}^{-1}$ , radial velocity (RV) in  $\text{km s}^{-1}$ , telluric scale factor ( $\alpha$ ), nuisance flux parameter ( $C_F$ ) in count/s, telluric wavelength parameter ( $C_{\lambda}$ ) in  $\text{\AA}$ , and noise scale factor ( $C_{\text{noise}}$ ). The black dash lines are the 16<sup>th</sup> and 84<sup>th</sup> percentiles in the marginalized distributions (diagonal plots), and the blue lines denote the median values in both marginalized distributions and interior parameter correlation plots.

for early- to mid-T dwarfs in both orders 33 and 58, with a median offset of  $240 \pm 110$  K. For late-T dwarfs, the Sonora model fits are cooler. More striking is the difference in  $\log g$  values inferred for order 58 (J-band) data, for which BT-Settl models typically converge to

$\log g \approx 3.5$  dex, the minimum of the model parameter range. In contrast,  $\log g$  values inferred from fits to order 33 (K-band) data are generally consistent between the models, with a median difference of only  $0.14 \pm 0.40$

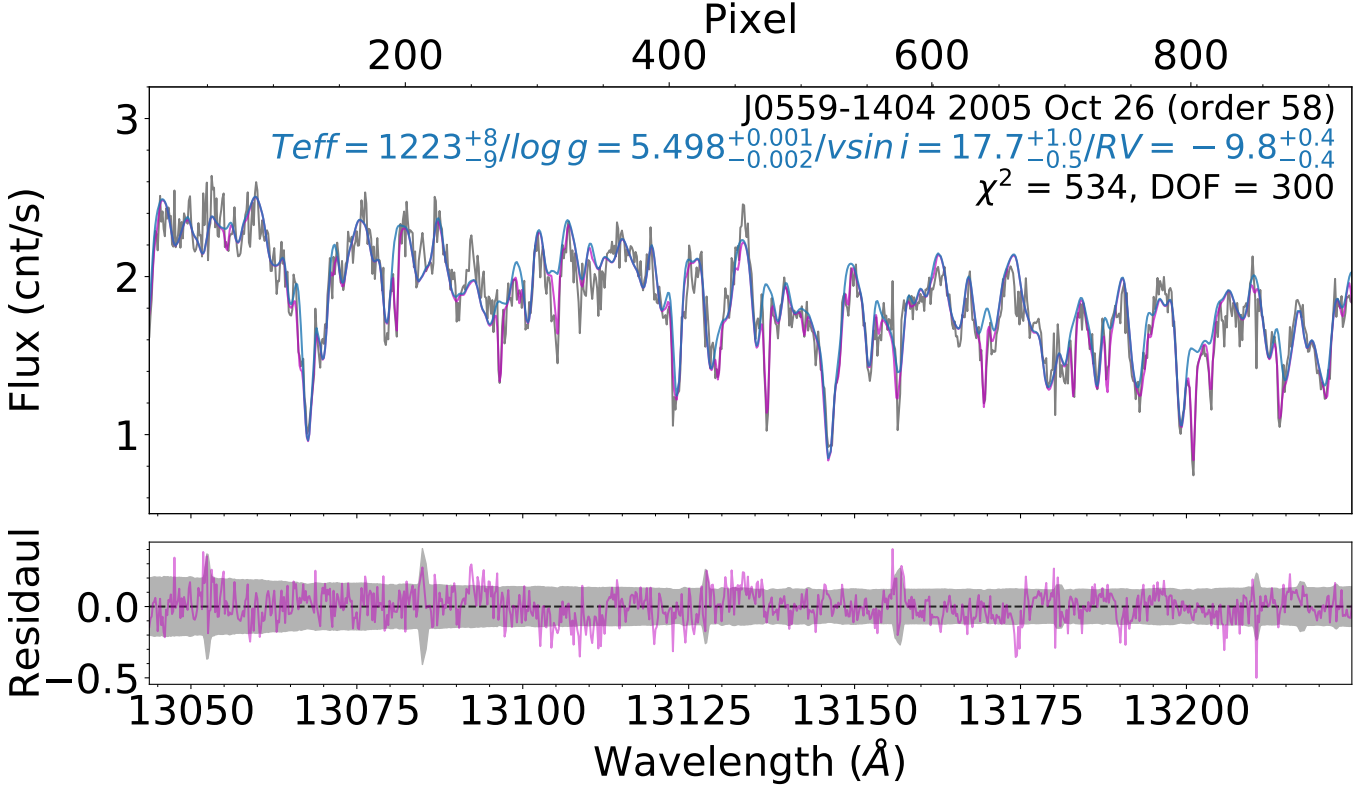


**Figure 3.** Sonora model fit of the order 58 spectrum of the T4.5 J0559–1404, observed on 2005 October 26 (UT). Notation is identical to Figure 1.

dex, although both models often converge to the maximum model parameter value of 5.5 dex.

2011 Jun 10 and J1928+2356 on 2019 Sep 12<sup>12</sup>) and binaries (J1106+2754 and J2126+7617).

The best-fit parameters for sources observed in multiple orders were determined generally by spectral type: *N7* for early T dwarfs and *N3* for mid- and late-T dwarfs. For J1254–0122, we used the order with the higher S/N data.

### 3.3.3. Examination of Fits Across Different Orders

For the sources with measurements in both bands, we examined the consistency of  $T_{\text{eff}}$  and  $\log g$  measurements between orders for six sources with measurements with both *J*- and *K*-band spectra. These sources are J0136+0933, J0559–1404, J1106+2754, J1254–0122 (orders 33 and 58), J1928+2356 (orders 37 and 58), and J2126+7617 (orders 33 and 57).  $T_{\text{eff}}$  values inferred from *K*-band data are consistently higher than those inferred from *J*-band data (average  $\Delta T_{\text{eff}} = 187$  K, range –182 K to 341 K; excluding J2126+7617 yields an average  $\Delta T_{\text{eff}} = 260$  K, range 140 K to 341 K).  $\log g$  values differed by up to 1.20 dex between orders but with no clear trend (average  $\log g = 0.27$  dex, range –0.39 dex to 1.20 dex). For J1928+2356 and J2126+7617, the average differences in  $T_{\text{eff}}$  and  $\log g$  between orders are more than 150 K and 0.08 dex, respectively. RV and  $v \sin i$  values are generally consistent across the orders, except for sources with low S/N data (J1254–0122 on

### 3.3.4. Minimum $v \sin i$

The finite resolution of NIRSPEC data places a fundamental limit on our ability to measure rotational broadening for the slowest rotators, which scales with the width of the instrumental LSF. Blake et al. (2010) found a minimum detectable  $v \sin i$  of 9 km s<sup>–1</sup> for their NIRSPEC sample of M8–L6 dwarfs. Our T dwarf spectra contain a higher density of molecular features, with overlapping CO and CH<sub>4</sub> absorption bands, and lower S/N. We empirically determined the minimum detectable  $v \sin i$  limits for order 33 and 58 data by analyzing simulated NIRSPEC data derived from the model grids, using the same forward-modeling method as the science data. We evaluated a representative set of models with  $T_{\text{eff}} = 900, 1200, 1500$  K;  $\log g = 5.0$  dex; RV

<sup>12</sup> RV values are consistent, but  $v \sin i$  values are not.

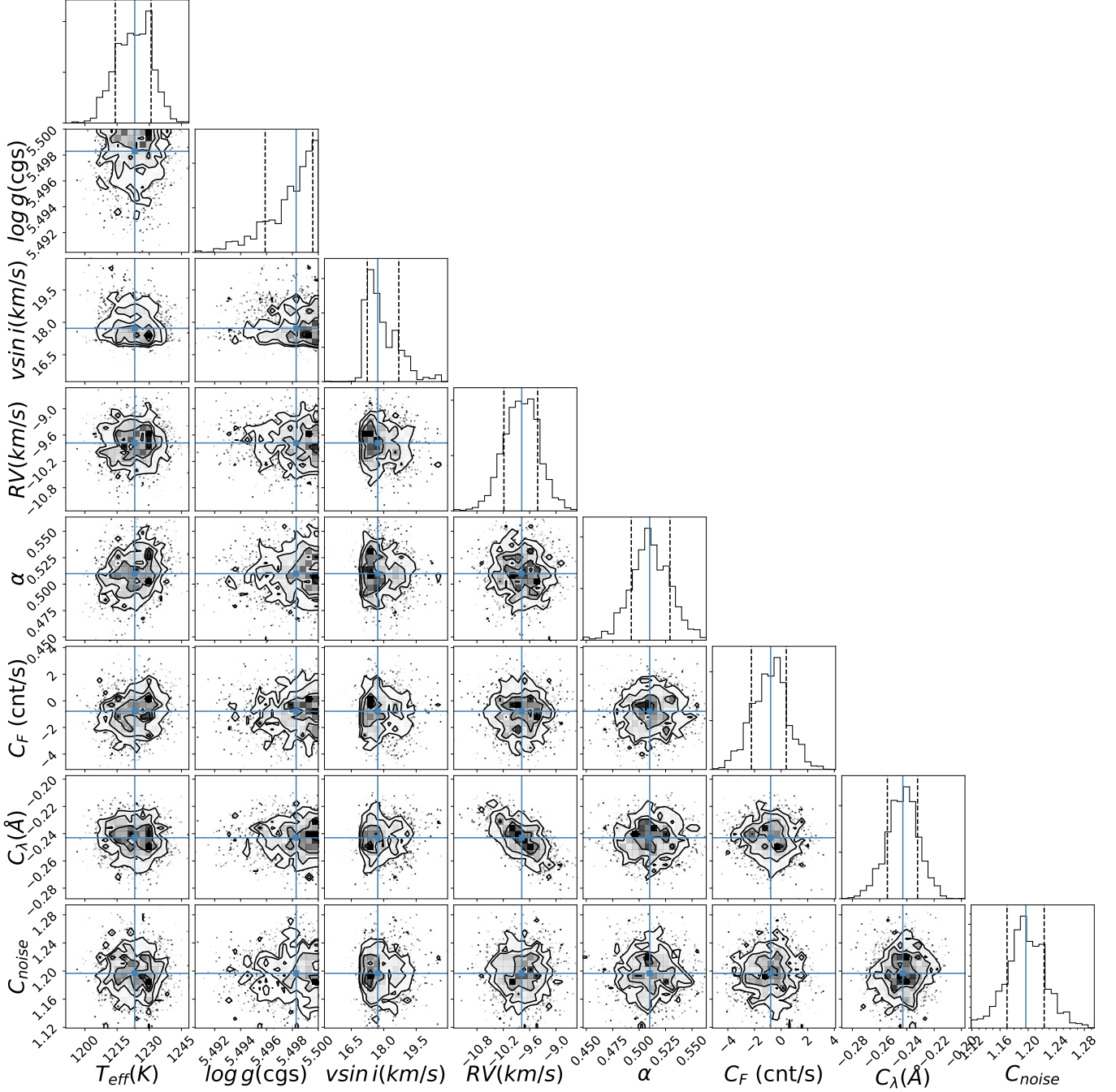


**Figure 4.** The posterior probability distribution of fits to the order 58 spectrum of the T4.5 J0559–1404, observed on 2005 October 26 (UT). Notation is identical to Figure 2.

$= 0 \text{ km s}^{-1}$ ; pwv = 1.5 mm; airmass = 1.0; instrumental LSF =  $4.8 \text{ km s}^{-1}$  (our typical value);  $v \sin i = 1\text{--}15 \text{ km s}^{-1}$  in steps of  $1 \text{ km s}^{-1}$ , and  $15\text{--}25 \text{ km s}^{-1}$  in steps of  $5 \text{ km s}^{-1}$ ; and S/N = 1–10 in steps of 1, and 10–25 in steps of 5. Gaussian noise was applied using pre-upgrade NIRSPEC values for detector gain, read noise, and dark current, and we assumed an integration time of 1500 s. We defined a robust measurement to

be the difference between the true  $v \sin i$  and measured  $v \sin i$  of less than  $1 \text{ km s}^{-1}$ . With this benchmark, we determined the minimum robust  $v \sin i$  to be  $9 \text{ km s}^{-1}$  for  $\text{S/N} \geq 5$  for both orders 33 and 58, equivalent to the minimum  $v \sin i$  for late-M and L dwarfs determined by Blake et al. (2010). Discrepancies generally increase

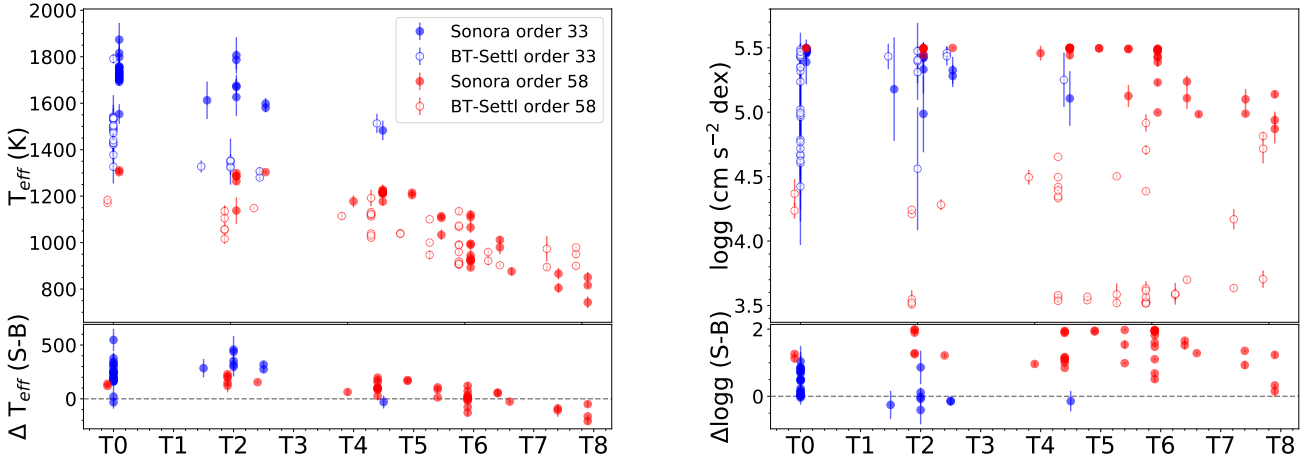


**Figure 5.** Comparison of inferred  $T_{\text{eff}}$  (left) and  $\log g$  (right) parameters between the BT-Settl (open circles) and Sonora (filled circles) models as a function of spectral type, in orders 33 (blue) and 58 (red). Differences (Sonora–BT-Settl) are shown in the lower panels.

from high to low S/N<sup>13</sup>. For  $S/N < 5$  data,  $v \sin i$  fits become much less robust and a more conservative  $v \sin i$  lower limit of  $15 \text{ km s}^{-1}$  is adopted. Hence, the slowest rotators in our sample, J0000+2554 ( $v \sin i = 4 \pm 2 \text{ km s}^{-1}$ ,  $S/N = 5$ ), J0627–1114 ( $v \sin i = 5.4^{+2.5}_{-2.0} \text{ km s}^{-1}$ ,  $S/N = 6$ ), J0819–0335 ( $v \sin i = 8.5^{+1.4}_{-2.4} \text{ km s}^{-1}$ ,  $S/N = 9$ ), and J2236+5105 ( $v \sin i = 6.6 \pm 0.9 \text{ km s}^{-1}$ ,  $S/N = 22$ ) are assigned limits of  $< 9 \text{ km s}^{-1}$ ; while J2030+0749 ( $v \sin i = 14.0^{+0.9}_{-1.0} \text{ km s}^{-1}$ ,  $S/N = 4$ ), is assigned a limit of  $< 15 \text{ km s}^{-1}$ .

### 3.4. Analysis of Fit Parameters

#### 3.4.1. Radial Velocities

Our RV measurements range over  $-43$  to  $+56 \text{ km s}^{-1}$  with a median value of  $1.2 \text{ km s}^{-1}$  and a median uncertainty of  $0.6 \text{ km s}^{-1}$ . These measurements are consistent with a population drawn from the local disk, as verified in further detail below. These measurements are also largely consistent with 14 sources previously reported in the literature (Figure 6; Table 4), but with a median factor of 5.5 improvement in uncertainty. The only significant ( $> 3\sigma$ ) RV outlier is J1346–0031, for which our measurement of  $-17.5^{+0.6}_{-0.5} \text{ km s}^{-1}$  is  $5.1 \text{ km s}^{-1}$  higher than that reported in Zapatero Osorio et al. (2007). For this source (and others), we found our RVs to be consistent between nod pairs in individual epochs and across 2 epochs, albeit with a relatively large  $C_\lambda$  correction of

$4 \text{ km s}^{-1}$ , which may explain the difference with the previously reported value. We found no correlation between RV discrepancies and spectral type. The spatial kinematics of our sources are described further in Section 5.

#### 3.4.2. Rotational Velocities

Our  $v \sin i$  measurements range over  $4^{14}$  to  $90 \text{ km s}^{-1}$ , with a median value of  $27 \text{ km s}^{-1}$  and a median uncertainty of  $0.9 \text{ km s}^{-1}$ . These velocities correspond to maximum rotational periods of 1.5 hr to 28 hr for spheres of radius  $R = 1 R_{\text{Jup}}$  observed at an inclination of  $90^\circ$  (equator-on), and indicate a population of rapid rotators as previously inferred from other studies (Zapatero Osorio et al. 2006; Prato et al. 2015; Radigan et al. 2012; Metchev et al. 2015; Vos et al. 2017; Tannock et al. 2021a). Our  $v \sin i$  measurements are generally consistent with those previously reported in the literature (Figure 6), with a median factor of 2.7 improvement in uncertainties. Again, we found internal agreement between nod pairs and across multiple epochs for  $v \sin i$  measurements of these sources. The largest discrepancies were values reported in Prato et al. (2015) for J2254+3123 and J2356–1553. That study visually compared their spectra with spectral templates convolved with a rotational broadening profile for different  $v \sin i$  values. Forward-model fits to these spectra with  $v \sin i$

<sup>13</sup> See the diagnostic plots in Appendix A

<sup>14</sup> In Section 3.3.4, we determined the minimum  $v \sin i$  to be  $9 \text{ km s}^{-1}$ , with four sources of our sample under such limit.

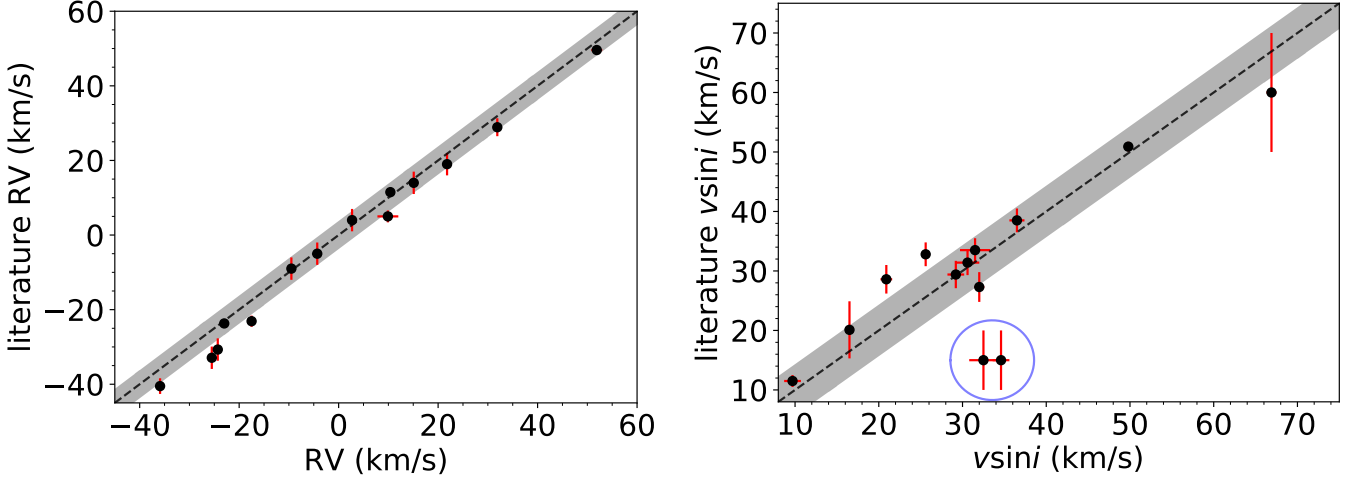


**Figure 6.** Comparison of RV (left) and  $v \sin i$  (right) measurements from our NIRSPEC data to previously reported values for the same sources in the literature (see Table 4). The black dashed line delineates perfect agreement. The shaded region indicates the  $\pm 1\sigma$  scatter ( $3.8 \text{ km s}^{-1}$  for RV and  $4.3 \text{ km s}^{-1}$  for  $v \sin i$ ) between observed and previously reported values. Two outliers in the  $v \sin i$  plot, noted by a blue circle, are excluded in computation of the  $v \sin i$  scatter and are discussed in Section 3.4.2.

values fixed to the Prato et al. (2015) measurements result in significantly worse fits, with p-values<sup>15</sup> of  $<0.001$  and 0.003, respectively.

Figure 7 compares the distribution of our T dwarf  $v \sin i$  measurements along with values reported in the literature (Crossfield 2014, and references therein; Tannock et al. 2021a) between M4 and T9 dwarfs. The median  $v \sin i$  for T dwarfs in our sample is greater than those of both mid/late M dwarfs ( $12 \text{ km s}^{-1}$ ) and L dwarfs ( $20 \text{ km s}^{-1}$ ), continuing a previously identified trend of increasing rotation rate with decreasing mass and later spectral type (Mohanty & Basri 2003; Reiners & Basri 2010; Irwin et al. 2011). Such a correlation is expected for both the smaller radii of lower mass stars and brown dwarfs, and the reduced angular momentum loss from weakened magnetic winds among lower-temperature dwarfs (Mohanty & Basri 2003; Reiners & Basri 2008). It should be noted that many of the M and L dwarfs shown in this panel were observed with higher-resolution spectrometers than NIRSPEC, and therefore have a lower  $v \sin i$  floor. However, the observed trend persists even when a minimum cutoff of  $v \sin i = 9 \text{ km s}^{-1}$  is applied. Among the T dwarfs, there is no significant correlation between  $v \sin i$  and spectral type ( $R = 0.10$ , p-value = 0.56).

### 3.4.3. $T_{\text{eff}}$ and $\log g$

We evaluated our  $T_{\text{eff}}$  and  $\log g$  values by examining spectral type correlations with RV and  $v \sin i$ , and comparing to literature measurements. Table 4 lists the best-fit  $T_{\text{eff}}$  and  $\log g$  for each source (744 K to 1700 K and 4.2 dex to 5.5 dex, respectively)<sup>16</sup>. These are based on order 33 or 58 fits, averaged over all spectra with a specific order. Note that the uncertainties reported here for  $T_{\text{eff}}$  and  $\log g$  are just the Monte Carlo uncertainty, and do not reflect systematic error that may be present due to the narrow spectral bands we chose to model. As expected,  $T_{\text{eff}}$  is strongly correlated with spectral type, decreasing to later types (Figure 8;  $R=-0.94$ , p-value  $< 10^{-3}$ ), although the scatter about a linear trend can be as high as  $\pm 300$  K (standard deviation = 77 K). Differences in  $T_{\text{eff}}$  among equivalently-classified sources can be related to other physical properties (e.g., metallicity,  $\log g$ ), but may also reflect systematic offsets between orders and between models, as discussed in Section 3.3.2. We also find that our  $\log g$  measurements based on Sonora model fits to order 58 data are strongly correlated with spectral type ( $R=-0.62$ , p-value  $< 0.01$ ). Up to spectral type T5,  $\log g$  is consistently around 5.5 dex, and then drops to lower values

<sup>15</sup> Throughout this paper, we adopt the convention that a p-value  $\leq 0.1$  is marginally significant, a p-value  $\leq 0.05$  is significant, and a p-value  $\leq 0.01$  is highly significant (Nuzzo 2014).

<sup>16</sup> The observations of J1520+3546 on 2012 Apr 2 and J2126+7617 on 2020 Sep 3 have  $T_{\text{eff}} \sim 1700$  K, which are determined with a wider  $T_{\text{eff}}$  prior range to ensure the values are robust. The MCMC bounds are well above these temperatures. See Section 3.2.3 for more details.

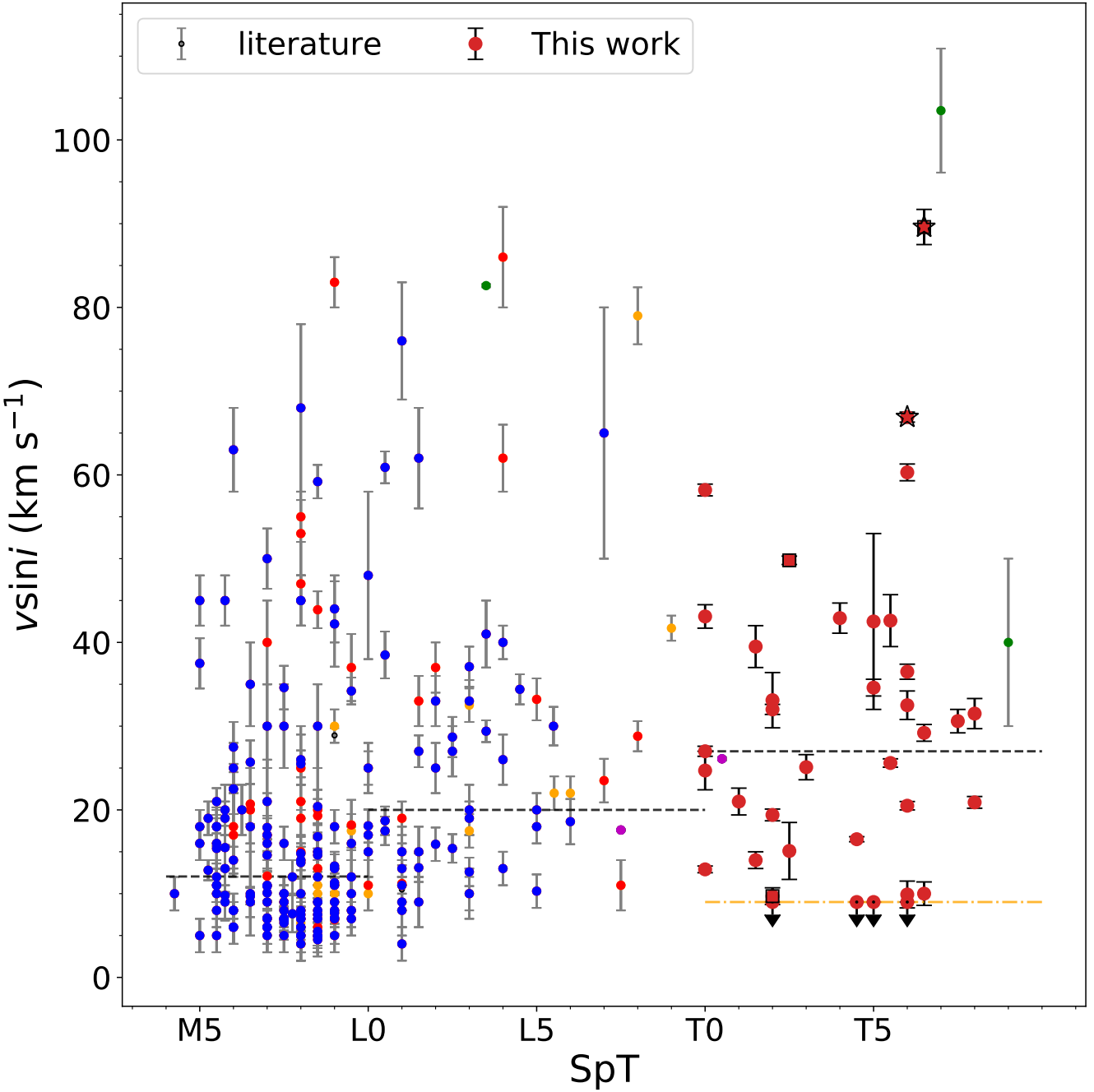


**Figure 7.**  $v \sin i$  measurements as a function of spectral type for a compilation of M4–T9 dwarfs from this work (large symbols) and the literature (small symbols). All symbols are color-coded by instrument resolutions (green for  $R < 10,000$ , orange for  $10,000 \leq R < 20,000$ , red for  $20,000 \leq R < 30,000$ , blue for  $30,000 \leq R < 50,000$ , magenta for  $R \geq 50,000$ ). Our T dwarf measurements are further segregated into normal sources (circles), young cluster members (squares), and spectrally peculiar (stars). The horizontal grey dashed lines indicate the median rotational velocities for late-M, L, and T dwarfs, respectively, in this sample. The horizontal orange dashed line indicates the NIRSPEC minimum  $v \sin i$  floor.

for later spectral types. This could reflect a systematic error or a real physical shift to lower average masses for cooler brown dwarfs.

Next, we evaluated correlations among  $T_{\text{eff}}$ ,  $\log g$ , RV, and  $v \sin i$ . We find our inferred  $T_{\text{eff}}$  and  $\log g$  values to be positively correlated (Figure 9) for Sonora model fits because of the temperature and pressure dependence of the CO $\rightarrow$ CH<sub>4</sub> reduction reaction as described above (see Figure 2). Such a trend is not found in BT-Settl model fits, however, for which the lowest  $\log g$  values correspond to L+T binaries (J0629+2418 and J2126+7617) and the blue L dwarf J1331–0116 (see Section 4.4). Excluding these three sources, the  $\log g$  values are greater than 5.2 cm s<sup>-2</sup> dex for all fits, close to the  $\log g$  ceiling of the models. There are clear positive trends between  $T_{\text{eff}}$  and  $\log g$  paralleled to isoage lines (Figure 9). We found no significant correlations between  $\log g$  and  $v \sin i$ ,  $\log g$  and RV,  $T_{\text{eff}}$  and  $v \sin i$ , or  $T_{\text{eff}}$  and RV.

Several T dwarfs in our sample have  $T_{\text{eff}}$  and  $\log g$  values inferred from other analysis, including high-resolution spectra, medium-/low-resolution spectra, and spectral energy distribution (SED) measurements. Figure 10 shows our measurements of  $T_{\text{eff}}$  and  $\log g$  compared to the literature measurements.<sup>17</sup> Comparing against high-resolution spectra, our  $T_{\text{eff}}$  values are on average  $22\pm280$  K lower and  $\log g$  values on average are  $0.6\pm0.4$  dex higher than literature values, indicating overall consistency but with large scatter. Large discrepancies in  $T_{\text{eff}}$  values inferred from high-resolution spectra have been previously reported in the literature. Gagné et al. (2017) and Vos et al. (2017) analyzed NIRSPEC data for J0136+0933, both using forward-modeling techniques with the same model set, and report  $T_{\text{eff}}$  and  $\log g$  values that differ by 192 K and 1.14 dex cm s<sup>-2</sup>, respectively. Del Burgo et al. (2009) found a comparable degree of scatter in  $T_{\text{eff}} \approx 200$  K and  $\log g \approx 0.7$  dex in fits of PHOENIX AMES-COND cloudless models (Allard et al. 2001) across multiple orders of T dwarf NIRSPEC spectra. Outdated methane opacities in the PHOENIX AMES-COND may be responsible for this scatter, as discussed in Section 3.3.2. Comparing against low- and medium-resolution spectra, we find smaller differences and scatter, with our  $T_{\text{eff}}$  values on average  $63\pm150$  K higher and  $\log g$  values on average  $0.4\pm0.4$  dex higher than literature values. Similarly, our  $T_{\text{eff}}$  values are

on average  $68\pm145$  K higher and  $\log g$  values on average  $0.3\pm0.4$  dex higher than SED measurements from Filippazzo et al. (2015). Again, such discrepancies are common in the literature, and reflect ongoing challenges in accurately modeling brown dwarf spectra. In accord with our analysis, Logsdon et al. (2018) found that  $\log g$  values inferred from medium-resolution spectra of late-T dwarfs were highly dependent on the spectral band used, with the best-fit values of 3.0–3.5 dex in the  $Y$ -band ( $\sim 0.95$ – $1.12$   $\mu\text{m}$ ) and 5.0–5.5 dex in the  $H$ -band ( $\sim 1.5$ – $1.68$   $\mu\text{m}$ ) using the BT-Settl models. Different atmosphere models also yielded significantly different  $\log g$  values, as discussed in Section 3.3.2 (see Table 3 in Logsdon et al. 2018).

Given the differences in  $T_{\text{eff}}$  and  $\log g$  values inferred between orders and in comparison with prior results, we urge caution in interpreting these quantities as they may not be accurate. Nevertheless, we have found that they are weakly correlated or uncorrelated with RV and  $v \sin i$  and will not significantly influence the subsequent kinematic analysis.

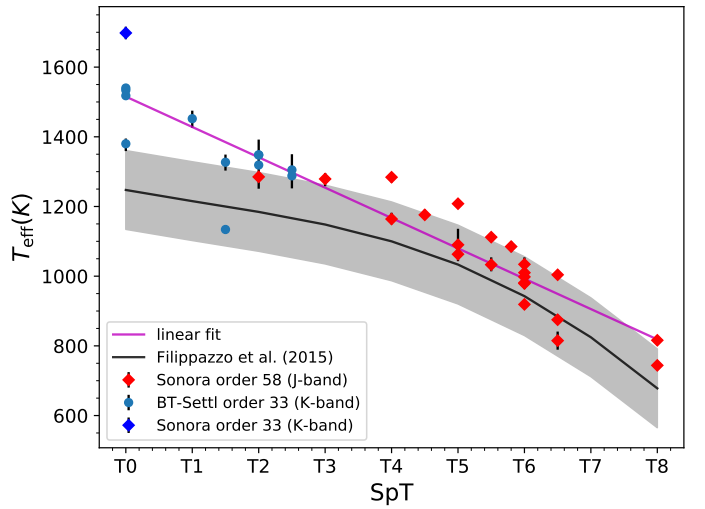


**Figure 8.** Measured  $T_{\text{eff}}$  values as a function of spectral type based on fits to orders 33 (blue) and 58 (red) data, compared to the  $T_{\text{eff}}$ /spectral type relation of Filippazzo et al. (2015) (black line with  $\pm 1\sigma$  uncertainty shaded in grey). The BT-Settl and Sonora model fits are marked as circles and diamonds, respectively. A linear fit to all of the measurements is indicated by the magenta line.

<sup>17</sup> The literature  $T_{\text{eff}}$  and  $\log g$  are drawn from Stephens et al. (2009, medium-/low-resolution spectroscopy); Del Burgo et al. (2009, high-resolution spectroscopy); Liu et al. (2011, medium-resolution spectroscopy); Sorahana & Yamamura (2012, low- and medium-resolution spectroscopy); Filippazzo et al. (2015, SEDs); Line et al. (2017, low-resolution spectroscopy); Vos et al. (2017, high-resolution spectroscopy); Gagné et al. (2017, high-resolution spectroscopy); Gagné et al. (2018a, high-resolution spectroscopy); and Miles et al. (2020, low-resolution spectroscopy).

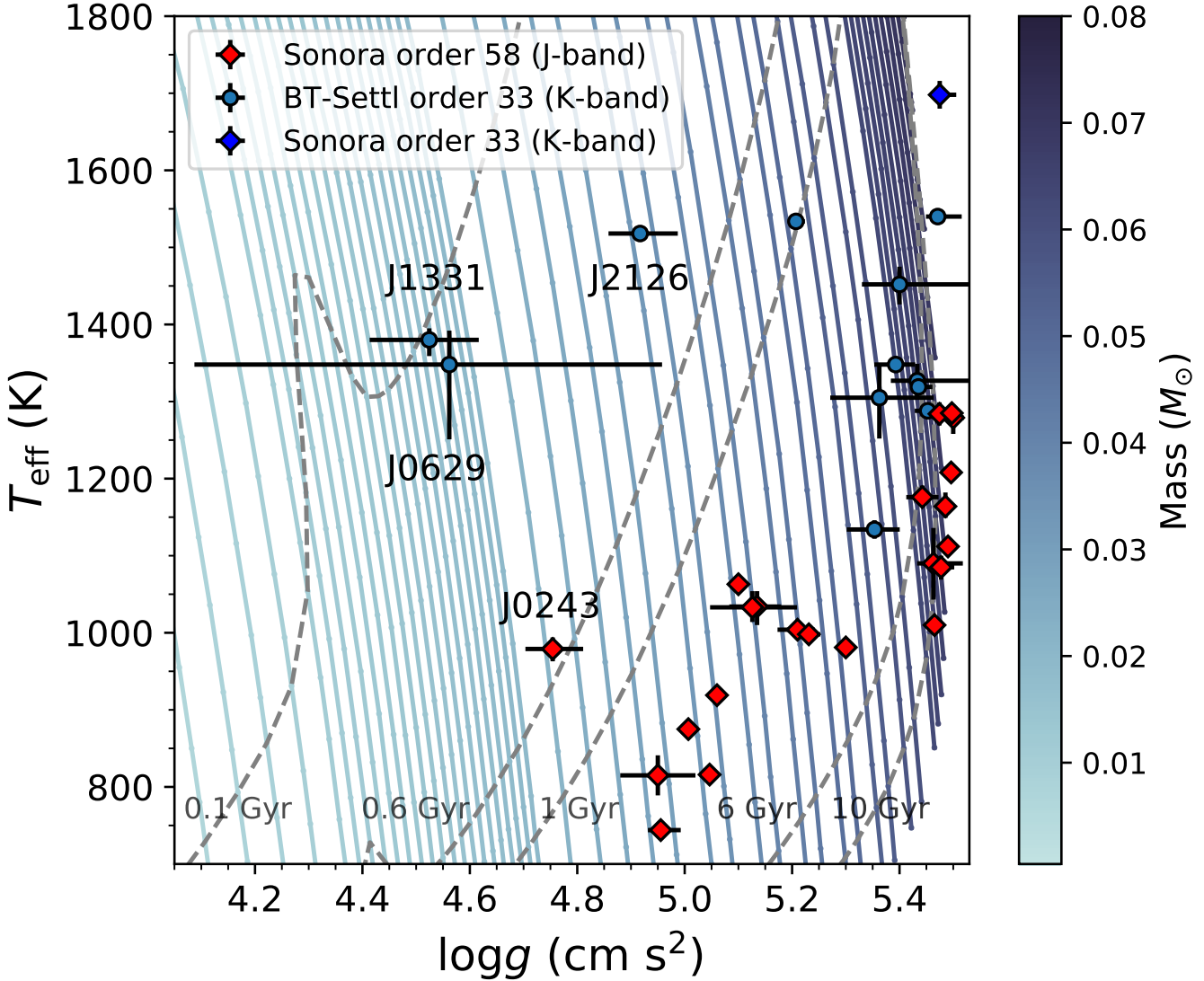


**Figure 9.** Comparison of measured  $T_{\text{eff}}$  and  $\log g$  values based on fits to orders 33 (blue) and 58 (red) data. The BT-Settl and Sonora model fits are marked as circles and diamonds, respectively. The Marley et al. (2018) evolutionary models are plotted, with lines of constant mass indicated by solid color-coded lines and lines of constant age (0.1, 0.6, 1, 6, and 10 Gyr) indicated by labeled dashed grey lines. There are clear positive trends between  $T_{\text{eff}}$  and  $\log g$  for both BT-Settl and Sonora model fits that run parallel to isoage lines. Note that earlier T dwarfs are mostly observed in  $K$ -band (orders 33), while later T dwarfs are mostly observed in  $J$ -band (order 58).

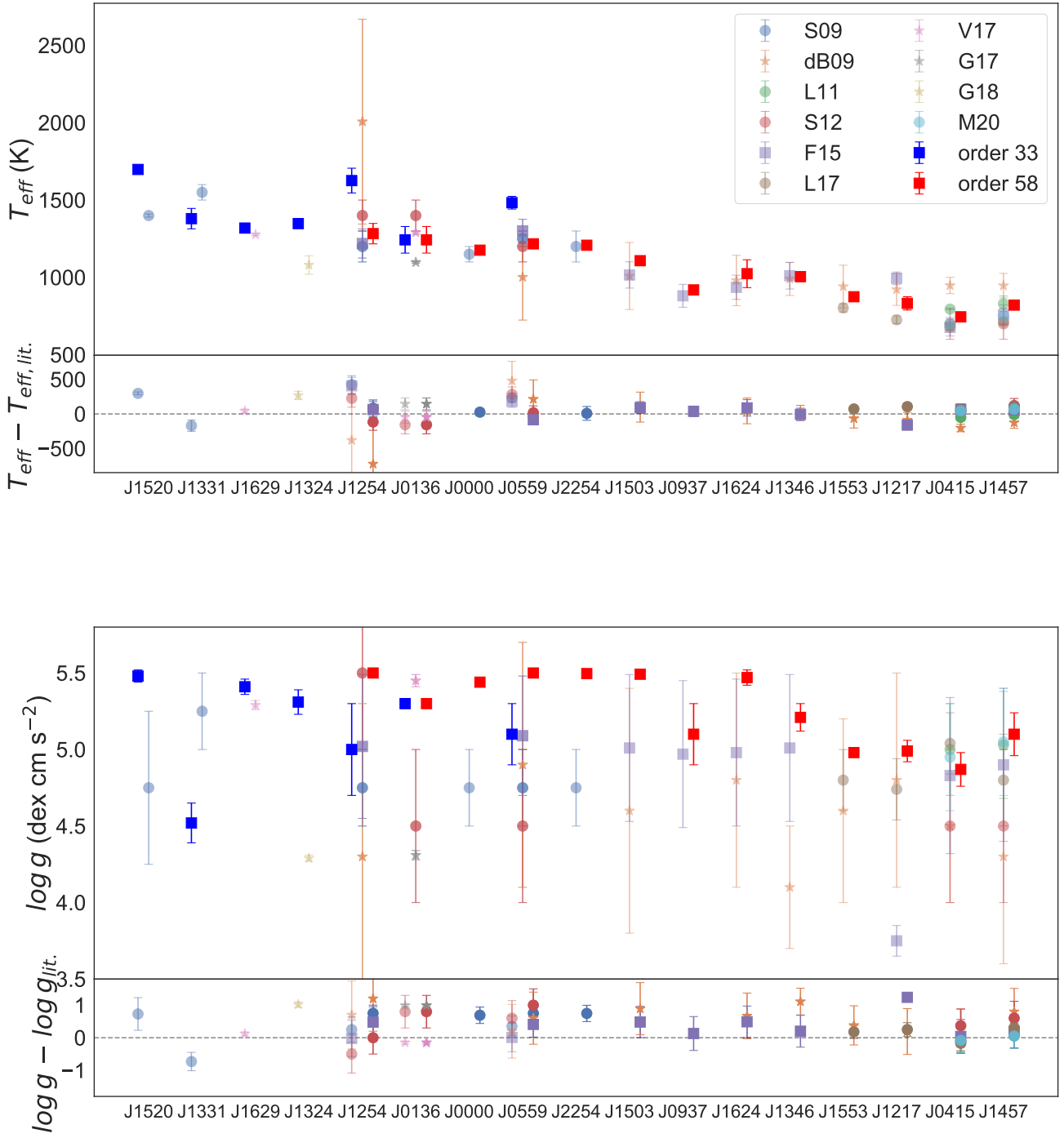


**Figure 10.** Comparison of  $T_{\text{eff}}$  measurements (top) and  $\log g$  measurements (bottom) from our analysis with measurements from the literature. For each figure, the top panels show the measurements, with literature values slightly offset horizontally for clarity; the lower panels show the difference between measurement and literature values for each source. Measurements for orders 33 and 58 fits are labeled as blue and red squares, respectively. Literature references (from top to bottom in the legend) are: (S09): Stephens et al. (2009) (light blue), (dB09): Del Burgo et al. (2009) (orange), (L11): Liu et al. (2011) (green), (S12): Sorahana & Yamamura (2012) (red), (F15): Filippazzo et al. (2015) (purple), (L17): Line et al. (2017) (brown), (V17): Vos et al. (2017) (pink), (G17): Gagné et al. (2017) (grey), (G18): Gagné et al. (2018a) (olive), and (M20): Miles et al. (2020) (cyan). The stars, circles, and squares denote literature measurements based on high-resolution spectroscopy, medium-/low-resolution spectroscopy, and spectral energy distribution, respectively.





Table 4 (continued)

Source	SpT	UT Date	O <i>a</i>	S/N	RV	<i>v</i> sin <i>i</i>	$\langle RV \rangle \mathbf{b}$	$_{\rm RV} \mathbf{LIT} \mathbf{c}$	$\langle v \sin i \rangle \mathbf{b}$	$v \sin i \mathbf{LIT} \mathbf{C}$	Teff	$\langle T_{\rm eff} \rangle \mathbf{a}$	$\log g$	$\langle \log g \rangle \mathbf{b}$	$_{\rm M} d$	Ref. <i>c</i>
					(km s <sup>-1</sup> )	(km s <sup>-1</sup> )	(km s <sup>-1</sup> )	(km s <sup>-1</sup> )	(km s <sup>-1</sup> )	(km s <sup>-1</sup> )	(K)	(K)	(cm s <sup>-2</sup> )	(cm s <sup>-2</sup> )		
J1952+7240	T4	2019 Oct 17	58	5	-11.8 <sup>+2.0</sup> <sub>-1.0</sub>	40.2 <sup>+3.0</sup> <sub>-2.7</sub>	-12.0 <sup>+1.3</sup> <sub>-0.7</sub>	...	42.9 <sup>+1.8</sup> <sub>&lt; 1.8</sub>	...	11.64 <sup>+15</sup> <sub>-18</sub>	11.64 <sup>+15</sup> <sub>-18</sub>	5.46 <sup>+0.03</sup> <sub>-0.06</sub>	5.485 <sup>+0.008</sup> <sub>-0.017</sub>	S	
J2030+0749	T1.5	2020 Jul 10	33	4	-21.2 <sup>+0.6</sup> <sub>-0.7</sub>	14.0 <sup>+0.9</sup> <sub>-1.0</sub>	-21.2 <sup>+0.6</sup> <sub>-0.7</sub>	...	< 15 $K_b^h$	...	11.34 <sup>+12</sup> <sub>-12</sub>	11.34 <sup>+12</sup> <sub>-12</sub>	5.35 <sup>+0.05</sup> <sub>-0.05</sub>	5.35 <sup>+0.05</sup> <sub>-0.05</sub>	B	
J2126+7617	TOp	2011 Jun 10	33	6	-17.7 <sup>+1.0</sup> <sub>-1.1</sub>	58.8 <sup>+1.9</sup> <sub>-1.8</sub>	-18.4 <sup>+0.4</sup> <sub>-0.4</sub>	...	58.2 <sup>+0.7</sup> <sub>-0.7</sub>	...	14.62 <sup>+20</sup> <sub>-29</sub>	15.18 <sup>+15</sup> <sub>-9</sub>	4.66 <sup>+0.14</sup> <sub>-0.3</sub>	4.92 <sup>+0.06</sup> <sub>-0.07</sub>	B	
...	...	2011 Jul 6	33	10	-18.8 <sup>+1.1</sup> <sub>-1.2</sub>	59.5 <sup>+2.1</sup> <sub>-1.8</sub>	...	...	...	...	15.04 <sup>+16</sup> <sub>-21</sub>	...	4.77 <sup>+0.25</sup> <sub>-0.15</sub>	...	B	
...	...	2011 Aug 11	33	2	-24.3 <sup>+5.3</sup> <sub>-4.2</sub>	51.1 <sup>+10.3</sup> <sub>-10.3</sub>	...	...	...	...	15.52 <sup>+61</sup> <sub>-61</sub>	...	4.7 <sup>+0.7</sup> <sub>-0.7</sub>	...	B	
...	...	2011 Sep 7	33	8	-18.7 <sup>+1.6</sup> <sub>-1.2</sub>	56.1 <sup>+2.7</sup> <sub>-2.5</sub>	...	...	...	...	15.53 <sup>+8</sup> <sub>-23</sub>	...	5.0 <sup>+0.3</sup> <sub>-0.3</sub>	5.0 <sup>+0.3</sup> <sub>-0.3</sub>	B	
...	...	2013 Sep 17	33	5	-20.3 <sup>+2.1</sup> <sub>-2.0</sub>	58.4 <sup>+3.2</sup> <sub>-2.9</sub>	...	...	...	...	14.75 <sup>+23</sup> <sub>-34</sub>	...	5.0 <sup>+0.2</sup> <sub>-0.2</sub>	5.0 <sup>+0.2</sup> <sub>-0.2</sub>	B	
...	...	2013 Oct 16	33	4	-20.7 <sup>+1.8</sup> <sub>-1.8</sub>	59.7 <sup>+2.8</sup> <sub>-2.9</sub>	...	...	...	...	14.48 <sup>+11</sup> <sub>-19</sub>	...	4.6 <sup>+0.4</sup> <sub>-0.4</sub>	4.6 <sup>+0.4</sup> <sub>-0.4</sub>	B	
...	...	2014 Sep 02	33	6	-19.5 <sup>+1.6</sup> <sub>-1.7</sub>	57.5 <sup>+2.7</sup> <sub>-2.5</sub>	...	...	...	...	15.40 <sup>+11</sup> <sub>-17</sub>	...	4.7 <sup>+0.3</sup> <sub>-0.3</sub>	4.7 <sup>+0.3</sup> <sub>-0.3</sub>	B	
...	...	2020 Aug 25	33	4	-14.9 <sup>+1.7</sup> <sub>-1.5</sub>	54.9 <sup>+2.1</sup> <sub>-2.1</sub>	...	...	...	...	15.07 <sup>+104</sup> <sub>-156</sub>	...	5.2 <sup>+0.19</sup> <sub>-0.2</sub>	5.2 <sup>+0.19</sup> <sub>-0.2</sub>	B	
...	...	2020 Sep 3	57 <sup>j</sup>	14	-14.1 <sup>+0.9</sup> <sub>-1.0</sub>	60.4 <sup>+1.0</sup> <sub>-0.9</sub>	...	...	...	...	17.00 <sup>+12</sup> <sub>-2</sub>	...	5.0 <sup>+0.01</sup> <sub>-0.01</sub>	5.0 <sup>+0.01</sup> <sub>-0.01</sub>	B	
HN Peg B	T2.5	2017 Jun 09	33	5	-19.5 <sup>+1.3</sup> <sub>-1.3</sub>	15.1 <sup>+3.0</sup> <sub>-3.4</sub>	-19.5 <sup>+1.3</sup> <sub>-1.3</sub>	...	15.1 <sup>+3.0</sup> <sub>-3.4</sub>	...	13.05 <sup>+53</sup> <sub>-45</sub>	13.05 <sup>+53</sup> <sub>-53</sub>	5.36 <sup>+0.09</sup> <sub>-0.10</sub>	5.36 <sup>+0.09</sup> <sub>-0.10</sub>	B	
J2236+5105	T5	2020 Sep 3	58	22	-1.2 <sup>+0.3</sup> <sub>-0.3</sub>	6.6 <sup>+0.9</sup> <sub>-0.9</sub>	-1.2 <sup>+0.3</sup> <sub>-0.3</sub>	...	< 9 $K_b^h$	...	10.63 <sup>+8</sup> <sub>-8</sub>	10.63 <sup>+8</sup> <sub>-8</sub>	5.1 <sup>+0.01</sup> <sub>-0.01</sub>	5.1 <sup>+0.01</sup> <sub>-0.01</sub>	S	
J2234+3123	T5	2003 Aug 10	58	17	14.3 <sup>+0.5</sup> <sub>-0.7</sub>	32.5 <sup>+1.2</sup> <sub>-1.2</sub>	15.1 <sup>+0.5</sup> <sub>-0.6</sub>	14 ± 3	34.6 <sup>+0.9</sup> <sub>-1.0</sub>	15 ± 5	12.14 <sup>+12</sup> <sub>-11</sub>	12.08 <sup>+7</sup> <sub>-7</sub>	5.5 <sup>+0.03</sup> <sub>-0.03</sub>	5.496 <sup>+0.002</sup> <sub>-0.005</sub>	S (3)	
...	...	2005 Jul 19	58	16	16.8 <sup>+1.0</sup> <sub>-0.9</sub>	37.4 <sup>+1.3</sup> <sub>-1.5</sub>	...	14 ± 3	...	12.04 <sup>+9</sup> <sub>-11</sub>	...	5.5 <sup>+0.03</sup> <sub>-0.03</sub>	5.5 <sup>+0.03</sup> <sub>-0.03</sub>	S		
J2356-1553	T6	2005 Jul 19	58	6	23.6 <sup>+1.3</sup> <sub>-1.5</sub>	30.6 <sup>+2.2</sup> <sub>-2.1</sub>	21.8 <sup>+0.9</sup> <sub>-1.0</sub>	19 ± 3	32.5 <sup>+1.7</sup> <sub>-1.6</sub>	15 ± 5	10.65 <sup>+22</sup> <sub>-22</sub>	10.85 <sup>+16</sup> <sub>-15</sub>	5.48 <sup>+0.01</sup> <sub>-0.03</sub>	5.477 <sup>+0.013</sup> <sub>-0.025</sub>	S	
...	...	2005 Dec 10	58	6	20.3 <sup>+1.3</sup> <sub>-1.4</sub>	35.4 <sup>+2.7</sup> <sub>-2.6</sub>	...	19 ± 3	...	15 ± 5	11.09 <sup>+24</sup> <sub>-23</sub>	...	5.43 <sup>+0.05</sup> <sub>-0.07</sub>	5.43 <sup>+0.05</sup> <sub>-0.07</sub>	S	

HSU ET AL.

*References*—(1) Zapatero Osorio et al. (2006), (2) Zapatero Osorio et al. (2007), (3) Prato et al. (2015), (4) Gagné et al. (2017), (5) Gagné et al. (2018a)*a* Spectral order of data.*b* Weighted average over all epochs.*c* Previously reported values in the literature.*d* Models used: S = Sonora 2018 (Marley et al. 2018); B = BT-Settl (Allard et al. 2012).*e* References for prior RV and *v* sin *i* measurements*f* No telluric observations available for this epoch.*g* Measurements are considered unreliable due to low S/N.*h* Adopted Teff and log *g* are determined using order 33 measurements only; see Section 3.4.3.*i* Adopted Teff and log *g* are determined using order 58 measurements only; see Section 3.4.3.*j* The spectra of order 57 are modeled in this case, as order 58 spectra are almost featureless due to large large *v* sin *i*.*k* The *v* sin *i* detection floor for NIRSPEC is 9 km s<sup>-1</sup> for S/N ≥ 5, and 15 km s<sup>-1</sup> for S/N < 5 data; see Section 3.3.4.Note—Measurements from individual spectra over individual or multiple epochs are combined using inverse uncertainty weighting (weight = 1/( $\sigma_{\text{upper}}^2 + \sigma_{\text{lower}}^2$ )); upper and lower uncertainties are also combined using inverse uncertainty weighting. In cases where individual spectra have S/N < 10, spectral data are combined first, the modeled.

## 4. ANALYSIS

### 4.1. Galactic $UVW$ Space Motions and Kinematic Populations

We combined astrometry and our measured RVs to compute Galactic  $UVW$  space motions for our sample following the prescription of Johnson & Soderblom (1987).  $UVW$  velocities are defined here in a right-handed rectangular coordinate system centered on the Sun, with  $U$  in the direction toward the Galactic center,  $V$  in the direction of Galactic rotation, and  $W$  in the direction toward the Galactic North pole (opposite the Galactic angular velocity vector). Uncertainties were propagated from the input quantities using the Monte Carlo method assuming Gaussian noise. We adopted a correction from the heliocentric frame to the local standard of rest (LSR) of  $(U_\odot, V_\odot, W_\odot) = (11.1, 12.24, 7.25)$  km s $^{-1}$  from Schönrich et al. (2010). The T dwarf J1952+7240 does not have a parallax measurement, so we estimated its distance and uncertainty using the absolute magnitude/spectral type relations in Dupuy & Liu (2012). Results are tabulated in Table 5.

Figure 11 compares the distribution of  $UVW$  velocities to the  $2\sigma$  velocity dispersion volumes of local thin and thick disk populations from Bensby et al. (2003). The average  $U$  and  $W$  velocities of the T dwarfs are consistent with zero, while a marginally significant net negative average  $V$  velocity ( $\langle V \rangle = -3.6 \pm 2.7$  km s $^{-1}$ ) can be attributed to asymmetric drift (Strömberg 1924). We do not find any significant correlation between  $UV$ ,  $UW$ , or  $VW$  velocities.

Following Bensby et al. (2003), we computed relative probabilities of membership in the thick disk versus the thin disk ( $P(\text{TD})/P(\text{D})$ ) and halo versus the thin disk ( $P(\text{H})/P(\text{D})$ ) using the threshold criteria defined in Burgasser et al. (2015b): thin disk membership is assigned for  $P(\text{TD})/P(\text{D}) < 0.1$ , thick disk membership is assigned for  $P(\text{TD})/P(\text{D}) > 10$ , and intermediate population membership is assigned for  $0.1 < P(\text{TD})/P(\text{D}) < 10$ . All but one of our sources are thin disk members, with J1331–0116 being identified as an intermediate thin disk/thick disk member and an unusually blue L dwarf (see Section 4.4). None of the sources in our sample have a significant probability of halo membership.

### 4.2. Galactic Orbits

Additional insight into our sample’s kinematic properties can be inferred by computing their Galactic orbits and orbital parameters. We used the package *galpy* (Bovy 2015) to compute the orbits, which is an ordinary differential equation solver that satisfies conservation of energy and angular momentum. We assumed an axisymmetric Galactic potential in a galactocentric cylind-

rical coordinate system  $(R, \phi, Z)$  using the parameters of Miyamoto & Nagai (1975), a Solar azimuthal velocity  $v_\phi = 220$  km s $^{-1}$  (Bovy & Tremaine 2012), and a Solar coordinate of  $(R_\odot, Z_\odot) = (8.43, 0.027)$  kpc at  $\phi_\odot = 0$  (Chen et al. 2001; Reid et al. 2014). Orbits were sampled over the period  $-5$  to  $+5$  Gyr. Uncertainties in the present-day position and velocity of each source were propagated using Monte Carlo sampling assuming Gaussian noise, resulting in 1,000 orbits per source from which we computed minimum and maximum Galactic cylindrical radius ( $R_{\min}, R_{\max}$ ), maximum absolute Galactic vertical height ( $|Z|$ ), median orbital eccentricity ( $e \equiv \langle R_{\max} - R_{\min} \rangle / \langle R_{\max} + R_{\min} \rangle$ ), and median orbital inclination ( $\tan i \equiv |Z| / \sqrt{X^2 + Y^2}|$ ), with uncertainties determined from the distribution of simulated orbits.

The majority of our sample possess circular and planar orbits ( $e \leq 0.20$ ,  $i \leq 2^\circ$ ) as expected for a thin disk population. The intermediate thin/thick disk star J1331–0116 has the largest inclination and eccentricity in the sample ( $i = 2.5^\circ \pm 0.8^\circ$ ,  $e = 0.29 \pm 0.06$ ,  $R_{\min} = 4.6 \pm 0.6$  kpc). The median orbital parameters for the sample,  $R_{\min} = 7.5$  kpc,  $R_{\max} = 9.2$  kpc,  $e = 0.12$ , and  $i = 0.69^\circ$ , are consistent with the orbital parameters of local late-M and L dwarfs reported in Burgasser et al. (2015b).<sup>18</sup>

### 4.3. Cluster Membership

UCDs, including T dwarfs, have been found to be members of nearby association and clusters, which provide independent age determinations and can potentially break the age-mass- $L_{\text{bol}}$  degeneracy. Cluster membership probability can be determined by the alignment in 6D configuration space (heliocentric  $XYZ$  spatial and  $UVW$  velocity coordinates) with other association members.  $XYZ$  spatial coordinates are defined in the same direction as  $UVW$ . We used the BANYAN  $\Sigma$  web tool<sup>19</sup> (Gagné et al. 2018c) to compare the astrometry and radial velocities of our sources to 27 young clusters within 150 pc of the Sun. We confirmed that J0136+0933 (Gagné et al. 2017) and J1324+6358 (Gagné et al. 2018a) are probable members (99%) of the  $\sim 200$  Myr Carina-Near and 130 Myr AB Doradus moving groups, respectively (Zuckerman et al. 2006; Gagné et al. 2018b). We also confirmed that J0819–0335 is a candidate kinematic member of the  $\beta$  Pictoris moving group (age  $\tau = 24 \pm 3$  Myr, Bell et al. 2015), with a 95%

<sup>18</sup> These values are  $R_{\min} = 8.0$  kpc,  $R_{\max} = 9.5$  kpc, and  $e = 0.11$  for late-M dwarfs, and  $R_{\min} = 7.8$  kpc,  $R_{\max} = 10$  kpc, and  $e = 0.16$  for late L dwarfs, with  $i \leq 2^\circ$  for both populations.

<sup>19</sup> <http://www.exoplanetes.umontreal.ca/banyan/>

probability of membership and a 5% probability of being a field dwarf (Zhang et al. 2021). J1553+1532 is also confirmed as a kinematic member of Carina-Near moving group, with a 98% probability of membership (2% field object; Zhang et al. 2021). We discuss these two sources in further detail below. We are able to rule out three young moving group candidates reported in Zhang

et al. (2021), identified on the basis of spatial coordinates, proper motion, and the BANYAN  $\Sigma$  tool. These are J0627–1114 (99% field object), J1624+0029 (27% Carina-Near; 73% field object), and J2236+5105 (99% field object). Our ability to exclude these candidates highlights the importance of precise RV measurements in assessing cluster membership.

**Table 5.** Radial Velocities and Heliocentric Space Motions

Source Name	SpT	Adopted RV (km s <sup>-1</sup> )	<i>U</i> (km s <sup>-1</sup> )	<i>V</i> (km s <sup>-1</sup> )	<i>W</i> (km s <sup>-1</sup> )	P[TD]/P[D] <sup>a</sup>	Population <sup>a</sup>
J0000+2554	T4.5	6.4 <sup>+0.4</sup> <sub>-0.5</sub>	7.1±0.2	21.6±0.4	10.5±0.4	0.01	D
J0034+0523	T6.5	16.6 <sup>+1.4</sup> <sub>-1.6</sub>	-19.0±0.7	11.5±0.8	-4.6±1.4	0.01	D
J0136+0933	T2.5	10.4 <sup>+0.3</sup> <sub>-0.3</sub>	-21.5±0.2	-6.0±0.1	5.1±0.2	0.01	D
J0150+3827	T0	56.2 <sup>+0.9</sup> <sub>-0.9</sub>	-94.6±5.0	-15.5±4.6	-5.2±0.8	0.09	D
J0213+3648	T3	-3.8 <sup>+1.0</sup> <sub>-0.9</sub>	10.7±3.2	7.2±3.6	10.1±4.1	0.01	D
J0243–2453	T6	-0.6 <sup>+0.6</sup> <sub>-0.7</sub>	27.8±0.7	14.6±0.3	0.8±0.7	0.01	D
J0415–0935	T8	51.9 <sup>+1.1</sup> <sub>-1.1</sub>	-54.9±0.8	-31.8±0.4	21.2±0.8	0.05	D
J0559–1404	T4.5	-9.5 <sup>+0.1</sup> <sub>-0.1</sub>	31.1±0.1	-6.4±0.2	28.0±0.1	0.02	D
J0627–1114	T6	1.2 <sup>+0.9</sup> <sub>-1.1</sub>	23.8±1.0	-1.7±1.0	-3.0±0.5	0.01	D
J0629+2418	L7+T5.5 <sup>b</sup>	0.5 <sup>+2.3</sup> <sub>-2.1</sub>	13.9±2.3	-27.1±3.5	-17.8±2.3	0.01	D
J0755+2212	T5	22.3 <sup>+2.7</sup> <sub>-1.7</sub>	-5.9±2.3	-10.8±1.1	9.0±1.1	0.01	D
J0819–0335	T4	14.4 <sup>+0.8</sup> <sub>-0.9</sub>	0.3±0.6	-3.5±0.7	-4.5±0.6	0.01	D
J0909+6525	T1.5+T2.5 <sup>b</sup>	37.8 <sup>+1.6</sup> <sub>-1.6</sub>	-28.1±1.4	19.6±0.8	21.0±1.2	0.02	D
J0937+2931	T6	-4.3 <sup>+0.4</sup> <sub>-0.4</sub>	42.0±0.4	-21.6±0.4	18.8±0.4	0.02	D
J1106+2754	T0+T4.5 <sup>b</sup>	2.5 <sup>+0.2</sup> <sub>-0.2</sub>	3.2±0.2	-37.0±1.2	-2.0±0.3	0.01	D
J1217–0311	T7.5	9.9 <sup>+2.3</sup> <sub>-1.9</sub>	-37.0±1.2	-16.3±1.3	10.4±2.0	0.01	D
J1225–2739	T5.5+T8 <sup>b</sup>	18.5 <sup>+1.5</sup> <sub>-1.2</sub>	52.9±1.3	-7.4±1.1	-12.0±1.3	0.01	D
J1254–0122	T2e	2.7 <sup>+0.4</sup> <sub>-0.5</sub>	-17.8±1.0	-0.9±0.5	13.4±0.5	0.01	D
J1324+6358	T2p	-23.0 <sup>+0.5</sup> <sub>-0.4</sub>	5.5±0.7	-12.5±0.8	-6.8±0.5	0.01	D
J1331–0116	T0	-3.3 <sup>+0.4</sup> <sub>-0.4</sub>	25.4±1.6	-83.8±9.7	-36.3±4.1	0.27	D/TD
J1346–0031	T6.5	-17.5 <sup>+0.6</sup> <sub>-0.5</sub>	-19.2±0.8	-11.0±1.0	-4.1±0.5	0.01	D
J1457–2122	T8	31.9 <sup>+0.3</sup> <sub>-0.3</sub>	63.4±0.4	-11.2±0.2	-22.8±0.5	0.04	D
J1503+2525	T5.5	-35.9 <sup>+0.4</sup> <sub>-0.3</sub>	-13.8±0.2	14.9±0.1	-23.7±0.4	0.02	D
J1506+7027	T6	2.5 <sup>+0.4</sup> <sub>-0.5</sub>	-26.0±0.2	1.0±0.4	9.8±0.3	0.01	D
J1520+3546	T0	4.1 <sup>+1.0</sup> <sub>-1.0</sub>	42.4±2.4	13.3±0.5	0.8±1.1	0.01	D
J1553+1532	T6.5+T7.5 <sup>b</sup>	-25.5 <sup>+0.6</sup> <sub>-0.5</sub>	-21.6±0.4	-4.6±0.2	7.1±0.5	0.01	D
J1624+0029	T6	-24.3 <sup>+0.5</sup> <sub>-0.5</sub>	-14.4±0.4	-5.6±0.2	7.8±0.3	0.01	D
J1629+0335	T2	7.6 <sup>+0.6</sup> <sub>-0.6</sub>	26.0±0.7	16.9±0.2	-2.8±0.8	0.01	D
J1809–0448	T1	-43.4 <sup>+1.3</sup> <sub>-1.3</sub>	-12.0±1.5	-38.0±2.0	-11.8±0.9	0.02	D
J1928+2356	T6	-26.3 <sup>+0.2</sup> <sub>-0.3</sub>	-5.3±0.2	-9.1±0.3	16.0±0.1	0.01	D
J1952+7240	T4	-12.0 <sup>+1.3</sup> <sub>-0.7</sub>	39.2±0.7	5.4±1.2	9.7±0.5	0.01	D
J2030+0749	T1.5	-21.2 <sup>+0.6</sup> <sub>-0.7</sub>	-16.2±0.4	-3.3±0.5	-13.5±0.3	0.01	D
J2126+7617	L7+T3.5 <sup>b</sup>	-18.4 <sup>+0.4</sup> <sub>-0.4</sub>	-62.6±0.8	-36.7±0.5	3.5±0.1	0.05	D
HN Peg B	T2.5	-19.5 <sup>+1.3</sup> <sub>-1.3</sub>	-4.2±0.4	-11.1±1.1	-2.2±0.6	0.01	D
J2236+5105	T5	-1.2 <sup>+0.3</sup> <sub>-0.3</sub>	-25.2±1.3	2.6±0.4	3.6±0.2	0.01	D
J2254+3123	T5	15.1 <sup>+0.5</sup> <sub>-0.6</sub>	0.1±0.4	28.7±0.6	8.9±0.5	0.01	D
J2356–1553	T6	21.8 <sup>+0.9</sup> <sub>-1.0</sub>	55.4±3.3	-3.5±1.7	-15.9±1.0	0.02	D

<sup>a</sup> Galactic thin disk (D), thick disk (TD), intermediate populations (D/TD) are assigned according to probability ratios  $P(\text{TD})/P(\text{D}) < 0.1$ ,  $P(\text{TD})/P(\text{D}) > 10$ , and  $0.1 < P(\text{TD})/P(\text{D}) < 10$ , respectively, following Bensby et al. (2003).

<sup>b</sup> Known or candidate binary.

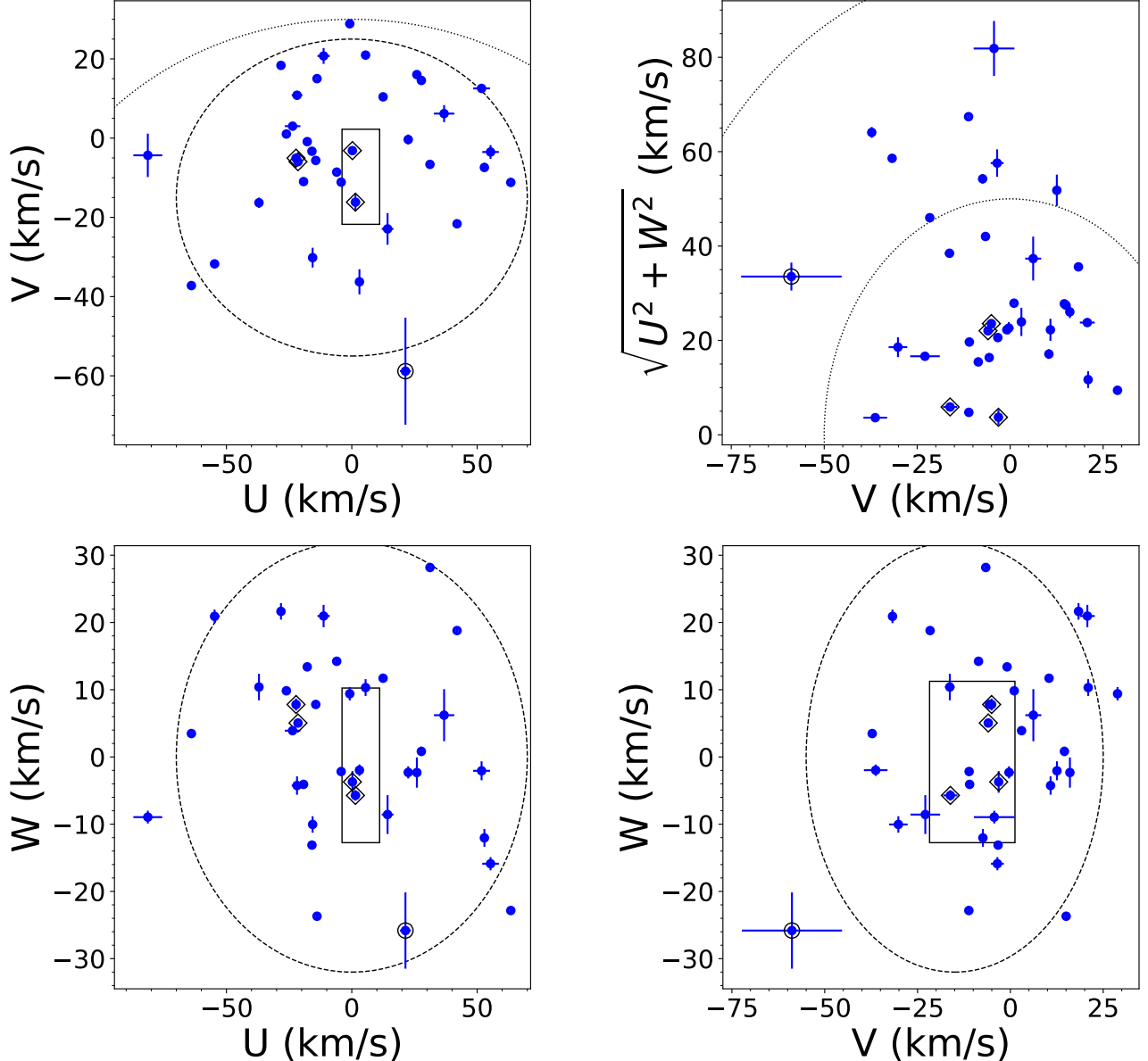


**Figure 11.** *UVW* space motions of the T dwarf sample in the Local Standard of Rest (Schönrich et al. 2010). The  $UV$ ,  $UW$ , and  $VW$  velocities are shown along with the  $2\sigma$  uncertainty spheres for the thin disk (dashed lines) and thick disk (dotted lines) populations from Bensby et al. (2003). The “good box” from Zuckerman & Song (2004) that segregates members of young moving groups is also labeled. The upper-right corner is a Toomre plot, with total velocities  $v_{\text{tot}} = \sqrt{U^2 + V^2 + W^2}$  indicated in steps of 50 km s $^{-1}$ . Young sources and intermediate thin/thick disk sources ( $0.1 < P(\text{TD})/P(\text{D}) < 10$ ) are highlighted with open diamonds and open circles, respectively.

#### 4.4. Individual Sources of Interest

*2MASS J00345157+0523050* is a peculiar T6.5/T7 (Chiu et al. 2006; Burgasser et al. 2004). It has the largest  $v \sin i$  in our sample ( $v \sin i = 90 \pm 2$  km s $^{-1}$ ), making it one of the fastest rotating brown dwarfs found

to date<sup>20</sup>. Assuming a radius of  $1 R_{\text{Jup}}$  and edge-on rotation, this corresponds to a *maximum* rotational pe-

<sup>20</sup> Other unusually fast rotators plotted in Figure 7 include 2MASS J04070752+1546457 ( $82.6 \pm 0.2$  km s $^{-1}$ ), LP 349-25B ( $83 \pm 3$  km s $^{-1}$ ), HD 130948BC ( $86 \pm 6$  km s $^{-1}$ ), and 2MASS J03480772-6022270 ( $104 \pm 7$  km s $^{-1}$ ); see Konopacky et al. (2012); Tannock et al. (2021b).

riod of 1.4 hr. Assuming a mass of  $0.05 M_{\odot}$  (which corresponds to a 900 K brown dwarf at 5 Gyr; Baraffe et al. 2003), the observed velocity corresponds to 30% of the break-up rotational velocity ( $v_{\text{break}} = \sqrt{GM/R} \sim 300 \text{ km s}^{-1}$ ). The source exhibits a very blue near-infrared color  $J - K = -0.93 \pm 0.03$  (Lawrence et al. 2013) and other spectral peculiarities that have been attributed to enhanced H<sub>2</sub> collision-induced absorption (CIA) in the high-pressure atmosphere of a relatively massive (high surface gravity) and/or low-metallicity (low opacity) brown dwarf (Linsky 1969; Burgasser et al. 2004). The absence of the K I doublet absorption at  $1.25 \mu\text{m}$ , which is generally present in the spectra of T6–T7 dwarfs (Martin et al. 2017), may be an indicator of low metallicity effects or shallowing of the line features due to the object's fast rotation. Either trait would imply that J0034+0523 is a relatively old brown dwarf with a high mass and compact radius which has not undergone significant angular momentum loss. We note that our forward-modeling fit utilizes solar-metallicity atmosphere models, and the potential subsolar metallicity of this peculiar T dwarf may influence the derived parameters, including  $v \sin i$ .

*2MASS J02431371–2453298* (Burgasser et al. 1999) stands out in Figure 9 as the only non-binary or UBL with a gravity-based model age significantly less than 1 Gyr. This T6 dwarf had previously been identified as a candidate member of the  $\sim 400$  Myr Ursa Majoris moving group based on its distance and proper motion (Bannister & Jameson 2007; Jameson et al. 2008b), and prior low-resolution spectral analyses have also indicated evidence of low surface gravity (Burgasser et al. 2006a). This source thus exhibits both kinematic and spectral indicators of relative youth, and is a potential benchmark for spectral age indicators for mid- and late-type T dwarfs. However, it should be noted that two other mid- to late-type T dwarfs identified by (Bannister & Jameson 2007) as potential members of the  $\sim 650$  Myr Hyades moving group, the T7 J1217–0311 and the T6 J1624+0029, are not identified as low surface gravity objects in this analysis.

*2MASS J05591914–1404488* (Burgasser et al. 2000b) is a relatively bright and seemingly overluminous T4.5 ( $M_J = 13.7$ ), but has not yet been confirmed as a binary system (Burgasser et al. 2003a; Golimowski et al. 2004; Liu et al. 2006; Stephens et al. 2009; Burgasser et al. 2010; Dupuy & Liu 2017; Manjavacas et al. 2019). It is one of five sources in our sample that has multi-epoch observations, with 10 observations spanning 2001 Oct 9 to 2021 Jan 1. These measurements show significant evidence of RV variation, differing from a constant velocity model by  $\chi^2 = 26$ , (Degrees of freedom DOF = 9,

p-value  $\leq 0.005$ ; Figure 12). This is in contrast to the conclusions of Zapatero Osorio et al. (2007) and Prato et al. (2015) who report constant—but differing—RVs based on subsets of the same data. Indeed, the standard deviation of our re-analyzed measurements ( $\sigma_{\text{RV}} = 1.2 \text{ km s}^{-1}$ ) is smaller than the difference between the previously published RVs ( $RV_{\text{Zap}} - RV_{\text{Pra}} = -5.0 \text{ km s}^{-1}$ ). The sparse sampling of the data prevents a robust assessment of potential orbital motion, and follow-up RV measurements are warranted to validate this RV variation and assess the multiplicity of this unresolved source.

*2MASS J08195820–0335266* (Kirkpatrick et al. 2011) is a T4 dwarf with spatial and kinematic evidence of membership in the 24 Myr-old  $\beta$  Pictoris moving group (see Section 4.3), consistent with Zhang et al. (2021) on the basis of 5D kinematics. At this age, and assuming  $T_{\text{eff}} = 1100 \text{ K}$  based on Filippazzo et al. (2015), evolutionary models predict a mass of only 7 Jupiter masses, well below the deuterium burning mass limit (Baraffe et al. 2003). However, spectral evidence of youth for this source is not clear. Its near-infrared low-resolution spectrum is fully consistent with the T4 standard 2MASSI J2254188+312349 (Figure 13; Burgasser et al. 2004). Pineda et al. (2016) reported the red optical (0.7–1.0  $\mu\text{m}$ ) spectrum of this source, recommending it as the T4 optical standard with features that naturally transition between T2 and T5 optical standards (Burgasser et al. 2003a). They found no evidence of H $\alpha$  emission to a limit of  $\log_{10} L_{\text{H}\alpha}/L_{\text{bol}} < -5.7$ . The lack of activity is consistent with its small  $v \sin i$ , for which we are only able to determine an upper limit of  $v \sin i < 9 \text{ km s}^{-1}$ . Heinze et al. (2015) report the possible detection of variability ( $> 3.6\%$  in amplitude) at red optical wavelengths (0.7–0.95  $\mu\text{m}$ ), which is common for both young brown dwarfs and objects spanning the L dwarf/T dwarf transition (Radigan et al. 2012; Metchev et al. 2015). Taken together, we suspect that this source is a field brown dwarf with a chance kinematic alignment with the  $\beta$  Pictoris moving group.

*2MASSI J0937347+293142* (Burgasser et al. 2002) is a peculiar T6 dwarf with the second largest rotational velocity in our sample,  $v \sin i = 66.9^{+0.5}_{-0.6} \text{ km s}^{-1}$ . Assuming a radius of 1 R<sub>Jup</sub>, this rotational speed corresponds to a maximum rotation period of 2 hours. Like J0034+0523, J0937+2931 has an unusually blue near-infrared color  $J - K = -1.10 \pm 0.06$  (Leggett et al. 2010). This and other spectral peculiarities, including the weak or absent K I lines at  $1.25 \mu\text{m}$ , have been cited as evidence of high surface gravity and/or subsolar metallicity for this source (Burgasser et al. 2002, 2006a; McLean et al. 2007; Prato et al. 2015; Martin et al. 2017; Zhang et al. 2019). The rapid rotation of J0937+2931 may also

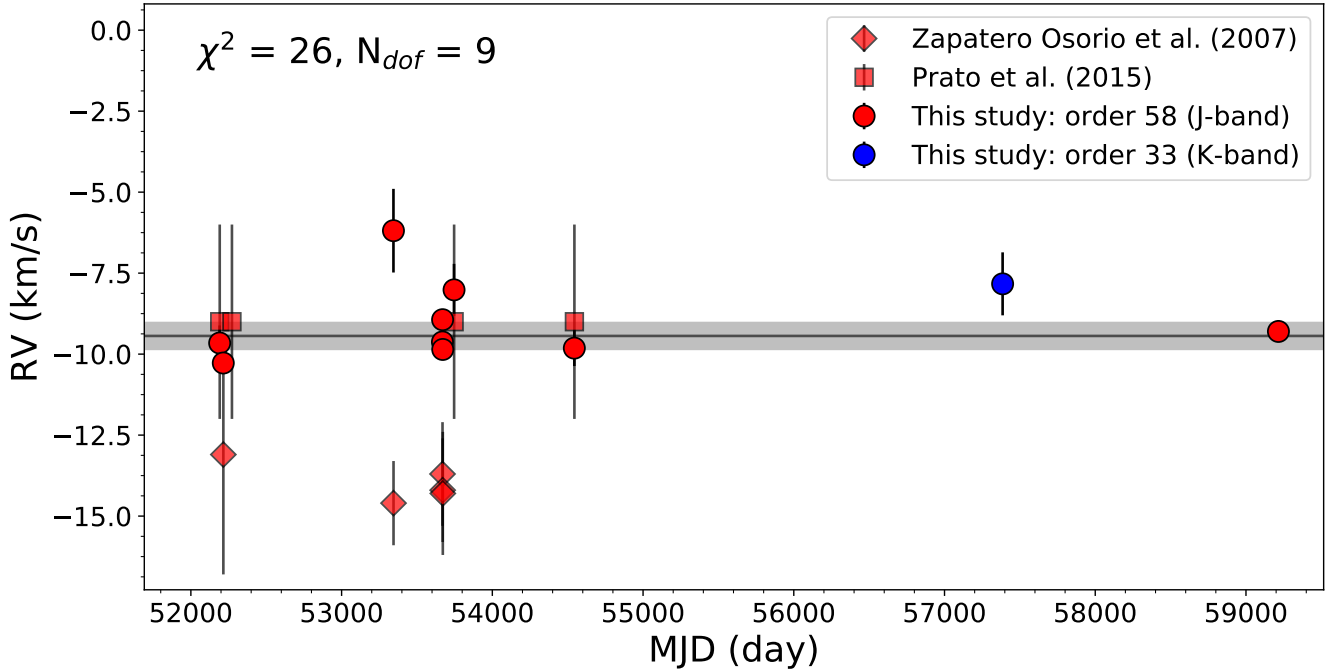


**Figure 12.** RV time series for all of the NIRSPEC measurement epochs for 2MASS J0559–1404. Measurements made in order 33 and 58 are shown as blue and red circles, respectively. The weighted average of our measurements and uncertainty are indicated by the horizontal line and grey shading. Prior measurements reported by Zapatero Osorio et al. (2007) and Prato et al. (2015) based on NIRSPEC data are indicated by red diamonds and red squares, respectively.

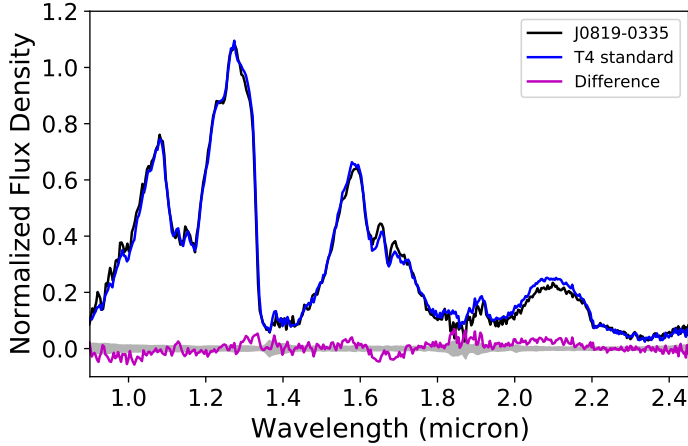


**Figure 13.** Low-resolution near-infrared spectrum of the T dwarf 2MASS J0819–0335 (black lines; uncertainty in grey shading centered at zero flux) from Burgasser et al. (2004) compared to (blue lines) the T4 near-infrared spectral standard 2MASSI J2254188+312349 (data from Kirkpatrick et al. 2011). The spectra are normalized to align in the 0.90–1.25  $\mu\text{m}$  region, and the magenta lines show the difference spectra (template minus J0819–0335).

be partly responsible for the weakened atomic features. Again, these physical traits imply an old age, indicating

that J0937+2931 is a massive and compact brown dwarf that has not had appreciable angular momentum loss in its late evolution.

2MASS J11061197+2754225 (Looper et al. 2007) is a previously reported candidate binary system with hypothesized T0.0+T4.5 components based on analysis of its low-resolution near-infrared spectrum (Looper et al. 2007; Burgasser et al. 2010; Bardalez Gagliuffi et al. 2014). It is also highly overluminous (Manjavacas et al. 2013), but has not been resolved by direct imaging (Looper et al. 2008). Our measurements show highly significant RV variations over 15 epochs spanning 2008 Mar 19 to 2021 Jan 1, deviating from a constant velocity model by  $\chi^2 = 318$  (DOF = 15, p-value < 0.001; Figure 14). We performed a preliminary orbit fit on 11 epochs of these data ( $\chi^2 = 155$ , p-value < 0.001), rejecting order 33 data from 2016 Jan 18 and 2018 Jan 1 due to the slit width  $0''.432$  being wider than the seeing on these nights; and order 58 data on 2008 Mar 19 and 2010 Dec 26 which are likely contaminated by light from the secondary, which is brighter than the primary in the *J*-band (see Burgasser et al. 2010). We used the package *RadVel* (Fulton et al. 2018), and converged on a set of solutions with primary semi-amplitude  $K_1 = 6.30 \pm 0.05 \text{ km s}^{-1}$ , period  $P = 3.92^{+0.07}_{-0.09} \text{ yr}$ , eccentricity  $e = 0.33^{+0.04}_{-0.02}$ , and

center of mass radial velocity  $V_{\text{COM}} = 2.0 \pm 0.1 \text{ km s}^{-1}$ . This system is examined in further detail in a companion paper (Burgasser et al., in prep).

*SDSS J133148.92–011651.4* (Hawley et al. 2002) is the only source in our sample identified as an intermediate member in the Galactic thin and thick disk populations. Like J0937+2931, this source has an unusually blue near-infrared color for an early-T dwarf ( $J - K = 1.279 \pm 0.008$ ; Lawrence et al. 2007) and a peculiar spectrum that has challenged classification. Optical spectral classifications have ranged from L1 pec (Marocco et al. 2013) to L6 (Hawley et al. 2002) while near-infrared spectral classifications have ranged from L6 (Bardalez Gagliuffi et al. 2014) to T0 (Schneider et al. 2014). There are also conflicting determinations of this source being either metal-poor (Marocco et al. 2013) or lacking in subdwarf spectral features (Kirkpatrick et al. 2016), and model fits indicate unusually thin clouds for a late L dwarf (Stephens et al. 2009). Figure 15 shows the low-resolution near-infrared spectrum of this source from Bardalez Gagliuffi et al. (2014) compared to L6 and T0 spectral standards, and the near-infrared spectrum of the L subdwarf 2MASS J11181292–0856106 (Kirkpatrick et al. 2010). The L subdwarf is the best match of the three, meaning that J1331–0116 is likely an old, slightly metal-poor L dwarf whose spectrum is shaped by enhanced H<sub>2</sub> CIA and possibly atmospheric condensates. Given its distinct classification from the rest of the T sample, we exclude this source from the T dwarf kinematic analysis presented below.

*2MASS J15530228+1532369AB* (Burgasser et al. 2002) is a resolved T6.5+T7.5 binary with a separation of  $0''.349 \pm 0''.005$ ,  $\Delta M_{\text{bol}} = 0.31 \pm 0.12$ , and mass ratio  $q = 0.90 \pm 0.02$ . Here, we find spatial and kinematic evidence of membership in the  $\sim 200$  Myr-old Carina-Near moving group (see Section 4.3), consistent with Zhang et al. (2021) on the basis of 5D kinematics. At this age, and assuming component  $T_{\text{effs}} = 750$  K and 890 K based on Filippazzo et al. (2015), evolutionary models predict masses of  $10^{+0.8}_{-1.6}$  and  $11.3^{+0.4}_{-0.5}$  Jupiter masses, below the deuterium burning mass limit (Baraffe et al. 2003). The kinematically young late-type T binary could join an exclusive club of AB Doradus T3.5 GU Psc b (Naud et al. 2014), AB Doradus T5.5 SDSS J111010.01+011613.1 (Gagné et al. 2015a), and candidate AB Doradus L+T binary WISE J135501.90–825838.9 (Bardalez Gagliuffi et al. 2018), and TW Hydrae L7 binary 2MASS J11193254–1137466 (Best et al. 2017). However, spectral evidence of youth for this source is lacking. Its near-infrared low-resolution spectrum is fully consistent with the T7 standard 2MASS J07271824+1710012 (Figure 16; Burgasser

et al. 2010) and inconsistent with the 20 Myr T dwarf 51 Eri b<sup>21</sup> ( $T_{\text{eff}} = 760 \pm 20$  K; data from VLT/SPHERE and Gemini Planet Imager; Macintosh et al. 2015; Samland et al. 2017). Line et al. (2017) measured a  $\log g$  of  $4.8^{+0.1}_{-0.2}$  dex for J1553+1532 after correcting for binarity, but with subsolar metallicity ( $[M/H] = -0.19^{+0.04}_{-0.06}$  dex and supersolar  $\log \text{C/O} = -0.11^{+0.09}_{-0.09}$ ). This source does not exhibit significant variability in  $JHKs$  or  $J_S$  (Koen et al. 2004; Wilson et al. 2014). Taken together, we suspect that this source is also a field brown dwarf with a chance kinematic alignment with the Carina-Near moving group.

*2MASS J21265916+7617440* is a T0p dwarf proposed to be an L7+T3.5 blended-light binary based on medium-resolution spectroscopy (Kirkpatrick et al. 2010). High-resolution imaging by Bardalez Gagliuffi et al. (2015) failed to resolve the system and constrained its angular separation to  $< 106$  mas or  $< 1.3$  au. Our measurements show significant RV variations over 10 epochs spanning 2011 Jun 10 to 2020 Sep 3, deviating from a constant velocity model by  $\chi^2 = 39$  (DOF = 9, p-value  $< 0.001$ ; Figure 17). Following the analysis of J1106+2754, we performed a preliminary orbit fit to the RV data using *RadVel*, and converged on a set of solutions with primary semi-amplitude  $K_1 = 3.0^{+0.7}_{-0.6}$  km s<sup>-1</sup>, period  $P = 12.0^{+1.5}_{-1.2}$  yr, and center of mass radial velocity  $V_{\text{COM}} = -17.5 \pm 0.4$  km s<sup>-1</sup>. This system is examined in detail in a companion paper (Hsu et al., in prep).

*HN Peg B* (Luhman et al. 2007) is a T2.5 dwarf that is a wide companion (782 au) to the young ( $\sim 300$  Myr) G0V star HN Peg. It is an important benchmark for testing brown dwarf evolutionary models near the L dwarf/T dwarf transition (Leggett et al. 2008a). Our best-fit models of HN Peg B for data from 2017 Jun 9 yield  $\text{RV} = -19.5 \pm 1.3$  km s<sup>-1</sup>, consistent with the primary star's  $\text{RV} = -17.18 \pm 0.17$  km s<sup>-1</sup> (Gaia Collaboration et al. 2018). HN Peg B is also a photometrically variable source (Metchev et al. 2015; Zhou et al. 2018; Vos et al. 2019). Our  $v \sin i = 15 \pm 3$  km s<sup>-1</sup> combined with the period measurement from Zhou et al. (2018) of  $15.4 \pm 0.5$  hr yields a rotation axis inclination angle of  $63^\circ \pm 7^\circ$  assuming a model radius of  $0.108^{+0.014}_{-0.006} R_\odot$  using the theoretical evolutionary models of Burrows et al. (1997) and Baraffe et al. (2003) (Luhman et al. 2007).

<sup>21</sup> The spectral features might not be the same between 20 Myr and 200 Myr T7 dwarf, as L dwarfs have different spectral features between intermediate and very-low gravity in Allers & Liu (2013). T7 dwarfs at the ages of 20 Myr and 200 Myr correspond to  $\log g = 3.5\text{--}4.0$  dex and  $4.2\text{--}4.5$  dex, respectively, using Baraffe et al. (2003) models.

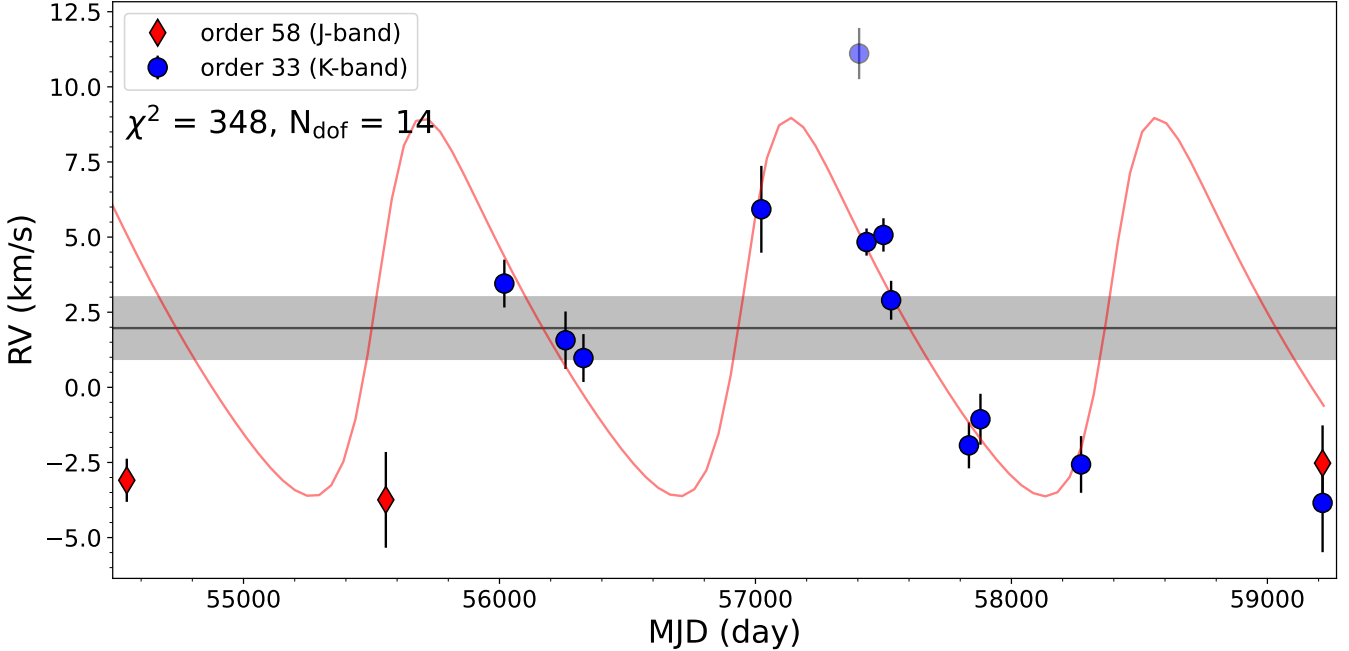


**Figure 14.** RV time series for all of the NIRSPEC measurement epochs of 2MASS J1106+2754. Measurements of orders 33 (*K*-band) and 58 (*J*-band) are labeled as blue circles and red diamonds, respectively. The horizontal line is the weighted average of our measurements, with the uncertainty shaded in grey. Also shown in a best-fit RV orbital curve with a semi-amplitude of  $K_1 = 6.30 \text{ km s}^{-1}$  and a period of  $P = 3.92 \text{ yr}$ , based on eleven epochs in order 33 with a removal of a bad observation on 2016 Jan 18 (light blue) and 2018 Jan 1 (outside of the range presented here). The data in order 58 were not fit because the secondary component is brighter at *J*-band. See Section 4.4 for details.

This is consistent with the current hypothesis that the frequency and amplitude of variability are higher for brown dwarfs observed at intermediate-to-high viewing angles ( $i > 60^\circ$ ; Heinze et al. 2013; Metchev et al. 2015; Vos et al. 2017).

## 5. KINEMATICS OF ULTRACOOL DWARFS

### 5.1. Velocity Dispersions and the Kinematic Age of *T* Dwarfs

The velocity dispersion,

$$\sigma_{\text{tot}}^2 = \sigma_U^2 + \sigma_V^2 + \sigma_W^2 \quad (5)$$

of a stellar population evolves as the population ages, as gravitational interactions with Galactic structures perturb orbits, increasing Galactic scale heights and relative velocities over time (Wielen 1977). Velocity dispersions thus provide a means of measuring the ages of stellar populations, including UCDs, which depend on the mass function, star formation history, and thermal evolution of brown dwarfs (Burgasser 2004).

We measured a total velocity dispersion for our T dwarfs to be  $\sigma_{\text{tot}} = 39.0 \pm 1.0 \text{ km s}^{-1}$ . To convert this into an age, we evaluated two age-dispersion relations. The first is the exponential decay law from Wielen (1977) based on the  $|W|$ -weighted total velocity disper-

sion:

$$\bar{\sigma}_{\text{tot}}(\tau)^3 = \sigma_{\text{tot},0}^3 + 1.5 \gamma_{\nu,p} T_\gamma (e^{\tau/T_\gamma} - 1), \quad (6)$$

where  $\tau$  is the statistical age in Gyr,  $\sigma_{\text{tot},0} = 10 \text{ km s}^{-1}$ ,  $\gamma_{\nu,p} = 1.1 \times 10^4 (\text{km s}^{-1})^3 \text{ Gyr}^{-1}$ ,  $T_\gamma = 5 \text{ Gyr}$ , and  $\bar{\sigma}_{\text{tot}}$  is the  $|W|$ -weighted total velocity dispersion in  $\text{km s}^{-1}$ :

$$\bar{\sigma}_{\text{tot}}^2 = \frac{\sum_i |W_i|(U_i - \bar{U})^2}{\sum_i |W_i|} + \frac{\sum_i |W_i|(V_i - \bar{V})^2}{\sum_i |W_i|} + 0.5 \frac{\sum_i |W_i|(W_i - \bar{W})^2}{\sum_i |W_i|}, \quad (7)$$

We also examined the age-dispersion law from Aumer & Binney (2009):

$$\sigma_{\text{tot}} = \nu_{1,0} \left( \frac{\tau + \tau_1}{10 \text{ Gyr} + \tau_1} \right)^\beta, \quad (8)$$

where  $\nu_{1,0} \in (55.179, 57.975) \text{ km s}^{-1}$ ,  $\tau_1 \in (0.148, 0.261) \text{ Gyr}$ , and  $\beta \in (0.349, 0.385)$  are model parameters drawn from Table 2 of Aumer & Binney (2009). It is noted that Bird (2019) measured a very similar  $\beta = 0.389 \pm 0.018$  using *Gaia* and APOGEE red clump stars.

Kinematic ages were inferred by inverting these relations to solve for  $\tau$ . The age uncertainty was estimated statistically through Monte-Carlo sampling, assuming that *UVW* velocity uncertainties follow normal

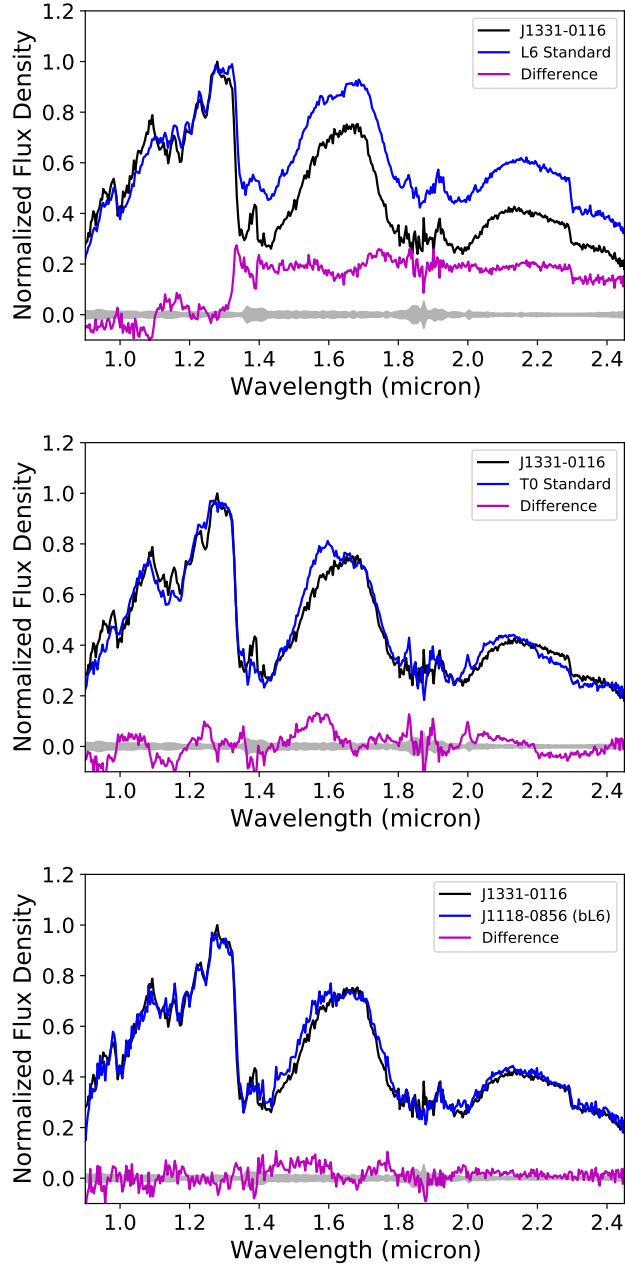


**Figure 15.** Low-resolution near-infrared spectrum of the peculiar L dwarf J1331–0116 (black lines; uncertainty in grey shading centered at zero flux) from Bardalez Gagliuffi et al. (2014) compared to (blue lines) the L6 near-infrared spectral standard 2MASSI J1010148–040649 (top; data from Reid et al. 2006), the T0 spectral standard SDSS J120747.17+024424.8 (middle; data fromLooper et al. 2007), and the unusually blue L6 dwarf 2MASS J11181292–0856106 (bottom; data from Kirkpatrick et al. 2010). All spectra are normalized to align in the 0.90–1.25  $\mu\text{m}$  region, and the magenta lines show the difference spectra (template minus J1331–0116).

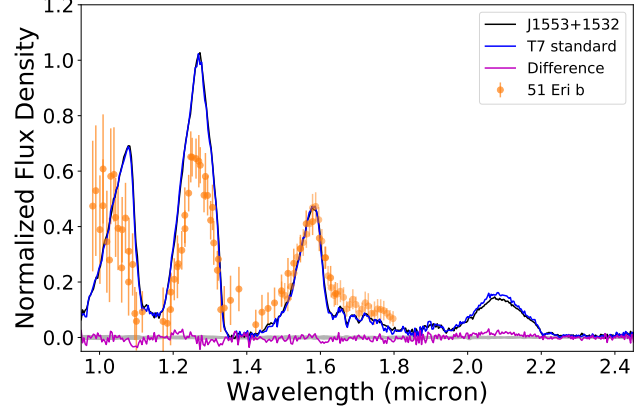


**Figure 16.** Low-resolution near-infrared spectrum of the T dwarf 2MASS J1553+1532 (black line; uncertainty in grey shading centered at zero flux) from Burgasser et al. (2010) compared to the T7 near-infrared spectral standard 2MASS J07271824+1710012 (blue line; data from Burgasser et al. 2006a). The spectra are normalized to align in the 0.90–1.25  $\mu\text{m}$  region, and the magenta line shows the difference spectrum (template minus J1553+1532). Also shown is the 51 Eri b spectrum from Samland et al. (2017), normalized to  $H$  band peak.

distributions. To account for sample bias, we applied a Jackknife test by iteratively removing one source from our sample and recomputing dispersions and kinematic ages for each of the resulting subsamples. The resulting  $UVW$  dispersions are summarized in Table 6.

Using the Aumer & Binney (2009) relation (averaged over all model parameters), we inferred a kinematic age of  $3.5 \pm 0.3$  Gyr for our full sample of 36 T dwarfs (excluding J1331–0116). The Wielen relation yields a smaller but statistically consistent age of  $3.0 \pm 0.1$  Gyr. To mitigate possible velocity biases, we also examined kinematic ages for the sample excluding the resolved and candidate binaries J0629+2418, J0909+6525, J1106+2754, J1225–2739, J1553+1532, and J2126+7617 (Burgasser et al. 2006b; Dupuy & Liu 2012; Manjavacas et al. 2013; Bardalez Gagliuffi et al. 2014); and separately the young T dwarfs J0136+0933, J0819–0335, J1324+6538, J1553+1532, and HN Peg b (Gagné et al. 2017, 2018a; Leggett et al. 2008b; Zhang et al. 2021), and found equivalent ages as the full sample (Table 6). We also found consistent kinematic ages between early-T (T0–T4;  $3.3 \pm 0.6$  Gyr) and late-T (T5–T8;  $3.6 \pm 0.4$  Gyr) subgroups. The age of local T dwarfs from the Aumer & Binney (2009) relation is consistent with the age of local M dwarfs, but is younger than local L dwarfs (Reid et al. 2002; Reiners & Basri 2009; Blake et al. 2010; Seifahrt et al. 2010; Burgasser et al. 2015b), as discussed in further detail below.

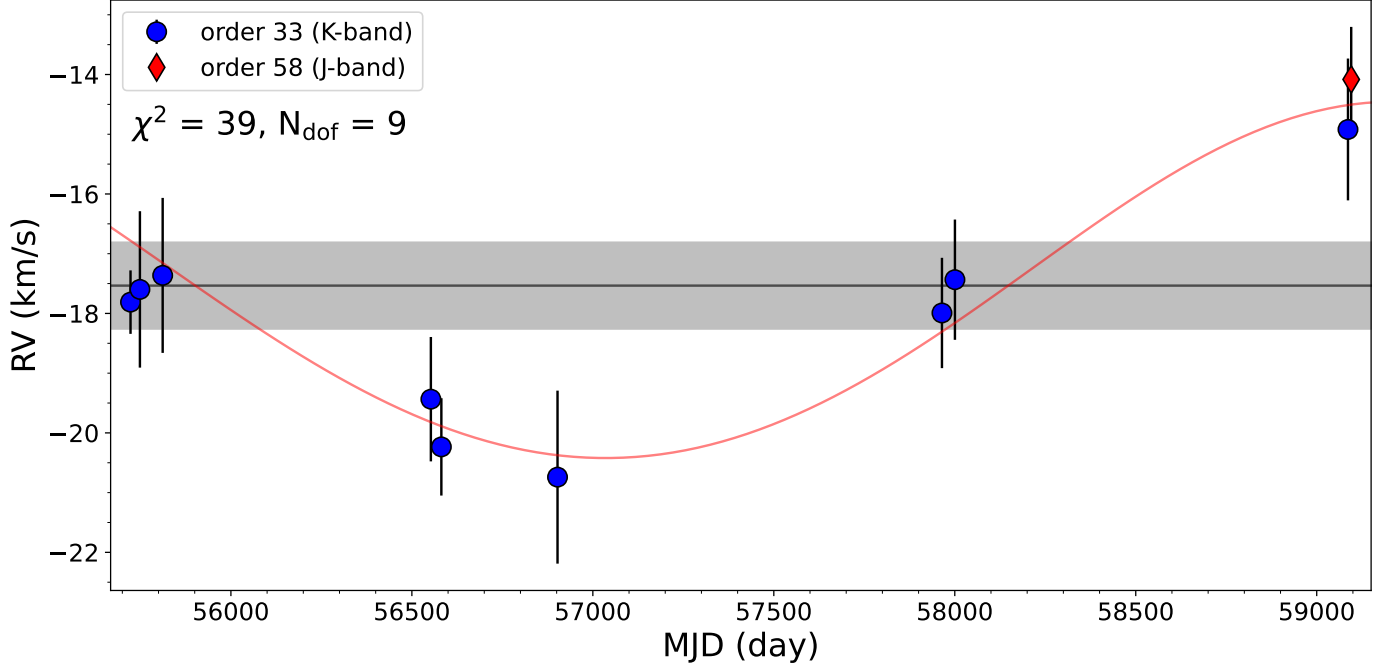


**Figure 17.** RV time series for all of the NIRSPEC measurement epochs of 2MASS J2126+7617. Measurements of orders 33 (*K*-band) and 57 (*J*-band) are labeled as blue circles and red diamonds, respectively. The horizontal line is the weighted average of our measurements, with the uncertainty shaded in grey. Also shown is a best-fit RV orbital curve with a semi-amplitude  $K_1 = 3.0 \text{ km s}^{-1}$  and period  $P = 12.0 \text{ yr}$ .

Figure 18 shows  $UVW$  velocity probability plots, or probit plots, following Lutz & Upgren (1980) and based on the percent point function defined in Filliben (1975); see also Reid et al. (2002) and Bochanski et al. (2007). Probit plots are linear if the velocities are drawn from a single normal distribution, with the slope equal to the distribution width ( $\sigma$ ). Both  $U$  and  $V$  velocities show two populations, with an inner “shallow” population in the  $\pm 1\sigma$  region and a steeper “wide” population. To quantify the difference in kinematic ages, we performed a piece-wise linear fit to each component and used the slopes to compute ages with the Aumer & Binney (2009) relations and Monte Carlo uncertainties (Bochanski et al. 2007; Burgasser et al. 2015b). The ages for the inner and outer components are  $3.2 \pm 0.5 \text{ Gyr}$  and  $4.0 \pm 0.3 \text{ Gyr}$ , respectively, and hence marginally consistent.

## 5.2. Velocity Dispersions and the Kinematic Ages of Late-M and L Dwarfs

To place the T dwarf velocity dispersions and kinematic ages in context, we compiled all late-M and L dwarfs within 20 pc with published RV measurements that have uncertainties of  $\leq 3 \text{ km s}^{-1}$ , based on medium and high-resolution spectroscopic measurements (Table 7). There are 65 late-M dwarfs (M7–M9) and 71 L dwarfs (L0–L9) that match these criteria (J1331–0116

is included here; see Section 4.4 for more details). Figure 19 shows the spectral type distribution of the full late-M, L, and T dwarf RV sample, overplotted with a simulated local population and local 20 pc UCDs found to date (see Section 5.4 for further discussion). We combined RV measurements with *Gaia* DR2 and eDR3 parallaxes and proper motions where available to improve the  $UVW$  precisions over prior studies, following the same analysis as that done for the T dwarfs.

Results are summarized in Table 8 and Figure 20. We note that two late-M dwarfs in this sample (M7 2MASS J02530084+1652532 and M9 2MASS J03341218–4953322) are kinematically associated with the thick disk population, the L5.5 2MASSI J1721039+334415 is associated with the intermediate thick disk/halo population, and 17 sources (6 late-M dwarfs and 11 L dwarfs) are associated with intermediate thin/thick disk population, which includes J1331–0116, which we classify as a blue L6. Evaluating the distribution of  $UVW$  velocities, we find that the L dwarfs in this sample exhibit significant correlations between  $UV$  ( $R = 0.33$ , p-value  $< 0.01$ ),  $UW$  ( $R = -0.32$ , p-value  $< 0.01$ ) and  $VW$  velocities ( $R = -0.27$ , p-value = 0.02). For the late-M dwarfs, we find a significant correlation between  $UV$  velocities ( $R = 0.32$ , p-value  $< 0.01$ ), but not between  $UW$  or  $VW$  velocities. The  $UV$  velocity correlation for the L dwarfs is

weaker than that previously reported in Burgasser et al. (2015b,  $R = 0.43 \pm 0.03$ ), but nevertheless significant. If we remove the thick disk, intermediate thick disk/halo, and intermediate thin/thick disk population members from our sample, the  $UV$  velocity correlation becomes less significant for the late-M dwarf sample ( $R = 0.25$ , p-value = 0.06) and insignificant for the L dwarfs in all three velocity pairs. This result indicates that the  $UVW$  velocity correlations are driven by the older kinematic populations. As noted above, the T dwarfs, which are all thin disk sources, show no significant correlations in  $UV$ ,  $UW$ , or  $VW$  velocity pairs. The average  $U$  and  $W$  velocities of the late-M and L dwarfs are each consistent with zero, while the negative average  $V$  velocity (greater for the L dwarfs) can again be attributed to asymmetric drift. We note that the average  $U$  velocity offset for the L dwarfs reported in Burgasser et al. (2015b) is not seen here and is likely an artifact of small sample statistics in that study.

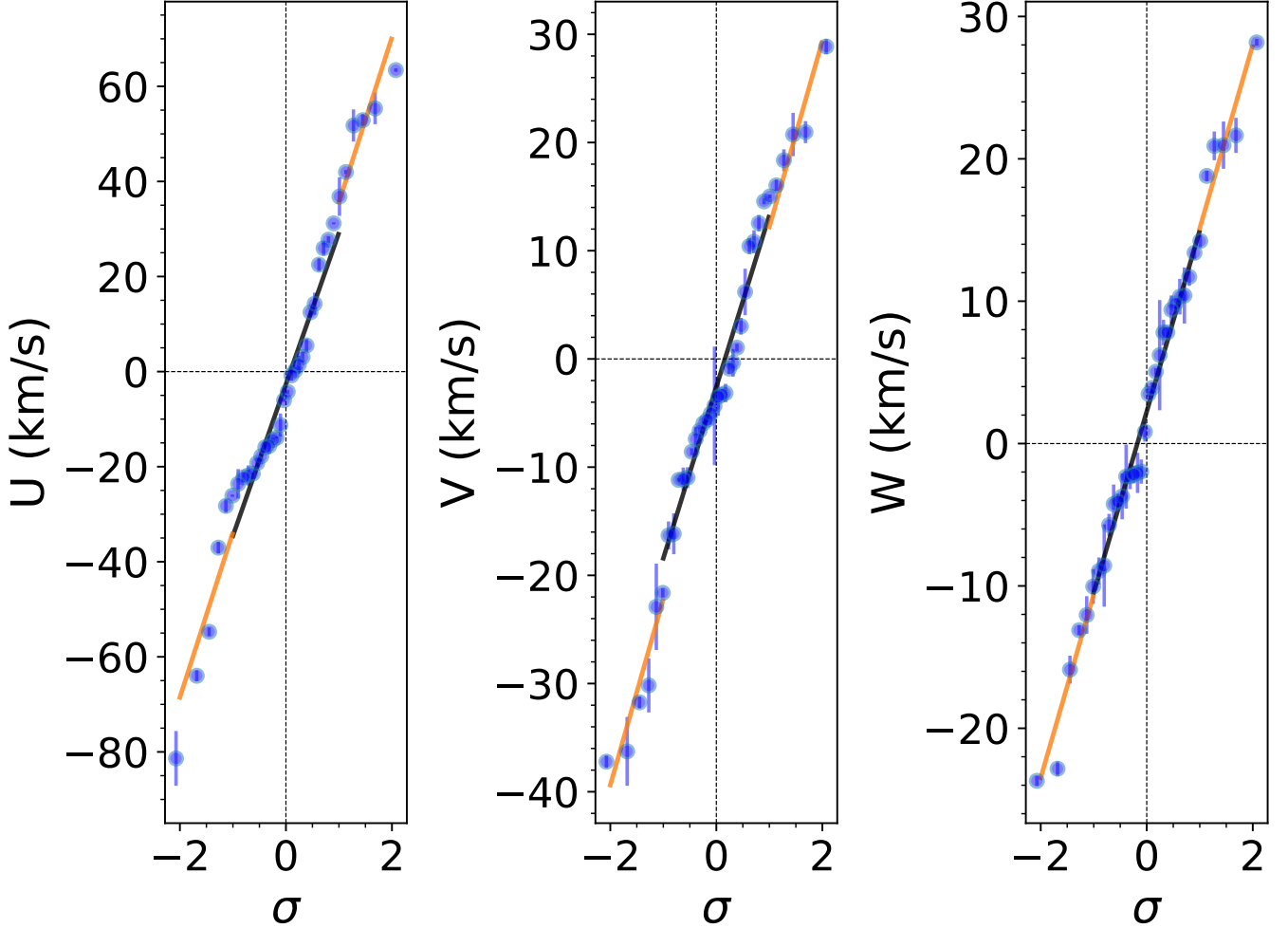
The corresponding kinematic ages for all of the late-M and L dwarfs in our sample using the Wielen (1977) and Aumer & Binney (2009) relations are given in Table 9. In our sample, we find highly significant correlations between  $v_{\text{tot}}^2$  and  $|W|$  for the late-M dwarfs ( $N = 65$ ,  $R = 0.42$ , p-value < 0.001) and L dwarfs ( $N = 71$ ,  $R = 0.61$ , p-value <  $10^{-4}$ ), and significant correlation for T dwarfs ( $N = 37$ ,  $R = 0.33$ , p-value = 0.05). However, if the thin/thick disk sources are removed, the significances of these correlations are reduced: marginally significant for late-M dwarfs ( $N = 57$ ,  $R = 0.22$  and p-value = 0.09), significant for L dwarfs ( $N = 59$ ,  $R = 0.27$  and p-value < 0.05), and insignificant for T dwarfs ( $N = 36$ ,  $R = 0.25$  and p-value = 0.13). These results suggest that the  $v_{\text{tot}}^2$ ,  $|W|$  correlation is dominated by a few sources from a distinct population, so that Wielen's age-dispersion relation may not be as accurate for this sample as the Aumer and Binney relations. The ages from the latter relations are  $4.9 \pm 0.3$  Gyr and  $7.1 \pm 0.4$  Gyr, respectively, for the full late-M and L dwarf samples (Figure 21, upper left panel). These values confirm the significant ( $4.4\sigma$ ) discrepancy between late-M and L dwarf kinematic ages found in previous studies. If we remove the thick disk sources, the kinematic ages are reduced to  $4.1 \pm 0.3$  Gyr for the late-M dwarfs and  $5.8 \pm 0.3$  Gyr for the L dwarfs. These ages are still significantly ( $4.0\sigma$ ) discrepant, while the late-M and T dwarfs in our sample have statistically equivalent ages.

Figure 22 displays the log probability of thin disk to thick disk membership for late-M, L and T dwarfs, again following Bensby et al. (2003). These distributions show

that there is a marginally higher proportion of intermediate thin/thick disk and thick disk sources relative to thin disk sources among the L dwarfs ( $8^{+5}_{-2}\%$ ). as compared to the late-M dwarfs ( $3^{+3}_{-1}\%$ ) and T dwarfs ( $3^{+6}_{-2}\%$ ), with ratio statistics computed using binomial statistics following Burgasser et al. (2003c). The intermediate thin/thick disk sources in particular skew the kinematic dispersions and ages toward higher values. To truly assess the kinematic age of the thin disk population without discarding too many old thin disk sources, we refined our selection requirement to  $P[\text{TD}]/P[\text{D}] \leq 1.0$ , since  $P[\text{TD}]/P[\text{D}] = 1.0$  denotes a 50% probability as a thin or thick disk source. This thin disk sample has similar kinematic ages of  $4.1 \pm 0.3$  Gyr and  $4.2 \pm 0.3$  Gyr for the late-M and L dwarfs, respectively, which are slightly older but consistent with the T dwarfs. These values imply equivalent ages across the entire late-MLT sequence.

Refining the sample to high-probability thin disk sources appears to resolve the long-standing discrepancy between late-M and L dwarf kinematics (Faherty et al. 2009; Seifahrt et al. 2010; Burgasser et al. 2015b). In Section 5.4, we will show the observed thin disk ages of late-MLT dwarfs are also consistent with our population simulations. What remains unclear is why the local L dwarf sample has a higher fraction of thick disk sources compared to late-M and T dwarfs. We will evaluate the properties of the thick disk L dwarfs, several of which are classified as unusually blue L dwarfs, in Section 6.2.

For completeness, we evaluated the more recent age-velocity dispersion relation of Yu & Liu (2018), based on the kinematics and ages of  $>3500$  sub-giant and giant branch stars. The ages were estimated from empirical trends in [C/M] and [N/M] abundances (Ho et al. 2017). Yu & Liu (2018) fit power-law relations to the velocity dispersions in Galactic cylindrical coordinates,  $\text{age} = C\sigma_i^\beta$ , where  $i = R, \phi$ , and Z direction, and  $C = 1$  Gyr ( $\text{km s}^{-1}$ ) $^{-\beta}$  is a unit conversion factor. Using the  $z$ -coordinate relation from this study with  $\beta_z = 0.56 \pm 0.14$ , and propagating uncertainties with Monte Carlo sampling, we compute ages for late-M dwarfs (all/thin disk =  $4.9^{+2.4}_{-1.6}$  Gyr/ $4.8^{+2.3}_{-1.5}$  Gyr), L dwarfs (all/thin disk =  $5.1^{+2.5}_{-1.7}$  Gyr/ $4.6^{+2.1}_{-1.4}$  Gyr), and T dwarfs ( $4.1^{+1.7}_{-1.2}$  Gyr) that are consistent with each other, albeit with higher statistical uncertainties. The  $R$  and  $\phi$  relations of Yu & Liu (2018) yield significantly younger ages (2.6–3.4 Gyr) which may be attributed to the very different spatial distributions of the sub-giant/giant sample as compared to the local ultracool dwarf sample.



**Figure 18.** Space velocity probability plots (probit plots) of the T dwarf sample. Individual velocities are indicated by blue circles, while a piece-wise linear fit broken at  $\pm 1\sigma$  for each velocity component (black and orange dashed lines, respectively) are shown. Note that the unusually blue L dwarf J1331–0116 is not included here.

**Table 6.** Velocity Dispersions and Group Kinematic Ages

Sample	N	$\langle U \rangle$ (km s $^{-1}$ )	$\langle V \rangle$ (km s $^{-1}$ )	$\langle W \rangle$ (km s $^{-1}$ )	$\sigma_U$ (km s $^{-1}$ )	$\sigma_V$ (km s $^{-1}$ )	$\sigma_W$ (km s $^{-1}$ )	$\sigma_{tot}$ (km s $^{-1}$ )	Age (Gyr)	Note
All Sources	36	-1.6 ± 5.5	-3.6 ± 2.7	2.1 ± 2.0	33.1 ± 0.8	16.5 ± 0.5	12.3 ± 0.3	39.0 ± 1.0	3.5 ± 0.3	Unweighted
Shallow <i>a</i>	24	-2.7 ± 3.5	-2.6 ± 1.7	2.3 ± 1.4	35.5 ± 0.9	16.4 ± 0.5	11.6 ± 0.3	40.8 ± 0.8	3.0 ± 0.1	W  Weighted
Wide <i>a</i>	12	0.9 ± 15.0	-5.0 ± 7.4	2.3 ± 5.5	34.7 ± 1.0	17.2 ± 0.7	12.9 ± 0.7	40.8 ± 0.9	3.2 ± 0.5	Unweighted
Not Young T Dwarfs	31	-0.2 ± 6.3	-2.6 ± 3.1	2.6 ± 2.3	35.1 ± 1.0	17.4 ± 0.5	13.1 ± 0.3	41.3 ± 1.1	4.1 ± 0.4	Unweighted
Not Binary T Dwarfs	30	-0.3 ± 5.9	-1.0 ± 2.7	2.4 ± 2.3	32.1 ± 1.1	16.8 ± 0.5	12.0 ± 0.3	41.8 ± 1.0	3.1 ± 0.2	W  Weighted
Not Binary or Young T Dwarfs	26	0.6 ± 6.7	0.2 ± 3.0	3.0 ± 2.6	35.3 ± 1.2	14.6 ± 0.4	12.6 ± 0.3	37.4 ± 1.2	3.1 ± 0.3	Unweighted
T0–T4 dwarfs	18	-3.7 ± 7.6	-5.2 ± 4.1	2.3 ± 2.6	34.2 ± 1.2	15.9 ± 0.6	11.9 ± 0.3	40.5 ± 1.0	2.9 ± 0.2	W  Weighted
T5–T8 dwarfs	18	0.7 ± 7.9	-1.6 ± 3.5	2.2 ± 3.2	36.1 ± 1.3	16.2 ± 0.6	12.1 ± 0.4	39.7 ± 1.3	3.7 ± 0.4	Unweighted
					32.1 ± 1.9	17.5 ± 0.7	11.0 ± 0.6	41.4 ± 1.2	3.1 ± 0.2	W  Weighted
					31.1 ± 2.3	15.8 ± 0.9	10.2 ± 0.5	38.2 ± 2.1	3.3 ± 0.6	Unweighted
					33.7 ± 1.1	14.9 ± 0.6	13.5 ± 0.5	36.4 ± 2.0	2.3 ± 0.3	W  Weighted
					39.2 ± 1.4	17.0 ± 0.8	12.2 ± 0.4	39.2 ± 1.4	3.6 ± 0.4	Unweighted
					39.2 ± 1.3	14.5 ± 1.3	12.2 ± 0.4	44.5 ± 1.3	3.6 ± 0.2	W  Weighted

NOTE—Ages for unweighted velocities are computed from equation (8) using the parameters in Aumer & Binney (2009). Ages for |W|-weighted velocities are computed from equation (6) using the parameters in Wielen (1977).

*a* Piece-wise linear fits to unweighted velocities, with separate fits for sources within  $\pm 1\sigma$  (shallow) and outside of  $\pm 1\sigma$  (wide); see Section 5.1.







**Table 7** (*continued*)

Source Name	Coordinates	SpT	2MASS $J$	$J - K$	$\mu_\alpha$	$\mu_\delta$	$d$	Published RV	References
(J2000)		(mag)	(mag)	(mas yr $^{-1}$ )	(mas yr $^{-1}$ )	(mas yr $^{-1}$ )	(pc)	(km s $^{-1}$ )	

*a* References are in the order of spectral classification, astrometry, and RV measurement.*b* Identified as a member of the Argus moving group using BANYAN  $\Sigma$ *c* Identified as a member of the AB Doradus moving group using BANYAN  $\Sigma$ *d* Identified as a member of the Carina-Near moving group using BANYAN  $\Sigma$ *e* Suspected young source from Faherty et al. (2016)*f* Weird red L dwarf, also reported as L4pc in Faherty et al. (2016)

**References**— Classification: (1) Kirkpatrick et al. (1991), (2) Leinert et al. (2000), (3) Reid et al. (2000), (4) Gizis et al. (2000), (5) McCaughey et al. (2002), (6) Goto et al. (2002), (7) Gizis (2002), (8) Scholz & Meusinger (2002), (9) Cruz et al. (2003), (10) Reid et al. (2003), (11) Salim et al. (2003), (12) Henry et al. (2004), (13) Lodieu et al. (2005), (14) Reid & Gizis (2005), (15) Reid et al. (2006), (16) Schmidt et al. (2007), (17) Reid et al. (2008), (18) Faherty et al. (2009), (19) Burgasser et al. (2010), (20) Konopacky et al. (2010), (21) West et al. (2011), (22) Gizis et al. (2011), (23) Burgasser et al. (2011), (24) Kirkpatrick et al. (2011), (25) Deshpande et al. (2012), (26) Dupuy & Liu (2012), (27) Marocco et al. (2013), (28) Thompson (2013), (29) Thompson (2015a), (30) Newton et al. (2013), (31) Schneider et al. (2014), (32) Dieterich et al. (2014), (33) Bardalez Gagliffi et al. (2014), (34) Burgasser et al. (2015), (35) Davidson et al. (2015), (36) West et al. (2015), (37) Gagné et al. (2015b), (38) Metcheva et al. (2015), (39) Faherty et al. (2016), (40) Koen et al. (2017), (73) Burgasser et al. (2008); Astrometry: (41) Monet et al. (2003), (42) Costa et al. (2016), (43) Jameson et al. (2008a), (44) Faherty et al. (2012), (45) Smartt et al. (2013), (46) Dittmann et al. (2014), (47) Burgasser et al. (2015b), (48) Weinberger et al. (2017), (53) Gaia Collaboration et al. (2018), (54) Gagné et al. (2018a); Radial Velocity: (55) Bairst et al. (2000), (56) Reid et al. (2002), (57) Bailler-Jones (2004), (58) Zapatero Osorio et al. (2007), (59) Blake et al. (2007), (60) Reiners & Basri (2009), (61) Blake et al. (2010), (62) Seifahrt et al. (2010), (63) Morin et al. (2010), (64) Deshpande et al. (2012), (65) Shkolnik et al. (2015), (66) Tanner et al. (2012), (67) Deshpande et al. (2013) (68) Barnes et al. (2014), (69) Prato et al. (2015), (70) Terrien et al. (2015), (71) Vos et al. (2017), (72) Vos et al. (2018)

**Table 8.** Radial Velocities and Heliocentric Space Motions of Late-M and L Dwarfs Within 20 pc of the Sun

Source Name	SpT	Published RV	<i>U</i>	<i>V</i>	<i>W</i>	P[TD]/P[D] <sup>a</sup>	Population <sup>a</sup>
			(km s <sup>-1</sup> )	(km s <sup>-1</sup> )	(km s <sup>-1</sup> )		
J0004–4044	L5+L5	32.84 ± 0.17	21.68 ± 0.05	−85.7 ± 0.4	−11.90 ± 0.17	3.42	D/TD
J0004–2058	M9	−33 ± 2	−42.5 ± 0.2	−13.2 ± 0.4	30 ± 2	0.04	D
J0015+3516	L1	−37.35 ± 0.16	28.01 ± 0.07	−27.23 ± 0.14	5.31 ± 0.14	0.01	D
J0019+5213	M9	−29 ± 3	4.2 ± 1.4	−30 ± 3	−16.9 ± 0.6	0.02	D
J0024–0158	L0.5	11.65 ± 1.6	9.4 ± 0.2	25.8 ± 0.7	0.8 ± 1.4	0.01	D
J0024–2708B	M8.5	−35 ± 3	−0.1 ± 0.4	31.2 ± 0.5	43 ± 3	0.24	D/TD
J0027+2219	M8e	−11.9 ± 1.3	−5 ± 3	−17 ± 3	3 ± 3	0.01	D
J0036+1821	L3.5	20.90 ± 0.14	−29.83 ± 0.08	9.08 ± 0.09	−5.9 ± 0.1	0.01	D
J0045+1634	L0β	3.29 ± 0.17	−10.8 ± 0.1	−1.89 ± 0.12	1.82 ± 0.12	0.01	D
J0047+6803	L7	−19.4 ± 1.3	21.5 ± 0.7	−4.1 ± 1.1	5.48 ± 0.11	0.01	D
J0102–3737	M9	−5 ± 2	−62.27 ± 0.16	−20.6 ± 0.4	13 ± 2	0.03	D
J0107+0041	L8	8.2 ± 0.5	−32 ± 3	−6.2 ± 1.7	6.1 ± 0.7	0.01	D
J0109–5100	M8.5e	−1.3 ± 0.2	−5.85 ± 0.05	7.54 ± 0.07	7.22 ± 0.18	0.01	D
J0109+2949	M9.5	38.9 ± 0.8	−78.6 ± 0.5	7.7 ± 0.6	14.6 ± 0.5	0.05	D
J0109–0343	M9e	−6.3 ± 1.8	−2.6 ± 0.5	0.04 ± 0.5	14.5 ± 1.65	0.01	D
J0140+2701	M8.5	8.2 ± 0.4	7.6 ± 0.2	1.0 ± 0.2	−14.8 ± 0.2	0.01	D
J0144–0716	L6.5	−2.6 ± 0.1	0.9 ± 0.1	−11.5 ± 0.2	10.2 ± 0.1	0.01	D
J0205–1159	L7+L7	7 ± 2	−23 ± 4	−9 ± 5	13 ± 3	0.01	D
J0213+4444	L1.5	−23.47 ± 0.11	30.89 ± 0.09	−5.3 ± 0.08	−0.06 ± 0.12	0.01	D
J0215–3040	M8	0.005 ± 0.009	−7.87 ± 0.04	−38.29 ± 0.11	24.28 ± 0.04	0.04	D
J0217+3526	M7	11 ± 3	−14 ± 2	−6 ± 2	0.5 ± 1.1	0.01	D
J0253+1652	M7	68.30 ± 0.05	−58.11 ± 0.04	−58.93 ± 0.09	−51.64 ± 0.03	14.17	TD
J0255–4700	L9	18 ± 3	6.2 ± 0.2	−19.2 ± 1.4	6.2 ± 2.4	0.01	D
J0306–3647	M8.5	11.44 ± 0.19	47.63 ± 0.07	−10.95 ± 0.09	−4.81 ± 0.16	0.01	D
J0314+1603	M9.5	−6.8 ± 0.2	25.9 ± 0.2	18.77 ± 0.06	0.76 ± 0.14	0.01	D
J0320+1854	M8	45.5 ± 0.6	−34.96 ± 0.5	−6.94 ± 0.15	−15.12 ± 0.31	0.01	D
J0331–3042	M7.5	19 ± 2	21.3 ± 0.8	−12.6 ± 0.9	−7.7 ± 1.6	0.01	D
J0334–4953	M9	71 ± 3	−60.60 ± 0.12	−88.1 ± 0.6	5.6 ± 0.8	10.77	TD
J0339–3525	M9β	7.4 ± 0.7	−2.4 ± 0.2	6.9 ± 0.4	6.8 ± 0.6	0.01	D
J0351–0052	M8	−11 ± 2	35.4 ± 1.5	−11.2 ± 0.3	0.0 ± 1.3	0.01	D
J0355+1133	L3–L6γ	11.9 ± 0.2	5.79 ± 0.19	−14.25 ± 0.19	−8.47 ± 0.14	0.01	D
J0417–0800	M7.5	40.6 ± 1.4	−34.0 ± 1.0	−21.5 ± 0.4	11.1 ± 0.9	0.01	D
J0423–0414	L6.5+T2	30.5 ± 0.6	−8.1 ± 0.5	23.3 ± 0.5	−25.2 ± 0.5	0.03	D
J0429–3123A	M7.5	40 ± 3	−15.2 ± 1.4	−9.8 ± 1.7	−14.8 ± 2.0	0.01	D
J0435–1606	M8e	48.5 ± 1.4	−34.5 ± 0.9	−3.5 ± 0.6	−11.3 ± 0.9	0.01	D
J0440–0530	M7.5e	29.9 ± 0.2	−19.6 ± 0.16	−2.64 ± 0.06	5.55 ± 0.11	0.01	D
J0500+0330	L4p	15.94 ± 0.16	6.30 ± 0.15	−8.9 ± 0.1	−9.00 ± 0.08	0.01	D
J0501–0010	L4γ	21.8 ± 0.7	−5.3 ± 0.7	−8.03 ± 1.13	3.7 ± 0.8	0.01	D
J0517–3349	M8	−39 ± 2	48.7 ± 0.9	8.0 ± 1.4	52.8 ± 1.1	0.9	D/TD
J0523–1403	L2.5	12.21 ± 0.09	−4.94 ± 0.07	8.28 ± 0.05	10.86 ± 0.05	0.01	D
J0539–0059	L5	13.91 ± 0.15	−10.82 ± 0.15	15.6 ± 0.1	20.45 ± 0.14	0.01	D
J0602+3911	L1β	7.94 ± 0.05	−1.11 ± 0.05	−15.20 ± 0.06	2.51 ± 0.02	0.01	D
J0641–4322	L2.5	74 ± 2	−60.3 ± 0.6	−51.6 ± 1.8	17.5 ± 0.7	0.2	D/TD
J0652–2534	M9	12 ± 2	−5.4 ± 1.1	12.2 ± 1.6	−8.2 ± 0.4	0.01	D
J0652+4710	L3.5+L6.5	−7.03 ± 0.07	17.96 ± 0.07	18.14 ± 0.04	2.10 ± 0.04	0.01	D
J0700+3157	L3+L6.5	−42.42 ± 0.09	52.30 ± 0.09	−13.74 ± 0.12	−10.94 ± 0.05	0.02	D
J0714+3702	M7.5β	40.03 ± 0.11	−30.1 ± 0.1	1.18 ± 0.06	10.94 ± 0.07	0.01	D
J0720–0846	M9.5+T5	83.8 ± 0.3	−47.6 ± 0.4	−47.7 ± 0.4	7.5 ± 0.6	0.07	D
J0741+1738	M7	41.8 ± 1.2	−23.1 ± 1.1	−37.7 ± 0.5	−11.7 ± 0.4	0.02	D

**Table 8** *continued*

**Table 8** (*continued*)

Source Name	SpT	Published RV	<i>U</i>	<i>V</i>	<i>W</i>	P[TD]/P[D] <sup>a</sup>	Population <sup>a</sup>
			(km s <sup>-1</sup> )	(km s <sup>-1</sup> )	(km s <sup>-1</sup> )		
J0746+2000	L0.5	52.37 ± 0.06	-43.3 ± 0.5	-1.8 ± 0.5	7.7 ± 1.1	0.01	D
J0751-2530	L1	32 ± 2	-46.9 ± 0.9	5.9 ± 1.8	-49.26 ± 0.16	0.44	D/TD
J0825+2115	L7.5	21 ± 2	-16.8 ± 1.6	-5.6 ± 0.7	-8.6 ± 1.1	0.01	D
J0828-1309	L2	25.85 ± 0.08	-22.18 ± 0.06	-3.6 ± 0.07	-11.49 ± 0.06	0.01	D
J0830+0947	M7.5	41 ± 2	-28.1 ± 1.5	-35 ± 1.0	-19.9 ± 0.9	0.03	D
J0835-0819	L6.5	29.89 ± 0.06	-22.66 ± 0.05	-1.78 ± 0.05	7.52 ± 0.03	0.01	D
J0847-1532	L1.5	2.0 ± 0.1	27.54 ± 0.11	0.7 ± 0.1	7.14 ± 0.05	0.01	D
J0853-0329	M9e	7 ± 2	-2.3 ± 1.1	2.7 ± 1.4	-10.0 ± 0.9	0.01	D
J0921-2104	L1	80.53 ± 0.11	31.37 ± 0.13	-83.91 ± 0.12	11.14 ± 0.08	2.99	D/TD
J0949+0806	M8.5	16 ± 2	34.9 ± 1.0	-54.5 ± 1.1	-5.5 ± 1.4	0.08	D
J1004-3335	L5	-8 ± 2	55.0 ± 0.5	16.2 ± 1.9	-0.6 ± 0.6	0.02	D
J1022+5825	L1β	19.29 ± 0.11	-58.8 ± 0.4	-55.8 ± 0.4	7.14 ± 0.12	0.19	D/TD
J1029+1626	L2.5	-28.2 ± 1.4	61.9 ± 0.8	0.8 ± 0.6	-7.1 ± 1.2	0.02	D
J1045-0149	L2	6.3 ± 0.1	-24.54 ± 0.14	-3.12 ± 0.08	-7.51 ± 0.11	0.01	D
J1048-3956	M9	-11 ± 2	-0.1 ± 0.3	13.0 ± 1.9	-22.2 ± 0.6	0.01	D
J1048+0111	L1	24.25 ± 0.06	-13.12 ± 0.07	-23.14 ± 0.08	4.53 ± 0.09	0.01	D
J1055+0808	M9	5 ± 2	-9.7 ± 0.5	-8.8 ± 1.0	-5.4 ± 1.7	0.01	D
J1058-1548	L2.5	19 ± 2	-10.2 ± 0.2	-7.7 ± 1.6	11.6 ± 1.3	0.01	D
J1108+6830	L1γ	-9.84 ± 0.11	0.84 ± 0.08	-10.88 ± 0.08	1.90 ± 0.08	0.01	D
J1121-1313	M8.5	33.9 ± 0.3	-14.65 ± 0.07	-25.4 ± 0.2	17.93 ± 0.19	0.01	D
J1124+3808	M8.5	-14 ± 3	26.0 ± 1.1	15.16 ± 0.07	-2 ± 3	0.01	D
J1126-5003	L5	49.3 ± 1.1	-92.2 ± 0.7	-76.6 ± 1.1	9.3 ± 0.2	9.53	D/TD
J1141-2232	M8	8 ± 3	-17.1 ± 0.5	17 ± 2	35.6 ± 1.8	0.06	D
J1155-3727	L2.5	45.51 ± 0.11	43.98 ± 0.06	-38.3 ± 0.1	-13.0 ± 0.1	0.04	D
J1155-2224	M7.5	-13 ± 3	-4.5 ± 0.7	9 ± 2	-12 ± 2	0.01	D
J1203+0016	L5	-0.22 ± 0.16	-54.2 ± 0.6	-41.5 ± 0.5	-17.7 ± 0.3	0.07	D
J1221+0257	L0.5	-8.79 ± 0.14	0.96 ± 0.07	6.67 ± 0.08	-3.75 ± 0.13	0.01	D
J1224-1238	M9	-2.9 ± 0.6	-4.26 ± 0.16	-8.1 ± 0.4	-7.4 ± 0.5	0.01	D
J1300+1912	L1.5	-17.60 ± 0.12	10.31 ± 0.03	-84.1 ± 0.3	-19.65 ± 0.12	3.55	D/TD
J1305-2541	L2+L3.5	6.4 ± 0.4	-8.0 ± 0.4	-8.4 ± 0.3	11.2 ± 0.2	0.01	D
J1309-2330	M8	15 ± 2	28.0 ± 1.0	-11.2 ± 1.2	-4.4 ± 1.3	0.01	D
J1315-2649	L3.5+T7	-8 ± 3	-34.9 ± 1.8	-31 ± 2	-12.3 ± 1.8	0.02	D
J1331-0116	T0/L6blue	-3.3 ± 0.4	21.4 ± 2.2	-58.8 ± 13.5	-25.8 ± 5.7	0.27	D/TD
J1332-0441	M7.5	-12 ± 2	10 ± 7	24 ± 7	-2 ± 5	0.01	D
J1356+4343	M8	-22 ± 3	-23.0 ± 0.4	-20.4 ± 1.1	-3.7 ± 3	0.01	D
J1403+3007	M8.5	-39.2 ± 0.4	-52.9 ± 0.2	-41.1 ± 0.2	-9.8 ± 0.4	0.05	D
J1425-3650	L4γ	5.4 ± 0.3	5.78 ± 0.19	-14.70 ± 0.17	-7.63 ± 0.12	0.01	D
J1428+3310	M9e	-39.1 ± 0.4	17.45 ± 0.08	-37.08 ± 0.13	-20.2 ± 0.4	0.03	D
J1438+6408	L0	-45 ± 3	64 ± 0.5	11.5 ± 1.9	-39 ± 2	0.22	D/TD
J1439+1929	L1	-26.74 ± 0.09	-71 ± 4	-28 ± 4	21.7 ± 1.7	0.08	D
J1450+2354	L4	5 ± 3	18.3 ± 1.0	23.5 ± 0.7	6 ± 2	0.01	D
J1454+1606B	M8.5	-10.5 ± 0.2	17.1 ± 0.2	14.92 ± 0.11	-8.8 ± 0.2	0.01	D
J1456-2809	M7e	1.0 ± 1.5	5.7 ± 1.2	-17.0 ± 0.6	-6.3 ± 0.7	0.01	D
J1501+2250	M9	6 ± 2	14.6 ± 0.8	10.1 ± 0.5	13.1 ± 1.7	0.01	D
J1504-2355	M7.5	-29.0 ± 2.0	-28.35 ± 1.61	-4.49 ± 0.65	1.97 ± 0.99	0.01	D
J1506+1321	L3	-0.68 ± 0.11	-21.87 ± 0.13	-27.94 ± 0.14	35.87 ± 0.13	0.07	D
J1507-1627	L5	-39.85 ± 0.05	-14.52 ± 0.04	-4.71 ± 0.07	-33.47 ± 0.05	0.03	D
J1510-0241	M9	-41 ± 2	-37.7 ± 1.4	-6.86 ± 0.16	-3.3 ± 1.4	0.01	D
J1515+4847	L6	-29.97 ± 0.11	-72.2 ± 1.1	-1.3 ± 0.8	-10.6 ± 0.6	0.03	D
J1521+5053	M7.5	1 ± 3	24.6 ± 0.2	9.6 ± 1.8	9 ± 2	0.01	D
J1524+2925	M7.5	-15.9 ± 0.5	33.41 ± 0.19	-21.0 ± 0.2	-6.2 ± 0.4	0.01	D

**Table 8** *continued*

**Table 8** (*continued*)

Source Name	SpT	Published RV	<i>U</i>	<i>V</i>	<i>W</i>	P[TD]/P[D] <sup>a</sup>	Population <sup>a</sup>
			(km s <sup>-1</sup> )	(km s <sup>-1</sup> )	(km s <sup>-1</sup> )		
J1534–1418	M7	−71 ± 2	−65.5 ± 1.7	−23.4 ± 0.3	−13.9 ± 1.1	0.04	D
J1539–0520	L4	27.3 ± 0.2	50.8 ± 0.2	50.4 ± 0.3	0.2 ± 0.2	0.14	D/TD
J1555–0956	L1.5	14.8 ± 0.1	65.30 ± 0.14	13.37 ± 0.02	−51.33 ± 0.18	1.34	D/TD
J1607–0442	M9	11 ± 2	32.7 ± 1.7	−10.4 ± 0.2	−1.5 ± 1.1	0.01	D
J1615+0546	M9	7 ± 2	25.3 ± 1.5	15.4 ± 0.5	−0.3 ± 1.2	0.01	D
J1615+3559	L3	−20.2 ± 0.9	46.2 ± 0.5	−26.1 ± 0.6	−7.6 ± 0.7	0.02	D
J1632+1904	L8	−6 ± 2	16.0 ± 1.4	20.4 ± 1.1	−13.0 ± 1.5	0.01	D
J1645–1320	L1	26.58 ± 0.06	43.5 ± 0.06	−31.25 ± 0.08	7.18 ± 0.03	0.02	D
J1655–0823	M7	15.39 ± 0.11	30.0 ± 0.1	−20.99 ± 0.03	18.36 ± 0.04	0.01	D
J1658+7026	L1	−25.6 ± 0.12	40.2 ± 0.1	−14.5 ± 0.1	8.7 ± 0.1	0.01	D
J1705–0516	L1	12.19 ± 0.11	28.04 ± 0.11	13.09 ± 0.06	−2.16 ± 0.11	0.01	D
J1707+6439	M8.5	−10.10 ± 0.06	22.41 ± 0.03	15.19 ± 0.06	−12.99 ± 0.05	0.01	D
J1707–0558	M9+L3	3 ± 2	14 ± 3	20 ± 4	4 ± 4	0.01	D
J1721+3344	L5	−102.8 ± 0.2	−88.9 ± 0.2	−122.5 ± 0.3	78.6 ± 0.4	>100	TD/H
J1731+2721	L0	−29.76 ± 0.11	6.28 ± 0.06	−17.78 ± 0.08	−6.62 ± 0.05	0.01	D
J1745–1640	L1.5	26 ± 2	38.5 ± 2.0	14.4 ± 0.4	−3.1 ± 0.2	0.01	D
J1750–0016	L5	19 ± 3	24 ± 3	17.7 ± 1.3	30.6 ± 0.7	0.04	D
J1757+7042	M7.5	−12.3 ± 0.6	−16.28 ± 0.17	−3.2 ± 0.5	−0.4 ± 0.3	0.01	D
J1807+5015	L1	−0.4 ± 0.5	20.18 ± 0.09	11.6 ± 0.4	4.0 ± 0.2	0.01	D
J1821+1413	L5	9.78 ± 0.16	24.16 ± 0.12	16.67 ± 0.11	−4.00 ± 0.05	0.01	D
J1835+3259	M8.5	8 ± 2	33.0 ± 0.9	11.5 ± 1.7	4.3 ± 0.6	0.01	D
J1843+4040	M7.5e	−19 ± 2	−30.4 ± 0.7	0.6 ± 1.8	21.7 ± 0.6	0.01	D
J1845–6357B	M8.5+T6	−18 ± 2	−8.0 ± 1.6	49.0 ± 0.9	−26.5 ± 0.8	0.18	D/TD
J1906+4011	L1	−22.8 ± 0.3	6.0 ± 0.1	0.6 ± 0.3	−34.93 ± 0.11	0.03	D
J1916+0508	M8	35.0 ± 1.5	64.6 ± 1.1	3.0 ± 1.0	2.15 ± 0.09	0.02	D
J2057–0252	L2β	−24.7 ± 0.4	−0.4 ± 0.3	−9.1 ± 0.3	16.2 ± 0.2	0.01	D
J2104–1037	L2	−21.09 ± 0.12	−26.02 ± 0.19	−18.04 ± 0.16	−25.6 ± 0.3	0.02	D
J2139+0220	L8.5+T3.5	−25.1 ± 0.3	−19.8 ± 0.4	−2.6 ± 0.2	9.6 ± 0.3	0.01	D
J2148+4003	L7	−14.5 ± 0.7	−23.23 ± 0.13	−2.5 ± 0.7	4.21 ± 0.13	0.01	D
J2224–0158	L4.5	−36.48 ± 0.01	0.84 ± 0.04	−52.0 ± 0.4	−0.5 ± 0.3	0.04	D
J2234+2359	M9.5	17.2 ± 0.7	−47.5 ± 0.2	7.7 ± 0.6	−42.1 ± 0.4	0.17	D/TD
J2244+2043	L6–L8γ	−16.0 ± 0.9	4.77 ± 0.13	−15.1 ± 0.8	−5.9 ± 0.6	0.01	D
J2306–0502	M8	−54 ± 2	−33.3 ± 0.4	−55.5 ± 1.0	19.9 ± 1.7	0.16	D/TD
J2322–3133	L2β	33.9 ± 1.1	57.5 ± 0.5	−25.3 ± 0.5	−16.0 ± 1.1	0.03	D
J2331–2749	M7	−3.0 ± 1.5	−14.2 ± 0.4	53.8 ± 0.2	9.0 ± 1.4	0.11	D/TD
J2346+1129	M8	0 ± 2	46.3 ± 0.2	22.3 ± 1.3	11.4 ± 1.5	0.02	D

<sup>a</sup> Galactic thin disk (D), thick disk (TD), intermediate thin/thick disk populations (D/TD), and intermediate thick disk/halo populations (D/H) assigned in the same manner as Table 5.

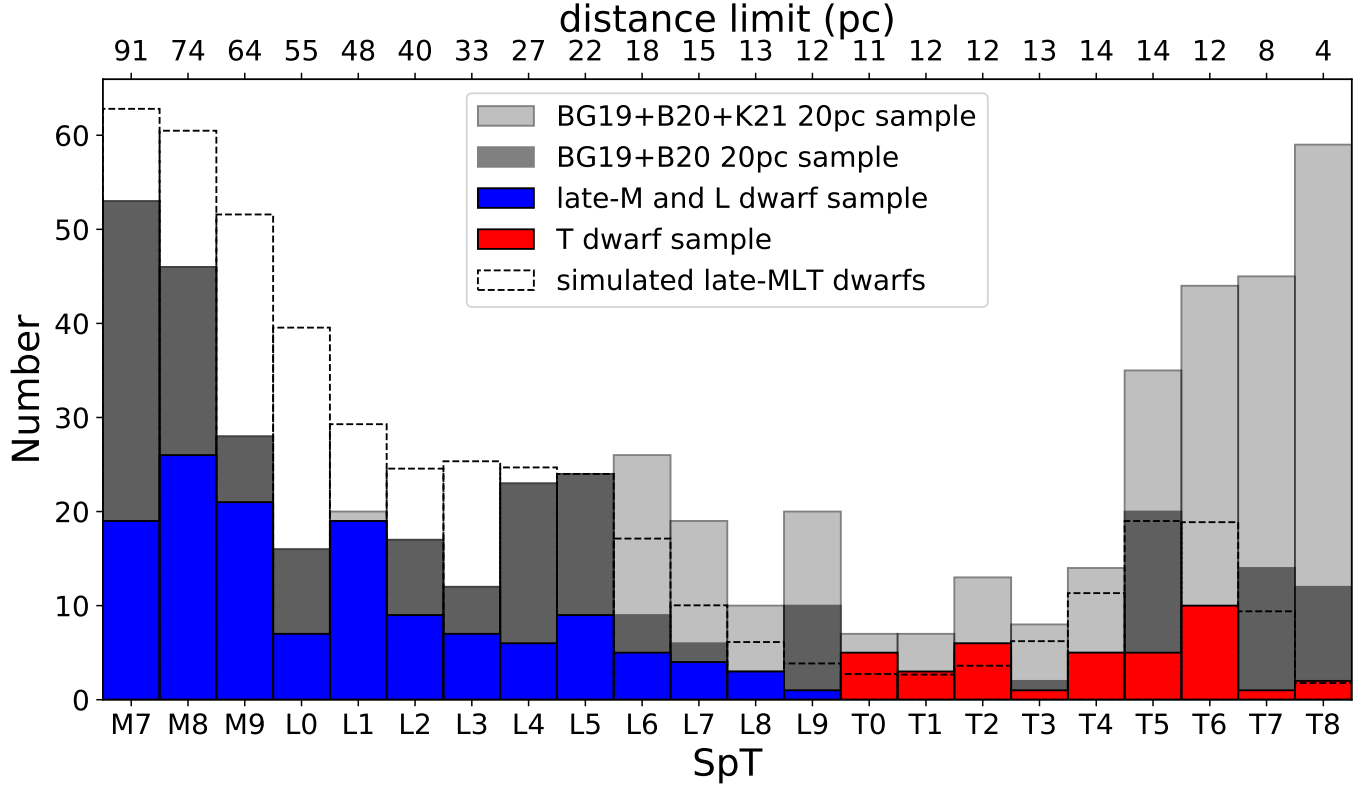


**Figure 19.** Spectral type distribution of our 20 pc late-M and L dwarf kinematic sample with RV uncertainty of  $\leq 3 \text{ km s}^{-1}$  (blue histogram), and our NIRSPEC T dwarf sample (red histogram). Also shown are the combined volume-limited samples of M7–L5 dwarfs from Bardalez Gagliuffi et al. (BG19; 2019) and L0–T8 dwarfs from (B20; Best et al. 2020b) (dark grey), a 20 pc full sample from BG19, B20, and Kirkpatrick et al. (K21; 2021) (light grey), and a simulated population (dashed histogram; Section 5.4) normalized to agree with the observed sample at spectral type L5. Distance limits assuming an apparent magnitude limit of  $J, K < 15.5$  are shown along the top x-axis.

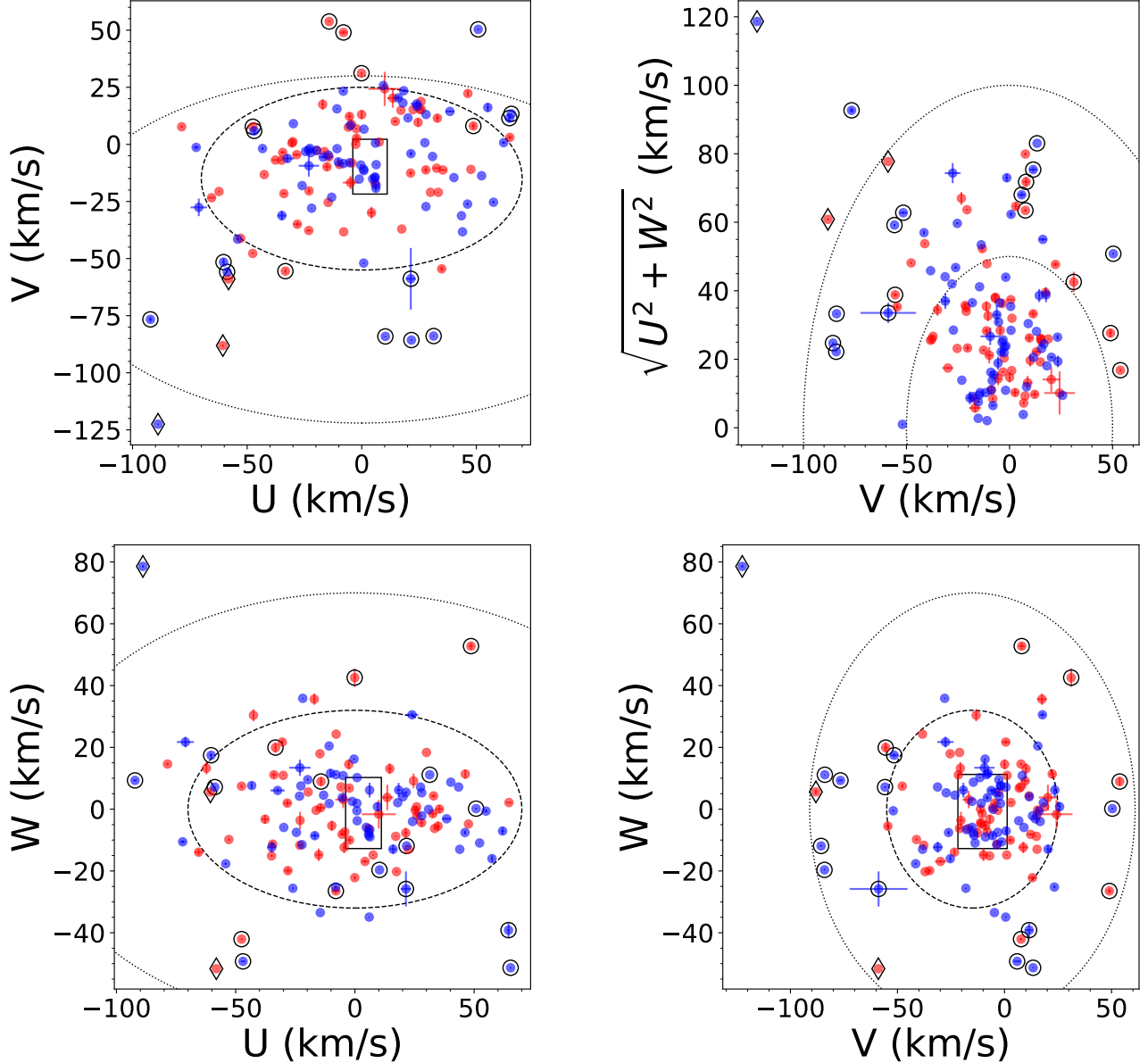


**Figure 20.** Same as Figure 11 for the late-M (red) and L dwarfs (blue) in our kinematic sample. The thick disk sources ( $P[\text{TD}]/P[\text{D}] > 10$ ) are highlighted as open diamonds.

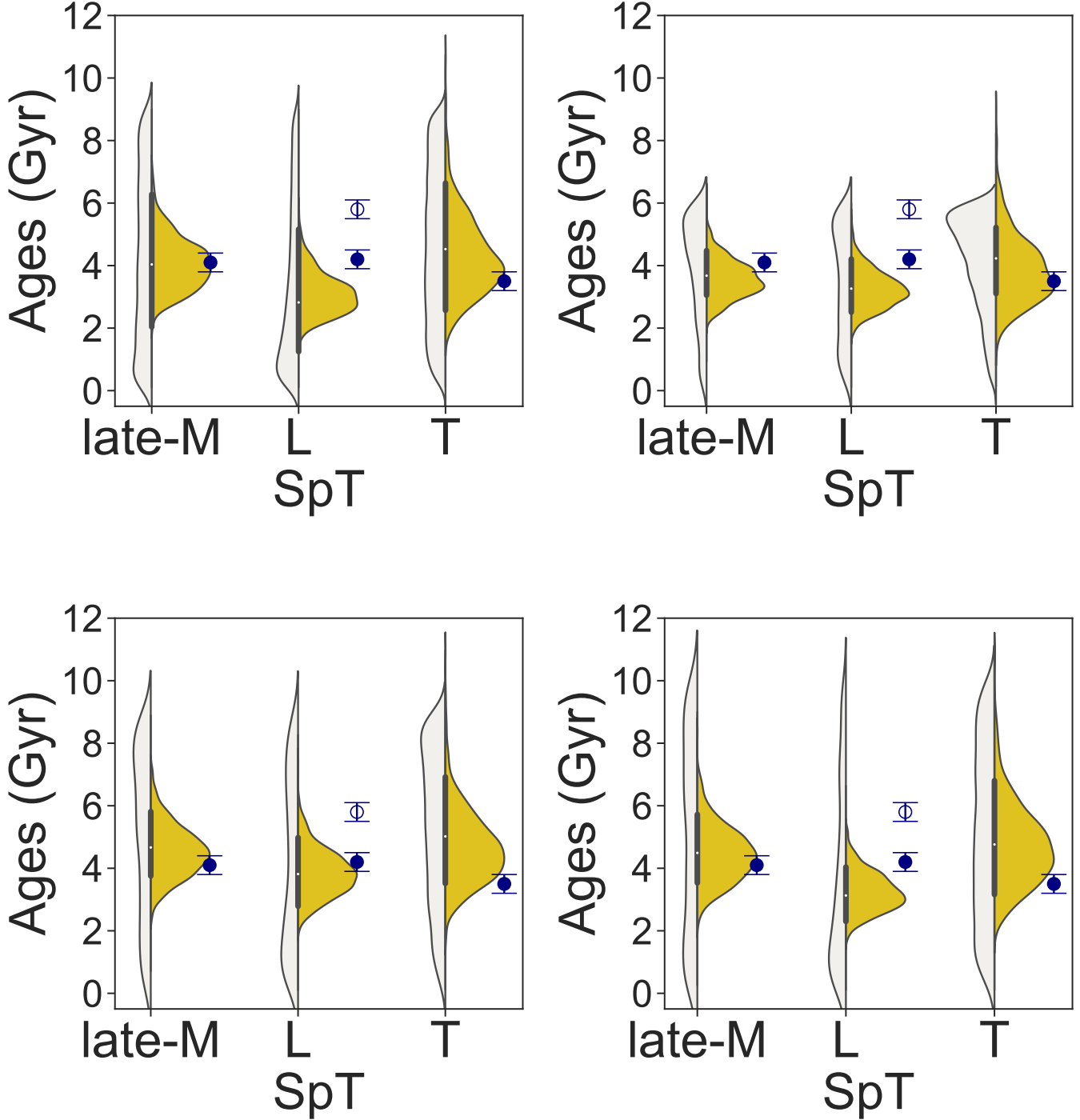


**Figure 21.** Simulated age distributions (white/yellow violin plots for individual/inferred ages, respectively) and measured kinematic ages (offset blue points and sampling uncertainties indicated) for all (empty blue points) and thin disk ( $P(\text{TD})/P(\text{D}) \leq 1$ ; solid blue point) late-M, L, and T dwarfs. Panels are for simulations that assume a mass function  $dN/dM \propto M^{-0.5}$ , Baraffe et al. (2003) evolutionary models, and the following star formation rates and population ages: *Upper left:* constant birthrate over 9 Gyr (baseline simulation); *Upper right:* Rujopakarn et al. (2013) cosmic birthrate over 6 Gyr; *Lower left:* Aumer & Binney (2009) exponential birthrate over 9 Gyr; *Lower right:* constant birthrate over 12 Gyr.

**Table 9.** Velocity Dispersions and Group Kinematic Ages of Late-M and L Dwarfs at Local 20 pc

Sample	N <sup>a</sup>	$\langle U \rangle$ (km s <sup>-1</sup> )	$\langle V \rangle$ (km s <sup>-1</sup> )	$\langle W \rangle$ (km s <sup>-1</sup> )	$\sigma_U$ (km s <sup>-1</sup> )	$\sigma_V$ (km s <sup>-1</sup> )	$\sigma_W$ (km s <sup>-1</sup> )	$\sigma_{tot}$ (km s <sup>-1</sup> )	Age (Gyr)	Note
late-M dwarfs	65	-4.7 ± 3.9	-6.8 ± 3.0	0.5 ± 2.1	31.9 ± 0.3	24.8 ± 0.4	17.3 ± 0.3	43.9 ± 0.6	4.9 ± 0.3	Unweighted
late-M dwarfs No Youth	60	-4.8 ± 4.2	-6.9 ± 3.3	0.0 ± 2.3	34.1 ± 0.5	27.7 ± 0.5	21.2 ± 0.7	48.8 ± 0.5	4.4 ± 0.1	W  Weighted
late-M dwarfs NTD <sup>b</sup>	63	-3.7 ± 3.8	-4.5 ± 2.8	1.0 ± 2.0	30.5 ± 0.4	22.1 ± 0.4	16.3 ± 0.3	45.2 ± 0.7	5.3 ± 0.3	Unweighted
late-M dwarfs D <sup>c</sup>	63	-3.7 ± 3.8	-4.5 ± 2.8	1.0 ± 2.0	32.5 ± 0.4	25.8 ± 0.4	17.9 ± 0.4	49.5 ± 0.7	4.5 ± 0.1	W  Weighted
L dwarfs	71	0.6 ± 4.2	-12.8 ± 3.5	-1.4 ± 2.2	30.5 ± 0.3	22.1 ± 0.3	16.3 ± 0.3	41.0 ± 0.6	4.1 ± 0.3	Unweighted
L dwarfs NTD <sup>b</sup>	70	1.9 ± 4.1	-11.2 ± 3.2	-2.6 ± 1.9	34.4 ± 0.4	26.8 ± 0.5	16.2 ± 0.3	46.5 ± 0.7	5.8 ± 0.3	Unweighted
L dwarfs NB <sup>d</sup>	67	3.8 ± 4.0	-10.8 ± 3.2	-3.3 ± 2.0	33.0 ± 0.4	26.0 ± 0.5	16.1 ± 0.3	45.0 ± 0.7	5.2 ± 0.1	W  Weighted
L dwarfs No Youth	57	0.9 ± 5.0	-12.4 ± 4.3	-1.7 ± 2.7	38.1 ± 0.5	32.5 ± 0.7	20.4 ± 0.5	53.3 ± 0.8	5.3 ± 0.3	Unweighted
L dwarfs No Binary	63	0.7 ± 4.6	-12.7 ± 3.7	-1.2 ± 2.4	36.7 ± 0.5	29.4 ± 0.7	19.2 ± 0.5	52.5 ± 0.8	5.1 ± 0.1	W  Weighted
L dwarfs No Binary D <sup>c</sup>	58	2.0 ± 4.3	-7.7 ± 2.8	-1.8 ± 2.0	33.0 ± 0.4	21.2 ± 0.7	15.4 ± 0.3	42.1 ± 0.9	4.4 ± 0.3	Unweighted
L dwarfs D <sup>c</sup>	65	1.5 ± 4.0	-7.2 ± 2.6	-1.8 ± 1.9	37.0 ± 0.7	21.5 ± 1.6	18.3 ± 0.4	46.5 ± 1.0	4.0 ± 0.2	W  Weighted
L0-L5 dwarfs	57	3.3 ± 5.0	-14.3 ± 4.2	-1.3 ± 2.6	37.6 ± 0.5	20.9 ± 0.6	15.3 ± 0.3	41.5 ± 0.8	4.2 ± 0.3	Unweighted
L0-L5 dwarfs D <sup>c</sup>	51	4.8 ± 4.7	-7.3 ± 3.0	-1.8 ± 2.2	33.6 ± 0.5	21.4 ± 0.3	15.9 ± 0.3	42.9 ± 0.7	4.6 ± 0.3	Unweighted
L6-L9 dwarfs	14	-10.5 ± 6.5	-6.7 ± 4.9	-1.9 ± 3.3	24.0 ± 2.1	18.4 ± 3.3	12.6 ± 1.0	32.8 ± 4.0	4.1 ± 0.1	W  Weighted
L1-L2 dwarfs	28	8.8 ± 6.6	-15.0 ± 4.7	-3.6 ± 3.5	26.0 ± 1.9	26.8 ± 6.0	15.1 ± 1.8	40.5 ± 4.9	3.0 ± 0.8	Unweighted
L0-L1 dwarfs	26	10.1 ± 6.9	-12.7 ± 5.3	-4.5 ± 3.7	34.9 ± 1.1	27.2 ± 1.1	18.8 ± 0.7	48.1 ± 1.7	6.4 ± 0.7	Unweighted
L2-L3 dwarfs	16	-0.9 ± 8.7	-13.0 ± 4.5	-1.3 ± 3.7	34.5 ± 1.3	18.0 ± 0.8	14.6 ± 0.9	41.6 ± 1.8	4.2 ± 0.6	Unweighted
L3-L4 dwarfs	13	8.6 ± 7.6	-7.4 ± 7.2	-1.1 ± 3.4	35.7 ± 2.0	28.1 ± 1.9	14.4 ± 1.1	47.7 ± 2.1	4.2 ± 0.4	W  Weighted
					28.6 ± 3.5	15.6 ± 3.3	43.7 ± 2.5	3.5 ± 0.4	3.5 ± 0.4	W  Weighted

**Table 9** *continued*

**Table 9 (continued)**

Sample	N <sup>a</sup>	$\langle U \rangle$ (km s <sup>-1</sup> )	$\langle V \rangle$ (km s <sup>-1</sup> )	$\langle W \rangle$ (km s <sup>-1</sup> )	$\sigma_U$ (km s <sup>-1</sup> )	$\sigma_V$ (km s <sup>-1</sup> )	$\sigma_W$ (km s <sup>-1</sup> )	$\sigma_{tot}$ (km s <sup>-1</sup> )	Age (Gyr)	Note
L4–L5 dwarfs	15	-3.9 ± 11.0	-18.3 ± 12.0	4.3 ± 6.4	42.2 ± 2.4	46.1 ± 2.6	24.4 ± 2.7	67.1 ± 4.4	16.2 ± 3.0	Unweighted
L4–L5 dwarfs NB <sup>d</sup>	12	11.1 ± 8.1	-7.6 ± 10.3	-3.7 ± 4.2	57.2 ± 7.3	72.9 ± 11.0	39.5 ± 6.2	100.8 ± 14.3	12.9 ± 2.0	W  Weighted
L4–L5 dwarfs D <sup>c</sup>	12	8.4 ± 8.2	0.8 ± 7.9	-1.0 ± 4.5	26.6 ± 3.1	32.1 ± 3.9	17.9 ± 2.6	45.6 ± 3.1	6.1 ± 1.4	Unweighted
L5–L6 dwarfs	15	-14.1 ± 11.1	-22.0 ± 11.2	1.4 ± 6.9	42.7 ± 1.8	43.3 ± 2.5	26.7 ± 2.5	66.4 ± 4.0	15.8 ± 2.7	W  Weighted
L5–L6 dwarfs NB <sup>d</sup>	11	-3.7 ± 10.5	-8.0 ± 9.2	-5.5 ± 5.1	34.9 ± 2.5	30.0 ± 3.7	16.7 ± 1.4	48.9 ± 4.7	11.6 ± 1.6	W  Weighted
L5–L6 dwarfs D <sup>c</sup>	12	-4.4 ± 9.7	-3.8 ± 7.0	-4.5 ± 5.4	29.7 ± 2.5	30.0 ± 3.4	16.5 ± 0.9	45.5 ± 2.8	6.8 ± 1.8	Unweighted
L6–L7 dwarfs	10	-11.8 ± 8.2	-8.7 ± 6.1	-3.5 ± 4.2	33.4 ± 2.3	24.1 ± 3.2	18.6 ± 1.2	45.2 ± 4.2	3.8 ± 0.5	W  Weighted
L6–L7 dwarfs NB <sup>d</sup>	9	-15.4 ± 8.2	-3.1 ± 3.5	-1.0 ± 3.9	28.3 ± 1.8	28.3 ± 5.1	17.1 ± 0.8	43.7 ± 3.7	5.4 ± 1.4	Unweighted
L7–L8 dwarfs	7	-11.1 ± 7.4	-1.4 ± 3.5	2.5 ± 3.4	25.7 ± 2.9	18.9 ± 4.5	13.3 ± 1.4	34.6 ± 5.5	3.5 ± 0.6	W  Weighted
L7–L8 dwarfs NB <sup>d</sup>	6	-9.7 ± 8.4	-1.2 ± 4.0	1.3 ± 3.7	27.2 ± 2.5	28.6 ± 7.5	16.3 ± 2.2	43.1 ± 6.1	2.6 ± 1.2	Unweighted
L8–L9 dwarfs	4	-7.5 ± 9.7	-1.9 ± 7.1	2.2 ± 4.4	19.1 ± 2.1	8.7 ± 2.7	8.7 ± 1.2	22.8 ± 3.6	3.4 ± 1.0	W  Weighted
L8–L9 dwarfs NB <sup>d</sup>	3	-3.4 ± 12.1	-1.7 ± 9.5	-0.2 ± 5.2	21.4 ± 3.3	10.8 ± 3.1	7.6 ± 1.2	25.3 ± 4.0	0.9 ± 0.4	Unweighted

NOTE—Ages for unweighted velocities are computed from equation (6) using the parameters in [Wielen \(1977\)](#). Ages for |W|-weighted velocities are computed from equation (8) using the parameters in [Aumer & Binney \(2009\)](#).

<sup>a</sup> Number of sources in sample

<sup>b</sup> Excluding thick disk sources

<sup>c</sup> Thin disk sources only

<sup>d</sup> Excluding unusual blue L dwarfs

### 5.3. Vertical Action Dispersion

Vertical action ( $J_Z$ ) measures the excursion of momentum perpendicular to the Galactic plane, which is invariant under orbital evolution provided that the Galactic potential is axisymmetric and perturbations are on average planar. The Galactic potential does have non-axisymmetric components, such as the spiral arms, interior bar, and giant molecular clouds above and below the Galactic disk, all of which can perturb  $J_Z$  and the planar actions  $J_R$  and  $J_\phi$  (Beane et al. 2018; Ting & Rix 2019). Nevertheless, it has been argued that vertical action may be a better physical quantity to probe statistical ages for stellar populations than  $UVW$  velocities (Kiman et al. 2019; Ting & Rix 2019).

Vertical actions and their dispersion can be computed directly from 6D spatial and velocity coordinates. We used *galpy* (Bovy 2015) to calculate  $J_Z$ , using a Galactocentric solar position of  $(R_\odot, Z_\odot) = (8.2, 0.025)$  kpc, an LSR Galactic circular velocity at the solar radius of  $\nu_\phi(R_\odot) = 240 \text{ km s}^{-1}$  (Ting & Rix 2019), and the LSR solar velocity vector used above. The position and circular velocity used here differ from our prior assumptions in Section 4.2 in order to align our analysis with that of Ting & Rix (2019).

By analyzing the APOGEE-*Gaia* DR2 red clump giant sample (Ting et al. 2018; Gaia Collaboration et al. 2018), Ting & Rix (2019) derived an empirical relation to estimate kinematic age from the mean vertical action  $\hat{J}_Z$  (kpc km s<sup>-1</sup>) as a function of mean Galactic radius  $\bar{R}_{\text{GC}}$  (kpc) and age  $\tau$  for a star:

$$\begin{aligned}\hat{J}_Z(\bar{R}_{\text{GC}}, \tau) &= \hat{J}_{Z,0}(\bar{R}_{\text{GC}}) + \Delta\hat{J}_{Z,1}\text{Gyr} \left(\frac{\tau}{1\text{Gyr}}\right)^{\gamma(\bar{R}_{\text{GC}})} \\ &= (0.91 + 0.18\Delta R_{\text{GC}} + 0.087\Delta R_{\text{GC}}^2 \\ &\quad + 0.014\Delta R_{\text{GC}}^3) \\ &\quad + (1.81 + 0.050\Delta R_{\text{GC}})\tau^{1.09+0.060\Delta R_{\text{GC}}},\end{aligned}\quad (9)$$

where  $\Delta R_{\text{GC}} = \bar{R}_{\text{GC}} - 8$  kpc,  $\bar{R}_{\text{GC}} = \frac{(R_{\text{GC}}+R_{\text{birth}})}{2}$ ,  $R_{\text{birth}}$  is the birth Galactic radius, and  $R_{\text{GC}}$  is the current Galactic radius. Since we cannot determine the birth radii for the sample, we simply use  $\bar{R}_{\text{GC}} = R_{\text{GC}}$ .

The Ting & Rix (2019) relation turns out to be problematic for this sample, as the zero-age baseline vertical action  $\hat{J}_{Z,0}(\bar{R}_{\text{GC}}) = 0.95 \text{ kpc km s}^{-1}$  is greater than the  $J_Z$  values of 66% of our sample, resulting in negative ages for these sources. Applying equation (9) to the remaining sources yields vertical action ages of  $1.9 \pm 2.7$  Gyr for late-M dwarfs ( $1.7 \pm 2.3$  Gyr for thin disk),  $2.3 \pm 2.5$  Gyr for L dwarfs ( $1.9 \pm 2.1$  Gyr for thin disk), and  $0.9 \pm 0.7$  Gyr for T dwarfs. These values are similar to the age of  $2.7 \pm 2.2$  Gyr inferred from vertical

action analysis of late-M and L dwarfs with SDSS spectra by Kiman et al. (2019), and both are considerably younger than the ages inferred from velocity dispersions. These age estimates are likely in error, as the Ting & Rix (2019) relations produce negative ages for a significant fraction of the stars in our sample. We therefore discard these age determinations as absolute measures, but note that the relative consistency of ages for thin disk late-M, L, and T dwarfs is concurrent with our velocity dispersion analysis.

### 5.4. Comparison to Simulated Populations

#### 5.4.1. Baseline Simulations

To evaluate whether the kinematic ages determined here are consistent with our understanding of the formation and evolution of UCDs, we conducted a Monte-Carlo population simulation for local thin disk late-M, L, and T dwarfs. We simulated  $10^5$  sources assuming a uniform spatial distribution and a uniform star formation rate over  $0.1 \text{ Gyr} \leq \tau \leq 9 \text{ Gyr}$ , with masses sampling the range  $0.01 M_\odot \leq M \leq 0.15 M_\odot$ <sup>22</sup> drawn according to a power-law initial mass function

$$\frac{dN}{dM} \propto M^{-\alpha}, \quad (10)$$

where  $M$  is mass,  $N$  is the number density of stars in the local volume, and  $\alpha$  is a power-law index. We chose a baseline value  $\alpha = 0.5$ , which is roughly consistent with UCD populations in young clusters (Bastian et al. 2010) and the local Galactic environment (Kirkpatrick et al. 2019, 2021). We used the evolutionary models of Baraffe et al. (2003) to convert ages and masses into effective temperatures ( $T_{\text{eff}}$ ), and assigned spectral types (SpT) using the empirical SpT- $T_{\text{eff}}$  relation of Filippazzo et al. (2015).  $UVW$  space velocities in the LSR were then assigned based on age, by assuming<sup>23</sup>  $UVW = 0$  at  $\tau = 0$  and drawing from normal distributions in all three components using widths based on the Aumer & Binney (2009) age-dispersion relations for each axis of motion. For the  $V$  velocity, we also added a time-dependent asymmetric drift term (Aumer & Binney 2009):

$$V_a = \frac{-\sigma_U^2(\tau)}{74 \text{ km s}^{-1}} = 23.7 \left(\frac{\tau}{10 \text{ Gyr}}\right)^{0.614} \text{ km s}^{-1}. \quad (11)$$

<sup>22</sup> The choice of lowest-mass  $0.01 M_\odot$  is limited by evolutionary models for the field sample. Saumon & Marley (2008) models have the lowest-mass  $0.01 M_\odot$  that evolve to 10 Gyr. A  $10 M_{\text{Jup}}$  T dwarf is relatively young (Baraffe 2003 models for  $T_{\text{eff}} = 953 \text{ K}$  and mass =  $0.01 M_\odot = 100 \text{ Myr}$ ), so it is unlikely that lower mass objects will be significant contributors to the field sample.

<sup>23</sup> This is consistent with our kinematic analysis for the observed sample; see Sections 5.1 and 5.2 for more details.

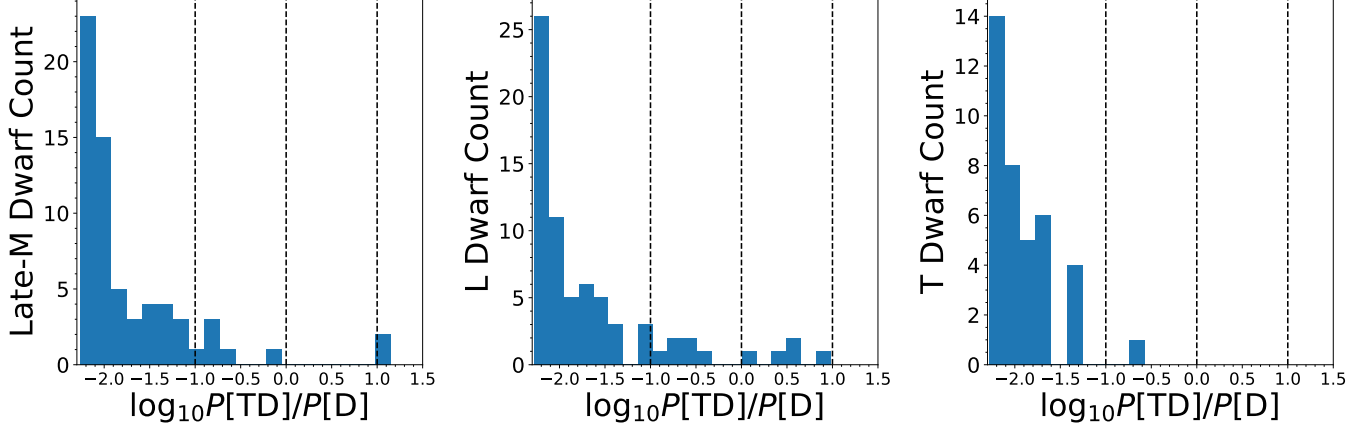


**Figure 22.** Distributions of log probability ratios of thick/thin disk (TD/D) sources for late-M, L, and T dwarfs, respectively. The vertical dashed lines denote the probability ratios of 0.1, 1, and 10, respectively.

**Table 10.** Simulated UCD Population Parameters

Sample	Simulated			Kinematic Age (Gyr)	
	Age <sup>a</sup> (Gyr)	$\langle U \rangle$ (km s <sup>-1</sup> )	$\langle V \rangle$ (km s <sup>-1</sup> )		
late-M dwarfs	4.1	$1 \pm 4$	$-13 \pm 3$	$0 \pm 2$	$4.1 \pm 0.8$
L dwarfs	2.8	$0 \pm 4$	$-11 \pm 3$	$0.1 \pm 1.7$	$3.1 \pm 0.7$
T dwarfs	4.6	$0 \pm 6$	$-14 \pm 4$	$0 \pm 3$	$4.3 \pm 1.2$

NOTE—Ages for simulated populations are computed from equation (8) using the parameters in Aumer & Binney (2009), with sampling errors accounted for using a Jackknife test statistic; see Section 5.4.

<sup>a</sup>Median simulation age  $< \tau >$

From this simulated (and assumed volume-complete) velocity sample, we computed the kinematic ages of UCD spectral subgroups using the same analysis as that of our observational sample. We simulated sample selection effects by making 1,000 random draws of  $N_s - 1$  sources from the simulated population, where  $N_s$  corresponds to the sizes of our late-M, L, and T dwarf RV samples (63, 65, and 36 sources, respectively) and  $-1$  corresponds to the Jackknife sampling. The median values and standard deviations from this sampling are summarized in Table 10 and Figure 23.

The resulting kinematic ages are  $4.1 \pm 0.8$  Gyr,  $3.1 \pm 0.7$  Gyr, and  $4.3 \pm 1.2$  Gyr for late-M, L, and T dwarfs, respectively. These ages are statistically equivalent, although the L dwarfs are about 1 Gyr younger on average. The relatively large uncertainties highlight the importance of sampling effects. Comparing to the kine-

matic ages of the observed thin disk sample, we find excellent agreement for the late-M and T dwarfs, but significant disagreement ( $\Delta\tau = 4.0$  Gyr,  $5.0\sigma$  deviation) compared to the full sample of L dwarfs. However, if we exclude potential thick disk sources ( $P[\text{TD}]/P[\text{D}] > 1$ ), the discrepancy for the L dwarfs is significantly reduced ( $\Delta\tau = 1.1$  Gyr) with only marginal significance of deviation ( $1.4\sigma$ ). Again, accounting for potential thick disk sources appears to mostly resolve the previously identified discrepancy between observed and simulated ages for L dwarfs, although our baseline simulations still predict a young L dwarf population compared to late-M and T dwarfs.

#### 5.4.2. Variations on Simulated Populations

The modest disagreement between simulated and observed kinematics suggests the need for some fine-tuning of simulation parameters as they relate to the kinematics of late-M, L, and T dwarfs. To explore this, we evaluated the influence of following simulation parameters on the ages of the late-M, L, and T dwarf disk population:

- *Star formation rate (SFR):* In addition to a uniform star formation rate, we examined an exponentially declining birth rate,  $SFR \propto e^{\gamma\tau}$ , where  $\gamma = 0.117 \text{ Gyr}^{-1}$  and  $\tau$  is age in Gyr (Aumer & Binney 2009); and a star formation rate that reflects cosmic star formation history,  $SFR \propto (1 + z(\tau))^\beta$ , where  $z$  is the redshift and  $\beta = 3.5$  (Rujopakarn et al. 2010; Planck Collaboration et al. 2016).
- *Mass function:* We examined additional power-law relations with  $\alpha = -1.5, -0.5$ , and  $+1.5$ ; and two cases of an age-dependent mass function:  $\alpha = 0.0$

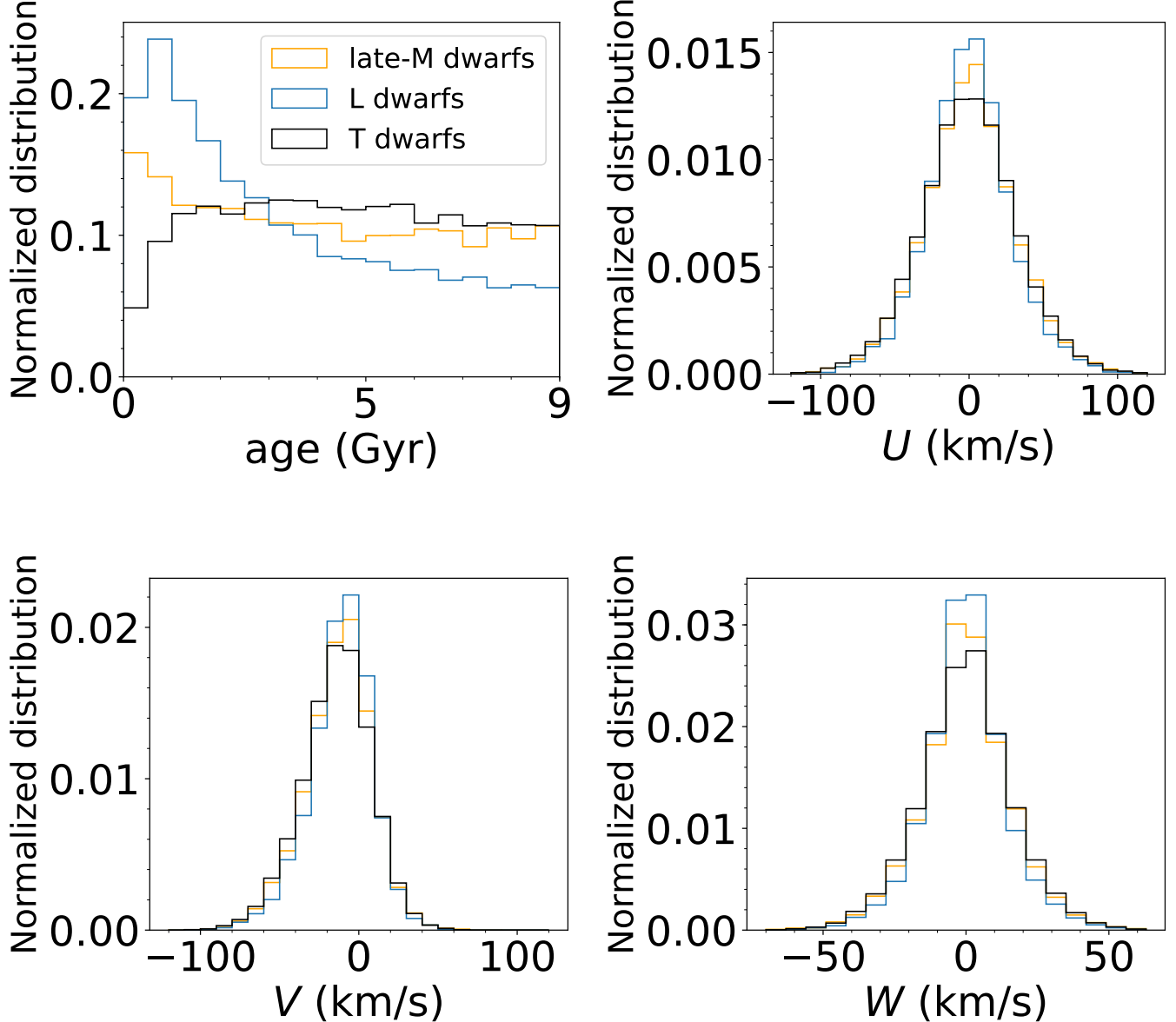


**Figure 23.** Normalized distributions of ages (upper-left) and  $UVW$  space motions for our baseline simulated population. Distributions are segregated between late-M (orange), L (blue), and T dwarfs (black).

$\Rightarrow +1.0$  and  $\alpha = +1.0 \Rightarrow 0.0$  10 Gyr in the past<sup>24</sup> (cf. Burgasser et al. 2015b). We also examined a log-normal mass function from Chabrier (2003).

- *Choice of brown dwarf evolution model:* In addition to the Baraffe et al. (2003) evolutionary mod-

els, we evaluated the models of Burrows et al. (2001), Saumon & Marley (2008), Marley et al. (2018), and Phillips et al. (2020).

- *Maximum simulation age:* In addition to the baseline maximum age of 9 Gyr, We considered maximum ages of 6 Gyr and 12 Gyr.
- *Minimum brown dwarf mass (MBDM):* The lowest-mass brown dwarfs are also the youngest in the L dwarf phase, which may skew simulated ages downward. We considered additional mini-

<sup>24</sup> The cosmological star formation rate peaks at  $z \sim 2$ , corresponding to a cosmic age of  $\sim 3$  Gyr ( $\sim 10$  Gyr in the past) under the standard  $\Lambda$ CDM cosmology (Madau & Dickinson 2014). The star formation rate of the inner Milky Way ( $R \leq 10$  kpc) peaks at  $\sim z = 1\text{--}3$  ( $\sim 8\text{--}12$  Gyr ago) (Haywood et al. 2016).

mum masses for our simulation of  $0.02 M_{\odot}$  and  $0.03 M_{\odot}$  to explore this effect.

For computational expediency, the number of simulated sources used for these simulations was  $10^4$  versus  $10^5$  for our baseline simulations. Varying each of these parameters individually, we produced 578 additional simulations. For Marley et al. (2018) and Phillips et al. (2020) models, we only ran the simulations for uniform star formation rate,  $\alpha = 0.5$  and minimum brown

dwarf mass of  $0.01 M_{\odot}$ . We quantified the agreement of the simulations to the observations using a  $\chi^2$  statistic:

$$\chi^2 = \sum_i \frac{(\tau_{\text{obs},i} - \tau_{\text{sim},i})^2}{\sigma_{\tau_{\text{obs},i}}^2 + \sigma_{\tau_{\text{sim},i}}^2} \quad (12)$$

with  $\tau_{\text{obs}}$  and  $\tau_{\text{sim}}$  being the observed and simulated ages,  $\sigma_{\text{obs}}$  and  $\sigma_{\text{sim}}$  the observed and simulated age uncertainties, and  $i = \text{late-M, L, and T dwarf thin disk samples}$  ( $P[\text{TD}]/P[\text{D}] \leq 1$ ). A select set of the results discussed here are summarized in Table 11. All simulations are fully compiled in Table B1.

**Table 11.** Select Simulated UCD Population Ages Under Different Assumptions

$\tau$	Star formation	$\alpha$	Models	MBDM	late-M dwarf age	L dwarf age	T dwarf age	$\chi^2$	Note
(Gyr)	(rate)			( $M_{\odot}$ )	(Gyr)	(Gyr)	(Gyr)		
Observations									
ALL SOURCES .....					$4.9 \pm 0.3$	$7.1 \pm 0.4$	$3.5 \pm 0.3$	...	
NOT THICK DISK ( $P[\text{TD}]/P[\text{D}] < 10$ ) .....					$4.1 \pm 0.3$	$5.8 \pm 0.3$	$3.5 \pm 0.3$	...	
THIN DISK ( $P[\text{TD}]/P[\text{D}] < 1$ ) .....					$4.1 \pm 0.3$	$4.2 \pm 0.3$	$3.5 \pm 0.3$	...	
Simulations									
9	uniform	0.5	B03	0.01	$4.1 \pm 0.8$	$3.1 \pm 0.7$	$4.3 \pm 1.2$	2.1	a
9	uniform	0.5	B01	0.01	$3.5 \pm 0.7$	$3.1 \pm 0.6$	$4.2 \pm 1.2$	3.0	
9	uniform	0.5	S08	0.01	$4.3 \pm 0.8$	$3.4 \pm 0.7$	$4.5 \pm 1.2$	1.7	
9	uniform	0.5	M19	0.01	$1.6 \pm 0.3$	$3.1 \pm 0.6$	$4.0 \pm 1.1$	42.1	
9	uniform	0.5	P20C	0.01	$0.2 \pm 0.0$	$2.6 \pm 0.5$	$4.2 \pm 1.2$	172.0	
9	uniform	0.5	P20NW	0.01	$0.3 \pm 0.0$	$2.6 \pm 0.6$	$4.3 \pm 1.2$	162.3	
9	uniform	0.5	P20NS	0.01	$0.4 \pm 0.0$	$2.7 \pm 0.6$	$4.1 \pm 1.2$	154.4	
9	exponential	0.5	B03	0.01	$4.5 \pm 0.8$	$3.8 \pm 0.8$	$4.7 \pm 1.2$	1.3	
9	exponential	0.5	B01	0.01	$3.6 \pm 0.6$	$3.7 \pm 0.7$	$4.9 \pm 1.4$	1.7	
9	exponential	0.5	S08	0.01	$4.6 \pm 0.8$	$4.2 \pm 0.8$	$4.8 \pm 1.2$	1.5	
9	log-normal	0.5	B03	0.01	$6.8 \pm 1.3$	$6.1 \pm 1.0$	$6.5 \pm 1.6$	11.6	
9	log-normal	0.5	B01	0.01	$7.4 \pm 1.3$	$6.0 \pm 1.0$	$6.2 \pm 1.5$	12.7	
9	log-normal	0.5	S08	0.01	$6.4 \pm 1.0$	$6.2 \pm 1.1$	$6.4 \pm 1.6$	11.3	
9	exponential	0.0/1.0/3.0	B03	0.01	$5.3 \pm 1.0$	$5.0 \pm 0.9$	$4.2 \pm 1.2$	2.5	b
9	exponential	1.0/0.0/3.0	B03	0.01	$4.2 \pm 0.7$	$4.8 \pm 0.8$	$5.2 \pm 1.3$	2.3	c
9	uniform	0.5	B03	0.01	$4.0 \pm 0.8$	$3.0 \pm 0.6$	$3.8 \pm 1.1$	2.8	d
9	uniform	0.5	B03*	0.01	$4.1 \pm 0.8$	$4.1 \pm 0.8$	$4.4 \pm 1.2$	0.5	e
9	uniform	1.5/-0.5/3.0	B03	0.01	$3.4 \pm 0.6$	$3.5 \pm 0.7$	$5.0 \pm 1.2$	3.2	c
9	uniform	1.5/-0.5/4.5	B03	0.01	$2.9 \pm 0.6$	$3.5 \pm 0.7$	$5.4 \pm 1.4$	5.6	c
9	uniform	1.5/-0.5/6.0	B03	0.01	$3.2 \pm 0.7$	$3.4 \pm 0.7$	$4.3 \pm 1.1$	2.7	c

**Table 11** *continued*

**Table 11** (*continued*)

$\tau$	Star formation	$\alpha$	Models	MBDM	late-M dwarf age	L dwarf age	T dwarf age	$\chi^2$	Note
(Gyr)	(rate)			( $M_\odot$ )	(Gyr)	(Gyr)	(Gyr)		

NOTE—Kinematics ages computed using the [Aumer & Binney \(2009\)](#) relation and the procedure described in Section 5.4.  $\tau$  is the maximum age of the sample,  $\alpha$  is the mass function power law index ( $\frac{dN}{dM} = M^{-\alpha}$ ), MBDM is the minimum brown dwarf mass. Evolving mass functions are labeled in the order of early  $\alpha$ , late  $\alpha$ , and age (in Gyr) of transition. A log-normal mass function from [Chabrier \(2003\)](#) is labeled as “log-normal”. Star formation rates considered in our simulations: uniform, exponential ([Aumer & Binney 2009](#)), and cosmic star formation rate ([Rujopakarn et al. 2010](#)). Brown dwarf evolution models are B03 ([Baraffe et al. 2003](#)), B01 ([Burrows et al. 2001](#)), S08 ([Saumon & Marley 2008](#)), M19 ([Marley et al. 2018](#)), and P20 ([Phillips et al. 2020](#)). For the last model set, C, NW, and NS stand for chemical equilibrium, weak, and strong chemical disequilibrium, respectively. Note that only substellar models are available in the P20 set. See Table B1 in Appendix B for the full list of simulations.

<sup>a</sup> Baseline simulation

<sup>b</sup> Simulations with an evolving mass function from top-heavy to bottom-heavy over time using [Baraffe et al. \(2003\)](#) evolutionary models. See Section 5.4 for details.

<sup>c</sup> Simulations with an evolving mass function from bottom-heavy to top-heavy over time using [Baraffe et al. \(2003\)](#) evolutionary models. See Section 5.4 for details.

<sup>d</sup> Baseline simulation with selection within 20 pc and  $J$  or  $K < 15.5$ . See Section 6.1 for details.

<sup>e</sup> Simulation with an artificial decrease in the HBMM for the [Baraffe et al. \(2003\)](#) evolutionary models by fixing the temperatures of brown dwarfs down to masses of  $0.060 M_\odot$  to their 1 Gyr values. See Section 5.4 for details.

Several simulations are consistent with the observed ages, which provides some constraints on the local UCD formation history. To explore these, we first compared the results for a fixed power-law mass function with  $\alpha = 0.5$  and  $MBDM = 0.01 M_\odot$ . Figure 24 shows the  $\chi^2$  distribution for different SFRs and evolved ages for each of the [Baraffe et al. \(2003\)](#), [Burrows et al. \(2001\)](#), and [Saumon & Marley \(2008\)](#) models. The diagonal elements of the simulations show the best agreements with the observed ages, which are cosmic/6 Gyr, exponential/9 Gyr, and uniform/12 Gyr, with the second of these being consistently best between the models. These parameters generally produce similar ages for late-M, L, T populations, with L dwarfs being slightly younger and T dwarfs being slightly older. The agreement between these parameter sets indicates a clear degeneracy between the SFR and population age that cannot be resolved by this coarse kinematic age comparison, although we are able to strongly rule out some combinations. For example, the cosmic/12 Gyr SFR/age combination can be ruled out to high probability using a BIC test ( $\Delta BIC > 10$ , highly significant).

Holding the SFR and sample age fixed to our baseline parameters, we compared the mass function power-law index to the MBDM (Figure 24 middle panels). The mass functions with  $\alpha = 0.5, -0.5$ , and  $-1.5$  are statistically equivalent, while the bottom-heavy  $\alpha = 1.5$  and log-normal mass functions are not favored ( $\Delta BIC > 2$ , positive; also see Figure 25). The results are insensitive to MBDM or evolutionary models. We also compared the SFR and mass function for a fixed age of 9 Gyr and  $MBDM = 0.01 M_\odot$  (Figure 24 bottom panels). Mod-

els using the cosmic star formation rate are significantly worse than other models. Again, the mass functions  $\alpha = 0.5, -0.5$ , and  $-1.5$  are statistically equivalent, while  $\alpha = 1.5$  and log-normal mass functions using the uniform star formation rate are not favored ( $\Delta BIC > 2$ , positive).

[Burgasser et al. \(2015b\)](#) considered whether the observed older L dwarfs in their sample could be the outcome of a mass function that evolves from bottom-heavy to top-heavy over time (i.e.,  $\alpha$  decreasing over time). Figure 26 shows that the original hypothesis  $\alpha = 1.5 \rightarrow -0.5$  at 4.5 Gyr is not consistent with the observed ages of late-MLT dwarfs ( $\chi^2 = 5.6$ ;  $\Delta BIC = 3.5$ ), overestimating in particular the ages of T dwarfs ( $5.4 \pm 1.4$  Gyr). However, scenarios with the same transition in at different transition ages (3 Gyr and 6 Gyr) are consistent ( $\Delta BIC \leq 2$ ). Similarly, a narrower range of mass function of evolution, either  $\alpha = 0 \rightarrow 1$  or  $\alpha = 1 \rightarrow 0$  with uniform and exponential birth rates cannot be ruled out ( $\Delta BIC \leq 2$ ; Figure 27).

Comparing the outcomes of different evolutionary models, we found the predictions of the [Burrows et al. \(2001\)](#), [Saumon & Marley \(2008\)](#), and [Baraffe et al. \(2003\)](#) models yield roughly identical results. Late-M dwarf ages using the [Marley et al. \(2018\)](#) and [Phillips et al. \(2020\)](#) cloudless atmosphere models were too young compared to L and T dwarfs, likely due to temperature limits in the model parameter space. We also found that increasing the maximum age or minimum brown dwarf mass in the simulations increased the mean ages of ultracool dwarfs, but retained the relative ages for late-M, L, and T dwarfs.

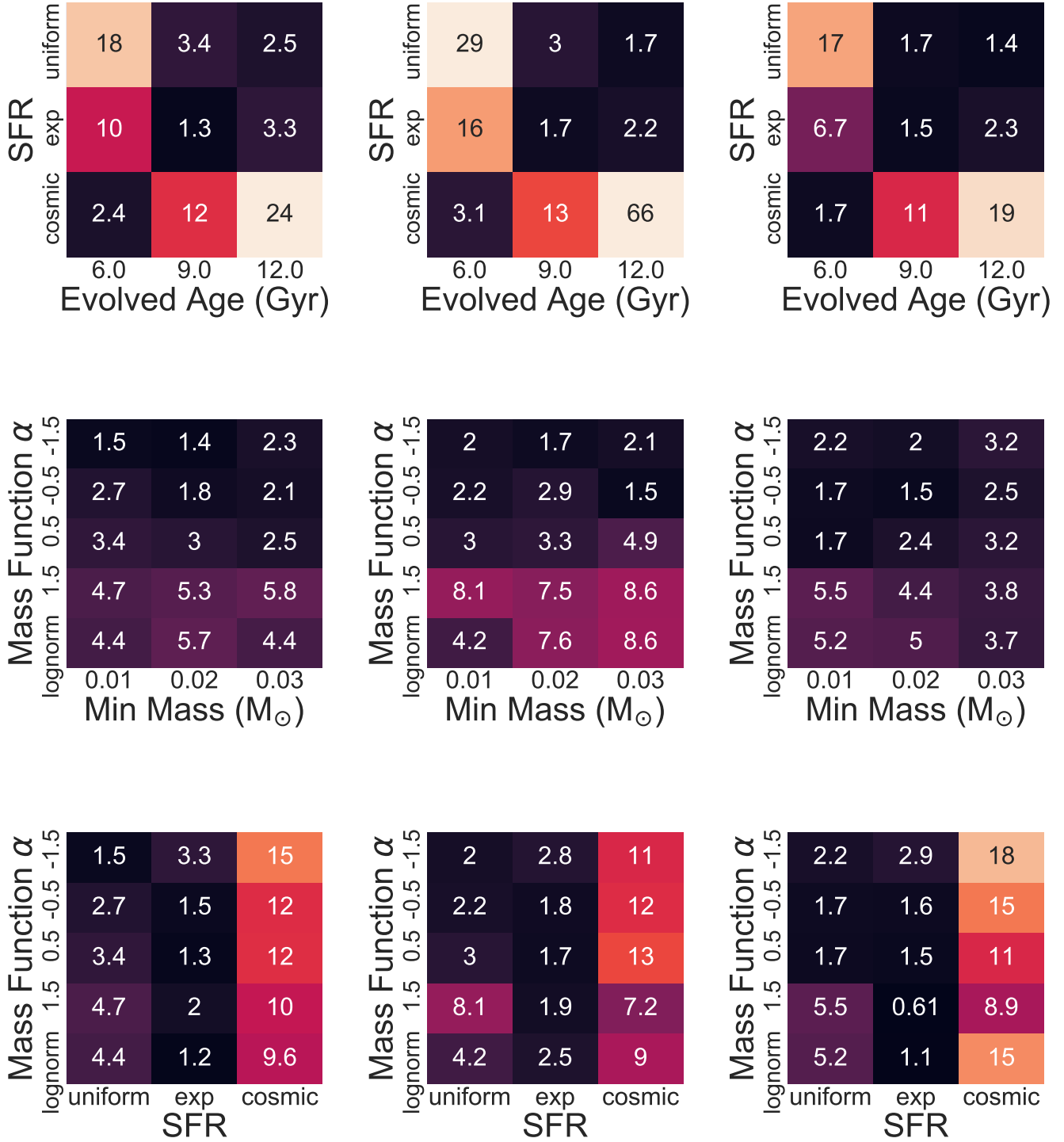


**Figure 24.**  $\chi^2$  distributions of simulated populations as a function of (1) top row: star formation rate (SFR) and evolved age; (2) middle row: minimum brown dwarf mass and mass function; (3) bottom row: star formation rate (SFR) and mass function across brown dwarf evolution models: left column: Baraffe et al. (2003); middle column: Burrows et al. (2001); right column: Saumon & Marley (2008). Lower  $\chi^2$  values have darker color.

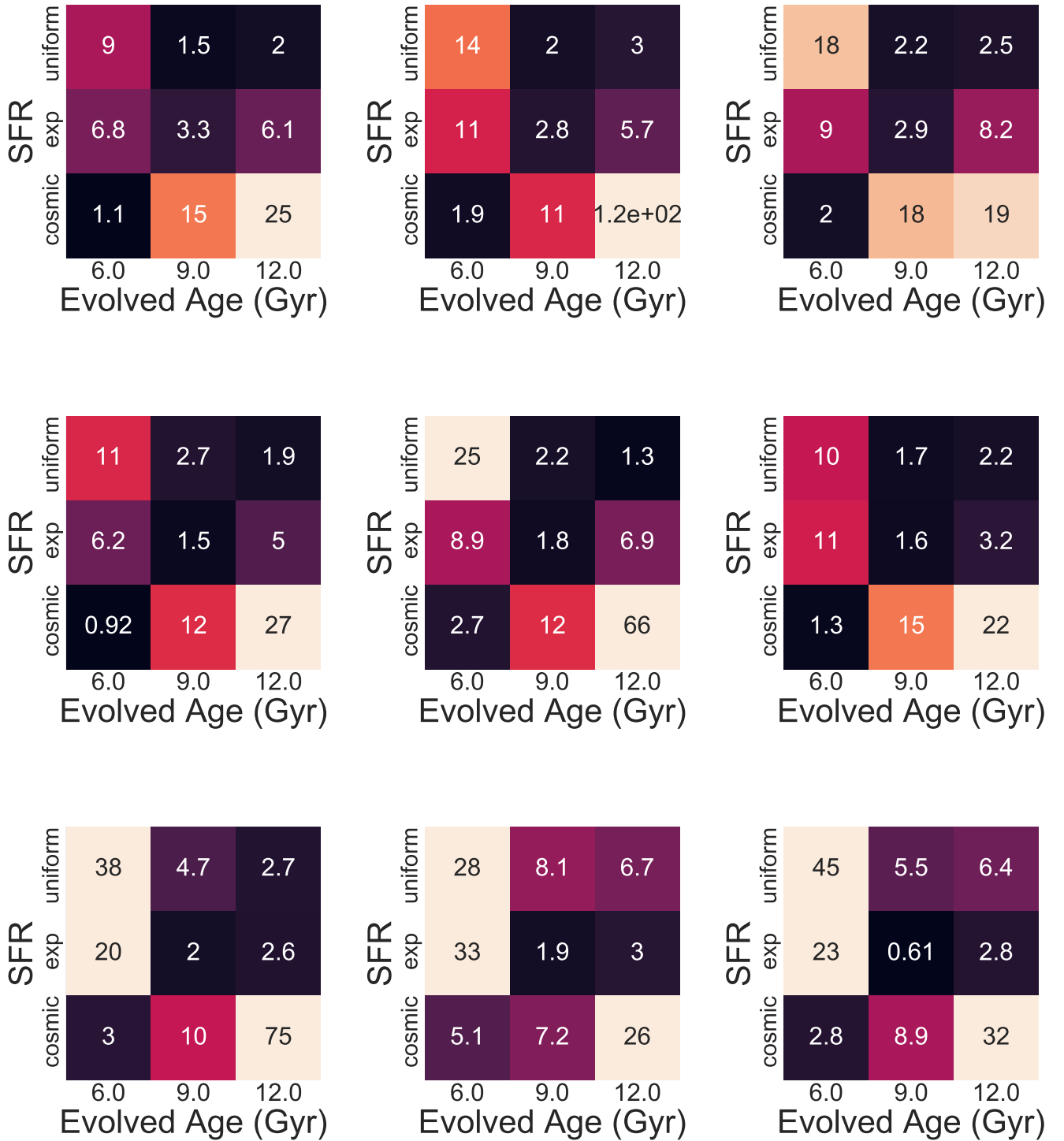


**Figure 25.** Same as Figure 24 top panel for  $\alpha = -1.5$  (top),  $-0.5$  (middle) and  $1.5$  (bottom).

Errors in evolutionary models could contribute to the marginal age discrepancy between simulations and observations for the L dwarfs. The ratio of L-type stars and brown dwarfs and the thermal evolution of the most massive brown dwarfs depends on the efficiency of hydrogen fusion reactions close to the critical temperature. An offset in the HBMM, particularly toward lower masses so that more L dwarfs are stars, could potentially increase the ages of L dwarfs in the simulations. To explore this effect, we imposed an artificial decrease in the HBMM for the Baraffe et al. (2003) evolutionary models by fixing the temperatures of brown dwarfs with masses  $M \geq 0.06 M_{\odot}$  to their 1 Gyr values. The resulting ages for late-M, L, and T dwarfs in these simulations are  $4.1 \pm 0.8$  Gyr,  $4.1 \pm 0.8$  Gyr,  $4.4 \pm 1.2$  Gyr, respectively, fully consistent with our observed ages (Figure 28). The fact that this adjustment provides the best match between the simulations and observed sources is suggestive of potential evolutionary model issues, which have also been raised with mass and luminosity measurements of brown dwarf companions to age-dated stars (Dupuy & Liu 2017) and the surprisingly high masses T-type brown dwarfs in binaries (e.g. Dupuy et al. 2019; Brandt et al. 2020; Sahlmann et al. 2020, 2021). These studies suggest that evolutionary model predictions of the temperatures and luminosities of objects around the HBMM may not align with the observed properties of these systems. However, with only a marginal age discrepancy, potential selection biases in our L dwarf kinematic sample (see below), and the degeneracies present among other simulation parameters, further work is needed to confirm this result. We note that increasing the timescale of cooling could also produce older L-type brown dwarfs, but also drives up the ages of T dwarfs and is therefore an unlikely scenario.

In summary, several variations in simulation parameters were able to reproduce the observed kinematic ages of the local late-M, L, and T dwarf populations self-consistently, and highlight some degeneracies in this approach. Nevertheless, we are able to rule out several parameter sets, and identify a potential indicator of a lower HBMM.

## 6. DISCUSSION

While our simulations are able to reproduce the kinematic ages of UCDs in the local thin disk population, the origin of the relatively high fraction of local thick disk L dwarfs remains unclear. As L dwarfs span the HBMM, in the local Galactic environment they consist of a mixed population of stars and (young) brown dwarfs. Accurate characterization of this population is therefore critical for validating brown dwarf evolutionary models and

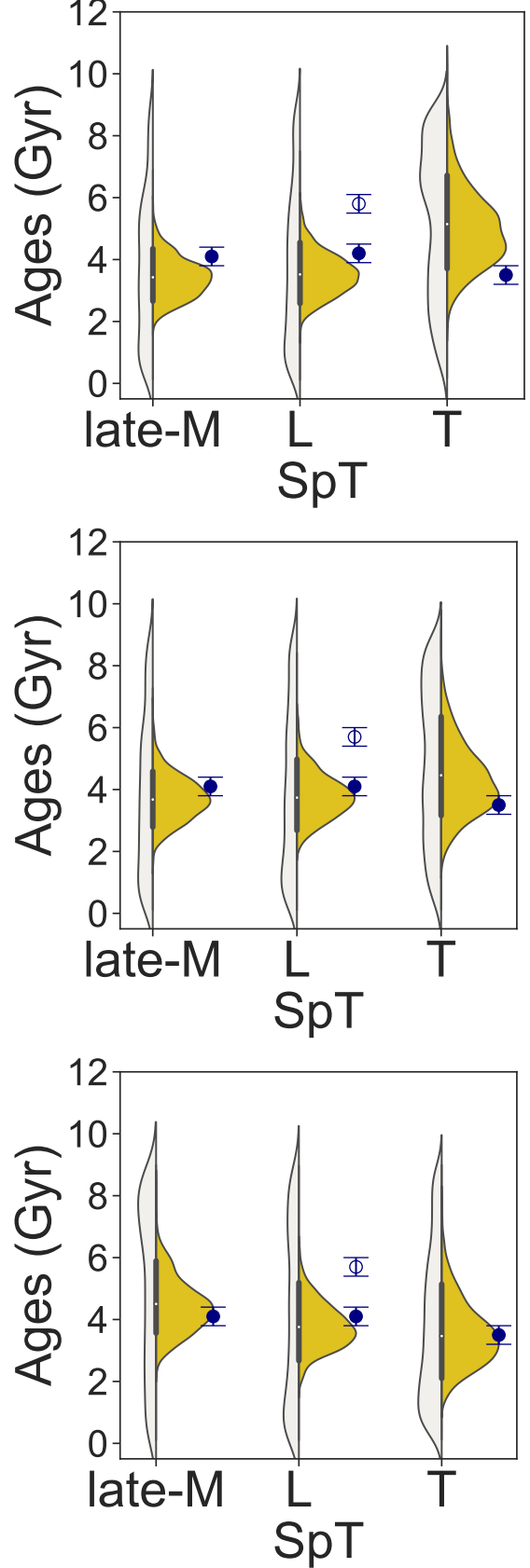


**Figure 26.** Same as Figure 21 comparing three simulations with baseline parameters and mass functions that evolve over time: (Top)  $\alpha = 1.5 \rightarrow -0.5$  (bottom-heavy to top-heavy; same model as Burgasser et al. 2015b); (Middle)  $\alpha = 1 \rightarrow 0$  (bottom-heavy to top-heavy); and (Bottom)  $\alpha = 0 \rightarrow 1$  (top-heavy to bottom-heavy).

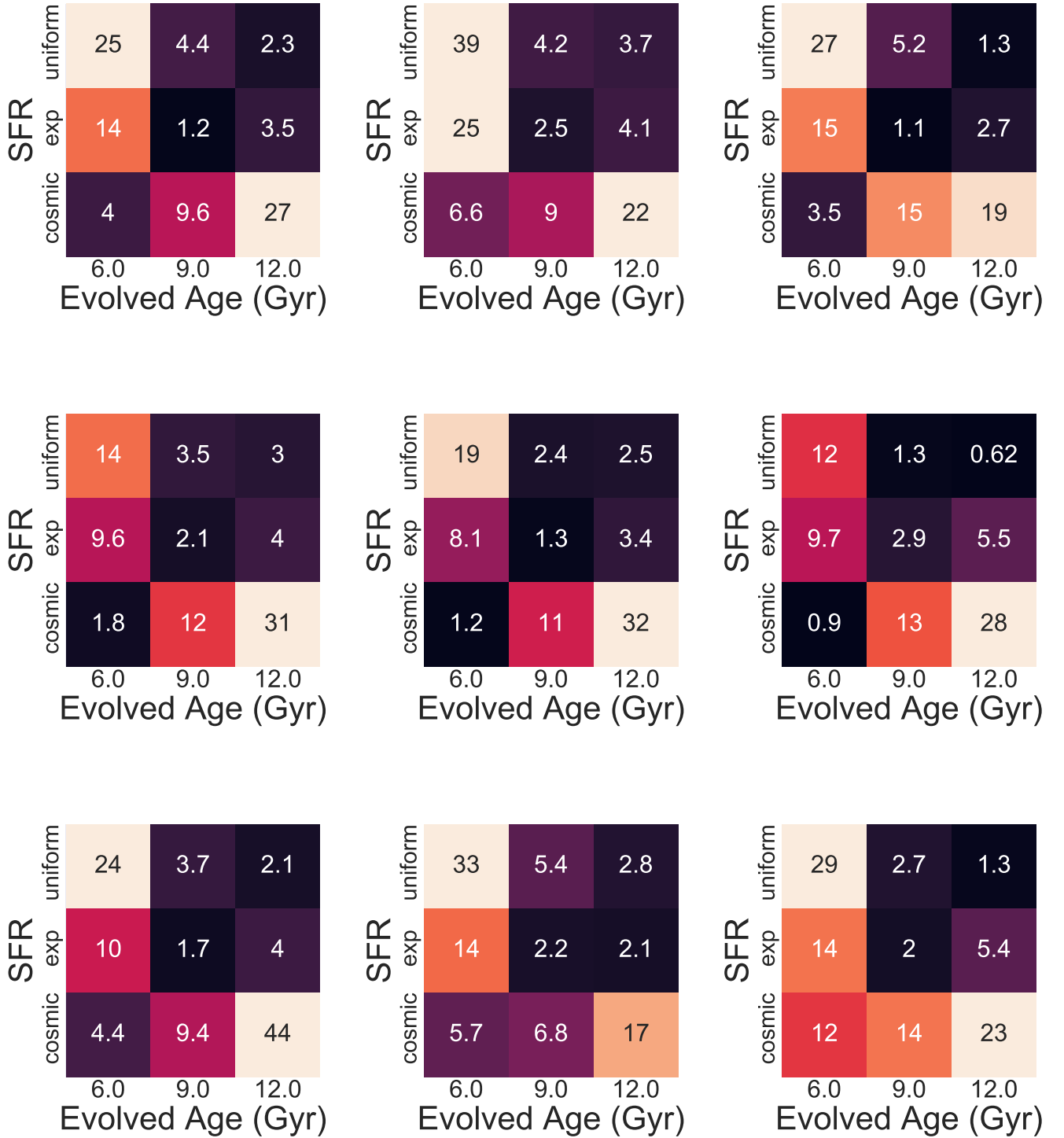


**Figure 27.** Same as Figure 24 top panel for the Chabrier et al. (2000) log-normal mass function (top), and for evolving mass functions  $\alpha = 0 \rightarrow 1$  at 3 Gyr (middle) and  $\alpha = 1 \rightarrow 0$  at 3 Gyr (bottom).

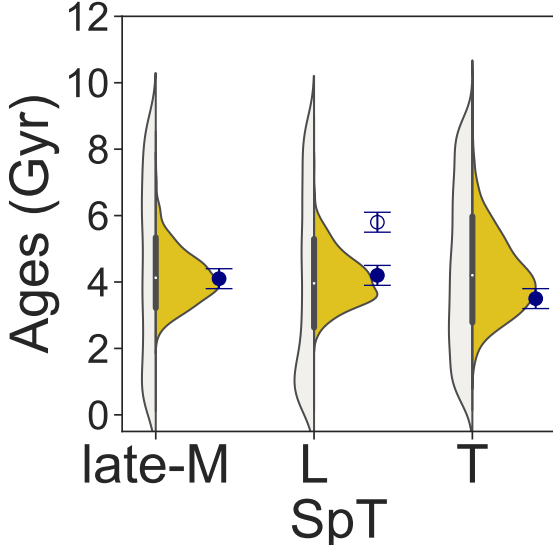


**Figure 28.** Same as Figure 21, comparing observed kinematic ages to a simulation assuming baseline parameters and a hydrogen burning minimum mass with an artificial decrease for the Baraffe et al. (2003) evolutionary models by fixing the temperatures of brown dwarfs with masses  $M \geq 0.06 M_{\odot}$  to their 1 Gyr values.

measuring brown dwarf formation history in the Galaxy. Here we explore some possible explanation as to why the local L dwarf sample studied in this paper are less well-modeled as compared to local late-M and T dwarfs.

#### 6.1. Sample incompleteness

The kinematic sample examined in this study, while larger than previous studies and limited to  $d < 20$  pc, is not uniformly volume complete. One primary reason for this is that fainter late-L and T dwarfs are detected at smaller distances for a given sensitivity limit. For Keck/NIRSPEC, an effective magnitude limit of 15 restricts observations of L5 dwarfs to 22 pc ( $K$ -band) and T5 dwarfs to 14 pc ( $J$ -band). RV measurements from the literature are also not volume- or magnitude-complete, as measurements were obtained with different optical and near-infrared spectrographs with varying sensitivity thresholds.

The underlying target sample is itself not volume-complete, either, particularly in the Galactic plane where nearby ultracool dwarfs sample smaller scale heights, and are hence younger, but where source contamination and crowding is high. Bardalez Gagliuffi et al. (2019) determined that the sample of late-M and early- to mid-L dwarfs is  $62^{+8}_{-7}\%$  and  $83^{+10}_{-9}\%$  complete within 20 pc, and new nearby sources are still being uncovered in wide-field surveys such as PanSTARRS (Best et al. 2020b), Gaia (Faherty et al. 2018; Reylé 2018; Scholz 2020), and WISE (Meisner et al. 2020;

Kirkpatrick et al. 2021). Figure 19 compares our simulated population to the 20 pc samples of Bardalez Gagliuffi et al. (2019, hereafter BG19), Best et al. (2020b, hereafter B20), and Kirkpatrick et al. (2021, hereafter K21). While these UCD samples are the most volume-complete constructed to date, there remain gaps particularly among the late-M, late-L, and T dwarfs. Our kinematic sample contains 48%–52% of the 20 pc UCDs in the BG19 and B20 samples, and based on these studies’ completeness estimates, only 32%–42% of M7–T8 dwarfs within 20 pc. Compared to K21, our sample contains only 27% of L0–T8 dwarfs within 20 pc.

One way this incompleteness can produce an age discrepancy is if the fraction of early-type and late-type L dwarfs in our sample is imbalanced. Early-type L dwarfs are predominantly low-mass stars of all ages and very young brown dwarfs, while late-type L dwarfs are predominantly young brown dwarfs, according to our simulations and the data. Figure 29 illustrates this trend in our kinematic sample, which shows a clear decline in velocity dispersion and inferred age as a function of L dwarf spectral subclass, with the exception of the L4–L6 subtypes (discussed in further detail below). More coarsely, while the overall kinematic age of thin disk L dwarfs is  $4.2 \pm 0.3$  Gyr, the kinematic age of 14 L6–L9 dwarfs is only  $2.2 \pm 0.8$  Gyr. We computed the ratio of L0–L5 to L5–L9 dwarfs in our baseline simulation sample, our kinematic sample, the samples of B20 and K21, and the combined sample of BG19 and B20. These ratios were found to be 1.3 (simulated), 4.1 (kinematic sample, L0–L5:L5–L9 = 57:14), 1.0 (B20, L0–L5:L5–L9 = 21:22), 1.3 (K21, L0–L5:L5–L9 = 96:75), and 3.3 (B19+B20, L0–L5:L5–L9 = 105:32), respectively. Our kinematic sample is clearly biased toward early L dwarfs compared to the simulated, B20, and K21 samples, but not compared to the combined B19 and B20 sample. However, if we try to reproduce the kinematic sample asymmetry through forced random draws from our baseline simulation, we find an average age for thin disk L dwarfs ( $3.0 \pm 0.6$  Gyr) that is still younger than observed. Similarly, sampling with replacement the thin disk L dwarfs from our kinematic sample to force a ratio of early-to-late L dwarfs of 1.3 (simulations) or 1.0 (B20) results a nearly identical age ( $4.1 \pm 0.8$  Gyr) as the original sample.

Our sample is also biased toward early T dwarfs due to the intrinsic faintness of later subtypes, with an early-to-late T dwarf ratio ( $T0–T4/T5–T8$ ) of 1.0, much higher than the most recent T dwarf sample from K21 (0.14) and our baseline population simulation (0.22). Again, if we randomly draw from the simulation to match the spectral type ratio of the observed kinematic sample,

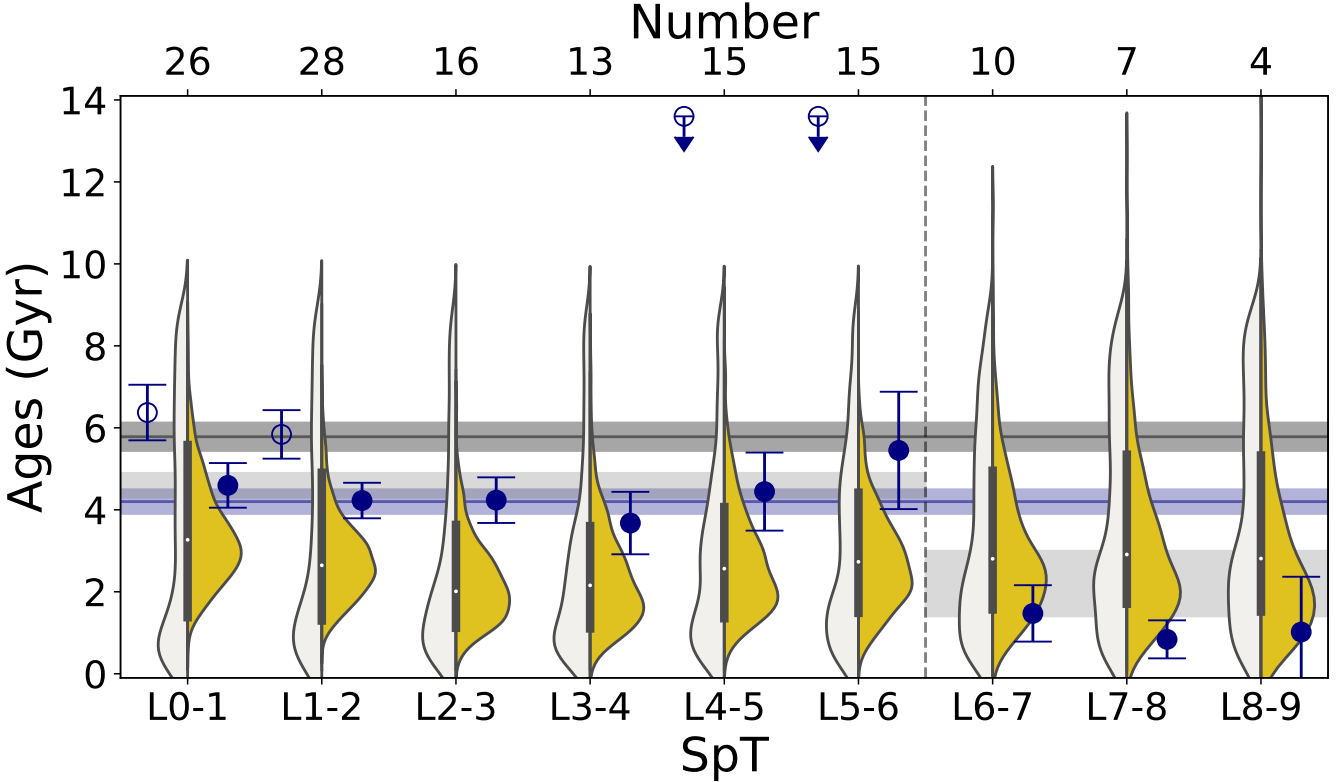


**Figure 29.** Age distributions of L dwarfs from the baseline simulation binned in groupings of two subtypes compared to measured kinematic ages with similar binning. Simulated age distributions are shown as individual source ages (white violin plots) and derived kinematic ages (yellow violin plots). Observed kinematic ages are shown with (open blue points) and without (solid blue points) L dwarfs for  $P[\text{TD}]/P[\text{D}] > 1$ . Our derived kinematic ages and uncertainties ( $5.8 \pm 0.3$  Gyr,  $4.2 \pm 0.3$  Gyr) for our nominal L dwarf sample ( $P[\text{TD}]/P[\text{D}] < 10$ ) are indicated by the black line, and for our constrained thin disk sample ( $P[\text{TD}]/P[\text{D}] < 1$ ) by the blue line. We also show the average kinematic ages for early- and late-L dwarfs separately as grey bands. The number of sources in each subtype bin is labeled at top. The ages of the discrepant L4–L5 and L5–L6 subtype bins are due to four unusually blue L dwarfs within these groups. Note that the very old tails of inferred ages for L6–L9 are due to small sampling effect.

we find an older but statistically equivalent age of  $4.3 \pm 1.2$  Gyr. Drawing from the kinematic sample to match the simulation T dwarf spectral type ratio yields a nearby identical age of  $3.5 \pm 0.2$  Gyr.

Another selection bias is the magnitude limit of the observed kinematic sample, which can similarly skew the number of early-type and later-type L dwarfs. We modeled this in our baseline simulation by assigning distances up to 20 pc over a uniform-density volume, assigning apparent magnitudes using the Dupuy & Liu (2012) absolute magnitude-spectral type relations, and constraining the simulated sample to be brighter than  $J$  or  $K < 15$ . The resulting magnitude-limited simulated late-M, L, and T dwarf kinematic ages are  $4.0 \pm 0.8$  Gyr,  $3.0 \pm 0.6$  Gyr, and  $3.8 \pm 1.1$  Gyr, respectively, fully consistent with our baseline simulation. Hence, a magnitude limit does not explain the older age for L dwarfs in the kinematic sample. A magnitude-limited sample can preferentially select younger sources, which haven't fully

contracted to their fully degenerate radii. This would affect all sources in our sample, but particularly those subgroups whose limiting magnitudes place them within the volume limit. This bias may explain the slightly younger kinematic age of T dwarfs compared to the simulations, but does not explain the presence of older L dwarfs in the kinematic sample.

## 6.2. Contamination by Distinct Sub-populations

Our kinematic L dwarf sample contains eight L-type binaries, fourteen young L dwarfs and four unusually blue L dwarfs, the latter based on the color outlier criteria of Faherty et al. (2009)<sup>25</sup>. Like the thick disk population, these distinct sub-populations have the potential of

<sup>25</sup> The blue L dwarfs in our sample are 2MASS J05395200–0059019 (Geballe et al. 2002), DENIS J112639.9–500355 (Phan-Bao et al. 2008), 2MASSI J1721039+334415 (Bardalez Gagliuffi et al. 2014), and 2MASS J05395200–0059019 (Fan et al. 2000).

skewing the kinematic dispersions and ages of the overall sample, so we re-evaluated the velocity dispersions and kinematic ages of the L dwarfs after removing each of these subgroups (Table 9). Removal of young L dwarfs and binaries increases the age of the total population to  $8.8 \pm 0.6$  Gyr and  $7.4 \pm 0.5$  Gyr. The former is expected as removal of young sources makes the population older while the latter is consistent with no change (when thick disk stars are left in). Removal of blue L dwarfs reduces the kinematic age to  $5.3 \pm 0.3$  Gyr, consistent with removal of thick disk stars. This result confirms the interpretation that unusually blue features are associated with higher surface gravities and/or lower metallicities, both of which correlate with older ages. We also examined whether removing L dwarfs with ages younger than 500 Myr in our baseline simulation would elevate the ages of the remaining sources; only a marginal shift to  $3.4 \pm 0.7$  Gyr was found. Finally, we considered the age without the binaries (8 sources) for our thin disk L dwarf sample, which results in a slightly older but statistically consistent age of  $4.4 \pm 0.3$  Gyr.

### 6.3. Evidence of a Kinematic Indicator of the Main Sequence Terminus

Kinematic variations as a function of spectral type, rather than across whole subclasses, provides a finer examination of UCD ages. Prior simulation work has predicted subtype age structure particularly among the L dwarfs due to brown dwarf evolutionary effects and the changing mixture of stars and brown dwarfs with spectral type (cf. Burgasser 2004). At late-M and early L subtypes, only the youngest and most massive brown dwarfs will have temperatures consistent with these types, restricting their representation among the overall sample and resulting in a relatively low brown dwarf-to-star ratio. As we proceed to later types, the mass range of stars with the appropriate temperatures declines, while both the age and mass range of allowed brown dwarfs expands, increasing the brown dwarf-to-star ratio. Since these brown dwarfs are preferentially young, this changing ratio drives down the average age of the population. At late enough spectral types, temperatures become sufficiently low that stars are not present, resulting in a “pure” brown dwarf sample that is relatively young but increases in mean age through the T and Y dwarf sequences.

As a preliminary assessment of these effects, we examined a more refined breakdown of L dwarfs by subtype. Figure 29 displays the observed kinematic ages and simulation predictions of thin disk L dwarfs broken down in bins of two subtypes. Both observations and simulations confirm an overall downward trend of age with

later spectral type, declining from  $5.8 \pm 0.6$  Gyr at L1–L2 to  $0.9 \pm 0.7$  Gyr for L8–L9. However, in the L4–L5 and L5–L6 subtypes this downward trend briefly reverses, with the latter having an average age of  $5.4 \pm 1.4$  Gyr. We note that this increase is present even with the removal of both thick-disk and unusually blue L dwarfs, which are clustered among these mid-L subtypes. The simulations show a concurrent reversal in average kinematic age, skewed by an older population of stars near the HBMM. By spectral type L6–L7, the observed kinematic ages drop back to the downward trend line, while the simulations show a more modest decrease in mean age and a broadened distribution of ages overall.

We interpret this newly-discerned “kinematic break” around spectral types L5–L6 to be an observable of the terminus of the stellar Main Sequence. The effective temperature range of L5–L6 dwarfs,  $1500 \text{ K} \lesssim T_{\text{eff}} \lesssim 1600 \text{ K}$  (Filippazzo et al. 2015), corresponds to evolutionary model predictions for the HBMM at ages of 4–5 Gyr (Baraffe et al. 2003), in rough agreement with the average age of the local UCD population. Dupuy & Liu (2017) identify a similar HBMM boundary at slightly earlier spectral types of L3–L5 based on the distribution of 38 dynamical mass measurements from binaries; while Dieterich et al. (2014) anchor the HBMM at  $\sim 2075$  K, corresponding to L1–L2 subtypes, based on an inferred radius minimum. The differences among these empirical indicators of the HBMM may reflect both sample variations and sensitivity to specific brown dwarf indicators. For example, the L1–L2 range may represent a threshold in the brown dwarf-to-star ratio in the field population, while the L5–L6 range represents the disappearance of stars entirely. We emphasize that all of these subtype samples are small and need to be expanded to confirm and quantify these empirical indicators of the transition between stars and brown dwarfs in the Galactic field population.

### 6.4. Refining Constraints on UCD Population Parameters

The segregation of kinematic ages by subtype also provides an opportunity to more finely constrain population parameters, albeit with lower statistical accuracy. In particular, the age distribution of the underlying population plays a specific role in setting the relative balance of stars and brown dwarfs, and the terminus of the Main Sequence, within the L dwarf class. To explore these effects, we compared a subset of our simulations to two subtype breakdowns of our kinematic sample. Following Section 5.4.2, we evaluated variations in SFR and population age with the MF, minimum mass, and evolutionary model fixed to our baseline assumptions.

Here we compare these to our thin disk L dwarf sample in groups of two subtypes, and our overall sample in groups of three subtypes to account for the small sample for T dwarfs. Figures 30 and 31 shows the  $\chi^2$  distributions and best-fit distributions of simulated kinematic ages for these comparisons. For the L dwarf sample, we find the cosmic/9 Gyr SFR/age combination provides the best overall fit, exceeding our baseline model ( $\Delta\text{BIC} > 10$ , highly significant) but consistent with the exponential/9 Gyr ( $\Delta\text{BIC} = 2.3$ , positive) and exponential/12 Gyr ( $\Delta\text{BIC} = 1.0$ , not significant). We can now rule out the cosmic/6 Gyr SFR/age combination by a BIC test ( $\Delta\text{BIC} > 10$ , highly significant). For the UCD sample, the exponential/9 Gyr SFR/age combination provides the best overall fit, exceeding our baseline model ( $\Delta\text{BIC} = 3.2$ , positive) but consistent with the uniform/12 Gyr model ( $\Delta\text{BIC} = 1.4$ , not significant). Therefore, exponential/9 Gyr combination gives consistently the best fit for both forms of sample binning.

The refinement of the population parameters from this analysis is clearly limited, a consequence of the small sample statistics and the necessity to average over spectral types. Nevertheless, these outcomes show that a larger and more complete kinematic sample broken down by subtype could break some of the simulation parameter degeneracies and lead to a well-constrained assessment of the local UCD population properties, particularly in conjunction with other observable distributions such as the luminosity function and independent age or mass diagnostics.

## 7. SUMMARY

The paper has presented new and refined multi-epoch RV and  $v \sin i$  measurements for a total of 37 T dwarfs. In addition to 23 sources without previously reported RV or  $v \sin i$  measurements, we improved the measurements of 14 T dwarfs by reducing RV uncertainties by a factor of 5 and  $v \sin i$  uncertainties by a factor of 3 using a forward-modeling approach.

Our key scientific results are summarized as follows:

1. Most of the local T dwarfs are fast rotators, with a median  $v \sin i$  of  $27 \text{ km s}^{-1}$  independent of T dwarf spectral type, larger than the median rotational velocities of late-M dwarfs ( $12 \text{ km s}^{-1}$ ) and L dwarfs ( $20 \text{ km s}^{-1}$ ). This trend supports prior work indicating that the angular momenta of brown dwarfs are not lost effectively to magnetic winds. In addition, T dwarfs with larger space velocities, which are likely older and more massive, have larger  $v \sin i$  values, which may reflect their larger moments of inertia (resistance to angular

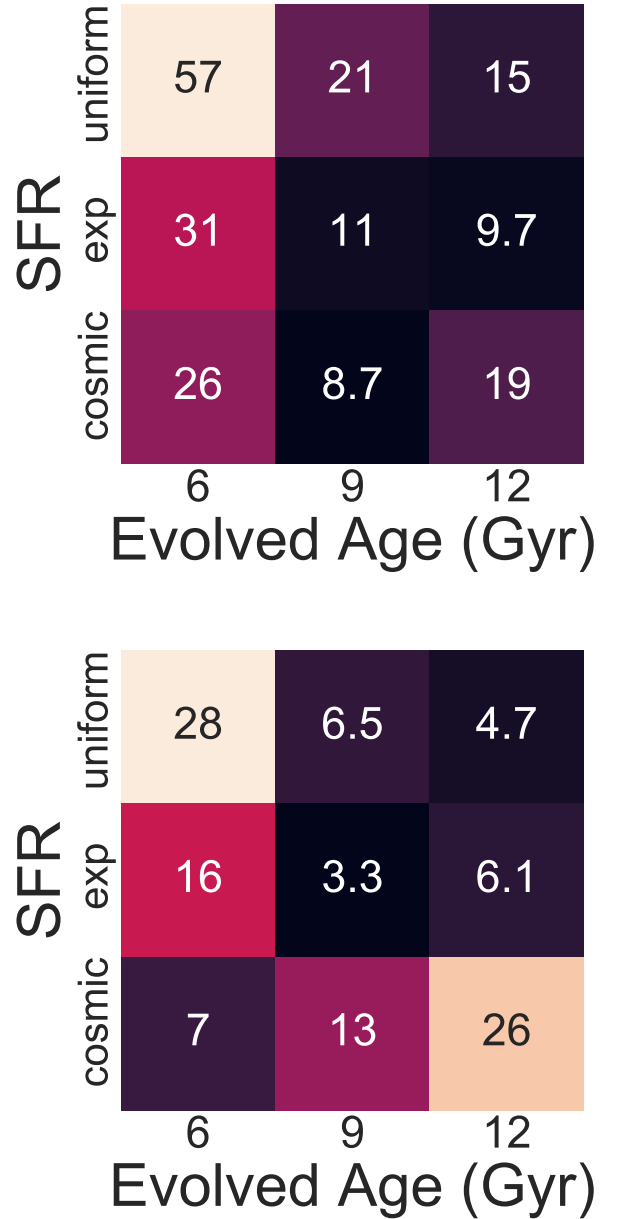


**Figure 30.**  $\chi^2$  distributions of simulated populations as a function of star formation rate (SFR) and evolved age for the L dwarf subtype (top) and UCD subtype samples (bottom). All simulations assume a power-law mass function with  $\alpha = 0.5$ , Baraffe et al. (2003) evolutionary models, and minimum mass of  $0.01 M_\odot$ .

momentum loss) or more compact radii (greater spin-up).

2. Combining our RVs with published and *Gaia* astrometry, we calculated the Galactic  $UVW$  velocities and orbits for our sample. We found that all of our T dwarfs are in the thin disk population; the

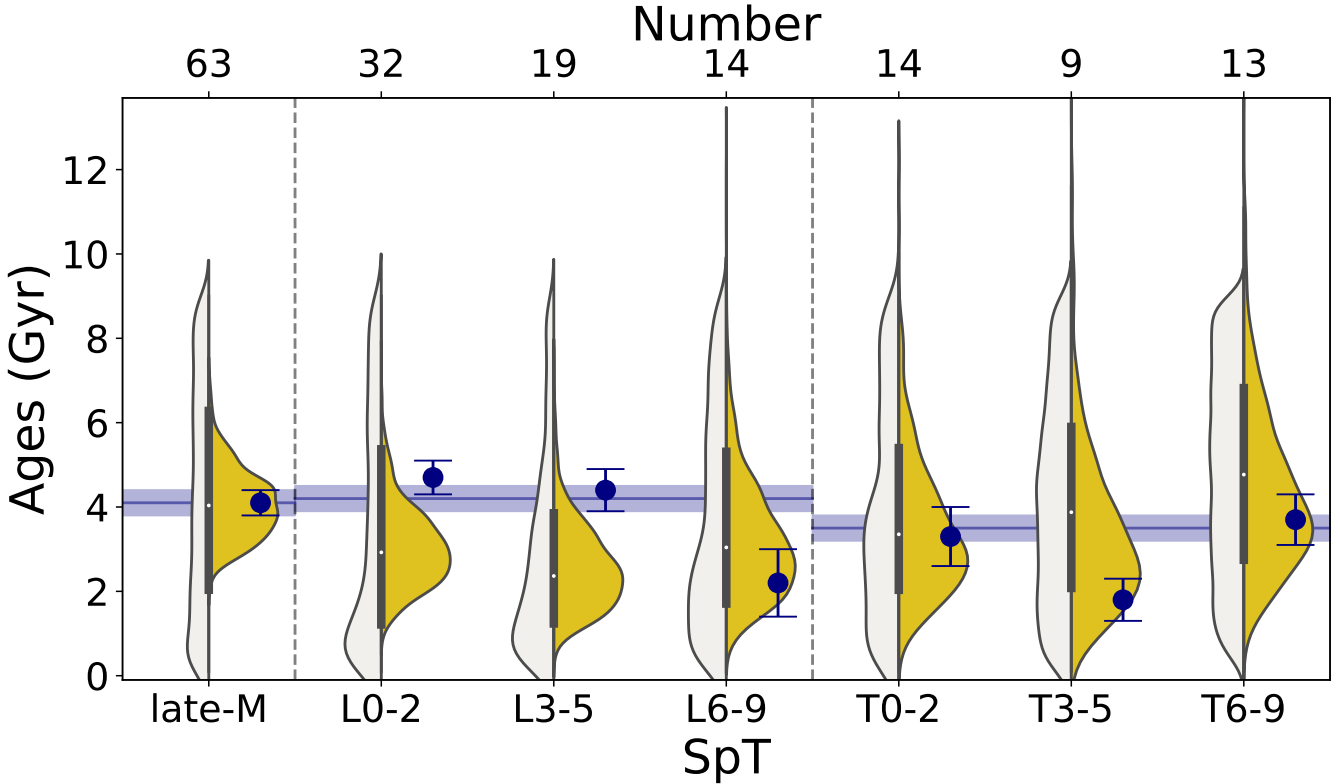


**Figure 31.** Observed kinematic ages of thin-disk UCDs in our kinematic sample grouped into bins of three subtypes (solid blue points) compared to similarly-binned best-fit simulation predictions using a power-law mass function with  $\alpha = 0.5$ , Baraffe et al. (2003) evolutionary models, minimum mass of  $0.01 M_{\odot}$ , the Aumer & Binney (2009) exponential SFR, and a population age of 9 Gyr (white/yellow violin plots for simulated ages/inferred population kinematic ages). The derived kinematic ages and uncertainties for the late-M, L, and T dwarf subgroups are indicated by blue bands. The number of sources in each subtype bin is labeled at top.

one exception in our sample, 2MASS J1331–0116, is an unusually blue L dwarf.

3. We kinematically confirmed two previously-identified, planetary-mass, young moving group members SIMP J0136+0933 (Carina-Near; Gagné et al. 2017) and 2MASS J1324+6358 (AB Doradus; Gagné et al. 2018a). The T4 dwarf 2MASS J0819–0335 and the T6.5+T7.5 binary J1553+1532AB are identified as candidate kinematic members of  $\beta$  Pictoris and Carina-Near moving groups, respectively, but the absence of spectral indicators of youth suggest that these are coincident field brown dwarfs.
4. Among 5 T dwarfs with multiple-epoch RV measurements, we found that two objects exhibited statistically significant RV variability consistent with binary orbital motion: the T0.0+T4.5 spectral binary 2MASS J1106+2754, which has an estimated orbital period of  $3.92^{+0.07}_{-0.09}$  yr and semi-amplitude of  $6.30 \pm 0.05$  km s $^{-1}$ ; and the L7+T3.5 spectral binary 2MASS J2126+7617 with an orbit

period of  $12^{+1.5}_{-1.2}$  yr and semi-amplitude of  $3.0^{+0.7}_{-0.6}$  km s $^{-1}$ . In addition, 2MASS J0559–1404, a suspected overluminous T4.5, shows evidence of RV variability over the course of 20 years, but no clear periodic signal; future observations are needed to confirm and assess the origin of these variations.

5. Using empirical age-velocity dispersion relations, we determined the kinematic age of local T dwarfs to be  $3.5 \pm 0.3$  Gyr, which is consistent with the kinematic age of local late-M dwarfs ( $4.1 \pm 0.3$  Gyr), but considerably younger than the kinematic age of local L dwarfs ( $5.8 \pm 0.3$  Gyr). By excluding likely thick disk population members ( $P(\text{TD})/P(\text{D}) > 1$ ), the kinematic age of local L dwarfs is lowered to  $4.2 \pm 0.3$  Gyr, in line with late-M and T dwarfs. This analysis appears to partly resolve the long-standing kinematic anomaly of local L dwarfs.
6. Population simulations reproduce the measured ages of local thin-disk late-M, L, and T dwarfs, although L dwarf ages are predicted to be younger

than observed. Varying the star formation history, mass function, evolutionary models, maximum age, and minimum mass of these simulations and comparing to our kinematic sample allows us to constrain some of these population parameters, but several degeneracies remain. We are able to rule out mass function evolution (bottom-heavy to top-heavy) as an explanation for old L dwarfs due to disagreement with the T dwarf velocity dispersion, but find tentative evidence of a lower hydrogen burning minimum mass (HBMM). A more refined breakdown in spectral type can improve this analysis, but will require larger samples to make robust constraints.

7. A detailed evaluation of kinematic age as a function of spectral type for L dwarfs reveals a linear trend of decreasing mean age with spectral type, as predicted by population simulations. We also identify an age upturn and sudden break in ages at subtypes L4–L6 which likely reflects the terminus of the stellar Main Sequence. This spectral type range aligns with evolutionary model predictions for the HBMM at an age of 4–5 Gyr.

This study provides a significant expansion in the number and spectral type range of UCDs with precise 6D coordinates, and the inclusion of T dwarfs in particular allows us to constrain many of the underlying population parameters. It has also allowed us to resolve the L dwarf age anomaly and identify empirical diagnostics of brown dwarf evolution and the Main Sequence terminus. However, the size of the current sample remains the primary limitation in precisely quantifying key aspects of this analysis, notably the contaminating fraction of thick disk/blue L dwarfs in the local population, the location and sharpness of the stellar Main Sequence, and degeneracies among simulation parameters. There is considerable capacity to increase the size of the kinematic sample even in the local volume, which is necessary to properly address issues related to completeness, resolution and accuracy in per-spectral-type analyses, as well as the sample bias induced by distinct subpopulations such as blue L dwarfs. Moreover, even a volume-complete 20 pc sample represents a tiny fraction of the Milky Way environment, and it is possible that the immediate local volume around the Sun is not representative of the Galactic disk, a form of cosmic scatter. This motivates a deeper kinematic survey, to 50 pc or 100 pc for example, which may be feasible with future spectroscopic survey facilities or through a more restricted analysis of 2D kinematics (cf. [Faherty et al. 2009](#)). Improvements can also be made to the character-

ization of the UCD kinematic sample. While we specifically evaluated the contributions of young, binary, and unusually blue UCDs, we did not explicitly evaluate or model metallicity or cloud variations or inclination angle, which are of particular importance for the L dwarfs and can influence both empirical calibrations and the underlying evolution of brown dwarfs. There are also improvements to made to the population simulations. We have not explicitly taken into account thick disk or halo populations in the simulation, which are likely well-mixed and not easily separable from the thin disk sample based on simple probability thresholds. There are also spatial-temporal correlations to consider, since sources found closer to the Sun (smaller scaleheights) will be preferentially younger than the broader Milky Way population (cf. [Ryan et al. 2017](#)). All of these considerations are open for exploration in future studies.

*Facility:* Keck: II (NIRSPEC)

*Software:* BANYAN  $\Sigma$  ([Gagné et al. 2018c](#)), Texmaker, Sublime Text, Python, *NumPy* ([van der Walt et al. 2011](#)), *SciPy* ([Virtanen et al. 2019](#)), *Matplotlib* ([Hunter 2007](#)), *pandas* ([Wes McKinney 2010](#)), *seaborn* ([Waskom & the seaborn development team 2020](#)), *Astropy* ([Astropy Collaboration et al. 2013](#)), *wavelets*, *SPLAT* ([Burgasser & Splat Development Team 2017](#)), *emcee* ([Foreman-Mackey et al. 2013](#)), *galpy* ([Bovy 2015](#))

#### ACKNOWLEDGMENTS

The authors thank Maria Rosa Zapatero Osorio and Emily Rice for providing their NIRSPEC data obtained on 2000 June 15 and on 2005 July 19, respectively. The authors also thank Gregory Doppmann, Percy Gomez, Carlos Alvarez, and other Keck Observatory staff and support astronomers for their assistance in obtaining Keck/NIRSPEC observations. C-CH and AJB acknowledge funding support from the National Science Foundation under award No. AST-1517177. The material presented in this paper is based upon work supported by the National Aeronautics and Space Administration under Grant No. NNX15AI75G. Support for this work was provided by NASA through the NASA Hubble Fellowship grant HST-HF2-51447.001-A awarded by the Space Telescope Science Institute, which is operated by the Association of Universities for Research in Astronomy, Inc., for NASA, under contract NAS5-26555. JB acknowledges support from National Science Foundation Graduate Research Fellowship Program grant DGE-1762114. This work utilizes the measurements from 2MASS catalogs and *Gaia* Data Release 2. The authors acknowledge the usefulness of the SIMBAD database and VizieR service. The authors thank the anonymous referee for his/her/their useful review that has improved the original manuscript.

The data presented herein were obtained at the W. M. Keck Observatory, which is operated as a scientific partnership among the California Institute of Technology, the University of California and the National Aeronautics and Space Administration. The Observatory was made possible by the generous financial support of the W. M. Keck Foundation. This research has made use of the Keck Observatory Archive (KOA), which is operated by the W. M. Keck Observatory and the NASA Exoplanet Science Institute (NExScI), under contract with the National Aeronautics and Space Administration. The authors recognize and acknowledge the very significant cultural role and reverence that the summit of Maunakea has with the indigenous Hawaiian community, and that the W. M. Keck Observatory stands on Crown and Government Lands that the State of Hawai'i is obligated to protect and preserve for future generations of indigenous Hawaiians. Portions of this work were conducted at the University of California, San Diego, which was built on the unceded territory of the Kumeyaay Nation, whose people continue to maintain their political sovereignty and cultural traditions as vital members of the San Diego community.

## APPENDIX

A. MINIMUM  $V \sin i$  DETERMINATION

In Section 3.3.4, we described our method to determine the minimum  $v \sin i$ . Here we provide the corresponding diagnostic plots on the minimum  $v \sin i$  values as a function of  $T_{\text{eff}}$  and S/N.

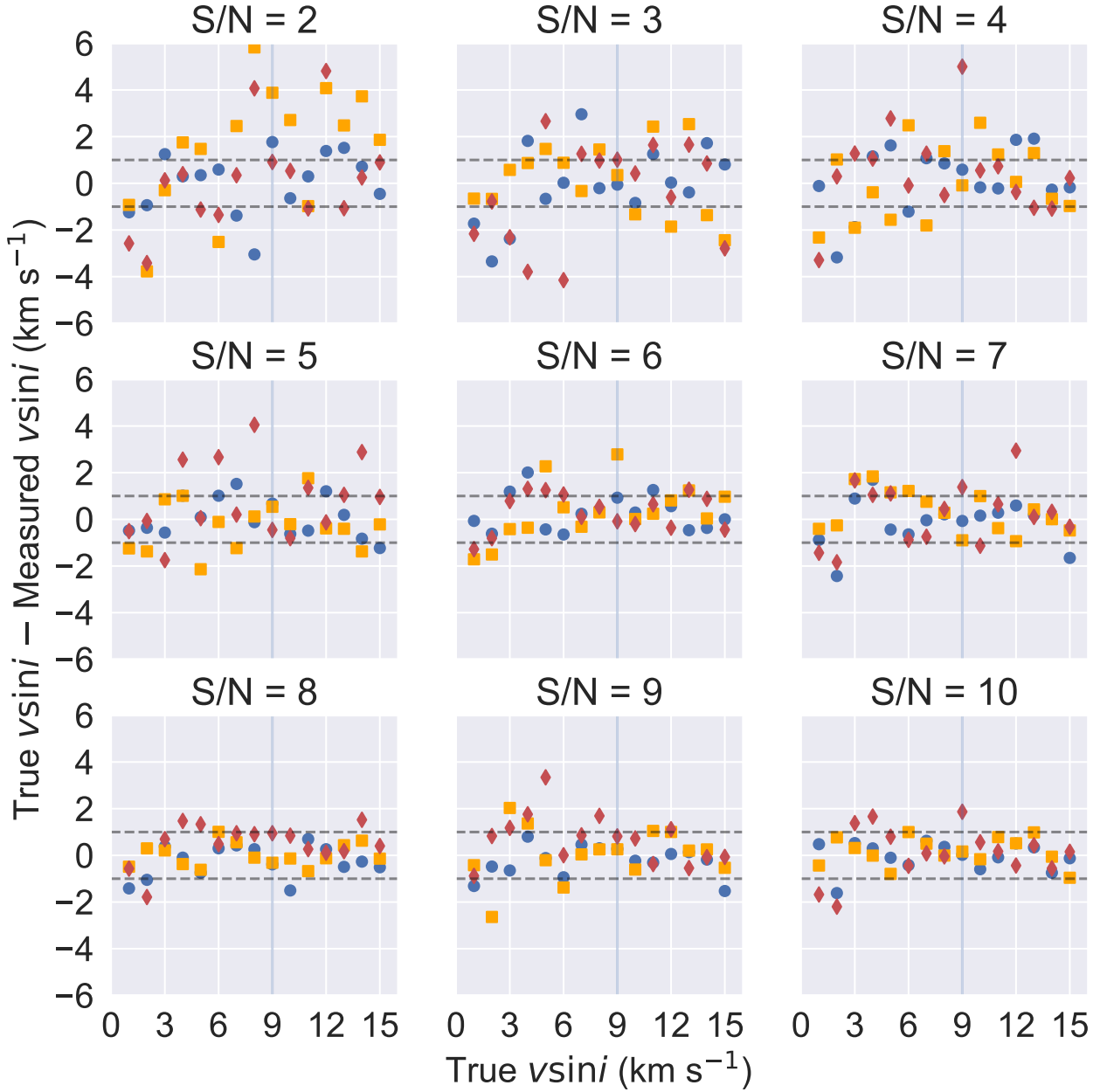


**Figure A1.** The difference between true and measured  $v \sin i$  compared to true  $v \sin i$  values as a function of S/N and  $T_{\text{eff}}$  for BT-Settl models. The  $T_{\text{eff}}$  grid points are 900 K (blue), 1200 K (orange), and 1500 K (red). The grey horizontal dash lines represent  $v \sin i$  difference = 1 km s $^{-1}$ . The vertical blue line indicates the  $v \sin i = 9$  km s $^{-1}$

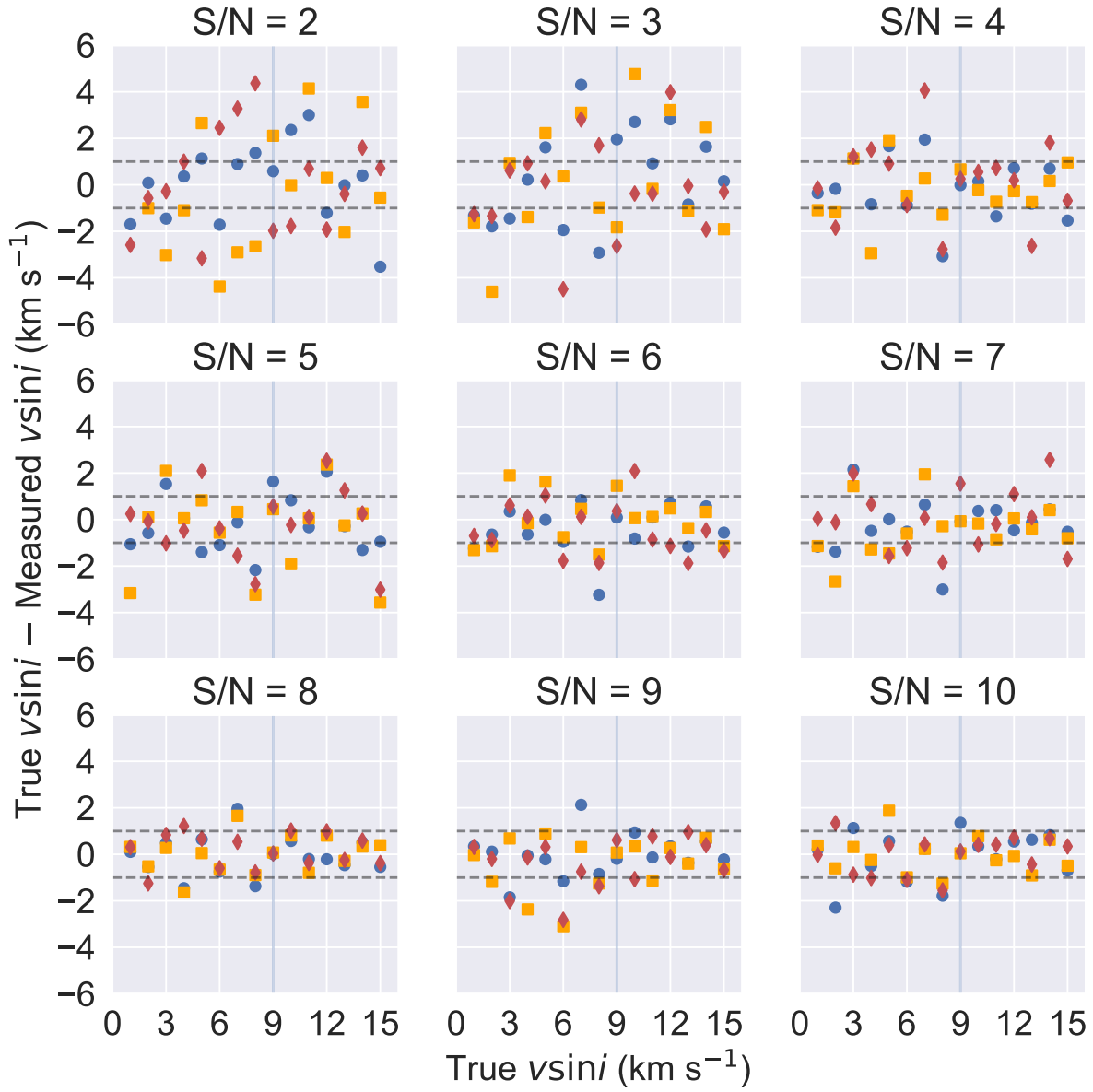


**Figure A2.** Same as Figure A1 for Sonora models.

## B. SIMULATED UCD POPULATION AGES UNDER DIFFERENT ASSUMPTIONS

This Appendix supplements the analysis in Section 5.4.2 by providing the full list of parameters and corresponding  $\chi^2$  fit values for the population simulation examined. Select visualizations of the age distributions and comparative  $\chi^2$  plots are provided in the main text.

**Table B1.** Simulated UCD Population Ages Under Different Assumptions

$\tau$	Star formation	$\alpha$	Models	MBDM	late-M dwarf age	L dwarf age	T dwarf age	$\chi^2$
(Gyr)	(rate)			( $M_\odot$ )	(Gyr)	(Gyr)	(Gyr)	
Observations								
ALL SOURCES .....					4.9 $\pm$ 0.3	7.1 $\pm$ 0.4	3.5 $\pm$ 0.3	...
NOT THICK DISK ( $P(\text{TD})/P(\text{D}) < 10$ ) .....					4.1 $\pm$ 0.3	5.8 $\pm$ 0.3	3.5 $\pm$ 0.3	...
THIN DISK ( $P(\text{TD})/P(\text{D}) < 1$ ) .....					4.1 $\pm$ 0.3	4.2 $\pm$ 0.3	3.5 $\pm$ 0.3	...
Simulations								
$9^a$	uniform	0.5	B03	0.01	4.1 $\pm$ 0.8	3.1 $\pm$ 0.7	4.3 $\pm$ 1.2	2.1
9	uniform	0.5	B01	0.01	3.5 $\pm$ 0.7	3.1 $\pm$ 0.6	4.2 $\pm$ 1.2	3.0
9	uniform	0.5	S08	0.01	4.3 $\pm$ 0.8	3.4 $\pm$ 0.7	4.5 $\pm$ 1.2	1.7
9	uniform	0.5	M19	0.01	1.6 $\pm$ 0.3	3.1 $\pm$ 0.6	4.0 $\pm$ 1.1	42.1
9	uniform	0.5	P20C	0.01	0.2 $\pm$ 0.0	2.6 $\pm$ 0.5	4.2 $\pm$ 1.2	172.0
9	uniform	0.5	P20NW	0.01	0.3 $\pm$ 0.0	2.6 $\pm$ 0.6	4.3 $\pm$ 1.2	162.3
9	uniform	0.5	P20NS	0.01	0.4 $\pm$ 0.0	2.7 $\pm$ 0.6	4.1 $\pm$ 1.2	154.4
9	exponential	0.5	B03	0.01	4.5 $\pm$ 0.8	3.8 $\pm$ 0.8	4.7 $\pm$ 1.2	1.3
9	exponential	0.5	B01	0.01	3.6 $\pm$ 0.6	3.7 $\pm$ 0.7	4.9 $\pm$ 1.4	1.7
9	exponential	0.5	S08	0.01	4.6 $\pm$ 0.8	4.2 $\pm$ 0.8	4.8 $\pm$ 1.2	1.5
9	log-normal	0.5	B03	0.01	6.8 $\pm$ 1.3	6.1 $\pm$ 1.0	6.5 $\pm$ 1.6	11.6
9	log-normal	0.5	B01	0.01	7.4 $\pm$ 1.3	6.0 $\pm$ 1.0	6.2 $\pm$ 1.5	12.7
9	log-normal	0.5	S08	0.01	6.4 $\pm$ 1.0	6.2 $\pm$ 1.1	6.4 $\pm$ 1.6	11.3
9	uniform	-1.5	B03	0.01	4.1 $\pm$ 0.7	3.6 $\pm$ 0.7	5.0 $\pm$ 1.3	1.5
9	uniform	-1.5	B01	0.01	3.6 $\pm$ 0.7	3.7 $\pm$ 0.7	5.1 $\pm$ 1.3	2.0
9	uniform	-1.5	S08	0.01	3.9 $\pm$ 0.6	3.9 $\pm$ 0.7	5.3 $\pm$ 1.2	2.2
9	uniform	-0.5	B03	0.01	4.0 $\pm$ 0.8	3.3 $\pm$ 0.6	5.1 $\pm$ 1.4	2.7
9	uniform	-0.5	B01	0.01	4.0 $\pm$ 0.8	3.2 $\pm$ 0.6	4.6 $\pm$ 1.3	2.2
9	uniform	-0.5	S08	0.01	3.5 $\pm$ 0.6	3.7 $\pm$ 0.7	4.7 $\pm$ 1.3	1.7
9	uniform	1.5	B03	0.01	3.8 $\pm$ 0.7	2.7 $\pm$ 0.6	3.6 $\pm$ 1.0	4.7
9	uniform	1.5	B01	0.01	3.6 $\pm$ 0.6	2.4 $\pm$ 0.5	3.6 $\pm$ 1.1	8.1
9	uniform	1.5	S08	0.01	3.5 $\pm$ 0.5	2.8 $\pm$ 0.6	3.6 $\pm$ 1.0	5.5
$9^b$	uniform	0.0/1.0/3.0	B03	0.01	4.4 $\pm$ 0.9	3.8 $\pm$ 0.7	3.5 $\pm$ 1.0	0.3
9	uniform	0.0/1.0/3.0	B01	0.01	3.6 $\pm$ 0.7	3.1 $\pm$ 0.6	4.0 $\pm$ 1.1	2.6
9	uniform	0.0/1.0/3.0	S08	0.01	5.4 $\pm$ 1.0	3.6 $\pm$ 0.7	3.8 $\pm$ 1.0	2.2
$9^c$	uniform	1.0/0.0/3.0	B03	0.01	3.7 $\pm$ 0.7	3.8 $\pm$ 0.7	4.3 $\pm$ 1.1	0.9
9	uniform	1.0/0.0/3.0	B01	0.01	3.1 $\pm$ 0.7	3.0 $\pm$ 0.6	4.4 $\pm$ 1.2	4.9
9	uniform	1.0/0.0/3.0	S08	0.01	3.8 $\pm$ 0.6	3.1 $\pm$ 0.6	4.8 $\pm$ 1.2	3.3
9	uniform	C03	B03	0.01	3.7 $\pm$ 0.7	2.8 $\pm$ 0.6	4.1 $\pm$ 1.1	4.4
9	uniform	C03	B01	0.01	3.6 $\pm$ 0.7	2.8 $\pm$ 0.6	4.0 $\pm$ 1.2	4.2
9	uniform	C03	S08	0.01	3.6 $\pm$ 0.6	2.8 $\pm$ 0.6	4.2 $\pm$ 1.2	5.2
9	exponential	-1.5	B03	0.01	5.2 $\pm$ 0.9	4.6 $\pm$ 0.9	5.5 $\pm$ 1.4	3.3
9	exponential	-1.5	B01	0.01	4.4 $\pm$ 0.8	4.8 $\pm$ 0.9	5.8 $\pm$ 1.6	2.8
9	exponential	-1.5	S08	0.01	4.8 $\pm$ 0.8	4.6 $\pm$ 0.8	5.2 $\pm$ 1.2	2.9
9	exponential	-0.5	B03	0.01	4.5 $\pm$ 0.8	4.2 $\pm$ 0.7	5.2 $\pm$ 1.5	1.5
9	exponential	-0.5	B01	0.01	4.1 $\pm$ 0.8	3.9 $\pm$ 0.8	5.4 $\pm$ 1.4	1.8
9	exponential	-0.5	S08	0.01	4.3 $\pm$ 0.8	4.4 $\pm$ 0.8	5.2 $\pm$ 1.4	1.6
9	exponential	1.5	B03	0.01	5.1 $\pm$ 0.9	3.6 $\pm$ 0.7	4.2 $\pm$ 1.2	2.0
9	exponential	1.5	B01	0.01	4.7 $\pm$ 1.0	3.3 $\pm$ 0.7	4.3 $\pm$ 1.2	1.9

**Table B1** *continued*

**Table B1** (*continued*)

$\tau$	Star formation	$\alpha$	Models	MBDM	late-M dwarf age	L dwarf age	T dwarf age	$\chi^2$
(Gyr)	(rate)			( $M_\odot$ )	(Gyr)	(Gyr)	(Gyr)	
9	exponential	1.5	S08	0.01	$4.0 \pm 0.5$	$3.8 \pm 0.8$	$4.4 \pm 1.2$	0.6
9	exponential	0.0/1.0/3.0	B03	0.01	$5.3 \pm 1.0$	$5.0 \pm 0.9$	$4.2 \pm 1.2$	2.5
9	exponential	0.0/1.0/3.0	B01	0.01	$3.9 \pm 0.7$	$3.6 \pm 0.7$	$4.5 \pm 1.2$	1.2
9	exponential	0.0/1.0/3.0	S08	0.01	$5.8 \pm 0.9$	$4.2 \pm 0.8$	$4.5 \pm 1.2$	3.9
9	exponential	1.0/0.0/3.0	B03	0.01	$4.2 \pm 0.7$	$4.8 \pm 0.8$	$5.2 \pm 1.3$	2.3
9	exponential	1.0/0.0/3.0	B01	0.01	$4.6 \pm 1.0$	$3.6 \pm 0.7$	$5.1 \pm 1.4$	2.0
9	exponential	1.0/0.0/3.0	S08	0.01	$4.3 \pm 0.8$	$3.8 \pm 0.7$	$5.5 \pm 1.4$	2.1
9	exponential	C03	B03	0.01	$4.5 \pm 0.9$	$3.8 \pm 0.8$	$4.8 \pm 1.3$	1.2
9	exponential	C03	B01	0.01	$3.6 \pm 0.7$	$3.2 \pm 0.6$	$4.6 \pm 1.2$	2.5
9	exponential	C03	S08	0.01	$4.5 \pm 0.7$	$3.9 \pm 0.8$	$4.6 \pm 1.3$	1.1
9	log-normal	-1.5	B03	0.01	$7.1 \pm 1.2$	$6.2 \pm 0.9$	$7.0 \pm 1.7$	14.6
9	log-normal	-1.5	B01	0.01	$6.4 \pm 1.1$	$5.8 \pm 0.8$	$6.6 \pm 1.6$	11.3
9	log-normal	-1.5	S08	0.01	$7.2 \pm 1.0$	$6.9 \pm 1.2$	$6.7 \pm 1.6$	17.5
9	log-normal	-0.5	B03	0.01	$6.9 \pm 1.2$	$6.0 \pm 1.0$	$6.4 \pm 1.5$	11.6
9	log-normal	-0.5	B01	0.01	$6.9 \pm 1.2$	$6.0 \pm 1.1$	$6.2 \pm 1.5$	11.6
9	log-normal	-0.5	S08	0.01	$7.1 \pm 1.1$	$6.0 \pm 0.9$	$6.8 \pm 1.8$	14.6
9	log-normal	1.5	B03	0.01	$6.5 \pm 1.0$	$5.7 \pm 1.0$	$6.1 \pm 1.6$	10.2
9	log-normal	1.5	B01	0.01	$5.7 \pm 0.8$	$5.1 \pm 0.8$	$6.2 \pm 1.6$	7.2
9	log-normal	1.5	S08	0.01	$5.7 \pm 0.8$	$5.6 \pm 0.9$	$6.3 \pm 1.6$	8.9
9	log-normal	0.0/1.0/3.0	B03	0.01	$7.4 \pm 1.2$	$6.0 \pm 0.9$	$6.1 \pm 1.6$	13.9
9	log-normal	0.0/1.0/3.0	B01	0.01	$6.3 \pm 1.0$	$6.3 \pm 1.0$	$6.2 \pm 1.5$	12.0
9	log-normal	0.0/1.0/3.0	S08	0.01	$6.2 \pm 0.9$	$6.3 \pm 1.1$	$6.2 \pm 1.5$	11.9
9	log-normal	1.0/0.0/3.0	B03	0.01	$6.4 \pm 1.1$	$6.1 \pm 0.9$	$6.4 \pm 1.6$	11.6
9	log-normal	1.0/0.0/3.0	B01	0.01	$5.7 \pm 0.9$	$5.8 \pm 1.0$	$6.6 \pm 1.8$	8.4
9	log-normal	1.0/0.0/3.0	S08	0.01	$6.1 \pm 1.0$	$5.8 \pm 1.0$	$6.3 \pm 1.5$	10.3
9	log-normal	C03	B03	0.01	$6.5 \pm 1.1$	$5.6 \pm 0.9$	$6.4 \pm 1.6$	9.6
9	log-normal	C03	B01	0.01	$6.3 \pm 1.0$	$5.1 \pm 0.8$	$6.2 \pm 1.5$	9.0
9	log-normal	C03	S08	0.01	$6.7 \pm 0.8$	$6.1 \pm 1.0$	$6.6 \pm 1.6$	15.4
9	uniform	-1.5	B03	0.02	$4.0 \pm 0.8$	$3.9 \pm 0.7$	$5.0 \pm 1.3$	1.4
9	uniform	-1.5	B03	0.03	$4.0 \pm 0.8$	$3.5 \pm 0.6$	$5.1 \pm 1.3$	2.3
9	uniform	-1.5	B01	0.02	$3.6 \pm 0.7$	$3.9 \pm 0.7$	$4.8 \pm 1.3$	1.7
9	uniform	-1.5	B01	0.03	$3.9 \pm 0.7$	$4.1 \pm 0.7$	$5.2 \pm 1.2$	2.1
9	uniform	-1.5	S08	0.02	$4.1 \pm 0.7$	$4.0 \pm 0.7$	$5.5 \pm 1.4$	2.0
9	uniform	-1.5	S08	0.03	$3.4 \pm 0.6$	$3.6 \pm 0.7$	$5.6 \pm 1.5$	3.2
9	uniform	0.5	B03	0.02	$4.2 \pm 0.8$	$3.1 \pm 0.6$	$4.9 \pm 1.4$	3.0
9	uniform	0.5	B03	0.03	$4.0 \pm 0.8$	$3.3 \pm 0.7$	$5.2 \pm 1.4$	2.5
9	uniform	0.5	B01	0.02	$3.4 \pm 0.7$	$3.1 \pm 0.6$	$4.5 \pm 1.2$	3.3
9	uniform	0.5	B01	0.03	$3.2 \pm 0.7$	$3.0 \pm 0.6$	$4.7 \pm 1.3$	4.9
9	uniform	0.5	S08	0.02	$4.1 \pm 0.8$	$3.1 \pm 0.6$	$4.5 \pm 1.2$	2.4
9	uniform	0.5	S08	0.03	$3.6 \pm 0.7$	$3.3 \pm 0.6$	$5.0 \pm 1.3$	3.2
9	uniform	-0.5	B03	0.02	$4.2 \pm 0.8$	$3.5 \pm 0.7$	$5.0 \pm 1.3$	1.8
9	uniform	-0.5	B03	0.03	$4.2 \pm 0.8$	$3.6 \pm 0.7$	$5.2 \pm 1.3$	2.1
9	uniform	-0.5	B01	0.02	$3.3 \pm 0.7$	$3.5 \pm 0.7$	$4.9 \pm 1.3$	2.9
9	uniform	-0.5	B01	0.03	$4.1 \pm 0.9$	$3.6 \pm 0.8$	$4.9 \pm 1.3$	1.5
9	uniform	-0.5	S08	0.02	$4.0 \pm 0.8$	$3.7 \pm 0.7$	$4.9 \pm 1.3$	1.5
9	uniform	-0.5	S08	0.03	$3.6 \pm 0.6$	$3.8 \pm 0.7$	$5.5 \pm 1.4$	2.5
9	uniform	1.5	B03	0.02	$4.0 \pm 0.8$	$2.6 \pm 0.6$	$4.3 \pm 1.2$	5.3
9	uniform	1.5	B03	0.03	$4.1 \pm 0.8$	$2.7 \pm 0.6$	$4.8 \pm 1.3$	5.8
9	uniform	1.5	B01	0.02	$3.3 \pm 0.7$	$2.5 \pm 0.6$	$4.1 \pm 1.2$	7.5
9	uniform	1.5	B01	0.03	$3.1 \pm 0.6$	$2.6 \pm 0.6$	$4.7 \pm 1.2$	8.6
9	uniform	1.5	S08	0.02	$3.3 \pm 0.6$	$3.0 \pm 0.6$	$4.2 \pm 1.2$	4.4
9	uniform	1.5	S08	0.03	$4.0 \pm 0.8$	$3.0 \pm 0.6$	$4.8 \pm 1.2$	3.8

**Table B1** *continued*

**Table B1** (*continued*)

$\tau$	Star formation	$\alpha$	Models	MBDM	late-M dwarf age	L dwarf age	T dwarf age	$\chi^2$
(Gyr)	(rate)			( $M_\odot$ )	(Gyr)	(Gyr)	(Gyr)	
9	uniform	0.0/1.0/3.0	B03	0.02	$4.5 \pm 0.9$	$3.2 \pm 0.6$	$4.1 \pm 1.1$	2.1
9	uniform	0.0/1.0/3.0	B03	0.03	$4.2 \pm 0.9$	$3.6 \pm 0.7$	$4.4 \pm 1.1$	0.9
9	uniform	0.0/1.0/3.0	B01	0.02	$3.7 \pm 0.8$	$3.1 \pm 0.6$	$4.2 \pm 1.2$	2.6
9	uniform	0.0/1.0/3.0	B01	0.03	$3.3 \pm 0.7$	$2.8 \pm 0.6$	$4.4 \pm 1.2$	5.9
9	uniform	0.0/1.0/3.0	S08	0.02	$3.5 \pm 0.6$	$3.0 \pm 0.6$	$4.3 \pm 1.2$	3.4
9	uniform	0.0/1.0/3.0	S08	0.03	$4.2 \pm 0.8$	$3.2 \pm 0.6$	$4.4 \pm 1.1$	2.2
9	uniform	1.0/0.0/3.0	B03	0.02	$3.7 \pm 0.7$	$3.8 \pm 0.7$	$5.2 \pm 1.4$	2.0
9	uniform	1.0/0.0/3.0	B03	0.03	$3.8 \pm 0.8$	$4.0 \pm 0.7$	$5.5 \pm 1.4$	2.0
9	uniform	1.0/0.0/3.0	B01	0.02	$3.0 \pm 0.6$	$3.0 \pm 0.6$	$4.8 \pm 1.3$	5.8
9	uniform	1.0/0.0/3.0	B01	0.03	$3.5 \pm 0.7$	$3.3 \pm 0.7$	$5.4 \pm 1.4$	3.5
9	uniform	1.0/0.0/3.0	S08	0.02	$3.4 \pm 0.6$	$3.4 \pm 0.6$	$4.9 \pm 1.2$	3.7
9	uniform	1.0/0.0/3.0	S08	0.03	$3.8 \pm 0.7$	$3.6 \pm 0.7$	$5.6 \pm 1.4$	2.6
9	uniform	C03	B03	0.02	$3.6 \pm 0.7$	$2.7 \pm 0.6$	$4.6 \pm 1.2$	5.7
9	uniform	C03	B03	0.03	$4.0 \pm 0.8$	$2.9 \pm 0.6$	$5.0 \pm 1.3$	4.4
9	uniform	C03	B01	0.02	$3.5 \pm 0.7$	$2.5 \pm 0.6$	$4.2 \pm 1.2$	7.6
9	uniform	C03	B01	0.03	$3.2 \pm 0.7$	$2.6 \pm 0.5$	$4.6 \pm 1.2$	8.6
9	uniform	C03	S08	0.02	$3.2 \pm 0.5$	$3.0 \pm 0.6$	$4.4 \pm 1.2$	5.0
9	uniform	C03	S08	0.03	$4.2 \pm 0.8$	$3.1 \pm 0.6$	$5.0 \pm 1.3$	3.7
9	exponential	-1.5	B03	0.02	$4.8 \pm 0.9$	$4.5 \pm 0.8$	$5.9 \pm 1.5$	3.3
9	exponential	-1.5	B03	0.03	$5.1 \pm 1.0$	$4.8 \pm 0.8$	$5.5 \pm 1.4$	3.7
9	exponential	-1.5	B01	0.02	$4.7 \pm 0.9$	$4.0 \pm 0.7$	$5.4 \pm 1.3$	2.4
9	exponential	-1.5	B01	0.03	$3.7 \pm 0.6$	$4.3 \pm 0.8$	$5.2 \pm 1.2$	2.2
9	exponential	-1.5	S08	0.02	$4.6 \pm 0.7$	$4.4 \pm 0.8$	$5.3 \pm 1.2$	2.5
9	exponential	-1.5	S08	0.03	$4.2 \pm 0.7$	$4.9 \pm 0.8$	$5.9 \pm 1.5$	3.4
9	exponential	0.5	B03	0.02	$4.6 \pm 0.9$	$4.2 \pm 0.8$	$5.1 \pm 1.3$	1.6
9	exponential	0.5	B03	0.03	$4.9 \pm 1.0$	$3.9 \pm 0.8$	$5.4 \pm 1.3$	2.6
9	exponential	0.5	B01	0.02	$4.5 \pm 0.7$	$4.1 \pm 0.7$	$5.0 \pm 1.4$	1.4
9	exponential	0.5	B01	0.03	$4.2 \pm 0.9$	$4.0 \pm 0.8$	$5.3 \pm 1.3$	1.8
9	exponential	0.5	S08	0.02	$4.7 \pm 0.7$	$4.1 \pm 0.8$	$5.3 \pm 1.4$	2.2
9	exponential	0.5	S08	0.03	$4.5 \pm 0.9$	$4.0 \pm 0.7$	$5.6 \pm 1.4$	2.4
9	exponential	-0.5	B03	0.02	$4.8 \pm 0.9$	$4.5 \pm 0.8$	$5.6 \pm 1.5$	2.6
9	exponential	-0.5	B03	0.03	$4.9 \pm 1.0$	$4.4 \pm 0.8$	$5.5 \pm 1.3$	3.1
9	exponential	-0.5	B01	0.02	$4.0 \pm 0.7$	$4.2 \pm 0.8$	$5.3 \pm 1.4$	1.5
9	exponential	-0.5	B01	0.03	$4.1 \pm 0.8$	$3.8 \pm 0.7$	$5.6 \pm 1.4$	2.3
9	exponential	-0.5	S08	0.02	$5.1 \pm 0.9$	$4.0 \pm 0.7$	$5.2 \pm 1.4$	2.7
9	exponential	-0.5	S08	0.03	$4.5 \pm 0.8$	$4.4 \pm 0.8$	$6.1 \pm 1.6$	3.1
9	exponential	1.5	B03	0.02	$4.2 \pm 0.8$	$3.5 \pm 0.6$	$4.8 \pm 1.3$	1.8
9	exponential	1.5	B03	0.03	$4.8 \pm 0.9$	$3.5 \pm 0.8$	$5.3 \pm 1.4$	2.9
9	exponential	1.5	B01	0.02	$3.6 \pm 0.6$	$3.0 \pm 0.6$	$4.8 \pm 1.3$	4.4
9	exponential	1.5	B01	0.03	$4.4 \pm 0.8$	$3.3 \pm 0.6$	$5.2 \pm 1.3$	3.1
9	exponential	1.5	S08	0.02	$4.7 \pm 0.6$	$3.7 \pm 0.7$	$4.8 \pm 1.3$	1.8
9	exponential	1.5	S08	0.03	$5.5 \pm 1.1$	$3.7 \pm 0.7$	$5.6 \pm 1.5$	3.8
9	exponential	0.0/1.0/3.0	B03	0.02	$4.9 \pm 0.8$	$4.3 \pm 0.8$	$4.6 \pm 1.2$	1.5
9	exponential	0.0/1.0/3.0	B03	0.03	$4.8 \pm 0.9$	$4.2 \pm 0.8$	$4.8 \pm 1.2$	1.6
9	exponential	0.0/1.0/3.0	B01	0.02	$4.2 \pm 0.8$	$3.7 \pm 0.7$	$4.8 \pm 1.3$	1.3
9	exponential	0.0/1.0/3.0	B01	0.03	$4.4 \pm 0.9$	$3.6 \pm 0.7$	$5.3 \pm 1.4$	2.0
9	exponential	0.0/1.0/3.0	S08	0.02	$5.4 \pm 0.9$	$4.0 \pm 0.7$	$4.9 \pm 1.3$	2.8
9	exponential	0.0/1.0/3.0	S08	0.03	$4.7 \pm 0.8$	$4.0 \pm 0.8$	$5.3 \pm 1.4$	1.9
9	exponential	1.0/0.0/3.0	B03	0.02	$4.7 \pm 0.9$	$4.7 \pm 0.8$	$5.6 \pm 1.4$	3.0
9	exponential	1.0/0.0/3.0	B03	0.03	$4.7 \pm 0.8$	$4.9 \pm 0.9$	$5.8 \pm 1.5$	3.4
9	exponential	1.0/0.0/3.0	B01	0.02	$4.2 \pm 0.8$	$3.6 \pm 0.8$	$5.3 \pm 1.3$	2.3
9	exponential	1.0/0.0/3.0	B01	0.03	$4.2 \pm 0.8$	$3.9 \pm 0.7$	$5.5 \pm 1.3$	2.3

**Table B1** *continued*

**Table B1** (*continued*)

$\tau$	Star formation	$\alpha$	Models	MBDM	late-M dwarf age	L dwarf age	T dwarf age	$\chi^2$
(Gyr)	(rate)			( $M_\odot$ )	(Gyr)	(Gyr)	(Gyr)	
9	exponential	1.0/0.0/3.0	S08	0.02	4.6 ± 0.8	4.1 ± 0.8	5.8 ± 1.5	2.7
9	exponential	1.0/0.0/3.0	S08	0.03	3.7 ± 0.6	4.2 ± 0.8	6.4 ± 1.6	3.7
9	exponential	C03	B03	0.02	4.4 ± 0.9	3.5 ± 0.7	4.9 ± 1.3	1.9
9	exponential	C03	B03	0.03	4.6 ± 0.9	3.9 ± 0.8	5.6 ± 1.4	2.4
9	exponential	C03	B01	0.02	4.8 ± 0.9	3.4 ± 0.6	5.0 ± 1.4	2.5
9	exponential	C03	B01	0.03	4.3 ± 0.9	3.2 ± 0.6	5.4 ± 1.4	3.2
9	exponential	C03	S08	0.02	3.4 ± 0.6	3.9 ± 0.8	5.1 ± 1.3	2.7
9	exponential	C03	S08	0.03	4.5 ± 0.7	3.9 ± 0.8	5.6 ± 1.4	2.4
9	log-normal	-1.5	B03	0.02	6.6 ± 1.2	6.1 ± 1.0	6.7 ± 1.6	11.8
9	log-normal	-1.5	B03	0.03	6.5 ± 1.1	6.2 ± 1.0	6.9 ± 1.7	12.0
9	log-normal	-1.5	B01	0.02	6.6 ± 1.1	6.1 ± 1.0	6.9 ± 1.6	12.3
9	log-normal	-1.5	B01	0.03	6.2 ± 1.1	6.4 ± 1.0	6.7 ± 1.7	11.2
9	log-normal	-1.5	S08	0.02	6.9 ± 1.1	6.6 ± 1.0	6.5 ± 1.5	15.9
9	log-normal	-1.5	S08	0.03	6.7 ± 1.0	6.2 ± 1.0	6.6 ± 1.6	13.8
9	log-normal	0.5	B03	0.02	6.8 ± 1.1	5.8 ± 0.9	6.2 ± 1.5	11.8
9	log-normal	0.5	B03	0.03	5.9 ± 0.9	6.2 ± 1.0	6.9 ± 1.7	10.8
9	log-normal	0.5	B01	0.02	5.7 ± 0.8	5.8 ± 0.9	6.3 ± 1.5	9.9
9	log-normal	0.5	B01	0.03	6.2 ± 1.0	6.0 ± 1.0	6.6 ± 1.6	11.1
9	log-normal	0.5	S08	0.02	6.7 ± 1.0	6.0 ± 1.0	6.6 ± 1.6	12.9
9	log-normal	0.5	S08	0.03	5.7 ± 0.8	6.4 ± 1.1	6.6 ± 1.6	11.0
9	log-normal	-0.5	B03	0.02	6.2 ± 1.1	6.5 ± 1.0	6.6 ± 1.7	12.0
9	log-normal	-0.5	B03	0.03	6.5 ± 1.0	6.2 ± 0.9	6.6 ± 1.6	13.0
9	log-normal	-0.5	B01	0.02	6.6 ± 1.2	6.5 ± 1.1	6.5 ± 1.6	11.8
9	log-normal	-0.5	B01	0.03	5.8 ± 0.9	6.3 ± 1.0	6.9 ± 1.7	11.6
9	log-normal	-0.5	S08	0.02	5.5 ± 0.9	6.2 ± 0.9	6.4 ± 1.6	9.8
9	log-normal	-0.5	S08	0.03	6.4 ± 1.0	6.5 ± 1.2	6.8 ± 1.7	12.1
9	log-normal	1.5	B03	0.02	6.6 ± 1.2	5.7 ± 1.0	6.2 ± 1.6	9.7
9	log-normal	1.5	B03	0.03	6.5 ± 1.1	5.6 ± 0.9	6.8 ± 1.6	11.0
9	log-normal	1.5	B01	0.02	6.0 ± 1.0	6.0 ± 0.9	6.3 ± 1.6	10.4
9	log-normal	1.5	B01	0.03	5.2 ± 0.9	5.8 ± 1.0	6.4 ± 1.6	7.3
9	log-normal	1.5	S08	0.02	6.9 ± 1.2	5.4 ± 0.9	6.2 ± 1.6	9.7
9	log-normal	1.5	S08	0.03	6.5 ± 1.0	6.1 ± 1.0	6.8 ± 1.7	12.4
9	log-normal	0.0/1.0/3.0	B03	0.02	7.0 ± 1.3	6.4 ± 1.0	6.0 ± 1.5	12.3
9	log-normal	0.0/1.0/3.0	B03	0.03	6.6 ± 1.1	6.7 ± 1.1	6.3 ± 1.6	12.8
9	log-normal	0.0/1.0/3.0	B01	0.02	6.8 ± 1.1	5.8 ± 0.8	6.0 ± 1.5	12.0
9	log-normal	0.0/1.0/3.0	B01	0.03	6.0 ± 0.9	5.7 ± 1.0	6.4 ± 1.6	9.0
9	log-normal	0.0/1.0/3.0	S08	0.02	5.7 ± 0.9	6.1 ± 1.1	6.2 ± 1.5	9.1
9	log-normal	0.0/1.0/3.0	S08	0.03	7.8 ± 1.3	5.8 ± 1.0	6.6 ± 1.5	14.6
9	log-normal	1.0/0.0/3.0	B03	0.02	6.2 ± 1.0	6.4 ± 1.0	6.4 ± 1.6	11.6
9	log-normal	1.0/0.0/3.0	B03	0.03	6.6 ± 1.1	6.8 ± 1.1	7.0 ± 1.7	14.9
9	log-normal	1.0/0.0/3.0	B01	0.02	5.5 ± 0.8	5.6 ± 0.9	6.5 ± 1.6	8.6
9	log-normal	1.0/0.0/3.0	B01	0.03	6.4 ± 1.0	5.7 ± 0.9	7.2 ± 1.8	11.5
9	log-normal	1.0/0.0/3.0	S08	0.02	6.3 ± 0.9	5.8 ± 1.0	6.7 ± 1.6	11.6
9	log-normal	1.0/0.0/3.0	S08	0.03	7.4 ± 1.3	6.2 ± 1.0	7.0 ± 1.7	14.5
9	log-normal	C03	B03	0.02	6.1 ± 1.1	5.4 ± 0.9	6.4 ± 1.5	8.5
9	log-normal	C03	B03	0.03	6.3 ± 1.1	5.8 ± 1.0	6.9 ± 1.7	10.2
9	log-normal	C03	B01	0.02	6.7 ± 1.1	5.0 ± 0.8	6.5 ± 1.7	9.7
9	log-normal	C03	B01	0.03	6.8 ± 1.2	6.0 ± 1.1	6.6 ± 1.6	11.5
9	log-normal	C03	S08	0.02	5.6 ± 0.9	5.6 ± 0.9	6.3 ± 1.6	7.9
9	log-normal	C03	S08	0.03	5.7 ± 0.9	5.9 ± 1.0	6.8 ± 1.7	9.8
6	uniform	0.5	B03	0.01	2.8 ± 0.6	2.2 ± 0.4	3.0 ± 0.8	18.1
6	uniform	0.5	B01	0.01	1.9 ± 0.4	2.4 ± 0.5	3.0 ± 0.9	28.6

**Table B1** *continued*

**Table B1** (*continued*)

$\tau$	Star formation	$\alpha$	Models	MBDM	late-M dwarf age	L dwarf age	T dwarf age	$\chi^2$
(Gyr)	(rate)			( $M_\odot$ )	(Gyr)	(Gyr)	(Gyr)	
6	uniform	0.5	S08	0.01	$2.7 \pm 0.5$	$2.2 \pm 0.5$	$3.0 \pm 0.9$	16.5
6	uniform	0.5	M19	0.01	$1.2 \pm 0.2$	$2.2 \pm 0.4$	$2.9 \pm 0.8$	72.8
6	uniform	0.5	P20C	0.01	$0.4 \pm 0.0$	$2.0 \pm 0.4$	$3.0 \pm 0.8$	164.1
6	uniform	0.5	P20NW	0.01	$0.3 \pm 0.0$	$2.0 \pm 0.4$	$3.0 \pm 0.8$	173.3
6	uniform	0.5	P20NS	0.01	$0.2 \pm 0.0$	$1.8 \pm 0.4$	$2.9 \pm 0.8$	189.3
6	exponential	0.5	B03	0.01	$3.0 \pm 0.6$	$2.5 \pm 0.5$	$3.2 \pm 0.9$	10.4
6	exponential	0.5	B01	0.01	$2.6 \pm 0.6$	$2.4 \pm 0.4$	$3.2 \pm 0.9$	16.2
6	exponential	0.5	S08	0.01	$3.2 \pm 0.6$	$2.7 \pm 0.6$	$3.2 \pm 0.9$	6.7
6	log-normal	0.5	B03	0.01	$3.6 \pm 0.6$	$3.2 \pm 0.6$	$3.9 \pm 1.1$	2.4
6	log-normal	0.5	B01	0.01	$3.4 \pm 0.6$	$3.2 \pm 0.6$	$3.7 \pm 1.0$	3.1
6	log-normal	0.5	S08	0.01	$3.7 \pm 0.7$	$3.3 \pm 0.6$	$3.5 \pm 0.9$	1.7
6	uniform	-1.5	B03	0.01	$2.8 \pm 0.6$	$2.8 \pm 0.5$	$3.8 \pm 1.0$	9.0
6	uniform	-1.5	B01	0.01	$2.5 \pm 0.5$	$2.6 \pm 0.5$	$3.8 \pm 1.1$	14.2
6	uniform	-1.5	S08	0.01	$2.3 \pm 0.4$	$2.7 \pm 0.5$	$3.8 \pm 1.1$	17.9
6	uniform	-0.5	B03	0.01	$2.8 \pm 0.6$	$2.5 \pm 0.5$	$3.4 \pm 1.0$	11.3
6	uniform	-0.5	B01	0.01	$2.1 \pm 0.5$	$2.3 \pm 0.4$	$3.1 \pm 0.9$	24.7
6	uniform	-0.5	S08	0.01	$2.6 \pm 0.5$	$2.8 \pm 0.6$	$3.4 \pm 0.9$	10.2
6	uniform	1.5	B03	0.01	$2.2 \pm 0.4$	$1.7 \pm 0.4$	$2.5 \pm 0.7$	38.3
6	uniform	1.5	B01	0.01	$2.4 \pm 0.6$	$1.8 \pm 0.4$	$2.6 \pm 0.8$	27.5
6	uniform	1.5	S08	0.01	$1.7 \pm 0.4$	$2.0 \pm 0.4$	$2.6 \pm 0.8$	44.9
6	uniform	0.0/1.0/3.0	B03	0.01	$2.9 \pm 0.6$	$2.6 \pm 0.5$	$2.4 \pm 0.7$	12.5
6	uniform	0.0/1.0/3.0	B01	0.01	$2.3 \pm 0.4$	$2.4 \pm 0.5$	$2.6 \pm 0.8$	20.4
6	uniform	0.0/1.0/3.0	S08	0.01	$3.1 \pm 0.6$	$2.3 \pm 0.5$	$2.6 \pm 0.8$	12.3
6	uniform	1.0/0.0/3.0	B03	0.01	$2.4 \pm 0.5$	$2.4 \pm 0.5$	$3.2 \pm 0.8$	18.1
6	uniform	1.0/0.0/3.0	B01	0.01	$2.0 \pm 0.4$	$2.2 \pm 0.4$	$3.1 \pm 0.8$	31.8
6	uniform	1.0/0.0/3.0	S08	0.01	$2.1 \pm 0.4$	$2.3 \pm 0.5$	$3.4 \pm 1.0$	23.8
6	uniform	C03	B03	0.01	$2.4 \pm 0.6$	$1.9 \pm 0.4$	$2.8 \pm 0.8$	24.7
6	uniform	C03	B01	0.01	$2.0 \pm 0.4$	$1.8 \pm 0.4$	$2.9 \pm 0.8$	38.7
6	uniform	C03	S08	0.01	$2.4 \pm 0.4$	$2.1 \pm 0.4$	$3.0 \pm 0.9$	27.3
6	exponential	-1.5	B03	0.01	$2.9 \pm 0.6$	$3.0 \pm 0.5$	$3.8 \pm 0.9$	6.8
6	exponential	-1.5	B01	0.01	$2.8 \pm 0.5$	$2.7 \pm 0.5$	$3.9 \pm 1.0$	11.0
6	exponential	-1.5	S08	0.01	$2.6 \pm 0.5$	$3.1 \pm 0.6$	$4.0 \pm 1.0$	9.0
6	exponential	-0.5	B03	0.01	$3.1 \pm 0.6$	$2.8 \pm 0.6$	$3.8 \pm 1.0$	6.2
6	exponential	-0.5	B01	0.01	$2.7 \pm 0.6$	$2.9 \pm 0.6$	$3.4 \pm 0.9$	8.9
6	exponential	-0.5	S08	0.01	$2.7 \pm 0.5$	$2.7 \pm 0.5$	$3.8 \pm 0.9$	10.7
6	exponential	1.5	B03	0.01	$2.9 \pm 0.5$	$2.1 \pm 0.4$	$2.9 \pm 0.8$	20.2
6	exponential	1.5	B01	0.01	$2.2 \pm 0.4$	$1.9 \pm 0.4$	$2.7 \pm 0.8$	33.1
6	exponential	1.5	S08	0.01	$2.5 \pm 0.4$	$2.2 \pm 0.4$	$2.9 \pm 0.9$	22.8
6	exponential	0.0/1.0/3.0	B03	0.01	$3.1 \pm 0.6$	$3.0 \pm 0.6$	$2.7 \pm 0.8$	5.6
6	exponential	0.0/1.0/3.0	B01	0.01	$2.6 \pm 0.5$	$2.4 \pm 0.5$	$2.9 \pm 0.8$	16.2
6	exponential	0.0/1.0/3.0	S08	0.01	$3.6 \pm 0.6$	$2.5 \pm 0.5$	$2.9 \pm 0.8$	8.5
6	exponential	1.0/0.0/3.0	B03	0.01	$2.6 \pm 0.5$	$2.5 \pm 0.5$	$3.6 \pm 1.0$	14.2
6	exponential	1.0/0.0/3.0	B01	0.01	$2.2 \pm 0.4$	$2.5 \pm 0.5$	$3.4 \pm 0.9$	18.8
6	exponential	1.0/0.0/3.0	S08	0.01	$2.9 \pm 0.5$	$2.6 \pm 0.5$	$3.7 \pm 1.0$	10.3
6	exponential	C03	B03	0.01	$3.1 \pm 0.6$	$2.3 \pm 0.4$	$3.1 \pm 0.9$	14.1
6	exponential	C03	B01	0.01	$2.3 \pm 0.5$	$2.0 \pm 0.4$	$3.0 \pm 0.8$	25.3
6	exponential	C03	S08	0.01	$2.9 \pm 0.5$	$2.3 \pm 0.5$	$3.2 \pm 0.9$	14.8
6	log-normal	-1.5	B03	0.01	$3.8 \pm 0.8$	$3.6 \pm 0.6$	$4.2 \pm 1.0$	1.1
6	log-normal	-1.5	B01	0.01	$3.5 \pm 0.6$	$3.5 \pm 0.6$	$4.1 \pm 1.0$	1.9
6	log-normal	-1.5	S08	0.01	$3.5 \pm 0.6$	$3.5 \pm 0.6$	$4.2 \pm 1.0$	2.0
6	log-normal	-0.5	B03	0.01	$3.7 \pm 0.7$	$3.6 \pm 0.6$	$4.0 \pm 1.1$	0.9
6	log-normal	-0.5	B01	0.01	$3.4 \pm 0.6$	$3.4 \pm 0.6$	$4.0 \pm 1.0$	2.7

**Table B1** *continued*

**Table B1** (*continued*)

$\tau$	Star formation	$\alpha$	Models	MBDM	late-M dwarf age	L dwarf age	T dwarf age	$\chi^2$
(Gyr)	(rate)			( $M_\odot$ )	(Gyr)	(Gyr)	(Gyr)	
6	log-normal	-0.5	S08	0.01	$3.6 \pm 0.6$	$3.6 \pm 0.6$	$4.0 \pm 1.0$	1.3
6	log-normal	1.5	B03	0.01	$4.1 \pm 0.7$	$3.0 \pm 0.5$	$3.5 \pm 1.0$	3.0
6	log-normal	1.5	B01	0.01	$3.2 \pm 0.6$	$2.9 \pm 0.6$	$3.5 \pm 1.0$	5.1
6	log-normal	1.5	S08	0.01	$3.7 \pm 0.5$	$3.1 \pm 0.6$	$3.4 \pm 0.9$	2.8
6	log-normal	0.0/1.0/3.0	B03	0.01	$3.9 \pm 0.7$	$4.0 \pm 0.7$	$3.5 \pm 0.9$	0.1
6	log-normal	0.0/1.0/3.0	B01	0.01	$3.3 \pm 0.6$	$3.0 \pm 0.6$	$3.7 \pm 1.0$	4.5
6	log-normal	0.0/1.0/3.0	S08	0.01	$3.8 \pm 0.6$	$3.4 \pm 0.6$	$3.4 \pm 0.9$	1.1
6	log-normal	1.0/0.0/3.0	B03	0.01	$3.4 \pm 0.6$	$3.5 \pm 0.6$	$3.8 \pm 1.0$	1.7
6	log-normal	1.0/0.0/3.0	B01	0.01	$3.0 \pm 0.5$	$2.9 \pm 0.5$	$4.1 \pm 1.1$	7.3
6	log-normal	1.0/0.0/3.0	S08	0.01	$3.0 \pm 0.6$	$3.2 \pm 0.6$	$4.1 \pm 1.0$	5.2
6	log-normal	C03	B03	0.01	$3.3 \pm 0.7$	$3.0 \pm 0.6$	$3.8 \pm 1.0$	4.0
6	log-normal	C03	B01	0.01	$3.3 \pm 0.5$	$2.8 \pm 0.5$	$3.6 \pm 1.0$	6.6
6	log-normal	C03	S08	0.01	$3.8 \pm 0.7$	$2.9 \pm 0.6$	$3.8 \pm 1.0$	3.5
6	uniform	-1.5	B03	0.02	$2.7 \pm 0.6$	$2.7 \pm 0.5$	$3.8 \pm 1.1$	10.2
6	uniform	-1.5	B03	0.03	$2.7 \pm 0.5$	$2.5 \pm 0.4$	$3.6 \pm 0.9$	14.5
6	uniform	-1.5	B01	0.02	$2.4 \pm 0.5$	$2.7 \pm 0.5$	$3.5 \pm 0.9$	12.8
6	uniform	-1.5	B01	0.03	$2.4 \pm 0.5$	$2.7 \pm 0.5$	$3.7 \pm 0.9$	16.0
6	uniform	-1.5	S08	0.02	$2.6 \pm 0.5$	$2.7 \pm 0.5$	$3.5 \pm 0.9$	12.2
6	uniform	-1.5	S08	0.03	$3.0 \pm 0.5$	$2.8 \pm 0.5$	$3.6 \pm 0.9$	8.6
6	uniform	0.5	B03	0.02	$2.7 \pm 0.6$	$2.3 \pm 0.5$	$3.4 \pm 0.9$	15.8
6	uniform	0.5	B03	0.03	$2.6 \pm 0.5$	$2.3 \pm 0.5$	$3.4 \pm 0.9$	16.1
6	uniform	0.5	B01	0.02	$2.0 \pm 0.5$	$2.2 \pm 0.5$	$3.3 \pm 0.9$	25.3
6	uniform	0.5	B01	0.03	$2.3 \pm 0.5$	$2.2 \pm 0.5$	$3.4 \pm 0.9$	22.6
6	uniform	0.5	S08	0.02	$2.2 \pm 0.4$	$2.2 \pm 0.5$	$3.6 \pm 0.9$	24.4
6	uniform	0.5	S08	0.03	$2.1 \pm 0.4$	$2.2 \pm 0.4$	$3.6 \pm 0.9$	28.8
6	uniform	-0.5	B03	0.02	$2.7 \pm 0.5$	$2.3 \pm 0.5$	$3.6 \pm 0.9$	15.5
6	uniform	-0.5	B03	0.03	$2.8 \pm 0.6$	$2.6 \pm 0.5$	$3.5 \pm 0.8$	10.4
6	uniform	-0.5	B01	0.02	$2.4 \pm 0.5$	$2.4 \pm 0.5$	$3.6 \pm 1.0$	17.4
6	uniform	-0.5	B01	0.03	$2.4 \pm 0.5$	$2.6 \pm 0.5$	$3.6 \pm 1.0$	16.7
6	uniform	-0.5	S08	0.02	$2.3 \pm 0.4$	$2.6 \pm 0.5$	$3.4 \pm 0.9$	17.6
6	uniform	-0.5	S08	0.03	$2.9 \pm 0.6$	$2.6 \pm 0.5$	$3.5 \pm 1.0$	10.0
6	uniform	1.5	B03	0.02	$2.6 \pm 0.5$	$2.0 \pm 0.4$	$3.1 \pm 0.8$	23.4
6	uniform	1.5	B03	0.03	$2.6 \pm 0.6$	$2.0 \pm 0.4$	$3.4 \pm 0.9$	21.5
6	uniform	1.5	B01	0.02	$2.5 \pm 0.6$	$1.7 \pm 0.4$	$3.0 \pm 0.9$	31.5
6	uniform	1.5	B01	0.03	$1.7 \pm 0.4$	$1.9 \pm 0.4$	$3.4 \pm 0.9$	44.0
6	uniform	1.5	S08	0.02	$2.1 \pm 0.4$	$2.0 \pm 0.4$	$3.1 \pm 0.9$	32.7
6	uniform	1.5	S08	0.03	$2.3 \pm 0.5$	$2.1 \pm 0.5$	$3.6 \pm 1.0$	23.2
6	uniform	0.0/1.0/3.0	B03	0.02	$2.8 \pm 0.6$	$2.3 \pm 0.5$	$2.6 \pm 0.7$	15.5
6	uniform	0.0/1.0/3.0	B03	0.03	$2.8 \pm 0.6$	$2.3 \pm 0.4$	$2.9 \pm 0.8$	15.0
6	uniform	0.0/1.0/3.0	B01	0.02	$2.6 \pm 0.6$	$2.3 \pm 0.5$	$2.7 \pm 0.7$	16.4
6	uniform	0.0/1.0/3.0	B01	0.03	$2.3 \pm 0.5$	$2.1 \pm 0.4$	$3.0 \pm 0.8$	25.0
6	uniform	0.0/1.0/3.0	S08	0.02	$2.7 \pm 0.5$	$2.2 \pm 0.5$	$2.9 \pm 0.8$	17.6
6	uniform	0.0/1.0/3.0	S08	0.03	$2.2 \pm 0.4$	$2.3 \pm 0.4$	$3.2 \pm 0.8$	24.3
6	uniform	1.0/0.0/3.0	B03	0.02	$2.8 \pm 0.6$	$2.7 \pm 0.5$	$3.5 \pm 1.0$	9.2
6	uniform	1.0/0.0/3.0	B03	0.03	$2.8 \pm 0.6$	$3.0 \pm 0.6$	$3.6 \pm 0.9$	6.7
6	uniform	1.0/0.0/3.0	B01	0.02	$2.2 \pm 0.5$	$2.1 \pm 0.4$	$3.5 \pm 0.9$	28.3
6	uniform	1.0/0.0/3.0	B01	0.03	$1.9 \pm 0.4$	$2.5 \pm 0.5$	$3.7 \pm 1.0$	27.0
6	uniform	1.0/0.0/3.0	S08	0.02	$2.0 \pm 0.4$	$2.3 \pm 0.4$	$3.7 \pm 1.0$	28.1
6	uniform	1.0/0.0/3.0	S08	0.03	$2.8 \pm 0.6$	$2.2 \pm 0.4$	$3.9 \pm 1.0$	16.4
6	uniform	C03	B03	0.02	$2.5 \pm 0.5$	$2.0 \pm 0.5$	$3.2 \pm 0.8$	22.6
6	uniform	C03	B03	0.03	$2.6 \pm 0.6$	$2.2 \pm 0.4$	$3.3 \pm 0.9$	18.2
6	uniform	C03	B01	0.02	$1.9 \pm 0.4$	$1.8 \pm 0.4$	$3.2 \pm 0.9$	39.4

**Table B1** *continued*

**Table B1** (*continued*)

$\tau$	Star formation	$\alpha$	Models	MBDM	late-M dwarf age	L dwarf age	T dwarf age	$\chi^2$
(Gyr)	(rate)			( $M_\odot$ )	(Gyr)	(Gyr)	(Gyr)	
6	uniform	C03	B01	0.03	2.2 ± 0.4	1.9 ± 0.4	3.4 ± 0.9	31.1
6	uniform	C03	S08	0.02	2.2 ± 0.4	2.1 ± 0.5	3.4 ± 0.9	26.9
6	uniform	C03	S08	0.03	2.2 ± 0.4	2.2 ± 0.5	3.6 ± 0.9	24.9
6	exponential	-1.5	B03	0.02	2.9 ± 0.6	2.9 ± 0.5	3.5 ± 0.9	8.2
6	exponential	-1.5	B03	0.03	2.9 ± 0.6	3.2 ± 0.6	4.2 ± 1.1	5.7
6	exponential	-1.5	B01	0.02	2.7 ± 0.5	3.0 ± 0.5	3.6 ± 0.9	9.7
6	exponential	-1.5	B01	0.03	2.9 ± 0.6	3.0 ± 0.5	3.5 ± 0.8	6.6
6	exponential	-1.5	S08	0.02	2.9 ± 0.6	3.0 ± 0.6	3.9 ± 0.9	6.3
6	exponential	-1.5	S08	0.03	3.1 ± 0.6	2.8 ± 0.5	4.2 ± 1.1	7.1
6	exponential	0.5	B03	0.02	3.0 ± 0.6	2.6 ± 0.5	3.6 ± 1.0	9.1
6	exponential	0.5	B03	0.03	3.0 ± 0.6	2.7 ± 0.5	3.6 ± 0.9	8.0
6	exponential	0.5	B01	0.02	2.4 ± 0.5	2.3 ± 0.5	3.4 ± 1.0	18.2
6	exponential	0.5	B01	0.03	2.3 ± 0.5	2.7 ± 0.6	3.5 ± 0.9	15.4
6	exponential	0.5	S08	0.02	2.7 ± 0.5	2.6 ± 0.6	3.5 ± 1.0	11.2
6	exponential	0.5	S08	0.03	2.6 ± 0.5	2.6 ± 0.5	3.8 ± 1.0	14.3
6	exponential	-0.5	B03	0.02	3.2 ± 0.6	2.7 ± 0.5	3.5 ± 0.9	6.6
6	exponential	-0.5	B03	0.03	3.0 ± 0.6	2.9 ± 0.6	3.9 ± 1.0	6.5
6	exponential	-0.5	B01	0.02	2.7 ± 0.5	2.6 ± 0.5	3.7 ± 1.0	13.4
6	exponential	-0.5	B01	0.03	2.4 ± 0.5	2.6 ± 0.4	3.7 ± 0.9	17.0
6	exponential	-0.5	S08	0.02	2.6 ± 0.4	2.8 ± 0.6	3.9 ± 1.0	11.9
6	exponential	-0.5	S08	0.03	2.9 ± 0.6	3.1 ± 0.6	3.8 ± 1.0	5.5
6	exponential	1.5	B03	0.02	2.8 ± 0.5	2.2 ± 0.5	3.5 ± 1.0	16.2
6	exponential	1.5	B03	0.03	3.0 ± 0.6	2.5 ± 0.5	3.7 ± 1.0	9.9
6	exponential	1.5	B01	0.02	2.6 ± 0.5	2.3 ± 0.5	3.3 ± 0.9	16.9
6	exponential	1.5	B01	0.03	2.4 ± 0.5	2.2 ± 0.4	3.7 ± 0.9	21.7
6	exponential	1.5	S08	0.02	2.7 ± 0.5	2.3 ± 0.5	3.4 ± 0.9	16.1
6	exponential	1.5	S08	0.03	2.6 ± 0.4	2.4 ± 0.5	3.7 ± 0.9	16.3
6	exponential	0.0/1.0/3.0	B03	0.02	3.1 ± 0.5	2.8 ± 0.5	3.0 ± 0.8	7.6
6	exponential	0.0/1.0/3.0	B03	0.03	3.3 ± 0.7	2.7 ± 0.5	3.4 ± 0.9	6.6
6	exponential	0.0/1.0/3.0	B01	0.02	2.5 ± 0.5	2.6 ± 0.5	3.2 ± 0.9	15.2
6	exponential	0.0/1.0/3.0	B01	0.03	2.6 ± 0.5	2.3 ± 0.5	3.4 ± 0.9	15.9
6	exponential	0.0/1.0/3.0	S08	0.02	2.6 ± 0.5	2.4 ± 0.4	3.2 ± 0.9	18.2
6	exponential	0.0/1.0/3.0	S08	0.03	2.8 ± 0.5	2.5 ± 0.5	3.5 ± 0.8	12.6
6	exponential	1.0/0.0/3.0	B03	0.02	2.9 ± 0.6	2.9 ± 0.5	3.9 ± 1.1	7.4
6	exponential	1.0/0.0/3.0	B03	0.03	3.1 ± 0.6	3.1 ± 0.6	4.1 ± 1.1	4.4
6	exponential	1.0/0.0/3.0	B01	0.02	2.3 ± 0.5	2.7 ± 0.5	3.6 ± 0.9	16.1
6	exponential	1.0/0.0/3.0	B01	0.03	2.6 ± 0.5	2.7 ± 0.5	4.0 ± 1.0	11.8
6	exponential	1.0/0.0/3.0	S08	0.02	2.7 ± 0.5	2.6 ± 0.5	3.9 ± 1.0	11.9
6	exponential	1.0/0.0/3.0	S08	0.03	2.7 ± 0.5	2.9 ± 0.6	4.1 ± 1.0	9.6
6	exponential	C03	B03	0.02	2.8 ± 0.6	2.4 ± 0.5	3.4 ± 0.9	13.1
6	exponential	C03	B03	0.03	2.9 ± 0.6	2.2 ± 0.4	3.6 ± 1.0	16.3
6	exponential	C03	B01	0.02	2.7 ± 0.5	2.3 ± 0.5	3.4 ± 0.9	17.1
6	exponential	C03	B01	0.03	2.4 ± 0.5	2.5 ± 0.5	3.8 ± 1.0	16.3
6	exponential	C03	S08	0.02	2.4 ± 0.6	2.4 ± 0.5	3.5 ± 0.9	15.6
6	exponential	C03	S08	0.03	3.0 ± 0.6	2.7 ± 0.5	4.0 ± 1.0	8.5
6	log-normal	-1.5	B03	0.02	4.0 ± 0.7	3.4 ± 0.6	4.5 ± 1.1	1.8
6	log-normal	-1.5	B03	0.03	3.6 ± 0.6	3.6 ± 0.7	4.4 ± 1.1	1.7
6	log-normal	-1.5	B01	0.02	3.5 ± 0.6	3.5 ± 0.6	4.1 ± 1.0	2.3
6	log-normal	-1.5	B01	0.03	3.4 ± 0.6	3.7 ± 0.6	4.3 ± 1.1	2.1
6	log-normal	-1.5	S08	0.02	3.2 ± 0.6	3.6 ± 0.6	4.1 ± 1.0	2.5
6	log-normal	-1.5	S08	0.03	3.1 ± 0.6	4.0 ± 0.7	4.1 ± 1.0	2.7
6	log-normal	0.5	B03	0.02	3.5 ± 0.6	3.4 ± 0.6	4.2 ± 1.1	2.4

**Table B1** *continued*

**Table B1** (*continued*)

$\tau$	Star formation	$\alpha$	Models	MBDM	late-M dwarf age	L dwarf age	T dwarf age	$\chi^2$
(Gyr)	(rate)			( $M_\odot$ )	(Gyr)	(Gyr)	(Gyr)	
6	log-normal	0.5	B03	0.03	$3.7 \pm 0.8$	$3.5 \pm 0.7$	$4.0 \pm 1.0$	1.2
6	log-normal	0.5	B01	0.02	$3.7 \pm 0.7$	$3.0 \pm 0.6$	$3.9 \pm 1.0$	3.3
6	log-normal	0.5	B01	0.03	$3.3 \pm 0.6$	$3.4 \pm 0.6$	$4.1 \pm 1.0$	3.1
6	log-normal	0.5	S08	0.02	$4.2 \pm 0.8$	$3.3 \pm 0.6$	$4.0 \pm 1.1$	1.7
6	log-normal	0.5	S08	0.03	$3.6 \pm 0.6$	$3.2 \pm 0.6$	$4.1 \pm 1.0$	2.6
6	log-normal	-0.5	B03	0.02	$3.5 \pm 0.7$	$3.6 \pm 0.6$	$4.0 \pm 1.0$	1.5
6	log-normal	-0.5	B03	0.03	$3.9 \pm 0.7$	$3.3 \pm 0.6$	$4.1 \pm 1.0$	1.9
6	log-normal	-0.5	B01	0.02	$3.1 \pm 0.6$	$3.0 \pm 0.5$	$4.2 \pm 1.1$	5.7
6	log-normal	-0.5	B01	0.03	$3.8 \pm 0.7$	$3.3 \pm 0.6$	$4.3 \pm 1.1$	2.1
6	log-normal	-0.5	S08	0.02	$3.6 \pm 0.6$	$3.6 \pm 0.6$	$4.1 \pm 1.0$	1.4
6	log-normal	-0.5	S08	0.03	$4.1 \pm 0.7$	$3.5 \pm 0.6$	$4.2 \pm 1.0$	1.2
6	log-normal	1.5	B03	0.02	$4.0 \pm 0.8$	$3.0 \pm 0.6$	$3.8 \pm 0.9$	3.1
6	log-normal	1.5	B03	0.03	$3.8 \pm 0.7$	$3.1 \pm 0.6$	$4.0 \pm 1.0$	2.4
6	log-normal	1.5	B01	0.02	$3.1 \pm 0.5$	$2.7 \pm 0.5$	$3.7 \pm 1.0$	7.9
6	log-normal	1.5	B01	0.03	$3.3 \pm 0.6$	$2.8 \pm 0.5$	$4.3 \pm 1.1$	6.2
6	log-normal	1.5	S08	0.02	$3.8 \pm 0.6$	$3.1 \pm 0.5$	$3.9 \pm 1.0$	2.9
6	log-normal	1.5	S08	0.03	$3.6 \pm 0.6$	$3.2 \pm 0.6$	$4.0 \pm 1.0$	2.6
6	log-normal	0.0/1.0/3.0	B03	0.02	$3.6 \pm 0.7$	$3.3 \pm 0.6$	$3.5 \pm 1.0$	1.9
6	log-normal	0.0/1.0/3.0	B03	0.03	$3.7 \pm 0.6$	$3.4 \pm 0.6$	$3.6 \pm 1.0$	1.6
6	log-normal	0.0/1.0/3.0	B01	0.02	$3.5 \pm 0.6$	$2.9 \pm 0.5$	$3.7 \pm 1.0$	4.6
6	log-normal	0.0/1.0/3.0	B01	0.03	$3.1 \pm 0.6$	$2.8 \pm 0.5$	$4.1 \pm 1.1$	7.0
6	log-normal	0.0/1.0/3.0	S08	0.02	$3.9 \pm 0.7$	$3.4 \pm 0.6$	$3.6 \pm 1.0$	1.2
6	log-normal	0.0/1.0/3.0	S08	0.03	$3.5 \pm 0.6$	$3.2 \pm 0.6$	$3.8 \pm 1.0$	2.8
6	log-normal	1.0/0.0/3.0	B03	0.02	$3.5 \pm 0.6$	$3.5 \pm 0.6$	$4.1 \pm 1.0$	1.9
6	log-normal	1.0/0.0/3.0	B03	0.03	$3.7 \pm 0.6$	$4.0 \pm 0.8$	$4.6 \pm 1.1$	1.1
6	log-normal	1.0/0.0/3.0	B01	0.02	$2.9 \pm 0.5$	$3.2 \pm 0.6$	$4.1 \pm 1.1$	6.4
6	log-normal	1.0/0.0/3.0	B01	0.03	$2.9 \pm 0.6$	$3.3 \pm 0.6$	$4.5 \pm 1.1$	5.4
6	log-normal	1.0/0.0/3.0	S08	0.02	$3.4 \pm 0.6$	$3.3 \pm 0.6$	$4.3 \pm 1.1$	3.4
6	log-normal	1.0/0.0/3.0	S08	0.03	$3.3 \pm 0.5$	$3.4 \pm 0.6$	$4.4 \pm 1.1$	3.8
6	log-normal	C03	B03	0.02	$3.6 \pm 0.6$	$2.9 \pm 0.6$	$3.9 \pm 1.0$	4.1
6	log-normal	C03	B03	0.03	$3.3 \pm 0.7$	$3.1 \pm 0.6$	$4.1 \pm 1.1$	3.4
6	log-normal	C03	B01	0.02	$2.7 \pm 0.5$	$2.9 \pm 0.6$	$3.7 \pm 1.0$	9.8
6	log-normal	C03	B01	0.03	$3.3 \pm 0.6$	$2.9 \pm 0.5$	$4.1 \pm 1.1$	5.7
6	log-normal	C03	S08	0.02	$2.9 \pm 0.5$	$3.2 \pm 0.6$	$4.0 \pm 1.1$	6.8
6	log-normal	C03	S08	0.03	$3.5 \pm 0.6$	$3.1 \pm 0.6$	$4.2 \pm 1.1$	3.5
12	uniform	0.5	B03	0.01	$4.4 \pm 0.9$	$3.2 \pm 0.6$	$4.7 \pm 1.3$	2.5
12	uniform	0.5	B01	0.01	$4.2 \pm 0.9$	$3.3 \pm 0.6$	$4.4 \pm 1.3$	1.7
12	uniform	0.5	S08	0.01	$3.6 \pm 0.7$	$3.7 \pm 0.8$	$4.7 \pm 1.2$	1.4
12	uniform	0.5	M19	0.01	$2.7 \pm 0.4$	$3.8 \pm 0.7$	$5.4 \pm 1.4$	10.4
12	uniform	0.5	P20C	0.01	$0.3 \pm 0.1$	$2.9 \pm 0.6$	$4.7 \pm 1.3$	153.5
12	uniform	0.5	P20NW	0.01	$0.3 \pm 0.1$	$2.8 \pm 0.6$	$4.7 \pm 1.3$	150.0
12	uniform	0.5	P20NS	0.01	$0.3 \pm 0.1$	$2.7 \pm 0.6$	$4.7 \pm 1.3$	153.4
12	exponential	0.5	B03	0.01	$5.5 \pm 1.1$	$4.3 \pm 0.7$	$5.4 \pm 1.5$	3.3
12	exponential	0.5	B01	0.01	$4.2 \pm 0.8$	$4.4 \pm 0.8$	$5.6 \pm 1.4$	2.2
12	exponential	0.5	S08	0.01	$4.7 \pm 0.7$	$4.2 \pm 0.8$	$5.3 \pm 1.4$	2.3
12	log-normal	0.5	B03	0.01	$7.3 \pm 0.9$	$6.4 \pm 0.8$	$7.3 \pm 1.8$	23.8
12	log-normal	0.5	B01	0.01	$7.3 \pm 0.4$	$7.3 \pm 0.8$	$7.6 \pm 1.8$	66.0
12	log-normal	0.5	S08	0.01	$7.1 \pm 1.0$	$7.0 \pm 1.1$	$7.3 \pm 1.9$	19.2
12	uniform	-1.5	B03	0.01	$4.3 \pm 0.8$	$4.3 \pm 0.7$	$5.5 \pm 1.4$	2.0
12	uniform	-1.5	B01	0.01	$5.0 \pm 1.0$	$4.4 \pm 0.8$	$5.4 \pm 1.3$	3.0
12	uniform	-1.5	S08	0.01	$4.7 \pm 0.8$	$4.2 \pm 0.8$	$5.7 \pm 1.5$	2.5
12	uniform	-0.5	B03	0.01	$4.3 \pm 0.8$	$3.6 \pm 0.6$	$5.1 \pm 1.3$	1.9

**Table B1** *continued*

**Table B1** (*continued*)

$\tau$	Star formation	$\alpha$	Models	MBDM	late-M dwarf age	L dwarf age	T dwarf age	$\chi^2$
(Gyr)	(rate)			( $M_\odot$ )	(Gyr)	(Gyr)	(Gyr)	
12	uniform	-0.5	B01	0.01	3.8 ± 0.8	3.8 ± 0.7	4.8 ± 1.2	1.3
12	uniform	-0.5	S08	0.01	4.7 ± 1.0	4.0 ± 0.7	5.2 ± 1.3	2.2
12	uniform	1.5	B03	0.01	4.4 ± 0.8	3.0 ± 0.6	3.8 ± 1.1	2.7
12	uniform	1.5	B01	0.01	2.9 ± 0.5	3.1 ± 0.6	3.8 ± 1.1	6.7
12	uniform	1.5	S08	0.01	3.1 ± 0.4	2.9 ± 0.6	4.0 ± 1.2	6.4
12	uniform	0.0/1.0/3.0	B03	0.01	4.7 ± 0.9	4.2 ± 0.8	4.1 ± 1.2	0.7
12	uniform	0.0/1.0/3.0	B01	0.01	4.1 ± 0.8	2.9 ± 0.7	4.4 ± 1.3	2.8
12	uniform	0.0/1.0/3.0	S08	0.01	3.7 ± 0.6	3.4 ± 0.7	4.2 ± 1.1	1.5
12	uniform	1.0/0.0/3.0	B03	0.01	4.0 ± 0.7	4.3 ± 0.8	4.6 ± 1.3	0.8
12	uniform	1.0/0.0/3.0	B01	0.01	4.0 ± 0.9	3.2 ± 0.6	5.0 ± 1.4	3.0
12	uniform	1.0/0.0/3.0	S08	0.01	3.7 ± 0.6	3.6 ± 0.7	5.2 ± 1.3	2.2
12	uniform	C03	B03	0.01	4.4 ± 0.8	3.2 ± 0.7	4.8 ± 1.4	2.3
12	uniform	C03	B01	0.01	4.2 ± 0.9	2.9 ± 0.6	4.4 ± 1.3	3.7
12	uniform	C03	S08	0.01	3.9 ± 0.6	3.4 ± 0.7	4.4 ± 1.3	1.3
12	exponential	-1.5	B03	0.01	5.5 ± 1.0	5.0 ± 0.8	6.2 ± 1.5	6.1
12	exponential	-1.5	B01	0.01	5.3 ± 0.9	4.8 ± 0.9	6.3 ± 1.5	5.7
12	exponential	-1.5	S08	0.01	5.5 ± 0.8	5.0 ± 0.9	7.0 ± 1.6	8.2
12	exponential	-0.5	B03	0.01	5.9 ± 1.1	4.7 ± 0.9	5.6 ± 1.4	5.0
12	exponential	-0.5	B01	0.01	6.0 ± 1.0	4.8 ± 0.8	6.5 ± 1.7	6.9
12	exponential	-0.5	S08	0.01	4.7 ± 0.7	4.4 ± 0.7	5.8 ± 1.4	3.2
12	exponential	1.5	B03	0.01	5.3 ± 0.9	3.9 ± 0.7	5.0 ± 1.3	2.6
12	exponential	1.5	B01	0.01	5.2 ± 0.8	3.6 ± 0.6	4.9 ± 1.4	3.0
12	exponential	1.5	S08	0.01	4.7 ± 0.4	3.9 ± 0.7	5.3 ± 1.5	2.8
12	exponential	0.0/1.0/3.0	B03	0.01	5.3 ± 1.0	4.8 ± 0.8	4.6 ± 1.3	2.6
12	exponential	0.0/1.0/3.0	B01	0.01	4.6 ± 0.8	3.8 ± 0.7	5.2 ± 1.5	2.0
12	exponential	0.0/1.0/3.0	S08	0.01	4.9 ± 0.7	4.4 ± 0.8	5.1 ± 1.4	2.6
12	exponential	1.0/0.0/3.0	B03	0.01	6.0 ± 1.1	5.3 ± 1.0	5.2 ± 1.4	5.7
12	exponential	1.0/0.0/3.0	B01	0.01	5.4 ± 1.0	3.9 ± 0.7	5.4 ± 1.4	3.4
12	exponential	1.0/0.0/3.0	S08	0.01	4.8 ± 0.8	5.0 ± 0.9	5.6 ± 1.3	4.0
12	exponential	C03	B03	0.01	5.6 ± 1.0	4.1 ± 0.8	5.2 ± 1.4	3.5
12	exponential	C03	B01	0.01	5.7 ± 1.0	3.7 ± 0.8	5.1 ± 1.4	4.1
12	exponential	C03	S08	0.01	4.9 ± 0.7	4.4 ± 0.8	5.1 ± 1.4	2.7
12	log-normal	-1.5	B03	0.01	6.6 ± 0.9	6.5 ± 0.6	7.6 ± 1.7	25.0
12	log-normal	-1.5	B01	0.01	8.9 ± 0.4	9.6 ± 0.9	7.7 ± 1.6	118.9
12	log-normal	-1.5	S08	0.01	6.7 ± 1.0	6.8 ± 1.0	7.9 ± 1.9	19.0
12	log-normal	-0.5	B03	0.01	7.3 ± 0.9	6.4 ± 0.7	7.8 ± 1.7	26.6
12	log-normal	-0.5	B01	0.01	8.6 ± 0.6	8.3 ± 0.9	7.1 ± 1.8	66.4
12	log-normal	-0.5	S08	0.01	7.5 ± 1.0	7.4 ± 1.3	7.9 ± 1.9	21.6
12	log-normal	1.5	B03	0.01	8.0 ± 0.5	6.3 ± 0.4	7.9 ± 1.7	75.2
12	log-normal	1.5	B01	0.01	8.0 ± 1.0	6.8 ± 0.9	7.0 ± 1.8	26.4
12	log-normal	1.5	S08	0.01	8.4 ± 0.9	7.3 ± 1.2	7.3 ± 1.8	32.0
12	log-normal	0.0/1.0/3.0	B03	0.01	9.1 ± 1.3	8.4 ± 1.1	6.7 ± 1.6	31.5
12	log-normal	0.0/1.0/3.0	B01	0.01	7.5 ± 1.0	6.4 ± 1.1	7.6 ± 1.8	19.3
12	log-normal	0.0/1.0/3.0	S08	0.01	8.1 ± 1.3	7.1 ± 1.2	7.1 ± 1.6	20.4
12	log-normal	1.0/0.0/3.0	B03	0.01	7.8 ± 1.0	7.0 ± 1.1	7.6 ± 1.8	24.2
12	log-normal	1.0/0.0/3.0	B01	0.01	7.3 ± 1.3	7.6 ± 1.2	7.6 ± 1.7	18.8
12	log-normal	1.0/0.0/3.0	S08	0.01	7.2 ± 1.2	7.4 ± 1.2	7.5 ± 1.8	18.2
12	log-normal	C03	B03	0.01	7.1 ± 0.8	6.2 ± 0.7	7.9 ± 1.8	26.9
12	log-normal	C03	B01	0.01	7.6 ± 0.9	6.0 ± 0.9	7.4 ± 1.8	21.9
12	log-normal	C03	S08	0.01	7.0 ± 1.0	6.8 ± 1.0	7.3 ± 1.7	19.3
12	uniform	-1.5	B03	0.02	4.5 ± 0.8	4.6 ± 0.9	6.0 ± 1.6	2.6
12	uniform	-1.5	B03	0.03	4.3 ± 0.8	4.7 ± 0.9	5.8 ± 1.5	2.6

**Table B1** *continued*

**Table B1** (*continued*)

$\tau$	Star formation	$\alpha$	Models	MBDM	late-M dwarf age	L dwarf age	T dwarf age	$\chi^2$
(Gyr)	(rate)			( $M_\odot$ )	(Gyr)	(Gyr)	(Gyr)	
12	uniform	-1.5	B01	0.02	$4.2 \pm 0.8$	$3.9 \pm 0.7$	$5.6 \pm 1.4$	2.1
12	uniform	-1.5	B01	0.03	$4.0 \pm 0.7$	$4.0 \pm 0.8$	$5.6 \pm 1.3$	2.4
12	uniform	-1.5	S08	0.02	$4.5 \pm 0.8$	$4.2 \pm 0.8$	$5.6 \pm 1.4$	2.4
12	uniform	-1.5	S08	0.03	$4.8 \pm 0.8$	$4.2 \pm 0.7$	$5.9 \pm 1.5$	3.1
12	uniform	0.5	B03	0.02	$4.5 \pm 0.9$	$3.3 \pm 0.7$	$5.2 \pm 1.3$	3.0
12	uniform	0.5	B03	0.03	$4.3 \pm 0.8$	$3.5 \pm 0.7$	$5.5 \pm 1.4$	2.7
12	uniform	0.5	B01	0.02	$3.6 \pm 0.7$	$3.2 \pm 0.7$	$4.9 \pm 1.3$	2.8
12	uniform	0.5	B01	0.03	$3.8 \pm 0.7$	$3.6 \pm 0.8$	$5.2 \pm 1.3$	2.0
12	uniform	0.5	S08	0.02	$4.0 \pm 0.7$	$3.5 \pm 0.6$	$5.0 \pm 1.3$	2.0
12	uniform	0.5	S08	0.03	$4.1 \pm 0.7$	$3.6 \pm 0.7$	$5.8 \pm 1.4$	2.8
12	uniform	-0.5	B03	0.02	$4.6 \pm 1.0$	$3.9 \pm 0.8$	$5.3 \pm 1.4$	1.9
12	uniform	-0.5	B03	0.03	$4.5 \pm 0.9$	$3.8 \pm 0.7$	$5.5 \pm 1.3$	2.4
12	uniform	-0.5	B01	0.02	$4.1 \pm 0.8$	$3.5 \pm 0.6$	$4.9 \pm 1.3$	1.9
12	uniform	-0.5	B01	0.03	$3.8 \pm 0.7$	$3.8 \pm 0.8$	$5.6 \pm 1.4$	2.3
12	uniform	-0.5	S08	0.02	$3.8 \pm 0.6$	$4.0 \pm 0.8$	$5.5 \pm 1.4$	2.1
12	uniform	-0.5	S08	0.03	$4.2 \pm 0.7$	$4.1 \pm 0.8$	$6.0 \pm 1.5$	2.6
12	uniform	1.5	B03	0.02	$4.3 \pm 0.8$	$2.8 \pm 0.7$	$4.6 \pm 1.3$	3.4
12	uniform	1.5	B03	0.03	$4.5 \pm 0.9$	$3.2 \pm 0.7$	$5.2 \pm 1.4$	3.1
12	uniform	1.5	B01	0.02	$4.5 \pm 0.8$	$2.7 \pm 0.6$	$4.5 \pm 1.2$	5.0
12	uniform	1.5	B01	0.03	$3.8 \pm 0.8$	$2.8 \pm 0.6$	$5.3 \pm 1.4$	5.9
12	uniform	1.5	S08	0.02	$4.7 \pm 0.8$	$3.4 \pm 0.7$	$4.6 \pm 1.2$	2.1
12	uniform	1.5	S08	0.03	$4.8 \pm 0.8$	$3.4 \pm 0.7$	$5.4 \pm 1.5$	3.3
12	uniform	0.0/1.0/3.0	B03	0.02	$4.3 \pm 0.8$	$4.0 \pm 0.7$	$4.6 \pm 1.2$	0.8
12	uniform	0.0/1.0/3.0	B03	0.03	$4.5 \pm 0.9$	$4.2 \pm 0.8$	$5.2 \pm 1.4$	1.6
12	uniform	0.0/1.0/3.0	B01	0.02	$3.7 \pm 0.8$	$3.2 \pm 0.7$	$4.6 \pm 1.3$	2.4
12	uniform	0.0/1.0/3.0	B01	0.03	$3.4 \pm 0.6$	$3.2 \pm 0.7$	$5.2 \pm 1.4$	3.9
12	uniform	0.0/1.0/3.0	S08	0.02	$3.5 \pm 0.6$	$3.5 \pm 0.7$	$4.9 \pm 1.3$	2.4
12	uniform	0.0/1.0/3.0	S08	0.03	$4.0 \pm 0.6$	$3.6 \pm 0.7$	$5.4 \pm 1.4$	2.2
12	uniform	1.0/0.0/3.0	B03	0.02	$4.6 \pm 0.8$	$4.1 \pm 0.8$	$5.2 \pm 1.4$	1.7
12	uniform	1.0/0.0/3.0	B03	0.03	$5.0 \pm 1.0$	$4.1 \pm 0.7$	$5.3 \pm 1.2$	2.7
12	uniform	1.0/0.0/3.0	B01	0.02	$3.6 \pm 0.8$	$3.3 \pm 0.6$	$5.0 \pm 1.3$	3.2
12	uniform	1.0/0.0/3.0	B01	0.03	$3.6 \pm 0.7$	$3.7 \pm 0.7$	$5.4 \pm 1.3$	2.7
12	uniform	1.0/0.0/3.0	S08	0.02	$3.8 \pm 0.7$	$3.7 \pm 0.7$	$5.4 \pm 1.4$	2.2
12	uniform	1.0/0.0/3.0	S08	0.03	$3.9 \pm 0.7$	$3.5 \pm 0.7$	$6.1 \pm 1.5$	3.3
12	uniform	C03	B03	0.02	$4.5 \pm 0.9$	$2.9 \pm 0.6$	$4.8 \pm 1.3$	4.2
12	uniform	C03	B03	0.03	$4.3 \pm 0.8$	$3.0 \pm 0.6$	$5.3 \pm 1.3$	4.8
12	uniform	C03	B01	0.02	$3.5 \pm 0.7$	$2.9 \pm 0.7$	$4.6 \pm 1.3$	4.1
12	uniform	C03	B01	0.03	$3.6 \pm 0.7$	$3.1 \pm 0.6$	$5.2 \pm 1.3$	3.8
12	uniform	C03	S08	0.02	$4.4 \pm 0.7$	$3.3 \pm 0.7$	$4.9 \pm 1.4$	2.2
12	uniform	C03	S08	0.03	$3.8 \pm 0.7$	$3.4 \pm 0.7$	$5.6 \pm 1.4$	3.0
12	exponential	-1.5	B03	0.02	$5.8 \pm 1.1$	$5.2 \pm 0.8$	$6.8 \pm 1.7$	7.2
12	exponential	-1.5	B03	0.03	$5.5 \pm 1.0$	$5.4 \pm 0.9$	$6.1 \pm 1.5$	6.4
12	exponential	-1.5	B01	0.02	$4.9 \pm 0.9$	$4.9 \pm 0.9$	$6.2 \pm 1.6$	4.2
12	exponential	-1.5	B01	0.03	$4.6 \pm 0.8$	$4.5 \pm 0.7$	$6.3 \pm 1.6$	3.7
12	exponential	-1.5	S08	0.02	$4.1 \pm 0.6$	$5.2 \pm 0.9$	$6.3 \pm 1.6$	4.5
12	exponential	-1.5	S08	0.03	$5.6 \pm 0.9$	$5.1 \pm 0.9$	$6.6 \pm 1.7$	6.8
12	exponential	0.5	B03	0.02	$5.5 \pm 1.0$	$4.4 \pm 0.8$	$5.9 \pm 1.5$	4.2
12	exponential	0.5	B03	0.03	$5.6 \pm 1.0$	$4.2 \pm 0.8$	$6.3 \pm 1.7$	4.6
12	exponential	0.5	B01	0.02	$4.8 \pm 0.8$	$4.4 \pm 0.9$	$5.4 \pm 1.4$	2.5
12	exponential	0.5	B01	0.03	$4.9 \pm 0.9$	$4.3 \pm 0.8$	$6.0 \pm 1.5$	3.5
12	exponential	0.5	S08	0.02	$4.6 \pm 0.7$	$5.0 \pm 0.9$	$6.1 \pm 1.6$	3.8
12	exponential	0.5	S08	0.03	$5.4 \pm 0.9$	$4.6 \pm 0.9$	$6.1 \pm 1.5$	4.7

**Table B1** *continued*

**Table B1** (*continued*)

$\tau$	Star formation	$\alpha$	Models	MBDM	late-M dwarf age	L dwarf age	T dwarf age	$\chi^2$
(Gyr)	(rate)			( $M_\odot$ )	(Gyr)	(Gyr)	(Gyr)	
12	exponential	-0.5	B03	0.02	$5.8 \pm 1.1$	$4.3 \pm 0.8$	$5.7 \pm 1.4$	4.6
12	exponential	-0.5	B03	0.03	$5.8 \pm 1.1$	$5.0 \pm 0.9$	$6.1 \pm 1.6$	6.0
12	exponential	-0.5	B01	0.02	$5.3 \pm 0.9$	$5.2 \pm 0.9$	$5.9 \pm 1.5$	5.4
12	exponential	-0.5	B01	0.03	$5.0 \pm 0.8$	$4.7 \pm 0.8$	$6.2 \pm 1.6$	4.3
12	exponential	-0.5	S08	0.02	$5.7 \pm 1.0$	$4.9 \pm 0.8$	$6.1 \pm 1.6$	5.8
12	exponential	-0.5	S08	0.03	$6.1 \pm 0.9$	$5.1 \pm 1.0$	$6.4 \pm 1.7$	8.7
12	exponential	1.5	B03	0.02	$5.5 \pm 1.0$	$4.3 \pm 0.9$	$5.5 \pm 1.5$	3.5
12	exponential	1.5	B03	0.03	$4.9 \pm 0.9$	$3.8 \pm 0.6$	$6.3 \pm 1.6$	3.9
12	exponential	1.5	B01	0.02	$4.7 \pm 0.7$	$3.7 \pm 0.8$	$5.4 \pm 1.5$	2.5
12	exponential	1.5	B01	0.03	$4.2 \pm 0.7$	$3.9 \pm 0.7$	$5.8 \pm 1.4$	2.7
12	exponential	1.5	S08	0.02	$5.4 \pm 0.8$	$4.5 \pm 0.9$	$5.2 \pm 1.4$	4.4
12	exponential	1.5	S08	0.03	$5.6 \pm 0.8$	$4.4 \pm 0.8$	$6.0 \pm 1.5$	5.8
12	exponential	0.0/1.0/3.0	B03	0.02	$5.3 \pm 1.0$	$4.7 \pm 0.8$	$5.4 \pm 1.5$	3.4
12	exponential	0.0/1.0/3.0	B03	0.03	$5.6 \pm 1.0$	$5.2 \pm 1.0$	$6.1 \pm 1.6$	5.9
12	exponential	0.0/1.0/3.0	B01	0.02	$4.1 \pm 0.8$	$3.7 \pm 0.7$	$5.3 \pm 1.4$	1.9
12	exponential	0.0/1.0/3.0	B01	0.03	$4.9 \pm 0.9$	$3.6 \pm 0.7$	$5.7 \pm 1.4$	3.4
12	exponential	0.0/1.0/3.0	S08	0.02	$5.7 \pm 0.9$	$4.3 \pm 0.8$	$5.4 \pm 1.4$	4.4
12	exponential	0.0/1.0/3.0	S08	0.03	$6.0 \pm 0.9$	$4.4 \pm 0.8$	$6.2 \pm 1.7$	6.4
12	exponential	1.0/0.0/3.0	B03	0.02	$5.4 \pm 1.0$	$5.7 \pm 1.0$	$5.6 \pm 1.6$	5.4
12	exponential	1.0/0.0/3.0	B03	0.03	$5.1 \pm 0.9$	$5.6 \pm 1.0$	$6.2 \pm 1.6$	6.0
12	exponential	1.0/0.0/3.0	B01	0.02	$5.5 \pm 0.9$	$4.3 \pm 0.7$	$6.0 \pm 1.5$	4.8
12	exponential	1.0/0.0/3.0	B01	0.03	$5.1 \pm 1.0$	$4.5 \pm 0.8$	$6.1 \pm 1.8$	3.1
12	exponential	1.0/0.0/3.0	S08	0.02	$5.3 \pm 0.9$	$4.6 \pm 0.9$	$5.8 \pm 1.5$	4.4
12	exponential	1.0/0.0/3.0	S08	0.03	$4.8 \pm 0.8$	$4.7 \pm 0.9$	$6.6 \pm 1.7$	4.5
12	exponential	C03	B03	0.02	$5.6 \pm 1.0$	$4.2 \pm 0.8$	$5.8 \pm 1.4$	4.3
12	exponential	C03	B03	0.03	$5.5 \pm 0.9$	$4.4 \pm 0.8$	$6.2 \pm 1.6$	5.0
12	exponential	C03	B01	0.02	$4.7 \pm 0.8$	$4.2 \pm 0.9$	$5.2 \pm 1.4$	2.1
12	exponential	C03	B01	0.03	$4.4 \pm 0.8$	$4.2 \pm 0.8$	$5.8 \pm 1.5$	2.5
12	exponential	C03	S08	0.02	$5.4 \pm 0.9$	$4.2 \pm 0.8$	$5.6 \pm 1.4$	3.7
12	exponential	C03	S08	0.03	$5.3 \pm 0.9$	$4.3 \pm 0.8$	$6.0 \pm 1.6$	4.2
12	log-normal	-1.5	B03	0.02	$6.9 \pm 0.9$	$6.8 \pm 0.8$	$6.8 \pm 1.5$	23.6
12	log-normal	-1.5	B03	0.03	$8.3 \pm 1.0$	$8.1 \pm 0.8$	$7.8 \pm 1.5$	47.0
12	log-normal	-1.5	B01	0.02	$6.0 \pm 0.5$	$5.6 \pm 0.3$	$7.2 \pm 1.5$	30.7
12	log-normal	-1.5	B01	0.03	$7.2 \pm 0.4$	$7.4 \pm 0.7$	$7.6 \pm 1.6$	60.8
12	log-normal	-1.5	S08	0.02	$7.2 \pm 1.0$	$7.5 \pm 1.2$	$7.6 \pm 1.6$	22.4
12	log-normal	-1.5	S08	0.03	$7.7 \pm 1.1$	$7.6 \pm 1.2$	$7.4 \pm 1.8$	22.6
12	log-normal	0.5	B03	0.02	$6.8 \pm 0.9$	$8.2 \pm 1.2$	$7.6 \pm 1.7$	23.2
12	log-normal	0.5	B03	0.03	$7.4 \pm 0.8$	$8.4 \pm 1.0$	$7.6 \pm 1.7$	35.3
12	log-normal	0.5	B01	0.02	$6.8 \pm 0.5$	$6.3 \pm 0.6$	$7.2 \pm 1.6$	34.9
12	log-normal	0.5	B01	0.03	$7.5 \pm 0.6$	$6.6 \pm 0.8$	$7.4 \pm 1.6$	42.2
12	log-normal	0.5	S08	0.02	$7.8 \pm 1.3$	$7.0 \pm 1.1$	$7.6 \pm 1.8$	19.1
12	log-normal	0.5	S08	0.03	$6.4 \pm 0.4$	$6.6 \pm 0.8$	$8.8 \pm 1.9$	40.4
12	log-normal	-0.5	B03	0.02	$6.6 \pm 0.8$	$7.5 \pm 0.8$	$7.0 \pm 1.5$	29.4
12	log-normal	-0.5	B03	0.03	$6.7 \pm 0.9$	$7.1 \pm 0.9$	$7.4 \pm 1.5$	24.1
12	log-normal	-0.5	B01	0.02	$7.4 \pm 0.5$	$7.6 \pm 1.1$	$7.7 \pm 1.7$	48.7
12	log-normal	-0.5	B01	0.03	$9.1 \pm 0.8$	$8.5 \pm 1.1$	$7.8 \pm 1.8$	51.7
12	log-normal	-0.5	S08	0.02	$8.2 \pm 1.4$	$7.2 \pm 1.2$	$8.1 \pm 1.9$	20.7
12	log-normal	-0.5	S08	0.03	$8.0 \pm 1.2$	$7.2 \pm 1.2$	$8.1 \pm 2.0$	22.7
12	log-normal	1.5	B03	0.02	$8.4 \pm 0.9$	$7.0 \pm 0.7$	$6.9 \pm 1.7$	39.1
12	log-normal	1.5	B03	0.03	$8.2 \pm 1.0$	$7.3 \pm 1.1$	$8.0 \pm 1.9$	28.6
12	log-normal	1.5	B01	0.02	$5.7 \pm 0.2$	$5.1 \pm 0.3$	$7.2 \pm 1.9$	28.0
12	log-normal	1.5	B01	0.03	$9.7 \pm 0.0$	$6.5 \pm 0.8$	$7.6 \pm 1.8$	359.3

**Table B1** *continued*

**Table B1** (*continued*)

$\tau$	Star formation	$\alpha$	Models	MBDM	late-M dwarf age	L dwarf age	T dwarf age	$\chi^2$
(Gyr)	(rate)			( $M_\odot$ )	(Gyr)	(Gyr)	(Gyr)	
12	log-normal	1.5	S08	0.02	$9.3 \pm 1.3$	$7.4 \pm 1.3$	$7.6 \pm 1.9$	26.1
12	log-normal	1.5	S08	0.03	$7.5 \pm 1.1$	$7.4 \pm 1.2$	$7.8 \pm 1.9$	21.7
12	log-normal	0.0/1.0/3.0	B03	0.02	$8.8 \pm 1.1$	$7.5 \pm 1.1$	$7.8 \pm 1.9$	32.5
12	log-normal	0.0/1.0/3.0	B03	0.03	$7.7 \pm 1.2$	$7.4 \pm 1.1$	$7.7 \pm 1.8$	22.6
12	log-normal	0.0/1.0/3.0	B01	0.02	$9.1 \pm 0.6$	$7.2 \pm 0.9$	$7.1 \pm 1.6$	79.2
12	log-normal	0.0/1.0/3.0	B01	0.03	$5.5 \pm 0.3$	$5.8 \pm 0.7$	$8.0 \pm 1.8$	20.6
12	log-normal	0.0/1.0/3.0	S08	0.02	$8.1 \pm 1.2$	$7.6 \pm 1.3$	$7.6 \pm 1.7$	22.6
12	log-normal	0.0/1.0/3.0	S08	0.03	$7.6 \pm 1.2$	$7.5 \pm 1.2$	$7.9 \pm 1.9$	19.6
12	log-normal	1.0/0.0/3.0	B03	0.02	$7.4 \pm 1.0$	$6.8 \pm 1.0$	$6.9 \pm 1.5$	20.5
12	log-normal	1.0/0.0/3.0	B03	0.03	$6.9 \pm 1.1$	$7.7 \pm 1.2$	$7.8 \pm 1.8$	19.9
12	log-normal	1.0/0.0/3.0	B01	0.02	$6.7 \pm 0.5$	$7.4 \pm 1.1$	$7.8 \pm 1.8$	34.2
12	log-normal	1.0/0.0/3.0	B01	0.03	$7.6 \pm 1.2$	$7.0 \pm 1.2$	$7.7 \pm 1.8$	18.4
12	log-normal	1.0/0.0/3.0	S08	0.02	$7.8 \pm 1.2$	$7.2 \pm 1.3$	$7.8 \pm 1.8$	20.1
12	log-normal	1.0/0.0/3.0	S08	0.03	$8.6 \pm 1.4$	$7.2 \pm 1.2$	$7.5 \pm 1.8$	20.4
12	log-normal	C03	B03	0.02	$6.8 \pm 0.9$	$7.4 \pm 0.9$	$8.0 \pm 1.9$	26.1
12	log-normal	C03	B03	0.03	$7.7 \pm 1.0$	$6.2 \pm 0.9$	$7.5 \pm 1.9$	20.2
12	log-normal	C03	B01	0.02	$7.3 \pm 0.3$	$7.4 \pm 0.7$	$7.6 \pm 1.8$	73.9
12	log-normal	C03	B01	0.03	$7.6 \pm 0.6$	$5.9 \pm 0.7$	$7.4 \pm 1.7$	37.2
12	log-normal	C03	S08	0.02	$7.3 \pm 1.1$	$7.0 \pm 1.2$	$7.6 \pm 1.9$	17.5
12	log-normal	C03	S08	0.03	$7.8 \pm 1.2$	$7.5 \pm 1.3$	$7.8 \pm 1.8$	21.3
9 <sup>d</sup>	uniform	0.5	B03	0.01	$4.0 \pm 0.8$	$3.0 \pm 0.6$	$3.8 \pm 1.1$	2.8
9 <sup>e</sup>	uniform	0.5	B03*	0.01	$4.1 \pm 0.8$	$4.1 \pm 0.8$	$4.4 \pm 1.2$	0.5
9 <sup>c</sup>	uniform	1.5/-0.5/3.0	B03	0.01	$3.4 \pm 0.6$	$3.5 \pm 0.7$	$5.0 \pm 1.2$	3.2
9 <sup>c</sup>	uniform	1.5/-0.5/4.5	B03	0.01	$2.9 \pm 0.6$	$3.5 \pm 0.7$	$5.4 \pm 1.4$	5.6
9 <sup>c</sup>	uniform	1.5/-0.5/6.0	B03	0.01	$3.2 \pm 0.7$	$3.4 \pm 0.7$	$4.3 \pm 1.1$	2.7

NOTE—Kinematics ages computed using the Aumer & Binney (2009) relation and the procedure described in Section 5.4.  $\tau$  is the maximum age of the sample,  $\alpha$  is the mass function power law index ( $\frac{dN}{dM} = M^{-\alpha}$ ), MBDM is the minimum brown dwarf mass. Evolving mass functions are labeled in the order of early  $\alpha$ , late  $\alpha$ , and age (in Gyr) of transition. A log-normal mass function from Chabrier (2003) is labeled as “log-normal”. Star formation rates considered in our simulations: uniform, exponential (Aumer & Binney 2009), and cosmic star formation rate (Rujopakarn et al. 2010). Brown dwarf evolution models are B03 (Baraffe et al. 2003), B01 (Burrows et al. 2001), S08 (Saumon & Marley 2008), M19 (Marley et al. 2018), and P20 (Phillips et al. 2020). For the last model set, C, NW, and NS stand for chemical equilibrium, weak, and strong chemical disequilibrium, respectively. Note that only substellar models are available in the P20 set. See Table B1 in Appendix B for the full list of simulations.

<sup>a</sup> Baseline simulation

<sup>b</sup> Simulations with an evolving mass function from top-heavy to bottom-heavy over time using Baraffe et al. (2003) evolutionary models. See Section 5.4 for details.

<sup>c</sup> Simulations with an evolving mass function from bottom-heavy to top-heavy over time using Baraffe et al. (2003) evolutionary models. See Section 5.4 for details.

<sup>d</sup> Baseline simulation with selection within 20 pc and  $J$  or  $K < 15.5$ . See Section 6.1 for details.

<sup>e</sup> Simulation with an artificial decrease in the HBMM for the Baraffe et al. (2003) evolutionary models by fixing the temperatures of brown dwarfs down to masses of  $0.060 M_\odot$  to their 1 Gyr values. See Section 5.4 for details.

## REFERENCES

- Allard, F., Hauschildt, P. H., Alexander, D. R., Tamanai, A., & Schweitzer, A. 2001, ApJ, 556, 357, doi: [10.1086/321547](https://doi.org/10.1086/321547)
- Allard, F., Homeier, D., Freytag, B., & Sharp, C. M. 2012, in EAS Publications Series, Vol. 57, EAS Publications Series, ed. C. Reylé, C. Charbonnel, & M. Schultheis, 3–43, doi: [10.1051/eas/1257001](https://doi.org/10.1051/eas/1257001)
- Allen, P. R., Koerner, D. W., Reid, I. N., & Trilling, D. E. 2005, ApJ, 625, 385, doi: [10.1086/429548](https://doi.org/10.1086/429548)

- Allers, K. N., Gallimore, J. F., Liu, M. C., & Dupuy, T. J. 2016, *ApJ*, 819, 133, doi: [10.3847/0004-637X/819/2/133](https://doi.org/10.3847/0004-637X/819/2/133)
- Allers, K. N., & Liu, M. C. 2013, *ApJ*, 772, 79, doi: [10.1088/0004-637X/772/2/79](https://doi.org/10.1088/0004-637X/772/2/79)
- Angus, R., Morton, T. D., Foreman-Mackey, D., et al. 2019, *AJ*, 158, 173, doi: [10.3847/1538-3881/ab3c53](https://doi.org/10.3847/1538-3881/ab3c53)
- Artigau, É., Doyon, R., Lafrenière, D., et al. 2006, *ApJL*, 651, L57, doi: [10.1086/509146](https://doi.org/10.1086/509146)
- Astropy Collaboration, Robitaille, T. P., Tollerud, E. J., et al. 2013, *A&A*, 558, A33, doi: [10.1051/0004-6361/201322068](https://doi.org/10.1051/0004-6361/201322068)
- Aumer, M., & Binney, J. J. 2009, *MNRAS*, 397, 1286, doi: [10.1111/j.1365-2966.2009.15053.x](https://doi.org/10.1111/j.1365-2966.2009.15053.x)
- Bailer-Jones, C. A. L. 2004, *A&A*, 419, 703, doi: [10.1051/0004-6361:20040965](https://doi.org/10.1051/0004-6361:20040965)
- Bannister, N. P., & Jameson, R. F. 2007, *MNRAS*, 378, L24, doi: [10.1111/j.1745-3933.2007.00312.x](https://doi.org/10.1111/j.1745-3933.2007.00312.x)
- Baraffe, I., Chabrier, G., Barman, T. S., Allard, F., & Hauschildt, P. H. 2003, *A&A*, 402, 701, doi: [10.1051/0004-6361:20030252](https://doi.org/10.1051/0004-6361:20030252)
- Bardalez Gagliuffi, D. C., Gagné, J., Faherty, J. K., & Burgasser, A. J. 2018, *ApJ*, 854, 101, doi: [10.3847/1538-4357/aaa961](https://doi.org/10.3847/1538-4357/aaa961)
- Bardalez Gagliuffi, D. C., Gelino, C. R., & Burgasser, A. J. 2015, *AJ*, 150, 163, doi: [10.1088/0004-6256/150/5/163](https://doi.org/10.1088/0004-6256/150/5/163)
- Bardalez Gagliuffi, D. C., Burgasser, A. J., Gelino, C. R., et al. 2014, *ApJ*, 794, 143, doi: [10.1088/0004-637X/794/2/143](https://doi.org/10.1088/0004-637X/794/2/143)
- Bardalez Gagliuffi, D. C., Burgasser, A. J., Schmidt, S. J., et al. 2019, *ApJ*, 883, 205, doi: [10.3847/1538-4357/ab253d](https://doi.org/10.3847/1538-4357/ab253d)
- Barnes, J. R., Jenkins, J. S., Jones, H. R. A., et al. 2014, *MNRAS*, 439, 3094, doi: [10.1093/mnras/stu172](https://doi.org/10.1093/mnras/stu172)
- Barnes, S. A. 2003, *ApJ*, 586, 464, doi: [10.1086/367639](https://doi.org/10.1086/367639)
- Basri, G., & Martín, E. L. 1999, *AJ*, 118, 2460, doi: [10.1086/301079](https://doi.org/10.1086/301079)
- Basri, G., Mohanty, S., Allard, F., et al. 2000, *ApJ*, 538, 363, doi: [10.1086/309095](https://doi.org/10.1086/309095)
- Bastian, N., Covey, K. R., & Meyer, M. R. 2010, *ARA&A*, 48, 339, doi: [10.1146/annurev-astro-082708-101642](https://doi.org/10.1146/annurev-astro-082708-101642)
- Beane, A., Ness, M. K., & Bedell, M. 2018, *ApJ*, 867, 31, doi: [10.3847/1538-4357/aae07f](https://doi.org/10.3847/1538-4357/aae07f)
- Bell, C. P. M., Mamajek, E. E., & Naylor, T. 2015, *MNRAS*, 454, 593, doi: [10.1093/mnras/stv1981](https://doi.org/10.1093/mnras/stv1981)
- Bensby, T., Feltzing, S., & Lundström, I. 2003, *A&A*, 410, 527, doi: [10.1051/0004-6361:20031213](https://doi.org/10.1051/0004-6361:20031213)
- Best, W. M. J., Liu, M. C., Dupuy, T. J., & Magnier, E. A. 2017, *ApJL*, 843, L4, doi: [10.3847/2041-8213/aa76df](https://doi.org/10.3847/2041-8213/aa76df)
- Best, W. M. J., Liu, M. C., Magnier, E. A., & Dupuy, T. J. 2020a, *AJ*, 159, 257, doi: [10.3847/1538-3881/ab84f4](https://doi.org/10.3847/1538-3881/ab84f4)
- . 2020b, *AJ*, 159, 257, doi: [10.3847/1538-3881/ab84f4](https://doi.org/10.3847/1538-3881/ab84f4)
- Best, W. M. J., Liu, M. C., Magnier, E. A., et al. 2013, *ApJ*, 777, 84, doi: [10.1088/0004-637X/777/2/84](https://doi.org/10.1088/0004-637X/777/2/84)
- Best, W. M. J., Magnier, E. A., Liu, M. C., et al. 2018, *ApJS*, 234, 1, doi: [10.3847/1538-4365/aa9982](https://doi.org/10.3847/1538-4365/aa9982)
- Bird, J. 2019, in American Astronomical Society Meeting Abstracts, Vol. 233, American Astronomical Society Meeting Abstracts #233, 231.03
- Blake, C. H., Charbonneau, D., & White, R. J. 2010, *ApJ*, 723, 684, doi: [10.1088/0004-637X/723/1/684](https://doi.org/10.1088/0004-637X/723/1/684)
- Blake, C. H., Charbonneau, D., White, R. J., Marley, M. S., & Saumon, D. 2007, *ApJ*, 666, 1198, doi: [10.1086/520124](https://doi.org/10.1086/520124)
- Blake, C. H., Charbonneau, D., White, R. J., et al. 2008, *ApJL*, 678, L125, doi: [10.1086/588754](https://doi.org/10.1086/588754)
- Bochanski, J. J., Munn, J. A., Hawley, S. L., et al. 2007, *AJ*, 134, 2418, doi: [10.1086/522053](https://doi.org/10.1086/522053)
- Bovy, J. 2015, *ApJS*, 216, 29, doi: [10.1088/0067-0049/216/2/29](https://doi.org/10.1088/0067-0049/216/2/29)
- Bovy, J., & Tremaine, S. 2012, *ApJ*, 756, 89, doi: [10.1088/0004-637X/756/1/89](https://doi.org/10.1088/0004-637X/756/1/89)
- Brandt, T. D., Dupuy, T. J., Bowler, B. P., et al. 2020, *AJ*, 160, 196, doi: [10.3847/1538-3881/abb45e](https://doi.org/10.3847/1538-3881/abb45e)
- Burgasser, A. J. 2004, *ApJS*, 155, 191, doi: [10.1086/424386](https://doi.org/10.1086/424386)
- Burgasser, A. J. 2009, in IAU Symposium, Vol. 258, The Ages of Stars, ed. E. E. Mamajek, D. R. Soderblom, & R. F. G. Wyse, 317–326, doi: [10.1017/S1743921309031974](https://doi.org/10.1017/S1743921309031974)
- Burgasser, A. J., Blake, C. H., Gelino, C. R., Sahlmann, J., & Bardalez Gagliuffi, D. 2016, *ApJ*, 827, 25, doi: [10.3847/0004-637X/827/1/25](https://doi.org/10.3847/0004-637X/827/1/25)
- Burgasser, A. J., Burrows, A., & Kirkpatrick, J. D. 2006a, *ApJ*, 639, 1095, doi: [10.1086/499344](https://doi.org/10.1086/499344)
- Burgasser, A. J., Cruz, K. L., Cushing, M., et al. 2010, *ApJ*, 710, 1142, doi: [10.1088/0004-637X/710/2/1142](https://doi.org/10.1088/0004-637X/710/2/1142)
- Burgasser, A. J., Kirkpatrick, J. D., Cruz, K. L., et al. 2006b, *ApJS*, 166, 585, doi: [10.1086/506327](https://doi.org/10.1086/506327)
- Burgasser, A. J., Kirkpatrick, J. D., Liebert, J., & Burrows, A. 2003a, *ApJ*, 594, 510, doi: [10.1086/376756](https://doi.org/10.1086/376756)
- Burgasser, A. J., Kirkpatrick, J. D., McElwain, M. W., et al. 2003b, *AJ*, 125, 850, doi: [10.1086/345975](https://doi.org/10.1086/345975)
- Burgasser, A. J., Kirkpatrick, J. D., Reid, I. N., et al. 2003c, *ApJ*, 586, 512, doi: [10.1086/346263](https://doi.org/10.1086/346263)
- Burgasser, A. J., Liu, M. C., Ireland, M. J., Cruz, K. L., & Dupuy, T. J. 2008, *ApJ*, 681, 579, doi: [10.1086/588379](https://doi.org/10.1086/588379)
- Burgasser, A. J., Luk, C., Dhital, S., et al. 2012, *ApJ*, 757, 110, doi: [10.1088/0004-637X/757/2/110](https://doi.org/10.1088/0004-637X/757/2/110)
- Burgasser, A. J., McElwain, M. W., Kirkpatrick, J. D., et al. 2004, *AJ*, 127, 2856, doi: [10.1086/383549](https://doi.org/10.1086/383549)
- Burgasser, A. J., Sitarski, B. N., Gelino, C. R., Logsdon, S. E., & Perrin, M. D. 2011, *ApJ*, 739, 49, doi: [10.1088/0004-637X/739/1/49](https://doi.org/10.1088/0004-637X/739/1/49)

- Burgasser, A. J., & Splat Development Team. 2017, in Astronomical Society of India Conference Series, Vol. 14, Astronomical Society of India Conference Series, 7–12. <https://arxiv.org/abs/1707.00062>
- Burgasser, A. J., Kirkpatrick, J. D., Brown, M. E., et al. 1999, ApJL, 522, L65, doi: [10.1086/312221](https://doi.org/10.1086/312221)
- Burgasser, A. J., Kirkpatrick, J. D., Cutri, R. M., et al. 2000a, ApJL, 531, L57, doi: [10.1086/312522](https://doi.org/10.1086/312522)
- Burgasser, A. J., Wilson, J. C., Kirkpatrick, J. D., et al. 2000b, AJ, 120, 1100, doi: [10.1086/301475](https://doi.org/10.1086/301475)
- Burgasser, A. J., Kirkpatrick, J. D., Brown, M. E., et al. 2002, ApJ, 564, 421, doi: [10.1086/324033](https://doi.org/10.1086/324033)
- Burgasser, A. J., Gillon, M., Melis, C., et al. 2015a, AJ, 149, 104, doi: [10.1088/0004-6256/149/3/104](https://doi.org/10.1088/0004-6256/149/3/104)
- Burgasser, A. J., Logsdon, S. E., Gagné, J., et al. 2015b, ApJS, 220, 18, doi: [10.1088/0067-0049/220/1/18](https://doi.org/10.1088/0067-0049/220/1/18)
- Burrows, A., Hubbard, W. B., Lunine, J. I., & Liebert, J. 2001, Reviews of Modern Physics, 73, 719, doi: [10.1103/RevModPhys.73.719](https://doi.org/10.1103/RevModPhys.73.719)
- Burrows, A., Marley, M., Hubbard, W. B., et al. 1997, ApJ, 491, 856, doi: [10.1086/305002](https://doi.org/10.1086/305002)
- Caiazzo, I., Heyl, J. S., Richer, H., & Kalirai, J. 2017, ArXiv e-prints. <https://arxiv.org/abs/1702.00091>
- Cale, B., Plavchan, P., LeBrun, D., et al. 2019, AJ, 158, 170, doi: [10.3847/1538-3881/ab3b0f](https://doi.org/10.3847/1538-3881/ab3b0f)
- Chabrier, G. 2003, PASP, 115, 763, doi: [10.1086/376392](https://doi.org/10.1086/376392)
- Chabrier, G., Brassard, P., Fontaine, G., & Saumon, D. 2000, ApJ, 543, 216, doi: [10.1086/317092](https://doi.org/10.1086/317092)
- Chambers, K. C., & et al. 2017, VizieR Online Data Catalog, II/349
- Chen, B., Stoughton, C., Smith, J. A., et al. 2001, ApJ, 553, 184, doi: [10.1086/320647](https://doi.org/10.1086/320647)
- Chiu, K., Fan, X., Leggett, S. K., et al. 2006, AJ, 131, 2722, doi: [10.1086/501431](https://doi.org/10.1086/501431)
- Claret, A. 2000, A&A, 363, 1081
- Costa, E., Méndez, R. A., Jao, W.-C., et al. 2005, AJ, 130, 337, doi: [10.1086/430473](https://doi.org/10.1086/430473)
- Crossfield, I. J. M. 2014, A&A, 566, A130, doi: [10.1051/0004-6361/201423750](https://doi.org/10.1051/0004-6361/201423750)
- Cruz, K. L., Reid, I. N., Liebert, J., Kirkpatrick, J. D., & Lowrance, P. J. 2003, AJ, 126, 2421, doi: [10.1086/378607](https://doi.org/10.1086/378607)
- Cushing, M. C., Kirkpatrick, J. D., Gelino, C. R., et al. 2011, ApJ, 743, 50, doi: [10.1088/0004-637X/743/1/50](https://doi.org/10.1088/0004-637X/743/1/50)
- Cutri, R. M., & et al. 2012, VizieR Online Data Catalog, II/311
- Dahn, C. C., Harris, H. C., Subasavage, J. P., et al. 2017, AJ, 154, 147, doi: [10.3847/1538-3881/aa880b](https://doi.org/10.3847/1538-3881/aa880b)
- Davison, C. L., White, R. J., Henry, T. J., et al. 2015, AJ, 149, 106, doi: [10.1088/0004-6256/149/3/106](https://doi.org/10.1088/0004-6256/149/3/106)
- Deacon, N. R., Liu, M. C., Magnier, E. A., et al. 2011, AJ, 142, 77, doi: [10.1088/0004-6256/142/3/77](https://doi.org/10.1088/0004-6256/142/3/77)
- Deacon, N. R., Magnier, E. A., Liu, M. C., et al. 2017, MNRAS, 467, 1126, doi: [10.1093/mnras/stx065](https://doi.org/10.1093/mnras/stx065)
- Del Burgo, C., Martín, E. L., Zapatero Osorio, M. R., & Hauschildt, P. H. 2009, A&A, 501, 1059, doi: [10.1051/0004-6361/200810752](https://doi.org/10.1051/0004-6361/200810752)
- Deshpande, R., Martín, E. L., Montgomery, M. M., et al. 2012, AJ, 144, 99, doi: [10.1088/0004-6256/144/4/99](https://doi.org/10.1088/0004-6256/144/4/99)
- Deshpande, R., Blake, C. H., Bender, C. F., et al. 2013, AJ, 146, 156, doi: [10.1088/0004-6256/146/6/156](https://doi.org/10.1088/0004-6256/146/6/156)
- Dieterich, S. B., Henry, T. J., Jao, W.-C., et al. 2014, AJ, 147, 94, doi: [10.1088/0004-6256/147/5/94](https://doi.org/10.1088/0004-6256/147/5/94)
- Dittmann, J. A., Irwin, J. M., Charbonneau, D., & Berta-Thompson, Z. K. 2014, ApJ, 784, 156, doi: [10.1088/0004-637X/784/2/156](https://doi.org/10.1088/0004-637X/784/2/156)
- Dupuy, T. J., & Liu, M. C. 2012, ApJS, 201, 19, doi: [10.1088/0067-0049/201/2/19](https://doi.org/10.1088/0067-0049/201/2/19)
- . 2017, ApJS, 231, 15, doi: [10.3847/1538-4365/aa5e4c](https://doi.org/10.3847/1538-4365/aa5e4c)
- Dupuy, T. J., Liu, M. C., Best, W. M. J., et al. 2019, AJ, 158, 174, doi: [10.3847/1538-3881/ab3cd1](https://doi.org/10.3847/1538-3881/ab3cd1)
- Faherty, J. K., Burgasser, A. J., Cruz, K. L., et al. 2009, AJ, 137, 1, doi: [10.1088/0004-6256/137/1/1](https://doi.org/10.1088/0004-6256/137/1/1)
- Faherty, J. K., Gagné, J., Burgasser, A. J., et al. 2018, ApJ, 868, 44, doi: [10.3847/1538-4357/aadd04](https://doi.org/10.3847/1538-4357/aadd04)
- Faherty, J. K., Burgasser, A. J., Walter, F. M., et al. 2012, ApJ, 752, 56, doi: [10.1088/0004-637X/752/1/56](https://doi.org/10.1088/0004-637X/752/1/56)
- Faherty, J. K., Riedel, A. R., Cruz, K. L., et al. 2016, ApJS, 225, 10, doi: [10.3847/0067-0049/225/1/10](https://doi.org/10.3847/0067-0049/225/1/10)
- Fan, X., Knapp, G. R., Strauss, M. A., et al. 2000, AJ, 119, 928, doi: [10.1086/301224](https://doi.org/10.1086/301224)
- Filippazzo, J. C., Rice, E. L., Faherty, J., et al. 2015, ApJ, 810, 158, doi: [10.1088/0004-637X/810/2/158](https://doi.org/10.1088/0004-637X/810/2/158)
- Filliben, J. J. 1975, Technometrics, 17, 111, doi: [10.1080/00401706.1975.10489279](https://doi.org/10.1080/00401706.1975.10489279)
- Foreman-Mackey, D., Hogg, D. W., Lang, D., & Goodman, J. 2013, PASP, 125, 306, doi: [10.1086/670067](https://doi.org/10.1086/670067)
- Fulton, B. J., Petigura, E. A., Blunt, S., & Sinukoff, E. 2018, PASP, 130, 044504, doi: [10.1088/1538-3873/aaaaaa8](https://doi.org/10.1088/1538-3873/aaaaaa8)
- Gagné, J., Allers, K. N., Theissen, C. A., et al. 2018a, ApJL, 854, L27, doi: [10.3847/2041-8213/aaacfdd](https://doi.org/10.3847/2041-8213/aaacfdd)
- Gagné, J., Burgasser, A. J., Faherty, J. K., et al. 2015a, ApJL, 808, L20, doi: [10.1088/2041-8205/808/1/L20](https://doi.org/10.1088/2041-8205/808/1/L20)
- Gagné, J., Fontaine, G., Simon, A., & Faherty, J. K. 2018b, ApJL, 861, L13, doi: [10.3847/2041-8213/aaacdff](https://doi.org/10.3847/2041-8213/aaacdff)
- Gagné, J., Faherty, J. K., Cruz, K. L., et al. 2015b, ApJS, 219, 33, doi: [10.1088/0067-0049/219/2/33](https://doi.org/10.1088/0067-0049/219/2/33)
- Gagné, J., Faherty, J. K., Burgasser, A. J., et al. 2017, ApJL, 841, L1, doi: [10.3847/2041-8213/aa70e2](https://doi.org/10.3847/2041-8213/aa70e2)

- Gagné, J., Mamajek, E. E., Malo, L., et al. 2018c, ApJ, 856, 23, doi: [10.3847/1538-4357/aaae09](https://doi.org/10.3847/1538-4357/aaae09)
- Gaia Collaboration, Brown, A. G. A., Vallenari, A., et al. 2020, arXiv e-prints, arXiv:2012.01533. <https://arxiv.org/abs/2012.01533>
- . 2018, A&A, 616, A1, doi: [10.1051/0004-6361/201833051](https://doi.org/10.1051/0004-6361/201833051)
- Geballe, T. R., Knapp, G. R., Leggett, S. K., et al. 2002, ApJ, 564, 466, doi: [10.1086/324078](https://doi.org/10.1086/324078)
- Gelman, A., & Rubin, D. B. 1992, Statistical Science, 7, 457, doi: [10.1214/ss/1177011136](https://doi.org/10.1214/ss/1177011136)
- Gizis, J. E. 2002, ApJ, 575, 484, doi: [10.1086/341259](https://doi.org/10.1086/341259)
- Gizis, J. E., Monet, D. G., Reid, I. N., et al. 2000, AJ, 120, 1085, doi: [10.1086/301456](https://doi.org/10.1086/301456)
- Gizis, J. E., Troup, N. W., & Burgasser, A. J. 2011, ApJL, 736, L34, doi: [10.1088/2041-8205/736/2/L34](https://doi.org/10.1088/2041-8205/736/2/L34)
- Golimowski, D. A., Leggett, S. K., Marley, M. S., et al. 2004, AJ, 127, 3516, doi: [10.1086/420709](https://doi.org/10.1086/420709)
- Goodman, J., & Weare, J. 2010, Communications in Applied Mathematics and Computational Science, Vol. 5, No. 1, p. 65-80, 2010, 5, 65, doi: [10.2140/camcos.2010.5.65](https://doi.org/10.2140/camcos.2010.5.65)
- Goto, M., Kobayashi, N., Terada, H., et al. 2002, ApJL, 567, L59, doi: [10.1086/339800](https://doi.org/10.1086/339800)
- Gray, D. F. 1992, Journal of the British Astronomical Association, 102, 230
- Hawley, S. L., Covey, K. R., Knapp, G. R., et al. 2002, AJ, 123, 3409, doi: [10.1086/340697](https://doi.org/10.1086/340697)
- Hayashi, C., & Nakano, T. 1963, Progress of Theoretical Physics, 30, 460, doi: [10.1143/PTP.30.460](https://doi.org/10.1143/PTP.30.460)
- Haywood, M., Lehnert, M. D., Di Matteo, P., et al. 2016, A&A, 589, A66, doi: [10.1051/0004-6361/201527567](https://doi.org/10.1051/0004-6361/201527567)
- Heinze, A. N., Metchev, S., & Kellogg, K. 2015, ApJ, 801, 104, doi: [10.1088/0004-637X/801/2/104](https://doi.org/10.1088/0004-637X/801/2/104)
- Heinze, A. N., Metchev, S., Apai, D., et al. 2013, ApJ, 767, 173, doi: [10.1088/0004-637X/767/2/173](https://doi.org/10.1088/0004-637X/767/2/173)
- Henry, T. J., Subasavage, J. P., Brown, M. A., et al. 2004, AJ, 128, 2460, doi: [10.1086/425052](https://doi.org/10.1086/425052)
- Ho, A. Y. Q., Rix, H.-W., Ness, M. K., et al. 2017, ApJ, 841, 40, doi: [10.3847/1538-4357/aa6db3](https://doi.org/10.3847/1538-4357/aa6db3)
- Hsu, C.-C., Theissen, C., Burgasser, A., & Birky, J. 2021, SMART: The Spectral Modeling Analysis and RV Tool, v1.0.0, Zenodo, doi: [10.5281/zenodo.4765258](https://doi.org/10.5281/zenodo.4765258)
- Hunter, J. D. 2007, Computing in Science and Engineering, 9, 90, doi: [10.1109/MCSE.2007.55](https://doi.org/10.1109/MCSE.2007.55)
- Irwin, J., Berta, Z. K., Burke, C. J., et al. 2011, ApJ, 727, 56, doi: [10.1088/0004-637X/727/1/56](https://doi.org/10.1088/0004-637X/727/1/56)
- Jameson, R. F., Casewell, S. L., Bannister, N. P., et al. 2008a, MNRAS, 384, 1399, doi: [10.1111/j.1365-2966.2007.12637.x](https://doi.org/10.1111/j.1365-2966.2007.12637.x)
- Jameson, R. F., Lodieu, N., Casewell, S. L., Bannister, N. P., & Dobbie, P. D. 2008b, MNRAS, 385, 1771, doi: [10.1111/j.1365-2966.2008.12973.x](https://doi.org/10.1111/j.1365-2966.2008.12973.x)
- Joergens, V., & Müller, A. 2007, ApJL, 666, L113, doi: [10.1086/521825](https://doi.org/10.1086/521825)
- Johnson, D. R. H., & Soderblom, D. R. 1987, AJ, 93, 864, doi: [10.1086/114370](https://doi.org/10.1086/114370)
- Kass, R. E., & Raftery, A. E. 1995, Journal of the American Statistical Association, 90, 773, doi: [10.1080/01621459.1995.10476572](https://doi.org/10.1080/01621459.1995.10476572)
- Kiman, R., Schmidt, S. J., Angus, R., et al. 2019, AJ, 157, 231, doi: [10.3847/1538-3881/ab1753](https://doi.org/10.3847/1538-3881/ab1753)
- Kirkpatrick, J. D. 2005, Annual Review of Astronomy and Astrophysics, 43, 195, doi: [10.1146/annurev.astro.42.053102.134017](https://doi.org/10.1146/annurev.astro.42.053102.134017)
- Kirkpatrick, J. D., Henry, T. J., & McCarthy, Jr., D. W. 1991, ApJS, 77, 417, doi: [10.1086/191611](https://doi.org/10.1086/191611)
- Kirkpatrick, J. D.,Looper, D. L.,Burgasser, A. J.,et al. 2010,ApJS, 190, 100, doi: [10.1088/0067-0049/190/1/100](https://doi.org/10.1088/0067-0049/190/1/100)
- Kirkpatrick, J. D., Cushing, M. C., Gelino, C. R., et al. 2011, ApJS, 197, 19, doi: [10.1088/0067-0049/197/2/19](https://doi.org/10.1088/0067-0049/197/2/19)
- Kirkpatrick, J. D., Kellogg, K., Schneider, A. C., et al. 2016, ApJS, 224, 36, doi: [10.3847/0067-0049/224/2/36](https://doi.org/10.3847/0067-0049/224/2/36)
- Kirkpatrick, J. D., Martin, E. C., Smart, R. L., et al. 2019, ApJS, 240, 19, doi: [10.3847/1538-4365/aaf6af](https://doi.org/10.3847/1538-4365/aaf6af)
- Kirkpatrick, J. D., Gelino, C. R., Faherty, J. K., et al. 2021, ApJS, 253, 7, doi: [10.3847/1538-4365/abd107](https://doi.org/10.3847/1538-4365/abd107)
- Knapp, G. R., Leggett, S. K., Fan, X., et al. 2004, AJ, 127, 3553, doi: [10.1086/420707](https://doi.org/10.1086/420707)
- Koen, C. 2013, MNRAS, 428, 2824, doi: [10.1093/mnras/sts208](https://doi.org/10.1093/mnras/sts208)
- Koen, C., Matsunaga, N., & Menzies, J. 2004, MNRAS, 354, 466, doi: [10.1111/j.1365-2966.2004.08208.x](https://doi.org/10.1111/j.1365-2966.2004.08208.x)
- Koen, C., Miszalski, B., Väistönen, P., & Koen, T. 2017, MNRAS, 465, 4723, doi: [10.1093/mnras/stw3106](https://doi.org/10.1093/mnras/stw3106)
- Konopacky, Q. M., Ghez, A. M., Barman, T. S., et al. 2010, ApJ, 711, 1087, doi: [10.1088/0004-637X/711/2/1087](https://doi.org/10.1088/0004-637X/711/2/1087)
- Konopacky, Q. M., Ghez, A. M., Fabrycky, D. C., et al. 2012, ApJ, 750, 79, doi: [10.1088/0004-637X/750/1/79](https://doi.org/10.1088/0004-637X/750/1/79)
- Kramida, A., Yu. Ralchenko, Reader, J., & and NIST ASD Team. 2019, NIST Atomic Spectra Database (ver. 5.7.1), NIST Atomic Spectra Database (ver. 5.7.1), [Online]. Available: <https://physics.nist.gov/asd> [2019, September 12]. National Institute of Standards and Technology, Gaithersburg, MD.
- Kumar, S. S. 1963, ApJ, 137, 1121, doi: [10.1086/147589](https://doi.org/10.1086/147589)
- Laughlin, G., Bodenheimer, P., & Adams, F. C. 1997, ApJ, 482, 420, doi: [10.1086/304125](https://doi.org/10.1086/304125)

- Lawrence, A., Warren, S. J., Almaini, O., et al. 2007, MNRAS, 379, 1599, doi: [10.1111/j.1365-2966.2007.12040.x](https://doi.org/10.1111/j.1365-2966.2007.12040.x)
- . 2013, VizieR Online Data Catalog, II/319
- Leggett, S. K., Geballe, T. R., Fan, X., et al. 2000, ApJL, 536, L35, doi: [10.1086/312728](https://doi.org/10.1086/312728)
- Leggett, S. K., Saumon, D., Albert, L., et al. 2008a, ApJ, 682, 1256, doi: [10.1086/589146](https://doi.org/10.1086/589146)
- . 2008b, ApJ, 682, 1256, doi: [10.1086/589146](https://doi.org/10.1086/589146)
- Leggett, S. K., Birmingham, B., Saumon, D., et al. 2010, ApJ, 710, 1627, doi: [10.1088/0004-637X/710/2/1627](https://doi.org/10.1088/0004-637X/710/2/1627)
- Leinert, C., Allard, F., Richichi, A., & Hauschildt, P. H. 2000, Astronomy and Astrophysics, 353, 691
- Line, M. R., Marley, M. S., Liu, M. C., et al. 2017, ApJ, 848, 83, doi: [10.3847/1538-4357/aa7ff0](https://doi.org/10.3847/1538-4357/aa7ff0)
- Linsky, J. L. 1969, ApJ, 156, 989, doi: [10.1086/150030](https://doi.org/10.1086/150030)
- Liu, M. C., Dupuy, T. J., & Allers, K. N. 2016, ApJ, 833, 96, doi: [10.3847/1538-4357/833/1/96](https://doi.org/10.3847/1538-4357/833/1/96)
- Liu, M. C., Leggett, S. K., Golimowski, D. A., et al. 2006, ApJ, 647, 1393, doi: [10.1086/505561](https://doi.org/10.1086/505561)
- Liu, M. C., Delorme, P., Dupuy, T. J., et al. 2011, ApJ, 740, 108, doi: [10.1088/0004-637X/740/2/108](https://doi.org/10.1088/0004-637X/740/2/108)
- Lodieu, N., Scholz, R.-D., McCaughean, M. J., et al. 2005, A&A, 440, 1061, doi: [10.1051/0004-6361:20042456](https://doi.org/10.1051/0004-6361:20042456)
- Logsdon, S. E., Mace, G. N., McLean, I. S., & Martin, E. C. 2018, ApJ, 867, 96, doi: [10.3847/1538-4357/aade9b](https://doi.org/10.3847/1538-4357/aade9b)
- Looper, D. L., Gelino, C. R., Burgasser, A. J., & Kirkpatrick, J. D. 2008, ApJ, 685, 1183, doi: [10.1086/590382](https://doi.org/10.1086/590382)
- Looper, D. L., Kirkpatrick, J. D., & Burgasser, A. J. 2007, AJ, 134, 1162, doi: [10.1086/520645](https://doi.org/10.1086/520645)
- Luhman, K. L., Patten, B. M., Marengo, M., et al. 2007, ApJ, 654, 570, doi: [10.1086/509073](https://doi.org/10.1086/509073)
- Lutz, T. E., & Upgren, A. R. 1980, AJ, 85, 1390, doi: [10.1086/112812](https://doi.org/10.1086/112812)
- Mace, G. N. 2014, VizieR Online Data Catalog, 5144
- Mace, G. N., Kirkpatrick, J. D., Cushing, M. C., et al. 2013, ApJS, 205, 6, doi: [10.1088/0067-0049/205/1/6](https://doi.org/10.1088/0067-0049/205/1/6)
- Macintosh, B., Graham, J. R., Barman, T., et al. 2015, Science, 350, 64, doi: [10.1126/science.aac5891](https://doi.org/10.1126/science.aac5891)
- Madau, P., & Dickinson, M. 2014, ARA&A, 52, 415, doi: [10.1146/annurev-astro-081811-125615](https://doi.org/10.1146/annurev-astro-081811-125615)
- Manjavacas, E., Goldman, B., Reffert, S., & Henning, T. 2013, A&A, 560, A52, doi: [10.1051/0004-6361/201321720](https://doi.org/10.1051/0004-6361/201321720)
- Manjavacas, E., Apai, D., Zhou, Y., et al. 2019, AJ, 157, 101, doi: [10.3847/1538-3881/aaf88f](https://doi.org/10.3847/1538-3881/aaf88f)
- Marley, M., Saumon, D., Morley, C., & Fortney, J. 2018, Sonora 2018: Cloud-free, solar composition, solar C/O substellar evolution models, 1.0, Zenodo, doi: [10.5281/zenodo.2628068](https://doi.org/10.5281/zenodo.2628068)
- Marocco, F., Andrei, A. H., Smart, R. L., et al. 2013, AJ, 146, 161, doi: [10.1088/0004-6256/146/6/161](https://doi.org/10.1088/0004-6256/146/6/161)
- Martin, E. C., Mace, G. N., McLean, I. S., et al. 2017, ApJ, 838, 73, doi: [10.3847/1538-4357/aa6338](https://doi.org/10.3847/1538-4357/aa6338)
- Martin, E. C., Fitzgerald, M. P., McLean, I. S., et al. 2018, in Society of Photo-Optical Instrumentation Engineers (SPIE) Conference Series, Vol. 10702, Ground-based and Airborne Instrumentation for Astronomy VII, ed. C. J. Evans, L. Simard, & H. Takami, 107020A, doi: [10.1117/12.2312266](https://doi.org/10.1117/12.2312266)
- Martín, E. L., Lodieu, N., Pavlenko, Y., & Béjar, V. J. S. 2018, ApJ, 856, 40, doi: [10.3847/1538-4357/aaaeb8](https://doi.org/10.3847/1538-4357/aaaeb8)
- McCaughrean, M. J., Scholz, R.-D., & Lodieu, N. 2002, A&A, 390, L27, doi: [10.1051/0004-6361:20020928](https://doi.org/10.1051/0004-6361:20020928)
- McLean, I. S., Graham, J. R., Becklin, E. E., et al. 2000, in Proc. SPIE, Vol. 4008, Optical and IR Telescope Instrumentation and Detectors, ed. M. Iye & A. F. Moorwood, 1048–1055, doi: [10.1117/12.395422](https://doi.org/10.1117/12.395422)
- McLean, I. S., Prato, L., McGovern, M. R., et al. 2007, ApJ, 658, 1217, doi: [10.1086/511740](https://doi.org/10.1086/511740)
- McLean, I. S., Becklin, E. E., Bendiksen, O., et al. 1998, in Proc. SPIE, Vol. 3354, Infrared Astronomical Instrumentation, ed. A. M. Fowler, 566–578, doi: [10.1117/12.317283](https://doi.org/10.1117/12.317283)
- McQuillan, A., Aigrain, S., & Mazeh, T. 2013, MNRAS, 432, 1203, doi: [10.1093/mnras/stt536](https://doi.org/10.1093/mnras/stt536)
- Meisner, A. M., Faherty, J. K., Kirkpatrick, J. D., et al. 2020, ApJ, 899, 123, doi: [10.3847/1538-4357/aba633](https://doi.org/10.3847/1538-4357/aba633)
- Metchev, S. A., Kirkpatrick, J. D., Berriman, G. B., & Looper, D. 2008, ApJ, 676, 1281, doi: [10.1086/524721](https://doi.org/10.1086/524721)
- Metchev, S. A., Heinze, A., Apai, D., et al. 2015, ApJ, 799, 154, doi: [10.1088/0004-637X/799/2/154](https://doi.org/10.1088/0004-637X/799/2/154)
- Metodieva, Y., Antonova, A., Golev, V., et al. 2015, MNRAS, 446, 3878, doi: [10.1093/mnras/stu2370](https://doi.org/10.1093/mnras/stu2370)
- Miles, B. E., Skemer, A. J. I., Morley, C. V., et al. 2020, arXiv e-prints, arXiv:2004.10770, <https://arxiv.org/abs/2004.10770>
- Miyamoto, M., & Nagai, R. 1975, PASJ, 27, 533
- Moehler, S., Modigliani, A., Freudling, W., et al. 2014, A&A, 568, A9, doi: [10.1051/0004-6361/201423790](https://doi.org/10.1051/0004-6361/201423790)
- Mohanty, S., & Basri, G. 2003, ApJ, 583, 451, doi: [10.1086/345097](https://doi.org/10.1086/345097)
- Monet, D. G., Levine, S. E., Canzian, B., et al. 2003, AJ, 125, 984, doi: [10.1086/345888](https://doi.org/10.1086/345888)
- Morin, J., Donati, J. F., Petit, P., et al. 2010, MNRAS, 407, 2269, doi: [10.1111/j.1365-2966.2010.17101.x](https://doi.org/10.1111/j.1365-2966.2010.17101.x)
- Naud, M.-E., Artigau, É., Malo, L., et al. 2014, ApJ, 787, 5, doi: [10.1088/0004-637X/787/1/5](https://doi.org/10.1088/0004-637X/787/1/5)
- Newton, E. R., Charbonneau, D., Irwin, J., et al. 2014, AJ, 147, 20, doi: [10.1088/0004-6256/147/1/20](https://doi.org/10.1088/0004-6256/147/1/20)

- Newton, E. R., Mondrik, N., Irwin, J., Winters, J. G., & Charbonneau, D. 2018, AJ, 156, 217, doi: [10.3847/1538-3881/aad73b](https://doi.org/10.3847/1538-3881/aad73b)
- Nuzzo, R. 2014, Nature, 506, 150, doi: [10.1038/506150a](https://doi.org/10.1038/506150a)
- Outred, M. 1978in
- Phan-Bao, N., Bessell, M. S., Martín, E. L., et al. 2008, MNRAS, 383, 831, doi: [10.1111/j.1365-2966.2007.12564.x](https://doi.org/10.1111/j.1365-2966.2007.12564.x)
- Phillips, M. W., Tremblin, P., Baraffe, I., et al. 2020, arXiv e-prints, arXiv:2003.13717. <https://arxiv.org/abs/2003.13717>
- Pineda, J. S., Hallinan, G., Kirkpatrick, J. D., et al. 2016, ApJ, 826, 73, doi: [10.3847/0004-637X/826/1/73](https://doi.org/10.3847/0004-637X/826/1/73)
- Pinfield, D. J., Gomes, J., Day-Jones, A. C., et al. 2014, MNRAS, 437, 1009, doi: [10.1093/mnras/stt1437](https://doi.org/10.1093/mnras/stt1437)
- Planck Collaboration, Ade, P. A. R., Aghanim, N., et al. 2016, A&A, 594, A13, doi: [10.1051/0004-6361/201525830](https://doi.org/10.1051/0004-6361/201525830)
- Popinchalk, M., Faherty, J. K., Kiman, R., et al. 2021, arXiv e-prints, arXiv:2105.05935. <https://arxiv.org/abs/2105.05935>
- Prato, L., Mace, G. N., Rice, E. L., et al. 2015, ApJ, 808, 12, doi: [10.1088/0004-637X/808/1/12](https://doi.org/10.1088/0004-637X/808/1/12)
- Radigan, J., Jayawardhana, R., Lafrenière, D., et al. 2012, ApJ, 750, 105, doi: [10.1088/0004-637X/750/2/105](https://doi.org/10.1088/0004-637X/750/2/105)
- Reid, I. N., Cruz, K. L., Kirkpatrick, J. D., et al. 2008, AJ, 136, 1290, doi: [10.1088/0004-6256/136/3/1290](https://doi.org/10.1088/0004-6256/136/3/1290)
- Reid, I. N., & Gizis, J. E. 2005, PASP, 117, 676, doi: [10.1086/430462](https://doi.org/10.1086/430462)
- Reid, I. N., Kirkpatrick, J. D., Gizis, J. E., et al. 2000, AJ, 119, 369, doi: [10.1086/301177](https://doi.org/10.1086/301177)
- Reid, I. N., Kirkpatrick, J. D., Liebert, J., et al. 2002, AJ, 124, 519, doi: [10.1086/340805](https://doi.org/10.1086/340805)
- Reid, I. N., Lewitus, E., Allen, P. R., Cruz, K. L., & Burgasser, A. J. 2006, AJ, 132, 891, doi: [10.1086/505626](https://doi.org/10.1086/505626)
- Reid, I. N., Kirkpatrick, J. D., Liebert, J., et al. 1999, ApJ, 521, 613, doi: [10.1086/307589](https://doi.org/10.1086/307589)
- Reid, I. N., Cruz, K. L., Allen, P., et al. 2003, AJ, 126, 3007, doi: [10.1086/379173](https://doi.org/10.1086/379173)
- Reid, M. J., Menten, K. M., Brunthaler, A., et al. 2014, ApJ, 783, 130, doi: [10.1088/0004-637X/783/2/130](https://doi.org/10.1088/0004-637X/783/2/130)
- Reiners, A., & Basri, G. 2008, ApJ, 684, 1390, doi: [10.1086/590073](https://doi.org/10.1086/590073)
- . 2009, ApJ, 705, 1416, doi: [10.1088/0004-637X/705/2/1416](https://doi.org/10.1088/0004-637X/705/2/1416)
- . 2010, ApJ, 710, 924, doi: [10.1088/0004-637X/710/2/924](https://doi.org/10.1088/0004-637X/710/2/924)
- Reylé, C. 2018, A&A, 619, L8, doi: [10.1051/0004-6361/201834082](https://doi.org/10.1051/0004-6361/201834082)
- Rojo, P. M., & Harrington, J. 2006, ApJ, 649, 553, doi: [10.1086/506136](https://doi.org/10.1086/506136)
- Rujopakarn, W., Rieke, G. H., Weiner, B. J., et al. 2013, ApJ, 767, 73, doi: [10.1088/0004-637X/767/1/73](https://doi.org/10.1088/0004-637X/767/1/73)
- Rujopakarn, W., Eisenstein, D. J., Rieke, G. H., et al. 2010, ApJ, 718, 1171, doi: [10.1088/0004-637X/718/2/1171](https://doi.org/10.1088/0004-637X/718/2/1171)
- Ryan, Jr., R. E., Thorman, P. A., Schmidt, S. J., et al. 2017, ApJ, 847, 53, doi: [10.3847/1538-4357/aa85ea](https://doi.org/10.3847/1538-4357/aa85ea)
- Sahlmann, J., Burgasser, A. J., Bardalez Gagliuffi, D. C., et al. 2020, MNRAS, 495, 1136, doi: [10.1093/mnras/staa1235](https://doi.org/10.1093/mnras/staa1235)
- Sahlmann, J., Dupuy, T. J., Burgasser, A. J., et al. 2021, MNRAS, 500, 5453, doi: [10.1093/mnras/staa3577](https://doi.org/10.1093/mnras/staa3577)
- Salim, S., Lépine, S., Rich, R. M., & Shara, M. M. 2003, ApJL, 586, L149, doi: [10.1086/374794](https://doi.org/10.1086/374794)
- Samland, M., Mollière, P., Bonnefoy, M., et al. 2017, A&A, 603, A57, doi: [10.1051/0004-6361/201629767](https://doi.org/10.1051/0004-6361/201629767)
- Saumon, D., & Marley, M. S. 2008, ApJ, 689, 1327, doi: [10.1086/592734](https://doi.org/10.1086/592734)
- Schmidt, S. J., Cruz, K. L., Bongiorno, B. J., Liebert, J., & Reid, I. N. 2007, AJ, 133, 2258, doi: [10.1086/512158](https://doi.org/10.1086/512158)
- Schmidt, S. J., West, A. A., Hawley, S. L., & Pineda, J. S. 2010, AJ, 139, 1808, doi: [10.1088/0004-6256/139/5/1808](https://doi.org/10.1088/0004-6256/139/5/1808)
- Schneider, A. C., Cushing, M. C., Kirkpatrick, J. D., et al. 2014, AJ, 147, 34, doi: [10.1088/0004-6256/147/2/34](https://doi.org/10.1088/0004-6256/147/2/34)
- Schneider, A. C., Greco, J., Cushing, M. C., et al. 2016, ApJ, 817, 112, doi: [10.3847/0004-637X/817/2/112](https://doi.org/10.3847/0004-637X/817/2/112)
- Scholz, R. D. 2020, A&A, 637, A45, doi: [10.1051/0004-6361/201937373](https://doi.org/10.1051/0004-6361/201937373)
- Scholz, R. D., & Meusinger, H. 2002, Monthly Notices of the Royal Astronomical Society, 336, L49, doi: [10.1046/j.1365-8711.2002.05998.x](https://doi.org/10.1046/j.1365-8711.2002.05998.x)
- Schönrich, R., Binney, J., & Dehnen, W. 2010, MNRAS, 403, 1829, doi: [10.1111/j.1365-2966.2010.16253.x](https://doi.org/10.1111/j.1365-2966.2010.16253.x)
- Schwarz, G. 1978, Ann. Statist., 6, 461, doi: [10.1214/aos/1176344136](https://doi.org/10.1214/aos/1176344136)
- Seifahrt, A., Reiners, A., Almaghrbi, K. A. M., & Basri, G. 2010, A&A, 512, A37, doi: [10.1051/0004-6361/200913368](https://doi.org/10.1051/0004-6361/200913368)
- Shkolnik, E. L., Anglada-Escudé, G., Liu, M. C., et al. 2012, ApJ, 758, 56, doi: [10.1088/0004-637X/758/1/56](https://doi.org/10.1088/0004-637X/758/1/56)
- Skrutskie, M. F., Cutri, R. M., Stiening, R., et al. 2006, AJ, 131, 1163, doi: [10.1086/498708](https://doi.org/10.1086/498708)
- Smart, R. L., Tinney, C. G., Bucciarelli, B., et al. 2013, MNRAS, 433, 2054, doi: [10.1093/mnras/stt876](https://doi.org/10.1093/mnras/stt876)
- Smart, R. L., Bucciarelli, B., Jones, H. R. A., et al. 2018, MNRAS, 481, 3548, doi: [10.1093/mnras/sty2520](https://doi.org/10.1093/mnras/sty2520)
- Song, I., Bessell, M. S., & Zuckerman, B. 2002, ApJL, 581, L43, doi: [10.1086/345927](https://doi.org/10.1086/345927)
- Sorahana, S., & Yamamura, I. 2012, ApJ, 760, 151, doi: [10.1088/0004-637X/760/2/151](https://doi.org/10.1088/0004-637X/760/2/151)
- Stauffer, J. R., Schultz, G., & Kirkpatrick, J. D. 1998, ApJL, 499, L199+, doi: [10.1086/311379](https://doi.org/10.1086/311379)
- Stephens, D. C., Leggett, S. K., Cushing, M. C., et al. 2009, ApJ, 702, 154, doi: [10.1088/0004-637X/702/1/154](https://doi.org/10.1088/0004-637X/702/1/154)

- Strauss, M. A., Fan, X., Gunn, J. E., et al. 1999, ApJL, 522, L61, doi: [10.1086/312218](https://doi.org/10.1086/312218)
- Strömgren, G. 1924, ApJ, 59, 228, doi: [10.1086/142813](https://doi.org/10.1086/142813)
- Tanner, A., White, R., Bailey, J., et al. 2012, ApJS, 203, 10, doi: [10.1088/0067-0049/203/1/10](https://doi.org/10.1088/0067-0049/203/1/10)
- Tannock, M. E., Metchev, S., Heinze, A., et al. 2021a, arXiv e-prints, arXiv:2103.01990.  
<https://arxiv.org/abs/2103.01990>
- . 2021b, arXiv e-prints, arXiv:2103.01990.  
<https://arxiv.org/abs/2103.01990>
- Terrien, R. C., Mahadevan, S., Deshpande, R., & Bender, C. F. 2015, ApJS, 220, 16, doi: [10.1088/0067-0049/220/1/16](https://doi.org/10.1088/0067-0049/220/1/16)
- Thompson, M. A., Kirkpatrick, J. D., Mace, G. N., et al. 2013, PASP, 125, 809, doi: [10.1086/671426](https://doi.org/10.1086/671426)
- Ting, Y.-S., Hawkins, K., & Rix, H.-W. 2018, ApJL, 858, L7, doi: [10.3847/2041-8213/aabf8e](https://doi.org/10.3847/2041-8213/aabf8e)
- Ting, Y.-S., & Rix, H.-W. 2019, ApJ, 878, 21, doi: [10.3847/1538-4357/ab1ea5](https://doi.org/10.3847/1538-4357/ab1ea5)
- Torrence, C., & Compo, G. P. 1998, Bulletin of the American Meteorological Society, 79, 61, doi: [10.1175/1520-0477\(1998\)079<0061:APGTWA>2.0.CO;2](https://doi.org/10.1175/1520-0477(1998)079<0061:APGTWA>2.0.CO;2)
- Tran, H. D., Cohen, R., Colson, A., et al. 2016, in Proc. SPIE, Vol. 9910, Observatory Operations: Strategies, Processes, and Systems VI, 99102E, doi: [10.1117/12.2230963](https://doi.org/10.1117/12.2230963)
- van der Walt, S., Colbert, S. C., & Varoquaux, G. 2011, Computing in Science and Engineering, 13, 22, doi: [10.1109/MCSE.2011.37](https://doi.org/10.1109/MCSE.2011.37)
- Van Hoof, P. A. M. 2018, Galaxies, 6, doi: [10.3390/galaxies6020063](https://doi.org/10.3390/galaxies6020063)
- Virtanen, P., Gommers, R., Oliphant, T. E., et al. 2019, arXiv e-prints, arXiv:1907.10121.  
<https://arxiv.org/abs/1907.10121>
- Vos, J. M., Allers, K. N., & Biller, B. A. 2017, ApJ, 842, 78, doi: [10.3847/1538-4357/aa73cf](https://doi.org/10.3847/1538-4357/aa73cf)
- Vos, J. M., Allers, K. N., Biller, B. A., et al. 2018, MNRAS, 474, 1041, doi: [10.1093/mnras/stx2752](https://doi.org/10.1093/mnras/stx2752)
- Vos, J. M., Biller, B. A., Bonavita, M., et al. 2019, MNRAS, 483, 480, doi: [10.1093/mnras/sty3123](https://doi.org/10.1093/mnras/sty3123)
- Waskom, M., & the seaborn development team. 2020, mwaskom/seaborn, latest, Zenodo, doi: [10.5281/zenodo.592845](https://doi.org/10.5281/zenodo.592845)
- Weinberger, A. J., Boss, A. P., Keiser, S. A., et al. 2016, AJ, 152, 24, doi: [10.3847/0004-6256/152/1/24](https://doi.org/10.3847/0004-6256/152/1/24)
- Wes McKinney. 2010, in Proceedings of the 9th Python in Science Conference, ed. Stéfan van der Walt & Jarrod Millman, 56 – 61, doi: [10.25080/Majora-92bf1922-00a](https://doi.org/10.25080/Majora-92bf1922-00a)
- West, A. A., Weisenburger, K. L., Irwin, J., et al. 2015, ApJ, 812, 3, doi: [10.1088/0004-637X/812/1/3](https://doi.org/10.1088/0004-637X/812/1/3)
- West, A. A., Morgan, D. P., Bochanski, J. J., et al. 2011, AJ, 141, 97, doi: [10.1088/0004-6256/141/3/97](https://doi.org/10.1088/0004-6256/141/3/97)
- Wielen, R. 1977, A&A, 60, 263
- Wilson, P. A., Rajan, A., & Patience, J. 2014, A&A, 566, A111, doi: [10.1051/0004-6361/201322995](https://doi.org/10.1051/0004-6361/201322995)
- Yu, J., & Liu, C. 2018, MNRAS, 475, 1093, doi: [10.1093/mnras/stx3204](https://doi.org/10.1093/mnras/stx3204)
- Zapatero Osorio, M. R., Martín, E. L., Béjar, V. J. S., et al. 2007, ApJ, 666, 1205, doi: [10.1086/520673](https://doi.org/10.1086/520673)
- Zapatero Osorio, M. R., Martín, E. L., Bouy, H., et al. 2006, ApJ, 647, 1405, doi: [10.1086/505484](https://doi.org/10.1086/505484)
- Zhang, Z., Liu, M. C., Best, W. M. J., Dupuy, T. J., & Siverd, R. J. 2021, arXiv e-prints, arXiv:2102.05045.  
<https://arxiv.org/abs/2102.05045>
- Zhang, Z. H., Burgasser, A. J., Gálvez-Ortiz, M. C., et al. 2019, MNRAS, 486, 1260, doi: [10.1093/mnras/stz777](https://doi.org/10.1093/mnras/stz777)
- Zhou, Y., Apai, D., Metchev, S., et al. 2018, AJ, 155, 132, doi: [10.3847/1538-3881/aaabbd](https://doi.org/10.3847/1538-3881/aaabbd)
- Zuckerman, B., Bessell, M. S., Song, I., & Kim, S. 2006, ApJL, 649, L115, doi: [10.1086/508060](https://doi.org/10.1086/508060)
- Zuckerman, B., & Song, I. 2004, ARA&A, 42, 685, doi: [10.1146/annurev.astro.42.053102.134111](https://doi.org/10.1146/annurev.astro.42.053102.134111)